

OBSERVATIONS OF LONG PERIOD WAVES
IN THE TROPICAL OCEANS AND ATMOSPHERE

by

DOUGLAS SCOTT LUTHER
B.S. Massachusetts Institute of Technology
1973

SUBMITTED IN PARTIAL FULFILLMENT
OF THE REQUIREMENTS FOR THE
DEGREE OF
DOCTOR OF PHILOSOPHY

at the

MASSACHUSETTS INSTITUTE OF TECHNOLOGY

and

WOODS HOLE OCEANOGRAPHIC INSTITUTION
February 1980

Signature of Author

Douglas Scott Luther
Joint Program in Oceanography, Massachusetts Institute of
Technology-Woods Hole Oceanographic Institution, and the
Department of Earth and Planetary Sciences, Massachusetts
Institute of Technology, February 1980.

Certified by

[Signature]
Thesis Supervisor

Accepted by

[Signature]
Chairman, Joint Oceanographic Committee for Earth
Sciences, Massachusetts Institute of Technology-
Woods Hole Oceanographic Institution.

ARCHIVES
MASSACHUSETTS INSTITUTE
OF TECHNOLOGY

MAR 3 1980

LIBRARIES

OBSERVATIONS OF LONG PERIOD WAVES
IN THE TROPICAL OCEANS AND ATMOSPHERE

by

DOUGLAS SCOTT LUTHER

Submitted to the Joint Program in Oceanography, Massachusetts Institute of Technology - Woods Hole Oceanographic Institution, on December 17, 1979 in partial fulfillment of the requirements for the degree of Doctor of Philosophy.

ABSTRACT

The existence of resonant, baroclinic, equatorially-trapped inertia-gravity waves (discovered by Wunsch and Gill (1976)) is confirmed in the mid-Pacific by spectral analysis of long sea level records. The energy of the low-mode inertia-gravity waves is found to decrease toward the meridional boundaries. A simple spectral model, acknowledging the dispersive characteristics of the equatorial waves, adequately reproduces the observed mid-Pacific sea level spectra in the 1-6 day band. Model spectra computed at latitudes outside the equatorial waveguide of the gravest meridional modes suggest the presence of "inertial" peaks in several observed sea level spectra. Resonant, low-mode inertia-gravity waves may also exist in the Indian Ocean.

Sea level fluctuations along the Pacific equator are found to have Kelvin wave characteristics in the 35-80 day band, and, in particular, propagation from the western Pacific to the coast of South America is observed. The Kelvin waves are atmospherically-forced in the central-western Pacific and have a computed equivalent depth corresponding to the first-baroclinic mode.

Outside of the equatorial mid-Pacific, a non-static ocean response to air pressure in the 4-6 day band is dominated by a basin-wide, barotropic, planetary mode. The low Q of this mode suggests that the ocean is viscous with respect to large-scale barotropic oscillations.

The dynamical components of the observed long-period tides have been isolated for the first time using the "self-consistent" equilibrium tide of Agnew and Farrell (1978). The tides are slightly non-equilibrium with large horizontal scales. The relatively short-scale Rossby modes predicted by Wunsch (1967) are not observed, perhaps because of the poor spatial coverage of the dataset. Considering the low Q of the 4-6 day planetary basin mode, it is suggested that the long-period tides are frictionally-controlled.

The 4- and 5-day equatorial inertia-gravity waves, the 35-80 day Kelvin waves and the 4-6 day planetary basin mode are clearly atmospherically forced, and, perhaps surprisingly, they are forced by atmospheric waves that have similar horizontal structures, i.e., 4-5 day Rossby-gravity

waves, 40-50 day Kelvin waves and a 5-day global barotropic mode. The surface expressions of these atmospheric waves are determined in order to understand the nature of the oceanic response, e.g., resonant or forced. Much of the information about the surface atmospheric fields that has been collected, including frequency-wavenumber descriptions, awaits an accurate model of the coupling between wind stress and internal ocean waves.

Thesis Supervisor: Carl Wunsch
Title: Head, Department of Earth and
Planetary Sciences
Cecil and Ida Green Professor
of Physical Oceanography

Acknowledgments

I am grateful to Carl Wunsch for providing the opportunity, inspiration, resources, and critical guidance without which this dissertation could not have been attempted, might have faltered among numerous peripheral issues and would certainly never have been completed. It is rare to find a scientist who, after achieving a high level of success, still retains the imagination, patience and curiosity necessary to decipher and improve the mental machinations of students such as I.

Charles Eriksen, Joe Pedlosky, Jim Luyten, Ed Harrison, Claude Frankignoul and Kit O'Neill provided useful comments at various stages during the progress of this work.

Data was generously provided by Klaus Wyrtki (University of Hawaii), David Pugh (Institute of Oceanographic Sciences), the National Ocean Survey and the National Climatic Center.

Monetary support for this research was provided by the National Science Foundation through contract OCE73-01384. At various times, tuition and living expenses were paid by funds from the NSF contract above, the Office of Naval Research (contract N00014-C-75-0291), the Cecil and Ida Green Professorship in Earth Sciences, the J. P. Luther Educational Fund and by an M.I.T. Educational Tuition Award.

Kit O'Neill offered detailed editorial comments on the various drafts of this work. She tirelessly assisted in the production of the final manuscript. I am also grateful to Deborah Gillett for her help in the preparation of the final manuscript at crucial times. I cannot overestimate the value of the personal support provided to me by both these women and my family.

Table of Contents

Abstract	2
Acknowledgments	4
List of Figures	8
List of Tables.	12
CHAPTER 1. INTRODUCTION	
A. General	13
B. Free Oscillations in the Tropics; Review of Linear Theory . . .	19
CHAPTER 2. ATMOSPHERIC OSCILLATIONS AT THE TROPICAL SEA SURFACE	
A. Introduction.	31
1. Organization	33
2. Dataset preliminaries.	34
B. 3.5- to 7-Day Periods	37
1. Rossby-gravity and Easterly waves.	37
a. Wavenumber estimates.	41
b. Amplitude estimates; annual and interannual variability; Q.	46
2. Global five-day pressure waves	47
C. 7- to 20-Day Periods.	54
D. 20- to 90-Day Periods	57
E. Frequency - Wavenumber Spectra of Equatorial Surface Winds and Pressure.	65
CHAPTER 3. OCEANIC OSCILLATIONS AT THE TROPICAL SEA SURFACE	
A. Introduction.	71
1. Sea Level Dataset.	74

B. The Long-Period Tides	79
1. Data analysis.	81
2. Observed Fortnightly (Mf) tide	86
3. Brief remarks on the dynamics of the fortnightly tide.	98
4. Observed monthly (Mm) tide	99
5. Observed nine-day tide	101
6. Conclusions and discussion on the long-period tides.	104
C. Barotropic Normal Modes	105
1. Test for a static response to atmospheric pressure	106
2. Possible planetary basin modes	111
3. Wavenumber estimates of the oceanic wave	116
4. Power density.	118
5. Conclusions and discussion	123
D. Observations and Models of Equatorial Inertia-Gravity Waves	125
1. Identification of Pacific sea level spectra peaks as inertia-gravity waves by comparing observed and predicted periods.	129
2. Zonal variations of inertia-gravity wave energy in the Pacific.	135
3. Meridional structure of the gravest inertia-gravity modes in the Pacific	139
4. Identification of higher meridional modes, $n > 2$	145
5. Inertia-gravity wave signals in Indian Ocean sea level data.	148
6. Sea level deflection due to higher vertical modes.	153
7. Zonal wavenumbers and bandwidths	158
8. Temporal variability of 4-5 day inertia-gravity power.	163
9. Frequency bandwidths of the inertia-gravity peaks.	167
10. Observations of forcing.	169
11. Summary and discussion	173

12. Spectral models of equatorial inertia-gravity waves.176
a. Simple model to explain observed sea level spectra.177
b. Off-equatorial sea level inertial peaks183
c. Comparison of Eriksen's (1979) model spectrum with observed sea level spectra.185
d. Caveats188
E. Equatorially-Trapped Waves at Periods of 7-80 Days in the Pacific	
1. 6.5-7.5 Day inertia-gravity wave?190
2. 9-10 Day Rossby-gravity wave?191
3. 35-80 Day Kelvin waves192
CHAPTER 4. CONCLUSIONS199
References203
Biographical Note210

List of Figures

Figure

1.1	Dispersion relations for equatorially-trapped waves.	30
2.1	Power density spectrum of Canton north wind.	32
2.2	Maps indicating positions of stations in the central Pacific and Indian Oceans.	35
2.3	Power density spectra of north wind from Pacific stations. . . .	38
2.4	Power density spectra of north wind from Indian Ocean stations. .	40
2.5	Coherence of north wind between Canton and Betio	43
2.6	Zonal wavenumber estimates, from north wind coherence in the and 4-5 day band, plotted against zonal station separation, for 2.7 selected Pacific station pairs	44
2.8	Seasonal power density spectra of north wind from Canton, and power density spectra of selected one-year segments of Canton north wind	48
2.9	Theoretical meridional structure of the $s' = 1$, $n' = 2$ planetary wave for $\epsilon \rightarrow 0$ and $\epsilon = 10$	50
2.10	Power density spectra of air pressure from selected Pacific and Indian Ocean stations.	51
2.11	Coherence of air pressure between Wake and Canton.	52
2.12	Wavenumber spectrum of air pressure in the 4.6-6.0 day band using Pacific stations	53
2.13	Wavenumber spectrum of north wind from Canton, Arorae, Betio and Ocean in the 7.4-8.8 day band.	56
2.14	Power density spectra of east wind from Pacific stations	58
2.15	Power density spectra of east wind from Indian Ocean stations. .	60
2.16	Coherence of east wind between Canton and Betio.	62
2.17	Wavenumber spectrum of east wind from Canton, Arorae, Betio and Ocean in the 40-55 day band.	62
2.18	Superimposed coherences of air pressure between Kwajalein and Canton, and Wake and Midway.	64
2.19	Zonal wavenumber versus frequency contour plots of air pressure and wind power density using Pacific stations.	67

List of Figures (continued)Figure

2.20	Superposition of smoothed zonal wavenumber versus frequency plots of surface winds in the equatorial Pacific and the dispersion relations of the theoretical, first-baroclinic mode, equatorially-trapped waves.	70
3.1	Power density spectrum of sea level from Christmas Island.	72
3.2	Maps showing locations of sea level stations in the Pacific.	76
3.3	Map showing location of sea level stations in the Indian Ocean.	77
3.4	Estimates of admittance of the fortnightly (Mf) tide in the tropical Pacific plotted against longitude.	92
3.5	Estimates of Mf admittance in the Pacific plotted against latitude.	94
3.6	Power density spectrum of sea level from Truk.	102
3.7	Sea level coherence between Kwajalein and Wake.	107
3.8	Sea level coherences between Guam and Truk, and between Balboa and Talara.	108
3.9	Coherences between sea level and surface air pressure at Truk and Galapagos.	109
3.10	Sea level coherences between Honolulu and San Francisco, and between Canton and Balboa.	112
3.11	Wavenumber estimates of the 4-6 day barotropic normal mode, using coherence phases, plotted against zonal station separation distance.	119
3.12	Sea level power density spectra from, and coherence between, Eniwetok and Wake.	121
3.13	Surface displacement eigenfunction for the gravest, symmetric, barotropic planetary mode of a hemispherical basin centered on the equator.	124
3.14	Sea level coherence between Midway and Johnston.	126
3.15	Sea level power density spectra from Pacific stations that exhibit probable inertia-gravity peaks.	130

List of Figures (continued)Figure

3.16	Sea level power density spectra from selected Pacific stations to demonstrate zonal variations of inertia-gravity power.	136
3.17	Theoretical meridional structure of the meridional mode $n=2$ for two possible values of the first-baroclinic mode equivalent depth.140
3.18	Superposition of Pacific sea level spectra from selected stations demonstrating background level variations.142
3.19	Comparison of the observed meridional distribution of sea level power, at 4 and 5 days, with theory.144
3.20	Sea level power density spectra of two 2-year records from Christmas.147
3.21	Sea level spectra from near-equatorial stations in the Indian Ocean.149
3.22	Superposition of sea level spectra from islands at similar latitudes in the Pacific and Indian Oceans.152
3.23	The magnitude of the sea surface displacement divided by the maximum internal displacement plotted against mixed-layer depth, assuming the stratification is modeled as a decaying exponential with depth.157
3.24	Line spectrum of sea level displacement for the first three baroclinic modes.157
3.25	Sea level coherences between Christmas and Canton, and between Canton and Arorae.160
3.26	Sea level spectra of 1-year-long records from Canton165
3.27	Sea level spectra of consecutive 1-year-long records from Christmas.165
3.28	Sea level spectra of 152 days of Christmas data computed with different frequency-band averaging intervals.166
3.29	Seasonal sea level spectra from Canton.166
3.30	Coherence between sea level and surface winds at Canton.170
3.31	Computed inertia-gravity wave sea level spectra, from the model (3.20), superimposed on observed sea level spectra from the equatorial Pacific (Figure 3.15)181

List of Figures (continued)Figure

3.32	As in Figure 3.31, but for off-equatorial Pacific spectra from Kwajalein and Eniwetok.	184
3.33	Computed inertia-gravity wave sea level spectra, using Eriksen's (1979) model, superimposed on observed sea level spectra from Canton and Christmas in the Pacific. . . .	187
3.34	Computed inertia-gravity wave sea level spectra, using both the model (3.20) and Eriksen's model, superimposed on observed sea level spectra from Gan and Port Victoria in the Indian Ocean.	189
3.35	Sea level spectra from Canton, Christmas, and eastern Pacific stations.	193
3.36	Sea level coherences between selected equatorial Pacific stations.	195

List of TablesTable

2.1	Weather dataset information.	36
3.1	Locations and time intervals of sea level records.	75
3.2	Selected linear long-period tides: the seven strongest in the 2-90 day band	81
3.3	Fortnightly (Mf) tide amplitudes and admittances for stations in the Pacific and Indian Oceans.	87
3.4	Comparison of observed Mf admittances in the Pacific with previously published estimates	90
3.5	Mf tide at Canton computed from successive one year records.	96
3.6	Monthly (Mm) tide amplitudes and admittances for stations in the Pacific and Indian Oceans	100
3.7	Nine-day tide amplitudes and admittances for stations in the Pacific and Indian Oceans.	103
3.8	Coherence amplitude and phase between sea level and surface air pressure in the 4-6 day band.	110
3.9	Eigenfrequencies of the gravest planetary modes in a homogeneous, flat-bottomed ocean with dimensions on the order of the Pacific	114
3.10	Coherence amplitude and phase between sea level stations (3.5-6.0 day band)	117
3.11	Observed and predicted periods of inertia-gravity sea level peaks.	134
3.12	Periods of inertia-gravity peaks in sea level spectra of two-year-long records from Christmas	146
3.13	Equivalent depths of the first four baroclinic modes for different stratification models.	155
3.14	Sea level coherence amplitude and phase between "mid- Pacific" stations for the $n = 1$ and 2 modes.	162
3.15	Coherence amplitudes and phases between sea level and surface winds at Canton in the 3.5-7 day band.	173
3.16	Sea level coherence amplitude and phase between equatorial Pacific stations that have significantly non-zero coherence amplitude in the 35-80 day band.	196

CHAPTER 1

INTRODUCTION

A. General

Baroclinic waves that are dynamically confined to low latitudes have stimulated the imaginations of oceanographers and meteorologists alike, but for different reasons. Meteorologists have long believed that equatorially-trapped waves at periods of 5 to 15 days force longer period fluctuations of the atmospheric circulation (for a good review, see Holton (1975)), but a similar process in the ocean has only recently been suggested (Philander (1976), Wunsch (1978)). The theoretically important, yet largely unobserved, oceanic role of equatorial waves is their efficient and rapid zonal redistribution of the ocean's response to changing surface winds. This role derives from several properties. Freely propagating equatorial waves can be found at all frequencies, whereas at mid-latitudes a spectral gap exists between free inertia-gravity and Rossby waves. The equatorial trapping, like a waveguide, enables signals to propagate zonally without large losses in amplitude due to meridional dispersion. And the short time scales of the low-mode baroclinic equatorial waves imply rapid zonal propagation, the waves' most distinguishing feature in comparison with mid-latitude baroclinic waves.

Much of the theoretical work on the dynamics of equatorial waves incorporates unrealistic assumptions and neglects significant features of the real ocean environment. For example, the expansion

of the long-period atmospheric forcing and oceanic response in terms of vertical normal modes has a questionable physical basis (Philander, (1978), Wunsch (1978)). (Notably, Wunsch's (1977) model of the equatorial Indian Ocean response to an annual period wind is based on the likelihood that normal modes cannot be established in a dissipative environment when the vertical group velocities are small.) The poorly understood process of how the surface wind momentum is physically transferred through the boundary layer to produce large-scale motions in the interior of the equatorial oceans is frequently, and inaccurately, modeled by simply assuming the wind stress is evenly distributed in a surface mixed-layer. The dynamical consequences of realistic topography have also generally been ignored. Each ocean contains one or more ridges of varying steepness that cross the equator at nearly right angles. Aside from the probability that broad, rough ridges inhibit vertical mode formation, the ridges presumably alter the zonal propagation characteristics of equatorial waves.

Identifying narrow-band (in frequency) examples of equatorially-trapped waves and discriminating their propagation characteristics and energy sources in the real spatially-varying, rough-bottomed oceans may shed light on the general questions of how the equatorial oceans respond to changes in the surface winds and how efficiently equatorial waves will redistribute the responses. Information on the structure of narrow-band oscillations in the equatorial oceans is also needed to evaluate the possibility that the waves interact with the long-period flows. What we learn about the structure of the low

vertical mode equatorial inertia-gravity waves in the presence of rough topography, such as the East Pacific rise and the Solomon Plateau, is of direct relevance to studies of mid-latitude internal waves.

This dissertation details an investigation of long-period waves in the tropical oceans. Consequently, the motivation just discussed belies the true scope of the work which must distinguish barotropic oscillations as well. The study is restricted to periods of 1 to 90 days to exclude the daily tides and the annual cycle from consideration. In order to investigate phenomena with periods longer than 90 days the datasets should be extended in length.

Descriptions of the surface atmospheric fields are obviously required to understand forced ocean waves. In particular, the frequency-wavenumber spectra of the winds and pressure at sea level are needed. This information is not available from previous studies, so Chapter 2 is devoted to extracting frequency-wavenumber information from island station weather observations.

The emphasis in Chapter 2 is on delineating the surface amplitude, structure, and spatial and temporal variability of narrow-band (in frequency and wavenumber) atmospheric motions in the tropics (within 15° of the equator). There are physical and pragmatic reasons for concentrating on the narrow-band signals.

First, research in the past decade has resulted in the discovery of a number of narrow-band oscillations in the tropical atmosphere. These oscillations can force oceanic motions if they have sufficient amplitudes to dominate the power spectra, or are sufficiently

narrow-band in wavenumber space to dominate the atmospheric cross-spectra, at the sea surface. If their time and space scales are equivalent to the scales of oceanic normal modes, then resonance in the ocean is possible. The results from the analysis of weather observations tended to direct the search for narrow-band oceanic oscillations. Subsequent discovery of an oceanic wave is then more credible since the forcing function is already known.

Second, the dataset was collected from island stations in the Pacific and Indian Oceans, where stations are generally separated by hundreds to thousands of kilometers. Consequently, wide-band wavenumber phenomena will not be strong in the cross-spectra and their properties cannot be estimated confidently. Estimates of wavenumber spectra of winds and pressure for the entire 1-90 day band are included in Chapter 2, even though the estimates have weak statistical significance for many frequencies.

The results in Chapter 2 may be of interest to meteorologists irrespective of oceanographic applications, because new information on the properties of atmospheric waves is reported. Only a small portion of the information on the surface atmospheric fields that has been collected is reported in Chapter 2, however, since it contains only information that is utilized in Chapter 3 for studying forced ocean waves.

Long-period waves in the tropical oceans are studied in Chapter 3 using tide gauge records of sea level fluctuations from Pacific and Indian Ocean island and coastal stations. The sea level data, particularly in conjunction with available cotemporal surface wind

and air pressure observations, constitute a largely untapped reservoir of information on oceanic variability and air-sea interaction (but see Wyrтки (1975, 1977 and others)). There are, of course, limitations to what can be learned from measurements of sea level. Sea level displacements due to free baroclinic equatorial waves are proportional to the square root of the "equivalent depth"; in other words, sea level responds with larger amplitudes to the large-vertical-scale motions. The spatial coverage of available sea level measurements is not very dense, so that we are limited by the sea level dataset to studying large horizontal and vertical scale phenomena. On the other hand, the low-mode filtering effect of sea level increases the expected horizontal coherence between stations (assuming the vertical modes are independent). Ironically, in this study of data from the 1950's and 1960's, the limiting factor in determining sea level-weather relationships is the lack of sea level data, whereas current aggressive programs of sea level measurement in the tropics are failing to obtain cotemporal measurements of surface weather.

Equatorially-trapped waves are not the only oceanic phenomena that can produce sea level fluctuations. Consequently, the analysis of sea level data in Chapter 3 is approached with the broad objective of sorting out barotropic and baroclinic fluctuations, that are not equatorially confined, from the free equatorial waves.* For example, Philander (1978) suggested that the long-period ocean tides may be basin modes which have largest amplitudes at the equator and coasts.

*Steric fluctuations are not considered.

At the least, deterministic tidal signals can significantly mislead the unwary analyst searching for propagating waves in the tropics. The long-period tides, including the linear monthly (Mm), biweekly (Mf) and nine-day tides, are tabulated in Chapter 3 and discussed in relation to current theories. We suggest that the linear long-period tides may be frictionally controlled.

The cross-spectra of sea level between many stations suggest the presence of an oceanic oscillation at 4-6 days throughout the Pacific basin. The importance of this oscillation as a "noise" in the equatorial band and its intrinsic importance as a possible basin mode, require a thorough investigation of the oscillation's properties, in Chapter 3, before analyzing the sea level measurements for equatorial waves. Evidence of a barotropic planetary mode of the Pacific basin at 4-6 days period is presented. The 4-6 day mode crucially affects our conclusions as to the longitudinal structure of the equatorially-trapped inertia-gravity waves.

Chapter 3 continues with confirmation of the existence of low-mode, equatorially-trapped inertia-gravity waves in the Pacific Ocean. Zonal variation of the low-mode energy is significant, suggesting attenuation by rough topography, by reflection from convoluted meridional boundaries, or both. The presence of high meridional, first-baroclinic modes, to periods as small as one day, and second-baroclinic modes is suggested by the observed sea level spectra in conjunction with a simple spectral model. It is suggested that first-baroclinic mode inertia-gravity waves may be established in the Indian Ocean. Zonal wavenumbers and bandwidths, and annual and interannual variability of the strongest inertia-gravity waves in the Pacific are estimated.

The arguments for inertia-gravity wave resonance in the Pacific are fully summarized.

Comparison of the observed sea level spectra with Eriksen's (1979) model of inertia-gravity wave energy at the equator points out some possible improvements to the model.

Evidence of 35-80 day Kelvin waves concludes Chapter 3. Propagation from the central Pacific along the equatorial waveguide to South America is suggested by the sea level cross-spectra. The oscillation is apparently forced by an atmospheric Kelvin wave of similar frequency.

The results of this research are summarized in Chapter 4. Topics for future research, suggested throughout this work, are collected there.

B. Free Oscillations in the Tropics; Review of Linear Theory

The presentation in this section of the horizontal structures and dispersion relations of free oscillations on an equatorial beta-plane facilitates comparisons with the observations in the next two chapters. In addition, the similarity between the physics of atmospheric and oceanic oscillations is emphasized here.

Assuming a rotating globe is covered by a thin layer of an ideal compressible fluid or gas in local thermodynamic equilibrium, the conservation of momentum, mass and thermodynamic energy are described by the equations:

$$\frac{\partial \vec{v}}{\partial t} + \vec{v} \cdot \nabla \vec{v} + 2\vec{\Omega} \times \vec{v} = -\frac{1}{\rho} \nabla \hat{p} - \nabla \psi + \vec{F} \quad , \quad (1.1)$$

$$\frac{\partial \hat{\rho}}{\partial t} + \vec{v} \cdot \nabla \hat{\rho} + \hat{\rho} \nabla \cdot \vec{v} = 0 \quad , \quad (1.2)$$

$$\frac{\partial \hat{p}}{\partial t} + \vec{v} \cdot \nabla \hat{p} - c^2 \left(\frac{\partial \hat{\rho}}{\partial t} + \vec{v} \cdot \nabla \hat{\rho} \right) = G \quad , \quad (1.3)$$

where $\vec{v} \equiv (\hat{u}, \hat{v}, \hat{w}) \equiv$ velocity toward (east, north, outward); $\hat{p} \equiv$ pressure; $\hat{\rho} \equiv$ density; $\Psi \equiv$ gravitational potential; $\vec{\Omega} \equiv$ angular velocity of the Earth; $c \equiv$ speed of sound.

Ψ includes variations that drive tidal fluctuations, but for now $\Psi \equiv g(r-a)$, where g is a constant, r is the radial coordinate and a is the Earth's radius. \vec{F} represents body forces, such as friction, but for now $\vec{F} \equiv 0$. Additional forcing can enter via the boundary conditions. G represents changes in energy in a volume due to the net accession of heat (and salinity in the ocean), but $G \equiv 0$ here.

The velocity, pressure and density fields are each comprised of a basic state plus a small perturbation:

$$(\hat{u}, \hat{v}, \hat{w}, \hat{p}, \hat{\rho}) \equiv (\bar{u}, \bar{v}, \bar{w}, \bar{p}, \bar{\rho}) + (u, v, w, p, \rho)$$

The basic state is assumed motionless and hydrostatic. The perturbation fields are small enough so that (1.1)-(1.3) can be linearized.

The hydrostatic or "traditional" approximation (Eckart (1960)), corresponding to the limit of a vanishingly thin fluid layer, eliminates the radial component of the particle acceleration, the tangential components of the Coriolis force, and the radial variation of the metrical coefficients from (1.1)-(1.3). The validity of the hydrostatic approximation and neglect of the Earth's ellipticity are demonstrated by Veronis (1973) and Miles (1974) for long period oscillations. Miles gives a particularly complete analysis of the parametric limit process involved in the thin-layer approximation, including a demonstration of higher-order coupling, via the tangential Coriolis

terms, between barotropic and baroclinic oceanic modes. More restrictive assumptions in the present work are that the bottom boundary is smooth and rigid, the latter being relaxed for the long-period tides.

Equations (1.1)-(1.3), valid for both the atmosphere and ocean, have now been reduced to the following forms, in spherical coordinates,

$$\frac{\partial u}{\partial t} - 2\Omega \sin \theta v = -\frac{1}{\hat{\rho} a \cos \theta} \frac{\partial p}{\partial \phi} \quad , \quad (1.4a)$$

$$\frac{\partial v}{\partial t} + 2\Omega \sin \theta u = -\frac{1}{\hat{\rho} a} \frac{\partial p}{\partial \theta} \quad , \quad (1.4b)$$

$$0 = -\frac{\partial p}{\partial z} - \rho g \quad , \quad (1.4c)$$

$$\frac{\partial \rho}{\partial t} + w \frac{\partial \bar{\rho}}{\partial z} = -\hat{\rho} \nabla \cdot \vec{v} \quad , \quad (1.5)$$

$$\frac{1}{c^2} \left(\frac{\partial p}{\partial t} + w \frac{d\bar{p}}{dz} \right) = \frac{\partial \rho}{\partial t} + w \frac{d\bar{\rho}}{dz} \quad , \quad (1.6)$$

where $(\phi, \theta, z) = (\text{east longitude, north latitude, } r-a)$; $\Omega = |\vec{\Omega}|$;

and

$$\nabla \cdot \vec{v} = \frac{1}{a \cos \theta} \left(\frac{\partial u}{\partial \phi} + \frac{\partial}{\partial \theta} (v \cos \theta) \right) + \frac{\partial w}{\partial z} \quad . \quad (1.7)$$

The hydrostatic equation for the basic state is $\frac{d\bar{p}}{dz} = -\bar{\rho} g$.

In both the atmosphere and the ocean, $\hat{\rho}$ in (1.4) and (1.5) is replaced by $\bar{\rho}(z)$, incurring an error less than the error due to neglecting the nonlinear terms. Oceanographers frequently make the (unnecessary) simplification $\hat{\rho} = \text{constant}$ in (1.4) and (1.5), which adds only a trivial error.

Eliminating ρ and w from (1.4c), (1.5) and (1.6) yields

$$-\frac{\partial^2}{\partial t \partial z} \left[\left(\frac{N^2/g + g/c^2 + \frac{\partial}{\partial z}}{N^2} \right) p \right] + \bar{\rho} \nabla_H \cdot \vec{v} = 0 \quad , \quad (1.9)$$

where $\nabla_H \cdot \vec{v} = \nabla \cdot \vec{v} - \frac{\partial w}{\partial z}$ and $N(z)$ is the Brunt-Väisälä

frequency:

$$N^2(z) \equiv \left(-\frac{g}{\bar{\rho}} \frac{\partial \bar{\rho}}{\partial z} - \frac{g^2}{c^2} \right) \quad . \quad (1.10)$$

Of (1.4a), (1.4b) and (1.9), only (1.9) has vertical derivatives, suggesting the separation of variables

$$\{u, v, p\} = \text{Re} \left[\frac{z(z)}{\bar{p}(z)} \left\{ U'(\phi, \theta, t), V', \bar{p} P' \right\} \right] \quad (1.11)$$

[Note that ρ and w are simple functions of p , using (1.4c) and (1.6),

such that
$$\rho = -\frac{1}{g} \frac{\partial p}{\partial z} \quad , \quad (1.12)$$

and
$$w = \frac{-1}{\bar{p} N^2(z)} \left(\frac{g}{c^2} + \frac{\partial}{\partial z} \right) \frac{\partial p}{\partial t} \quad . \quad] \quad (1.13)$$

Substituting (1.11) into (1.4a), (1.4b) and (1.9) yields

$$\frac{\partial U'}{\partial t} - 2\Omega \sin \theta V' = \frac{-1}{a \cos \theta} \frac{\partial P'}{\partial \phi} \quad , \quad (1.14)$$

$$\frac{\partial V'}{\partial t} + 2\Omega \sin \theta U' = \frac{-1}{a} \frac{\partial P'}{\partial \theta} \quad , \quad (1.15)$$

$$\frac{\partial P'}{\partial t} + \gamma^2 \nabla_H \cdot (U', V') = 0 \quad , \quad (1.16)$$

and

$$\frac{d}{dz} \left[\left(\frac{N^2/g + g/c^2 + \partial/\partial z}{N^2} \right) z \right] + \frac{z(z)}{\gamma^2} = 0 \quad , \quad (1.17)$$

where γ^2 is a separation constant having units of speed squared;

$\gamma^2 = gh$, where h is the so-called "equivalent depth" in

analogy with the homogeneous ocean problem where h equals the ocean

depth. Equations (1.14)-(1.16) are the familiar Laplace Tidal

Equations (LTE) and are usually reduced to a single equation for

V' or P' , after assuming sinusoidal time and longitude dependences.

Let $(U', V', P') = (U(\theta), V, P)e^{is\phi - i\omega t}$, where s is longitudinal wavenumber in cycles/earth circumference and ω = angular frequency;

then eliminating U and V from LTE gives

$$\mathcal{L}(P) + \epsilon P = 0 \quad , \quad (1.18a)$$

where

$$\mathcal{L} \equiv \frac{1}{\cos \theta} \frac{d}{d\theta} \left(\frac{\cos \theta}{\sigma^2 - \sin^2 \theta} \frac{d}{d\theta} \right) + \frac{1}{\sigma^2 - \sin^2 \theta} \left(\frac{s}{\sigma} \frac{\sigma^2 + \sin^2 \theta}{\sigma^2 - \sin^2 \theta} - \frac{s^2}{\cos^2 \theta} \right) \quad , \quad (1.18b)$$

and $\sigma \equiv \frac{\omega}{2\Omega}$; $\epsilon \equiv \frac{4\Omega^2 a^2}{gh}$ is often called Lamb's parameter, after Lamb (1932, Art. 210).

The boundary condition that P be bounded at the poles ($\theta = \pm \frac{\pi}{2}$) with (1.18) define an eigenfunction-eigenvalue problem with ϵ or σ as eigenvalue, depending upon the application. Equation (1.18) does not have simple analytic solutions, except for certain limits of the parameter ϵ . Longuet-Higgins (1968) has numerically solved (1.18) for a complete range of ϵ , indicating when simple asymptotic forms obtain. Philander (1978, Appendix B) summarizes the known simplifications to (1.18) that yield analytic solutions.

Studies of ocean waves often begin by solving an approximate form of the vertical structure equation (1.17), obtained by invoking the Boussinesq approximation. Phillips (1977) recapitulates the scaling arguments that allow the left hand sides of (1.5) and (1.6) to be neglected, thus eliminating the first two terms in parentheses in (1.17) and the first term in parentheses in (1.13). The solutions to the resultant (1.17) subject to the boundary conditions,

$$w = 0 \quad \text{at} \quad z = -D \quad , \quad (1.19a)$$

$$\text{and} \quad \frac{\partial p}{\partial t} = \bar{\rho} g w \quad \text{at} \quad z = 0 \quad , \quad (1.19b)$$

where D = ocean depth, are a discrete set of eigenfunctions with ϵ as eigenvalue. The subsequent solutions of (1.18) with ϵ fixed (σ as eigenvalue) are referred to as Hough functions after the pioneering work of Hough (in 1897 and 1898) who solved LTE in the limit $\epsilon \rightarrow \infty$ ($h \rightarrow 0$).

Alternatively, as in studies of atmospheric waves (see Chapman and Lindzen (1970)), (1.18) is solved first with ϵ as eigenvalue (σ and s are determined by the forcing), which may now take positive or negative values for vertically propagating or trapped solutions of (1.17), respectively. [The set of eigenfunction solutions to (1.18) with ϵ as eigenvalue are also referred to as Hough functions even though they differ markedly from the set of eigenfunctions with ϵ fixed and frequency as eigenvalue, as pointed out by Philander (1978).]

The vertical structure equation (1.17) is transformed to a form more familiar to meteorologists by use of the linearized equation of state, $\bar{p} = \bar{p} R \bar{T} = \bar{p} g h$, and (1.10). Then (1.17) becomes

$$\frac{d}{dz} \left[\left(\frac{dH/dz + 1 + H d/dz}{g (dH/dz + \kappa)} \right) Z(z) \right] + \frac{Z(z)}{gh} = 0, \quad (1.20a)$$

where the thermodynamic symbols have the usual meanings.

For an isothermal atmosphere, H is constant and (1.20a) becomes

$$\frac{d^2 Z_0}{dz^2} + \left(\frac{\kappa}{Hh} - \frac{1}{4H^2} \right) Z_0 = 0, \quad (1.20b)$$

in canonical form, where $Z(z) = Z_0(z) \exp[-z/2H]$.

Equation (1.20b) is identical to equation (23) in Lindzen (1967), with the exception of his forcing term. The atmospheric vertical structure equation can be put in a simpler form than (1.20a) using a slightly different approach to the reduction of the equations of motion (Chapman and Lindzen (1970), Holton (1975)).

Simple solutions to the Laplace Tidal Equations obtain for special limits of Lamb's parameter, ϵ . For instance, as $\epsilon \rightarrow +\infty$

($h \rightarrow +0$) the solutions are accurately approximated by solutions to LTE cast on an equatorial β -plane. Even for relatively large values of h the equatorial β -plane solutions are reasonable approximations to the spherical coordinate solutions (Longuet-Higgins (1964)). Replacing $\cos \theta$ with 1 and $\sin \theta$ with θ in (1.14)-(1.16) produces the equatorial β -plane equations

$$\frac{\partial U'}{\partial t} - 2\Omega \theta V' = -\frac{1}{a} \frac{\partial P'}{\partial \phi} \quad , \quad (1.21a)$$

$$\frac{\partial V'}{\partial t} + 2\Omega \theta U' = -\frac{1}{a} \frac{\partial P'}{\partial \theta} \quad , \quad (1.21b)$$

$$\frac{\partial P'}{\partial t} + \frac{gh}{a} \left[\frac{\partial U'}{\partial \phi} + \frac{\partial V'}{\partial \theta} \right] = 0 \quad , \quad (1.21c)$$

The typical β -plane equations differ in form from (1.21) in that ϕ and θ are usually approximated by x/a and y/a (with no additional error), and β is defined as $2\Omega/a$, but for later convenience this substitution is not made here.

Assuming that the solutions are sinusoidal in time and longitude, using (1.11),

$$\{u, v, p\} = \text{Re} \left[\frac{\tilde{z}(\tilde{z})}{\bar{\tilde{z}}(\tilde{z})} \{U', V', \bar{p}'\} \right] = \text{Re} \left[\frac{\tilde{z}(\tilde{z})}{\bar{\tilde{z}}(\tilde{z})} \{U(\theta), V, \bar{p}\} e^{i s \phi - i \omega t} \right] \quad , \quad (1.22)$$

where ω and s are defined as before, equations (1.21) easily reduce to a single equation for $V(\theta)$, in canonical form,

$$\frac{d^2 V}{d\eta^2} + \left(\epsilon^{1/2} \sigma^2 - \frac{s^2}{\epsilon^{1/2}} - \frac{s}{\sigma \epsilon^{1/2}} - \eta^2 \right) V = 0 \quad , \quad (1.23)$$

where $\eta = \epsilon^{1/4} \theta$. (Occasionally, it is more convenient to work with the equation for $P(\theta)$; see Wunsch (1977).) Equation (1.23) is most

commonly known as the Parabolic Cylinder Equation or Schrödinger's Equation for a simple harmonic oscillator (see Bender and Orszag (1978)). Valid equatorial solutions, for which $V(\eta) \rightarrow 0$ as $|\eta| \rightarrow \infty$, exist if and only if

$$\epsilon^{1/2} \sigma^2 - \frac{5}{\epsilon^{1/2} \sigma} - \frac{5^2}{\epsilon^{1/2}} = 2n+1, \quad n=0, 1, 2, \dots \quad (1.24)$$

In fact, Lindzen (1967) noted that physically valid solutions must begin to decay before $|\eta| = |\eta_p|$, where $|\eta_p|$ is the magnitude of η at the poles. Consequently, there exists an upper bound for the meridional mode number, n , for every ϵ , or a lower bound on ϵ (upper bound on h) for every value of n .

The solutions of (1.23) which decay for large $|\eta|$ are a subset of the parabolic cylinder functions, that is, Hermite functions (Miller (1972)), which are the product of a Gaussian and a Hermite polynomial,

$$V_n = V_c e^{-\eta^2/2} H_n(\eta) = V_c e^{-\frac{\epsilon^{1/4} \theta^2}{2}} H_n(\epsilon^{1/4} \theta), \quad n=0, 1, 2, \dots \quad (1.25)$$

where V_c is a complex constant. The Hermite polynomials satisfy the following recursion relations:

$$\frac{d}{d\eta} H_n(\eta) = 2\eta H_{n-1}(\eta), \quad (1.26a)$$

$$H_{n+1}(\eta) = 2\eta H_n(\eta) - 2n H_{n-1}(\eta) \quad (1.26b)$$

The first five Hermite polynomials are

$$\left. \begin{aligned} H_0 &= 1, & H_1 &= 2\eta, & H_2 &= 4\eta^2 - 2, \\ H_3 &= 8\eta^3 - 12\eta, & H_4 &= 16\eta^4 - 48\eta^2 + 12, \\ H_5 &= 32\eta^5 - 160\eta^3 + 120\eta. \end{aligned} \right\} \quad (1.26c)$$

From (1.21), expressions for U and P in terms of V can be obtained:

$$U_n(\theta) = -i \frac{(s \frac{dV}{d\theta} - \epsilon \sigma \theta V)}{(\epsilon \sigma^2 - s^2)} = i \epsilon^{1/4} V_c e^{-\frac{\epsilon^{1/2} \theta^2}{2}} \left[\frac{H_{n+1}/2}{\epsilon^{1/2} \sigma - s} + \frac{n H_{n-1}}{\epsilon^{1/2} \sigma + s} \right], \quad (1.27a)$$

and

$$P_n(\theta) = -i 2 \Omega a \frac{(\sigma \frac{dV}{d\theta} - s \theta V)}{(\epsilon \sigma^2 - s^2)} = i \sqrt{g h} \epsilon^{1/4} V_c e^{-\frac{\epsilon^{1/2} \theta^2}{2}} \left[\frac{H_{n+1}/2}{\epsilon^{1/2} \sigma - s} - \frac{n H_{n-1}}{\epsilon^{1/2} \sigma + s} \right]. \quad (1.27b)$$

[For use in Chapter 3, an expression for sea-surface displacement is obtained from the linearized boundary condition (1.19b); thus

$$\mathcal{T} = \frac{P}{g \bar{\rho}(0)} = \frac{1}{g \bar{\rho}(0)} \operatorname{Re} \left[\zeta(\sigma) e^{i s \phi - i \omega t} p(\theta) \right]. \quad (1.28)$$

If ϵ has been determined from the vertical structure equation, as in most oceanic applications, ϵ will assume an infinite discrete set of values, ϵ_r , where r is baroclinic mode number. For each ϵ_r there exists the set of solutions defined by (1.25) (plus a Kelvin wave to be discussed shortly), and this set satisfies the orthogonality condition

$$\int_{-\infty}^{\infty} V_n V_m d\eta = \int_{-\infty}^{\infty} H_n H_m e^{-\eta^2} d\eta = \delta_{mn} 2^n n! \sqrt{\pi}. \quad (1.29a)$$

If, instead, ϵ is the eigenvalue of the horizontal structure equation (1.23), as in atmospheric work, then each solution, V_n , defined by (1.25) is associated with a different value of ϵ , i.e., ϵ_n . Then the V_n satisfy the following orthogonality condition (Philander (1978)):

$$\int_{-\infty}^{\infty} (\sigma^2 - \theta^2) V_n(\epsilon_n^{1/4} \theta) V_m(\epsilon_m^{1/4} \theta) d\theta = \delta_{mn} 2^n n! \sqrt{\pi} \left[\sigma^2 - \frac{2n+1}{2} \epsilon^{-1/2} \right] \epsilon^{-1/4}. \quad (1.29b)$$

The "turning" or "critical" latitude beyond which (1.23) is elliptic, admitting only decaying solutions, is given by

$$\Theta_c = \sqrt{\epsilon^{-1/2} (2n+1)} \quad , \quad n=0, 1, 2, \dots \quad (1.30)$$

Solutions to the vertical structure equation in the ocean yield $\epsilon^{1/2} \sim 4$ ($h \sim 5$ km) for the barotropic mode and $\epsilon^{1/2} > 296$ ($h < 1$ meter) for the baroclinic modes. From (1.30), $\Theta_c \sim 29^\circ$ for the barotropic, lowest meridional, mode and $\Theta_c \sim 3.5^\circ$ for the baroclinic, lowest meridional mode. So the baroclinic modes are clearly described as equatorially-trapped as long as the meridional mode number, n , is not too large, whereas the barotropic mode is only weakly confined to the tropics and is never well described as equatorially-trapped. In the atmosphere, a typical value for $\epsilon^{1/2}$ is 66 ($h \sim 20$ m), so $\Theta_c \sim 7^\circ$ and the waves are confined to the equatorial zone.

A solution to the equatorial β -plane equations (1.21) which is lost in the reduction to (1.23) is the equatorial Kelvin wave, for which $v \equiv 0$. Solving (1.21), with $V' = 0$, yields

$$U'(\theta) = A\left(\phi - \frac{\sqrt{gh}}{a} t\right) e^{-\frac{\epsilon^{1/2} \theta^2}{2}} \quad , \quad (1.31a)$$

and

$$P'(\theta) = A\left(\phi - \frac{\sqrt{gh}}{a} t\right) e^{-\frac{\epsilon^{1/2} \theta^2}{2}} \sqrt{gh} \quad , \quad (1.31b)$$

where $A(x)$ is an arbitrary function. This solution emphasizes the most important fact about Kelvin wave kinematics: the speed of propagation is independent of wavenumber so the form of the wave propagates intact, without dispersion. The Kelvin wave dispersion

relation is obviously

$$s = \epsilon^{1/2} \sigma \quad (1.32)$$

The dispersion relation (1.32) can be derived from (1.24) by setting $n = -1$. Hence the Kelvin wave solution is often identified as the $n = -1$ root. Note that two extraneous solutions of (1.24), occurring when $n = -1$ and 0 , have been discarded. Both solutions have u fields increasing exponentially away from the equator and for both $s = -\epsilon^{1/2} \sigma$.

The properties of the dispersion relations, i.e.,

$$s = \epsilon^{1/2} \sigma \quad , \quad n = -1, \quad (1.32)$$

$$s = \epsilon^{1/2} \sigma - \frac{1}{\sigma} \quad , \quad n = 0, \quad (1.33a)$$

$$\epsilon^{1/2} \sigma^2 - \frac{s}{\epsilon^{1/2} \sigma} - \frac{s^2}{\epsilon^{1/2}} = 2n+1 \quad , \quad n = 1, 2, 3, \dots, \quad (1.33b)$$

have been examined in detail by Lindzen (1967) and Holton (1975) with regard to atmospheric applications, and by Moore and Philander (1977) and Philander (1978) with regard to oceanic applications. Consequently, a full review is not necessary, but a few points need to be made. Assuming ϵ is fixed by the vertical structure equation, (1.32) and (1.33) are plotted in Figure 1.1. For $n > 0$, the solid curves correspond to inertia-gravity waves, if $\sqrt{2} \epsilon^{1/4} \sigma > 1$, or Rossby waves, if $\sqrt{2} \epsilon^{1/4} \sigma < 1$. The Kelvin wave is indicated as the $n = -1$ root. The $n = 0$ root is termed a mixed Rossby-gravity, or Yanai, wave root, since for $\sqrt{2} \epsilon^{1/4} \sigma > 1$ (< 1) the wave dynamically behaves as an inertia-gravity (Rossby) wave. The dashed curves represent the real and imaginary parts of the wavenumber as functions of frequency when the wavenumber is complex, that is, when

$$4 \epsilon \sigma^4 - 4 \epsilon^{1/2} \sigma^2 (2n+1) + 1 < 0 \quad , \quad n = 1, 2, 3, \dots \quad (1.34)$$

Waves with complex zonal wavenumbers exist only at meridional boundaries and are therefore important in the oceans (Moore (1968), Moore and Philander (1977)).

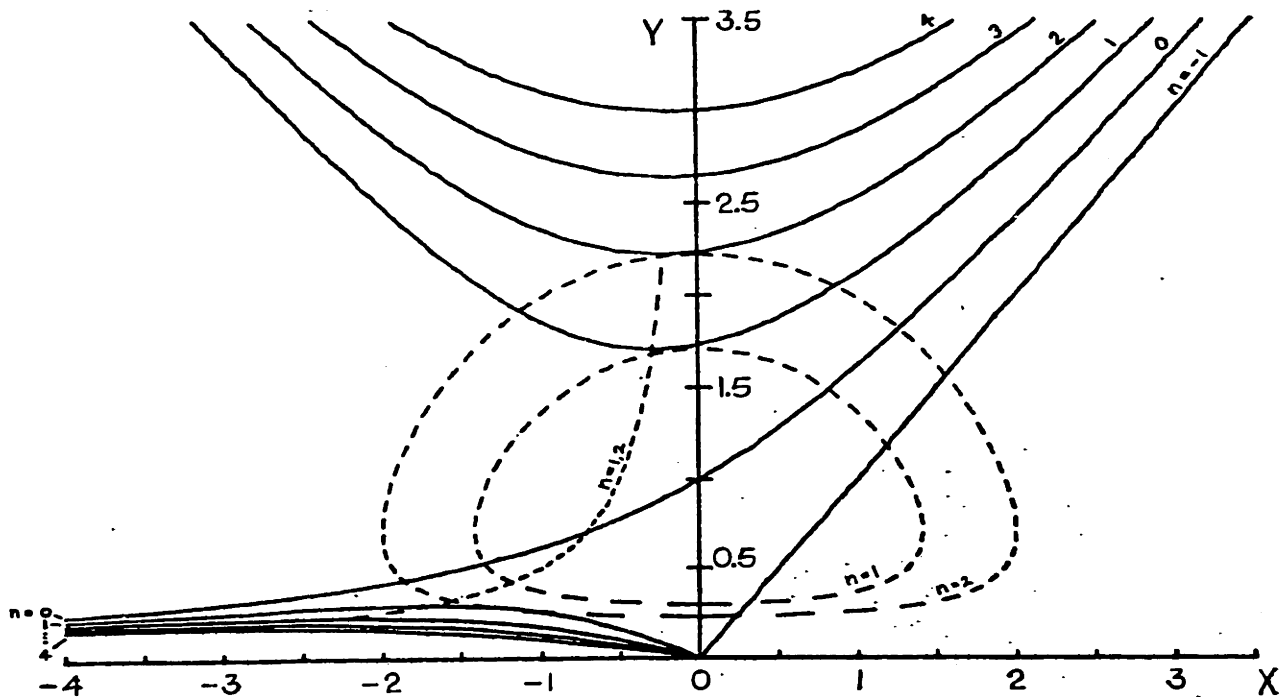


Figure 1.1 - Plot of dispersion relations (1.32) - (1.33). The abscissa is the scaled wavenumber, $X = \epsilon^{-1/4} s$, in units of cycles/circumference [$\epsilon = \frac{(2\Omega a)^2}{g h}$]. The ordinate is scaled frequency, $Y = \epsilon^{1/4} \sigma$, where σ is non-dimensional frequency and is numerically equivalent to $\frac{1}{2T}$ where T is the period in days. The meridional mode number n is indicated. For $n \geq 1$, s is a complex number for a specific range of σ (see text). The real part of the complex s , the dashed hyperbola $\sigma s = -1/2$, is independent of n as indicated. The imaginary part is also shown dashed.

For the first-baroclinic mode, if the equivalent depth $h_1 = 0.8$ m ($c_1 = \sqrt{g h_1} = 2.8$ m/s) then $\epsilon^{1/4} = 18.2$. Therefore, the zonal wavenumber, s , and period, T , are easily obtained from the figure, using

$$s = \epsilon^{1/4} X \approx 18.2 X,$$

and

$$T = \frac{\epsilon^{1/4}}{2Y} \approx \frac{9.1}{Y}.$$

CHAPTER 2

ATMOSPHERIC OSCILLATIONS AT THE TROPICAL SEA SURFACE

A. Introduction

Numerous narrow-band (in frequency and wavenumber) atmospheric oscillations have been observed in the tropics. Some of these oscillations, with large amplitudes in the troposphere, have non-zero surface amplitudes. The power density spectrum of north wind at Canton Island, for example, displays the sea-level expression of 4-5 day period tropospheric waves (Figure 2.1). Other atmospheric waves, with small Q^* , are not so clearly evident in the power spectra at sea level, yet dominate the cross-spectra between stations due to their narrow-band wavenumber structures. Any atmospheric oscillation prominent in surface auto- and/or cross-spectra may force an oceanic oscillation with similar narrow-band structure. Whether the relatively organized atmospheric waves generate oceanic waves more efficiently than a completely random forcing function has not been determined. It will be shown in Chapter 3 that equatorial oceanic oscillations are coherent with the surface atmospheric fields only at those periods corresponding to the atmospheric waves, discussed in this chapter, which have strong surface expressions.

Although the meteorological literature contains descriptions of wave structures above the planetary boundary layer, information at sea level is often not provided. The present analysis of surface weather observations is necessary for the subsequent investigation of how, where, and when, if at all, oceanic waves are forced by atmospheric waves, and whether oceanic

* Q , the "resonance quality", is defined as $\omega_0 / \Delta\omega$, where ω_0 is taken to be the peak frequency and $\Delta\omega$ is the half-power frequency bandwidth.

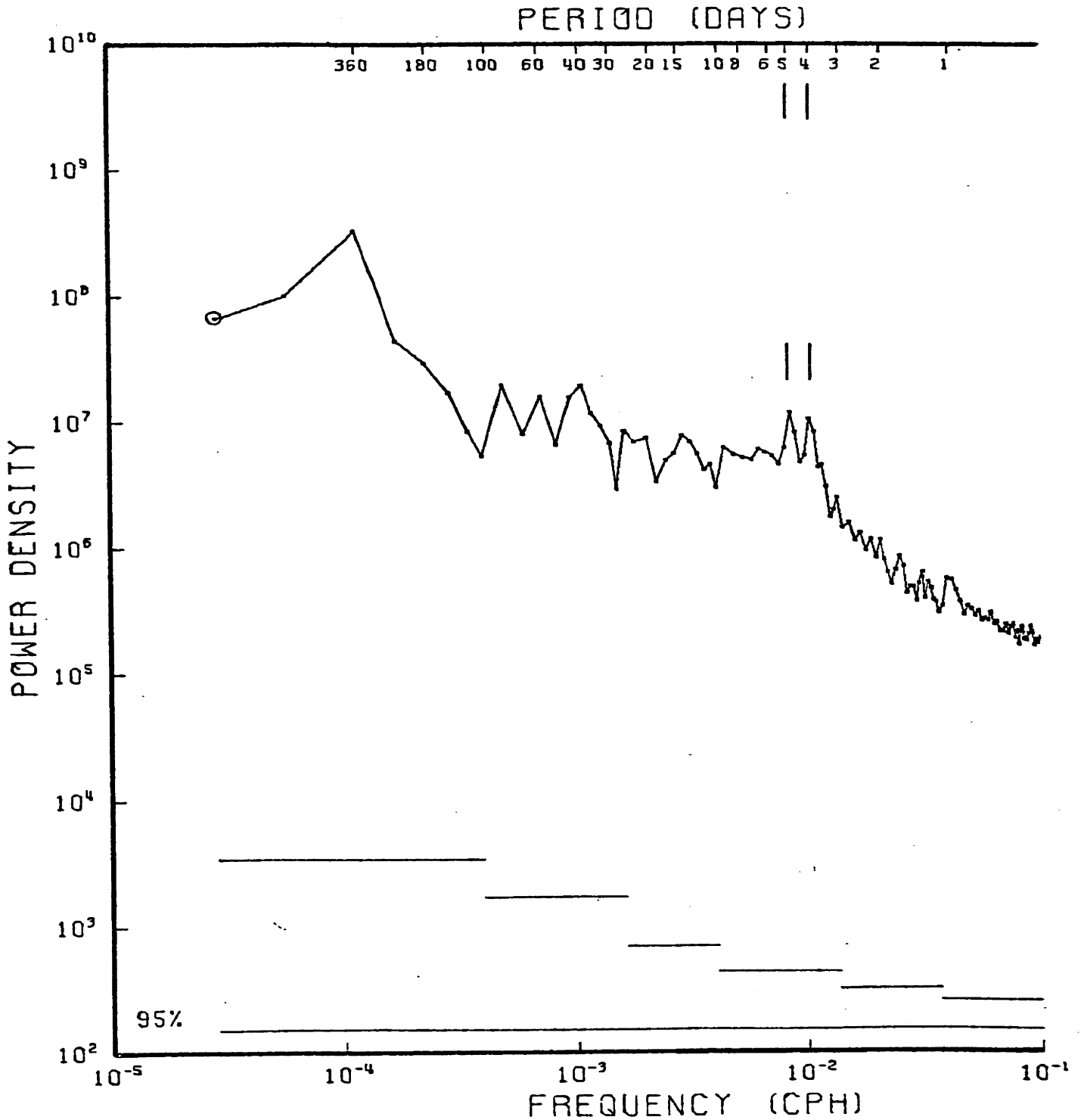


Figure 2.1 - Power density spectrum of surface north wind at Canton, using four years of data. The 4-5 day tropospheric Rossby-gravity waves are marked. Abscissa is frequency (cycles/hour) at the bottom and period (days) at the top, on a log scale. Ordinate is power density in $(\text{cm/sec})^2/\text{cph}$. Normalization is such that the power of a unit amplitude sine wave is 1. The 95% confidence intervals are at the bottom of the figure for all points except the zero-frequency estimate, which is circled when plotted.

resonance occurs. Auto- and cross-spectra are used here to determine whether previously observed tropospheric waves have surface expressions. Additional information on bandwidths, spatial amplitude variation and nonstationarity is garnered from the dataset whenever possible for use in understanding the ocean's response. Only rough details of the meridional structures can be obtained with the present dataset. For the purpose of modelling the theoretical oceanic responses to the atmospheric waves, the previously observed tropospheric wave structures can be extrapolated through the planetary boundary layer to the surface. This procedure is correct to lowest order, but ignores frictionally-produced components (Lindzen and Forbes (1978)) and possible structural changes incurred through interaction with the spatially and temporally variable "mean" zonal wind (Boyd (1978)).

Although we have completed an extensive analysis of the surface wind, pressure and temperature fields in the tropical Pacific and Indian Oceans, only information germane to the discussion of oceanic oscillations in Chapter 3 is presented here.

A.1. Organization. This chapter is organized into sections according to frequency bands in which one or more atmospheric wave motions have been found.* Section B, 3.5-day to 7-day periods, distinguishes the overlapping sea surface structure of three waves: (1) a tropospheric wave, with period $\sim 4-5$ days and wavelength $\sim 2000-4000$ km, frequently associated with the inter-tropical convergence zone (or ITCZ); (2) a lower tropospheric wave, with period $\sim 4-5$ days and wavelength $\sim 8,000-10,000$ km, which is probably a mixed Rossby-gravity wave and may be coupled to a lower stratospheric wave of the same type and characteristics; and (3) a ~ 5 -day period global,

*In the 1- to 3.5-day band, the only oscillation detected with our dataset is a barotropic oscillation that affects only the air pressure field. Since this oscillation apparently does not excite a detectable non-isostatic oceanic response, the 1- to 3.5-day band is not discussed in this work.

"barotropic" oscillation which is most pronounced in the pressure field. The 7-day to 20-day period range, Section C, includes previously observed stratospheric Kelvin and Rossby waves, but the surface data do not indicate the presence of any clear signals. Section D, 20-day to 90-day periods, includes a discussion of a strong 40-50 day oscillation that may be modelled as a dissipation-modified Kelvin wave.

Section E, departing from the study of waves, contains estimates of the frequency-wavenumber spectra of the surface atmospheric fields in the 2-90 day band. Only the wavenumber estimates for the frequency bands in which we have identified atmospheric waves are statistically significant at the 95% level. But these frequency-wavenumber spectra are still useful for determining which oceanic waves may be atmospherically-forced.

A.2. Dataset Preliminaries. The data consist of measurements from island platforms of atmospheric variables (wind velocity, pressure and temperature) near sea level. Pertinent information for the stations is listed in Table 2.1 (see Figure 2.2 for geographical distribution). Most of the sea level weather data was obtained from the National Climatic Center either in Tape Data Format 13 (TDF-13) or in WBAN format. The former generally consist of three observations per day and the latter are hourly samples. The datasets typically span four years or more and required only superficial editing for obviously bad points.

Enough observations per day were collected at all stations to eliminate aliasing from diurnal activity (either tidal oscillations or thermally-generated "sea breezes", although most of the islands do not contain enough land area to generate daily sea breezes).

There is a question as to whether wind measurements from mid-ocean islands are representative of open ocean conditions. This problem can be

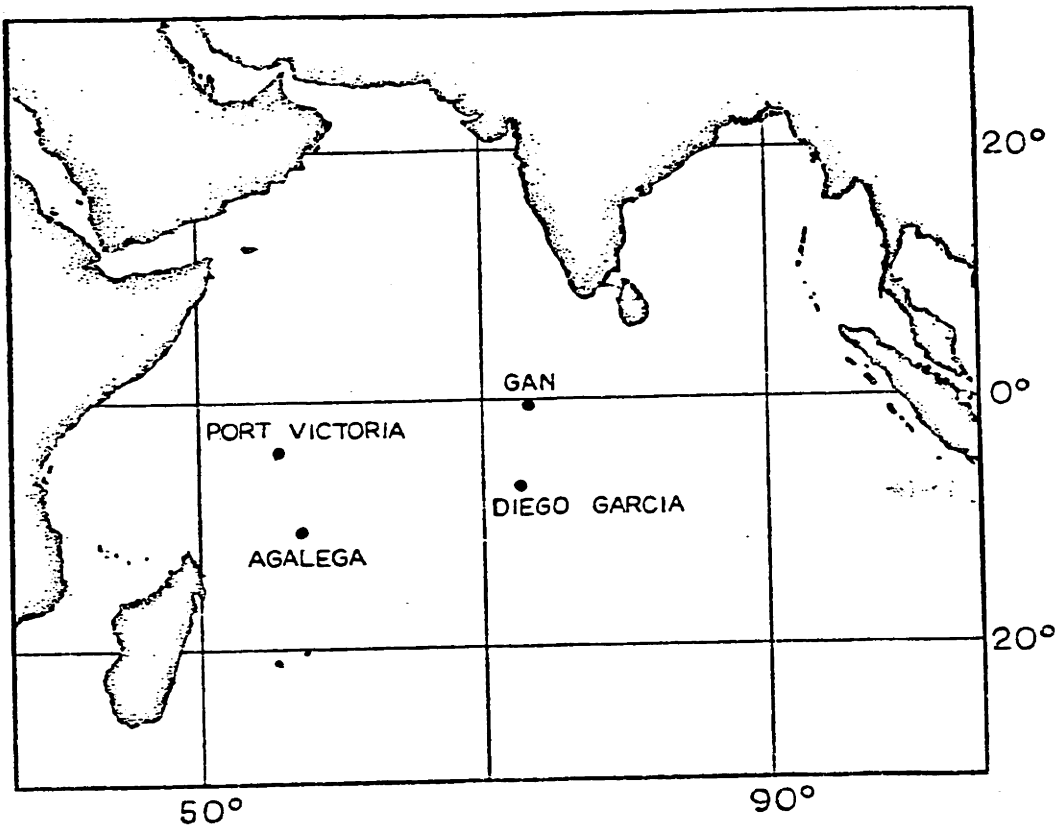
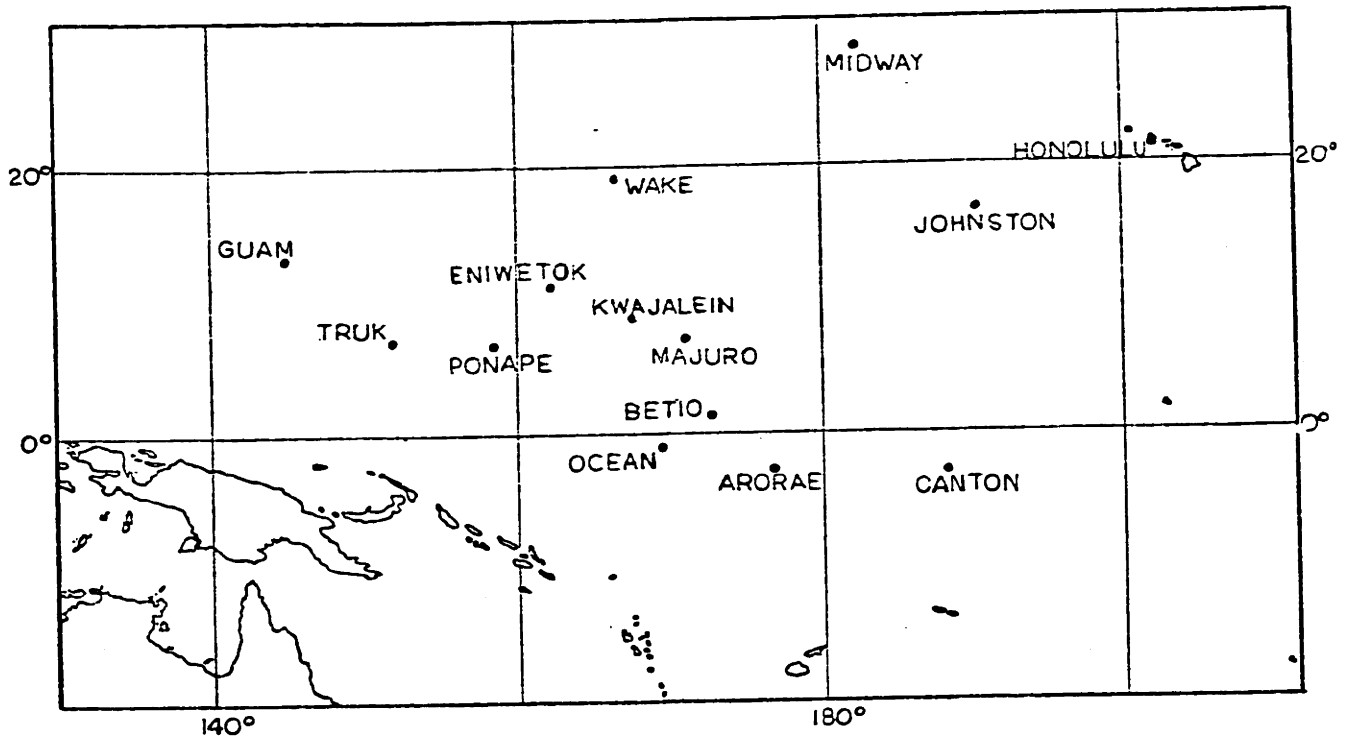


Figure 2.2 - Locations of surface weather stations.

regarded as a matter of degree depending on the topography of the island and the location of the instruments (see the evidence presented by Hwang (1970) and Wyrcki and Meyers (1975)). In any case, the island station data are evaluated here in groups, not singly. Considering the wide variety of topographic conditions, it is unlikely that unique island effects, even if present in individual power spectra, would be significant in the cross-spectra between the islands.

B. 3.5- to 7-Day Periods

We have found that three previously-discovered atmospheric waves in this period band have large surface amplitudes and small wavenumber bandwidths and are therefore capable of forcing narrow-band oceanic waves. Subsection 1 distinguishes the surface signals of the often-confused (in the literature), equatorially-trapped Rossby-gravity waves* (Wallace (1971)) and non-equatorially-trapped Easterly waves (Shapiro (1977)). A 4-6 day period "equivalent-barotropic" global oscillation is described in Subsection 2.

B.1. Rossby-gravity and Easterly Waves. Both Rossby-gravity and Easterly waves have large meridional wind components. The power density spectra for the meridional winds, measured at Pacific and Indian Ocean stations within 12° of the equator, are displayed in Figures 2.3 and 2.4, respectively. The spectra were computed by first removing the mean, tapering the data with a 10% cosine filter, fast-Fourier transforming the tapered series and finally frequency-band averaging the periodogram estimates (see Bingham et al. (1967)).

A reference line has been drawn for each spectrum in Figures 2.3 and 2.4, facilitating intercomparison. The lines have identical slopes

*These lower tropospheric waves may be simple extensions of stratospheric Rossby-gravity waves reviewed by Wallace (1973) and Holton (1975).

Figure 2.3 - Power density spectra of north wind from Pacific Ocean stations within 12° of the equator. Spectra are offset by two decades. Straight lines are intended for reference only. Sloping lines have identical y-intercepts and arbitrarily chosen -4/5 slopes. Number at left end of each spectrum refers to 95% confidence intervals at bottom of figure. Otherwise plotted as in Figure 2.1.

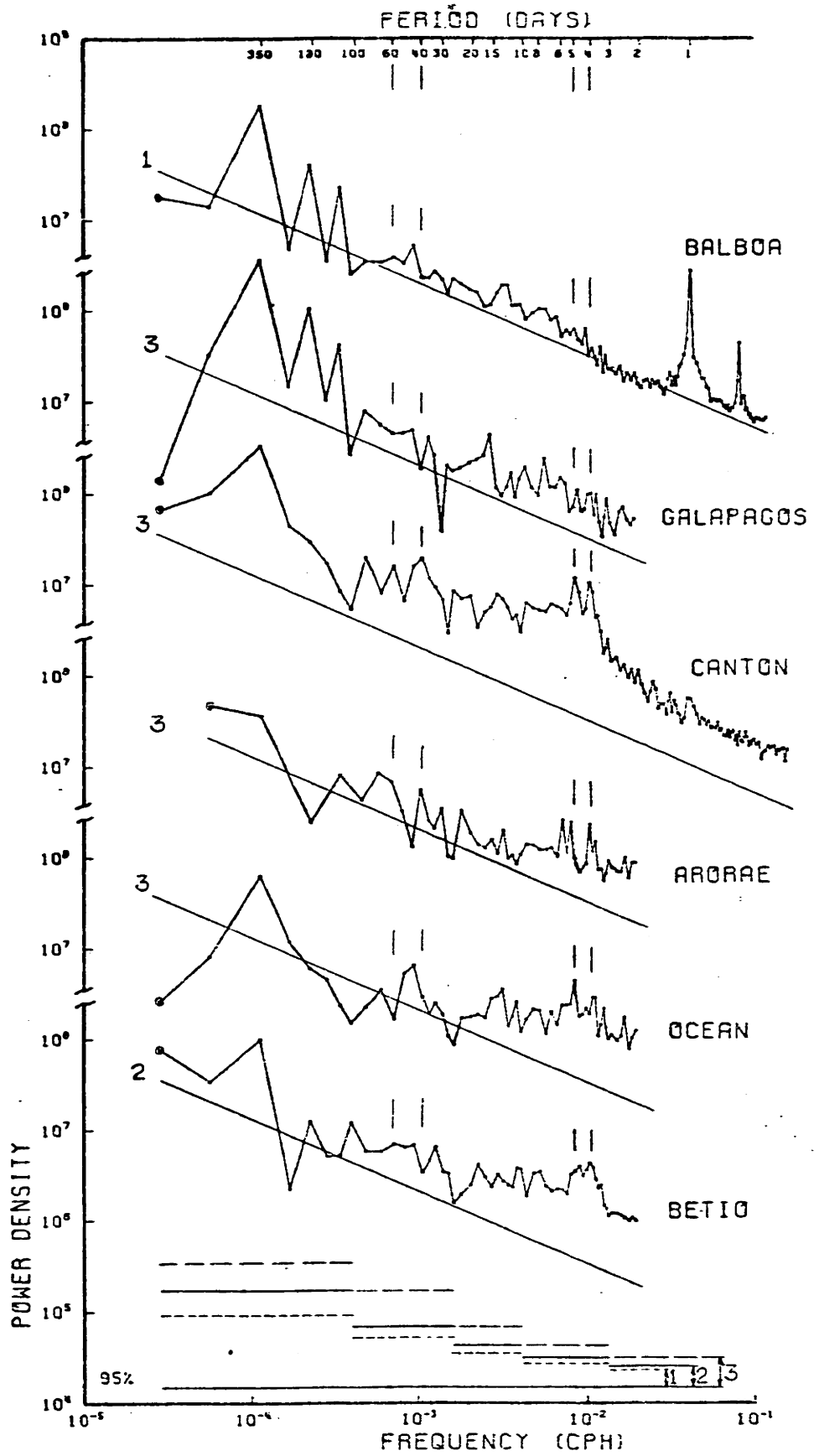


Figure 2.3a

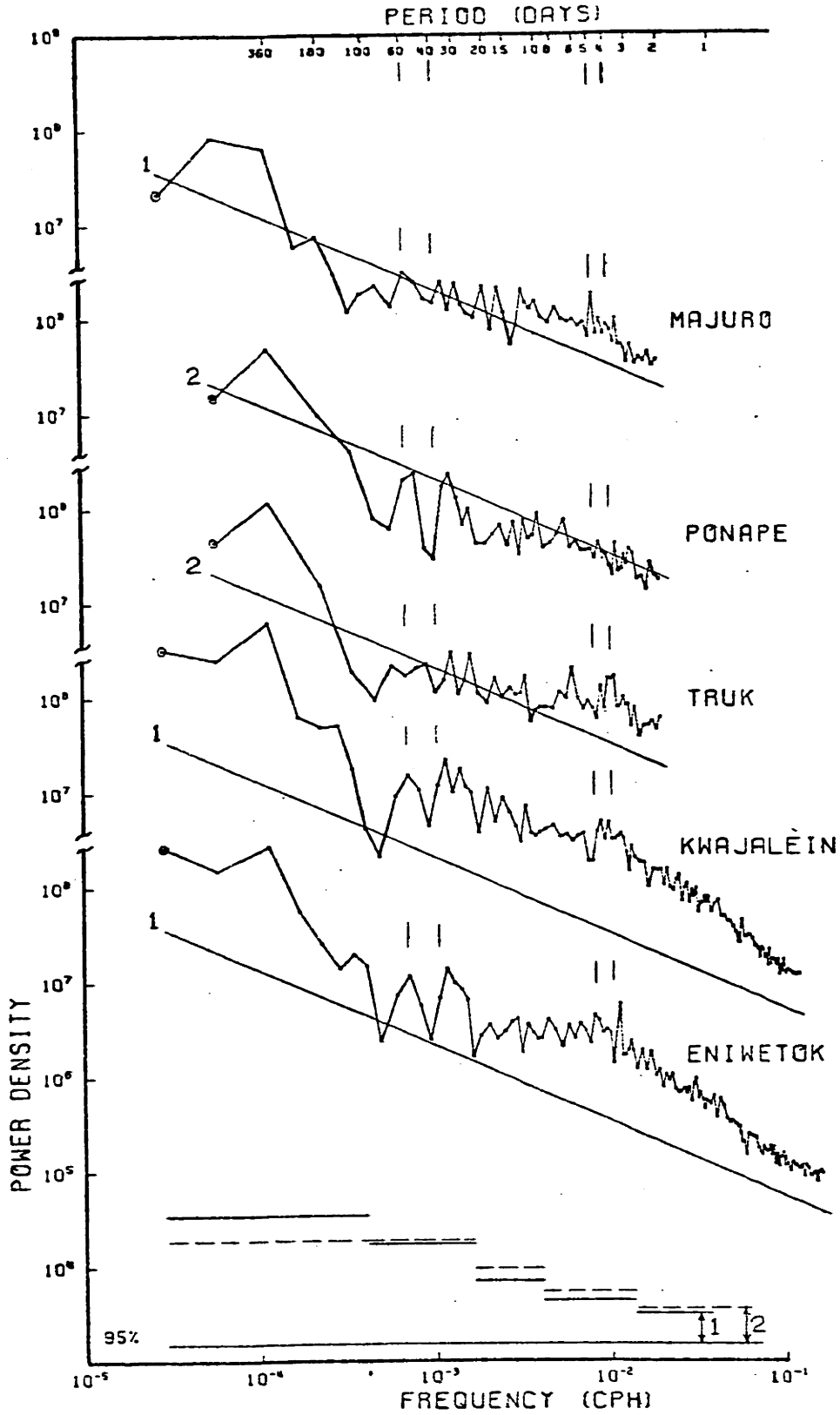


Figure 2.3b

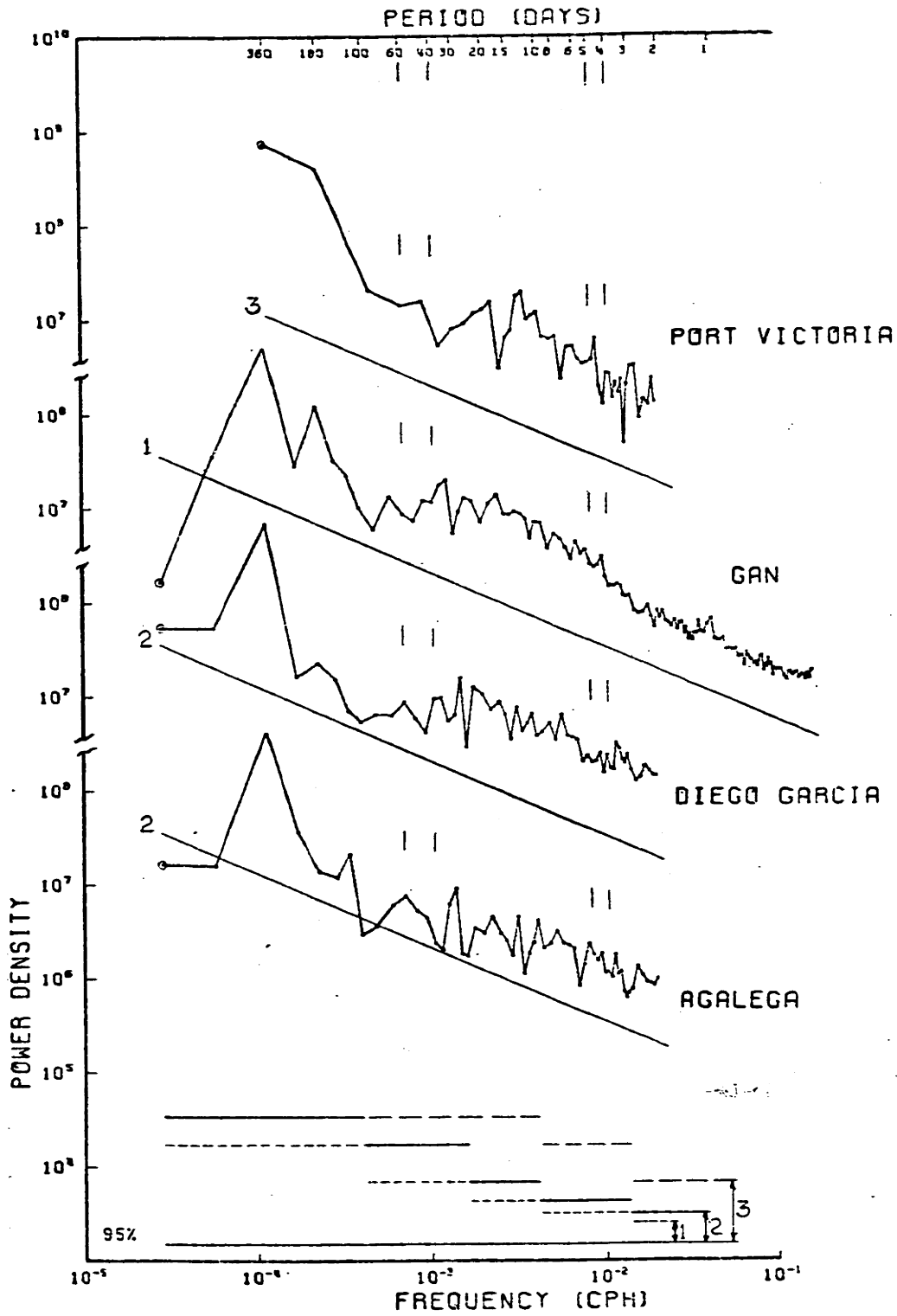


Figure 2.4 - Power density spectra of north wind from Indian Ocean Stations. Plotted as in Figure 2.3.

(arbitrarily chosen to be $-4/5$) and y-intercepts. The spectra are separated by two orders of magnitude in each plot. The 4-, 5-, 40- and 60-day periods are indicated by vertical lines above each spectrum for later reference.

The statistical significance of a peak in a single spectrum will not be stressed. Instead, the significance of a peak in terms of providing evidence for the existence of organized wave motion is based on its reproducibility in several spatially separate power spectra and on the coherence between stations at the peak period.

Canton, Arorae and Betio, in the western Pacific near the equator, exhibit large peaks in the 4-5 day band (Figure 2.3a). There are also suggestions of 4-5 day peaks at Ocean, Majuro, Truk, Kwajalein and Eniwetok. Both Rossby-gravity and Easterly waves have observed mean periods of 4-5 days in the lower troposphere (Wallace (1971)). Except for the three equatorial stations just mentioned, no station, including Galapagos and those in the Indian Ocean, can be considered to have statistically significant narrow-band peak(s) in the 4-5 day band.

Notice that the spectrum at Canton has two peaks, one at 4 days and one at 5 days. This double peak feature becomes pronounced in many of the meridional wind coherences and is suggested as well in the power spectra at Arorae, Betio and Ocean. The question arises (answered later) whether the two peaks imply the existence of two distinct wave motions. The apparent separation into two peaks indicates that the atmospheric waves have a high Q, an observation of some importance in determining oceanic resonance (Wunsch and Gill (1976)).

B.1.a. Wavenumber Estimates. Examination of the coherences* between stations is necessary to determine the spatial structure of any wave motion

*The coherence function is computed from auto- and cross-spectra that are calculated in a manner similar to that just described for auto-spectra.

that is present. An example of meridional wind coherence between Canton and Batio is given in Figure 2.5, which exhibits a broad amplitude peak in the 4-5 day band, typical of most tropical meridional wind coherences in the Pacific and possibly indicating the presence of atmospheric waves.

Since we expect the Rossby-gravity waves to dominate the meridional winds near the equator and the Easterly waves to dominate between 5° and 15°N (Wallace (1971)), we have separated the computed meridional wind coherences into groups according to the latitudes of the station pairs: A - both stations equatorward of 3° ; B - both stations between 7° and 22°N ; and C - at least one station between 3° and 7°N or one station north of 7°N and the other equatorward of 3° . The coherence phases from the 3.5-5.5 day band were used to obtain zonal wavenumber estimates by dividing the phase by the zonal station separation. This naturally assumes that the phase of the waves is independent of latitude, which is a reasonable assumption for the latitudinal separations considered here (see Figure 6 of Nitta (1970)). But since Burpee (1974) found a small northward phase lag for Easterly waves over Africa, we utilize only station pairs that are separated by greater distances in the zonal direction than in the meridional direction.

The zonal wavenumber estimates s , in cycles/circumference, for station pairs in Groups A and B are plotted against zonal station separation as \bullet 's and \times 's, respectively, in Figure 2.6. We have only used coherences with significant amplitude in the 3.5-5.5 day band at the 95% level. We have plotted only the gravest negative estimates of s .

The average wavenumber from the seven equatorial (Group A) coherence pairs is $s \sim -4.1$, in agreement with previous estimates of the Rossby-gravity wavelength. The average wavenumber from the eight Group B coherence pairs

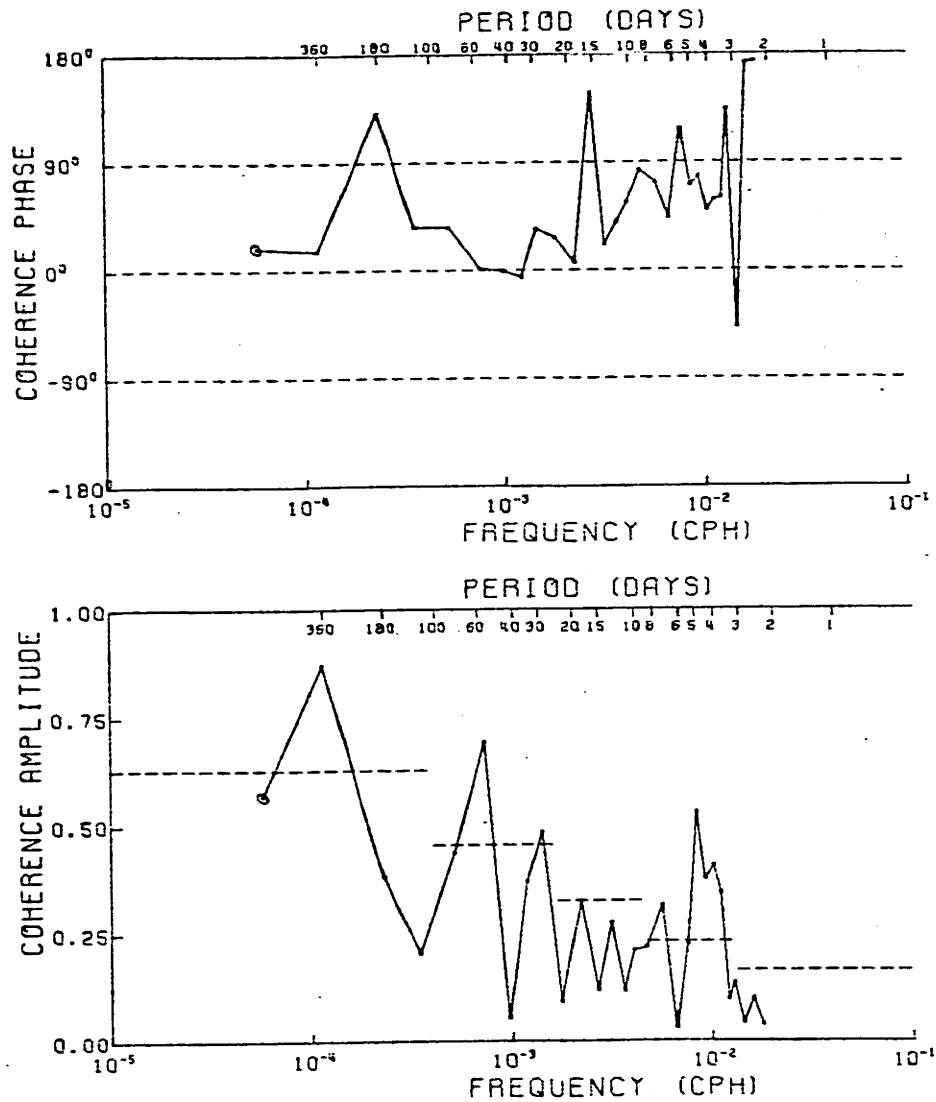


Figure 2.5 - Coherence of north wind between Canton and Betio using 8 years of data. Abscissae as in Figure 2.1. Positive phase (in degrees) indicates Canton leads. Dashed line in amplitude plot is 95% level of no significance, except for zero-frequency estimate (circled).

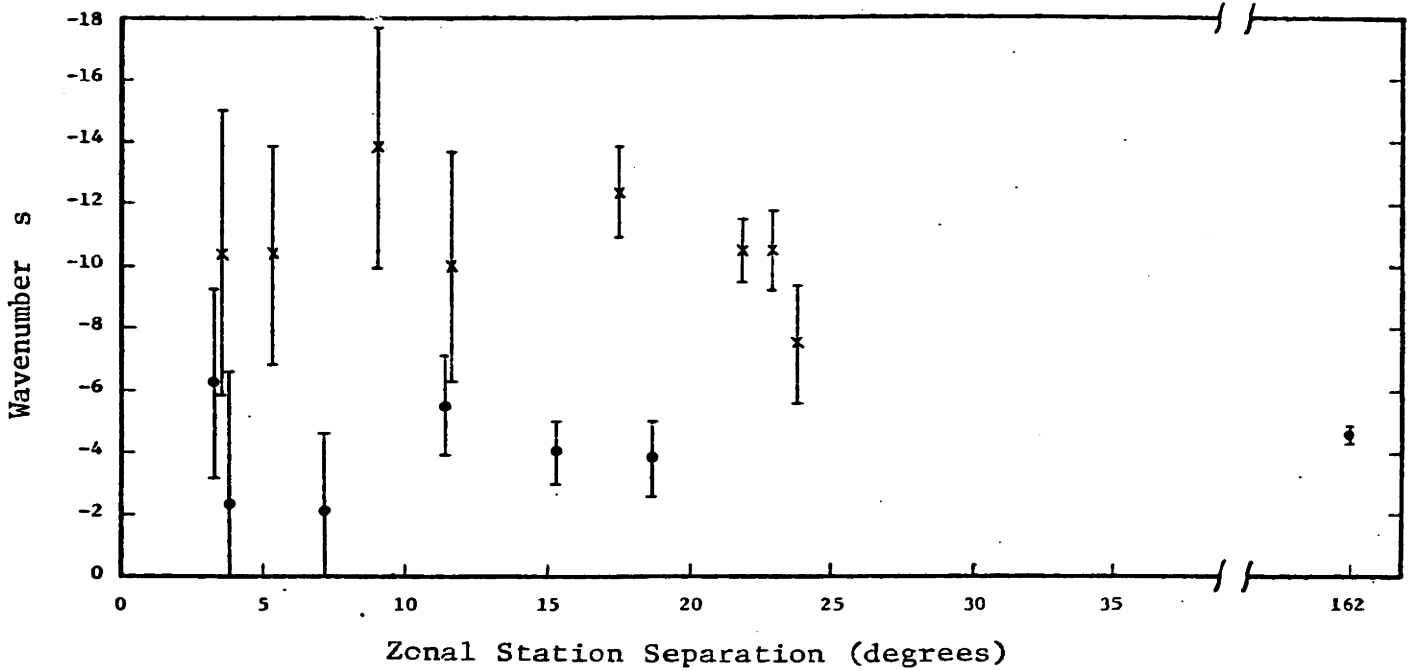


Figure 2.6 - Zonal wavenumber (in cycles/circumference) estimates, from north wind coherence in the 4-5 day band, plotted against zonal station separation for selected Pacific station pairs (see text). 95% error bars are indicated.

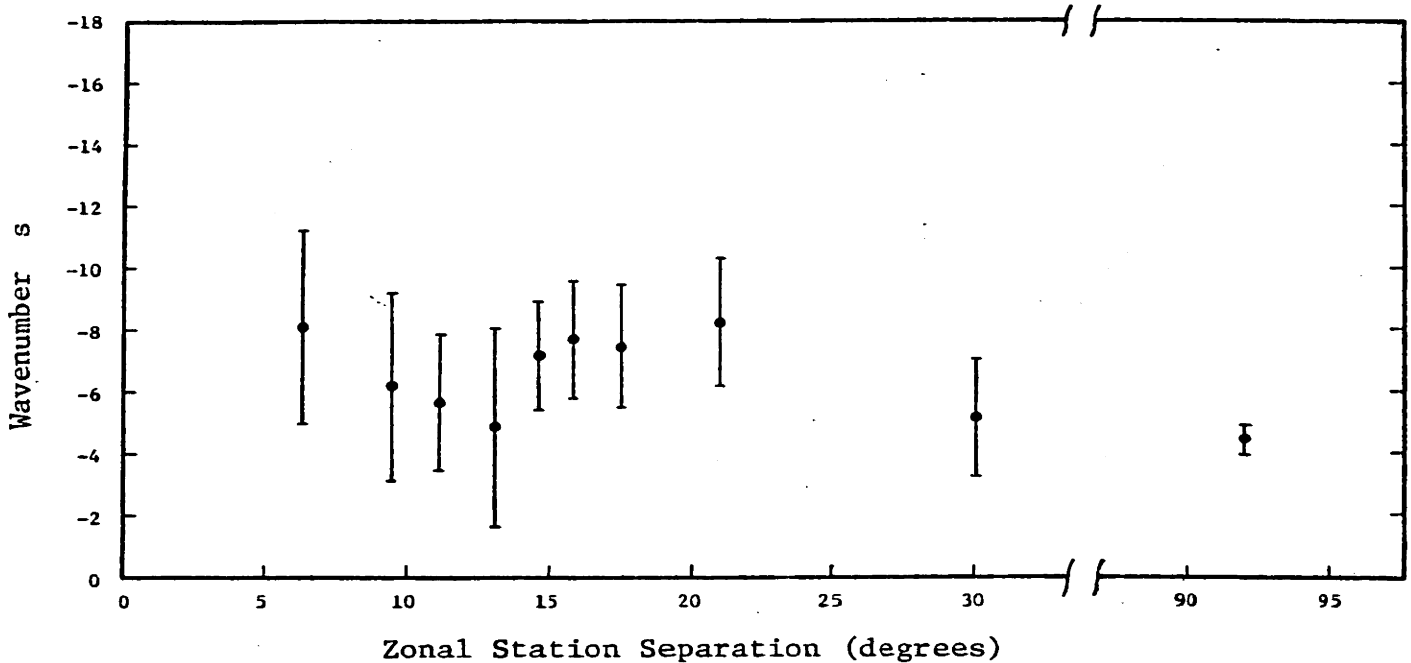


Figure 2.7 - As in Figure 2.6, but only for Pacific station pairs that are affected by both Easterly and Rossby-gravity waves.

is $s \sim -10.7$, in agreement with previous estimates of the Easterly wave wavelength. These wavenumber estimates have been corroborated by computations of high-resolution (maximum-likelihood) wavenumber spectra.* The delineation between Easterly wave wavenumbers and Rossby-gravity wave wavenumbers is clear.

The latitudinal separation between the Easterly and Rossby-gravity waves, which has been emphasized above, is not sharp. Wavenumber estimates from the Group C coherence pairs, which straddle the boundary between the wave types, are plotted in Figure 2.7. Their average is $s \sim -6.7$ indicating the presence of both wave types (see also Wallace (1971)).

The coherences between the four equatorial stations Canton, Arorae, Betio and Ocean frequently have two amplitude peaks in the 3.5-5.5 day band, as do the power spectra (Figure 2.3a). If each peak was due to a different wave, either an Easterly or a Rossby-gravity wave, the coherence phase would be expected to change by a factor of 2.5 from one peak to the other. This does not occur. The mean wavenumbers, calculated from six coherences between the four equatorial stations, are -3.2 and -5.8 in the 90-98 hour and 119-134 hour bands, respectively, estimates which are within the error bars for previous estimates of the mean Rossby-gravity wavelength.

Although the Easterly waves may produce important fluctuations of subtropical currents (e.g., Mofjeld and Wimbush (1977)), they are clearly not as important as Rossby-gravity waves for generating equatorially-trapped ocean waves in the central-western Pacific. Therefore, we will not discuss Easterly wave properties any further here. The situation may be different in the Atlantic Ocean where Easterly waves are strong and have been observed to extend to the equator, whereas the Rossby-gravity waves have not been

*For a description of the maximum-likelihood estimator see Capon (1969).

observed in the lower troposphere there. Neither wave type is strong at the surface within 10° of the equator in the eastern Pacific (see the Balboa and Galapagos spectra in Figure 2.3a) or the Indian Ocean.

The coherence amplitudes corresponding to the "equatorial" phases (Group A) of Figure 2.6 can be used to obtain an estimate of zonal wave-number bandwidth, Δs , following the formalism described by Munk and Phillips (1968; particularly equation 59). The best estimate of Δs is 8, in which case the range of zonal wavenumbers for the Rossby-gravity waves is $-8 < s < 0$, assuming the mean wavenumber is -4 .

B.1.b. Amplitude Estimates; Annual and Interannual Variability; Q.

The rms amplitude of the meridional wind in the 3.5-5.5 day band ranges from 0.4 to 0.8 m/s at the four equatorial stations in the central-western Pacific. The amplitude reached 5 m/s at Canton in the fall of 1955.

The surface zonal wind and pressure fields, associated with the Easterly and Rossby-gravity wave meridional winds just discussed, overlap considerably in latitude. Consequently, observational evidence of these fields is difficult to interpret unambiguously. The zonal wind power density spectra do not exhibit 4-5 day peaks analogous to the meridional wind spectra, and the 4-5 day band in air pressure is dominated by a barotropic oscillation discussed in the next subsection. Equations (1.27a and 1.27b) can be used to determine the theoretical amplitudes of u and p for the Rossby-gravity waves. For example, if the maximum meridional wind at the equator $v \sim 1$ m/s, then the maximum zonal wind $u \sim 1/2$ m/s and sea surface air pressure $p \sim .1$ mb. Both u and p will have maximum amplitudes between 5° and 10° from the equator.

Observations by Julian (1971) suggest that the 4-5 day Rossby-gravity waves are stronger in the late summer and fall. To estimate the magnitude

of this variability, a power spectrum was constructed from piece-wise averaging the power calculated from mid-August through mid-January data of each of the nine years of the Canton north wind dataset. This spectrum is superimposed in Figure 2.8a upon a similar calculation using the mid-February through mid-July data of each year. The power densities in the 3.7-5.3 day band are $850 \text{ (m/s)}^2/\text{cph}$ and $490 \text{ (m/s)}^2/\text{cph}$ for the August-January and February-July periods, respectively. These numbers are statistically different at the 99.5% level. Note that even in the February-July period the 4-5 day power is above the background level, so the waves do occur year-round.

Interannual variability of the 4-5 day Rossby-gravity wave power is also quite large. In Figure 2.8b are plotted the power spectra for Canton north wind from 1950 and 1957. The power densities in the 3.7-5.3 day band are $370 \text{ (m/s)}^2/\text{cph}$ and $980 \text{ (m/s)}^2/\text{cph}$ in 1950 and 1957, respectively. These numbers are statistically different at the 99% level. Note that even in 1950 the power in the 4-5 day band is above the background level.

These annual and interannual variations are observed at most of the stations where Easterly or Rossby-gravity wave activity in the 4-5 day band is found.

Lastly, the Q varies between 1 and 8 in the 4-5 day band in the equatorial central-western Pacific. The larger Q estimates occur at Canton and Arorae where the "double-peak" structure is strong (Figure 2.3).

B.2. Global Five-Day Pressure Waves. Madden and Julian (1972b and 1973) firmly established the characteristics of an "equivalent-barotropic" oscillation of the atmosphere with a mean period of five days, extant at all longitudes and at latitudes from at least 60°N to 60°S . The observed mean wave characteristics, such as period, zonal wavenumber and latitudinal

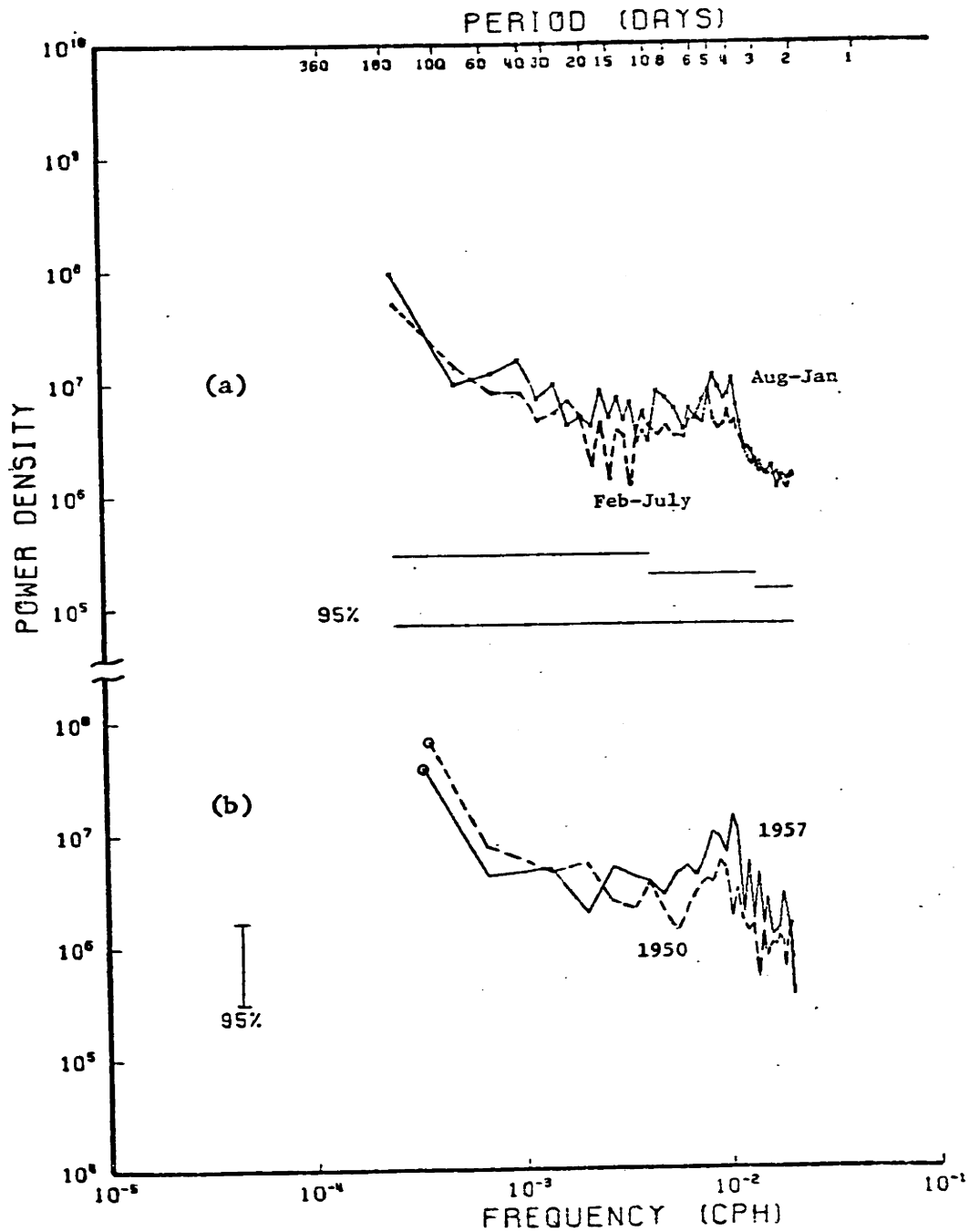


Figure 2.8 - (a) Power density spectra of north wind from Canton using only data from August through January, or February through July (dashed), from the years 1949 through 1957.

(b) Power density spectra of north wind from Canton for the years 1950 (dashed) and 1957. Plotted as in Figure 2.1.

structure, were shown to be consistent with a solution to the Laplace Tidal Equations (LTE) presented by Longuet-Higgins (1968). The solution is a wave of the second class (Rossby wave) with $s' = 1$ and $n' = 2$. [For convenience in referring to Longuet-Higgins' work, s' (≥ 0), rather than s , denotes zonal wavenumber, so propagation direction is indicated by the sign of the frequency. n' parameterizes the latitudinal structure, where $n'-s'$ equals the number of nodes in the streamfunction between the poles.] When the period is 5 days, the Lamb parameter $\epsilon = \frac{(2\Omega a)^2}{gh} \approx 8.6$, so the equivalent depth $h \approx 10$ km. Longuet-Higgins' (1968) numerical solution for the $s' = 1$, $n'=2$ planetary wave with $\epsilon = 10$ is plotted in Figure 2.9 (Example B). For comparison, the analytic solution for $\epsilon \rightarrow 0$ (Rossby-Haurwitz wave) is also shown (Example A). For the Rossby-Haurwitz wave, $\omega \approx \frac{-2\Omega s'}{n'(n'+1)}$, yielding a period of 3 days rather than the observed 5 days.

Some power spectra of sea level atmospheric pressure from the tropical Pacific and Indian Oceans are displayed in Figure 2.10. There is no clear suggestion of a narrow-band wave at 5 days, implying either low Q or that the barotropic oscillation is weak at sea level. Since every station pair separated by more than 500 km has a peak near five days in the atmospheric pressure coherence (e.g., Figure 2.11), the atmospheric oscillation is definitely not weak at sea level. The period of the coherence peak, when the peak is significantly above the background, is always within the range of $5 \pm .5$ days.

The high-resolution (maximum-likelihood) wavenumber spectrum* of atmospheric pressure in the 4.3-6.0 day band is shown in Figure 2.12, where two years of data from Canton, Johnston, Wake, Guam, Kwajalein and Eniwetok

*See Wunsch and Hendry (1972) for an example of an oceanographic application of the maximum-likelihood wavenumber spectrum and a summary of the computational procedure, aliasing, etc. (N.b., their Appendix B). Davis and Regier (1977) give a more general discussion of wavenumber spectrum estimators.

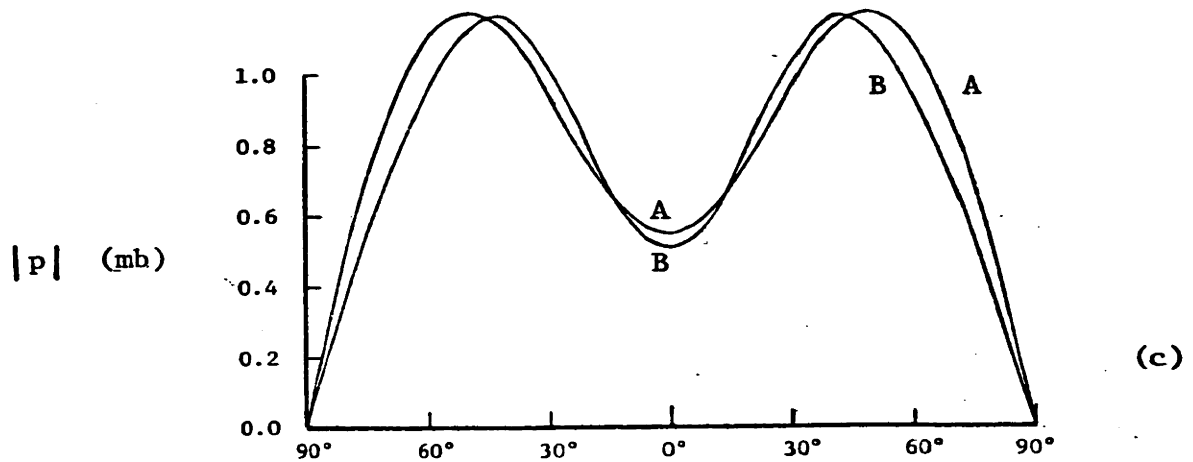
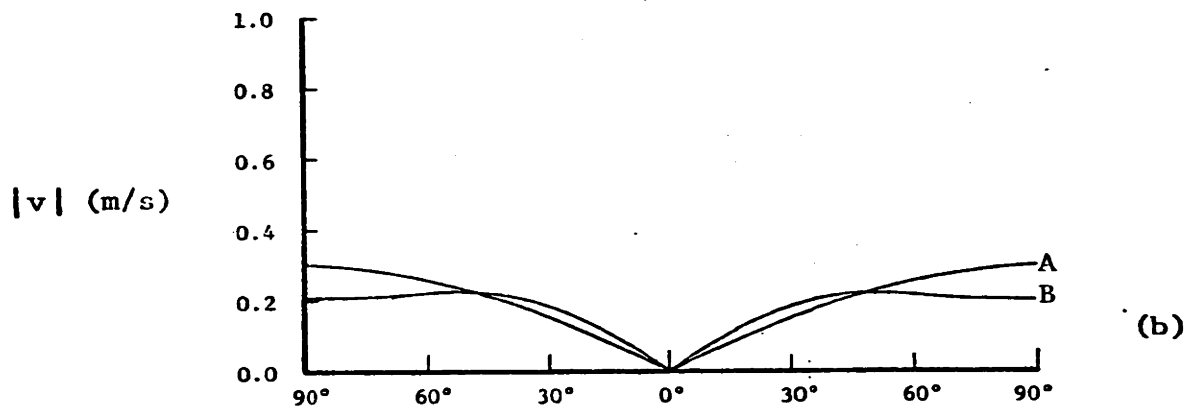
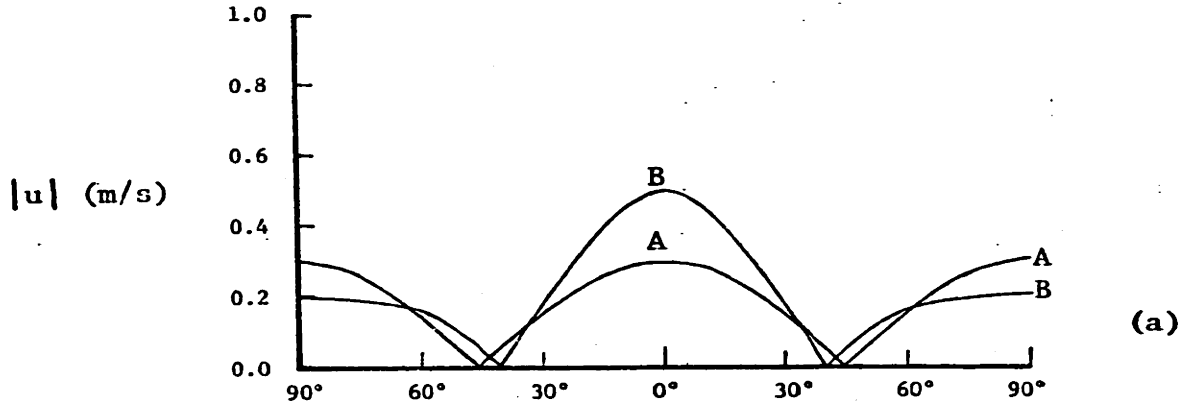
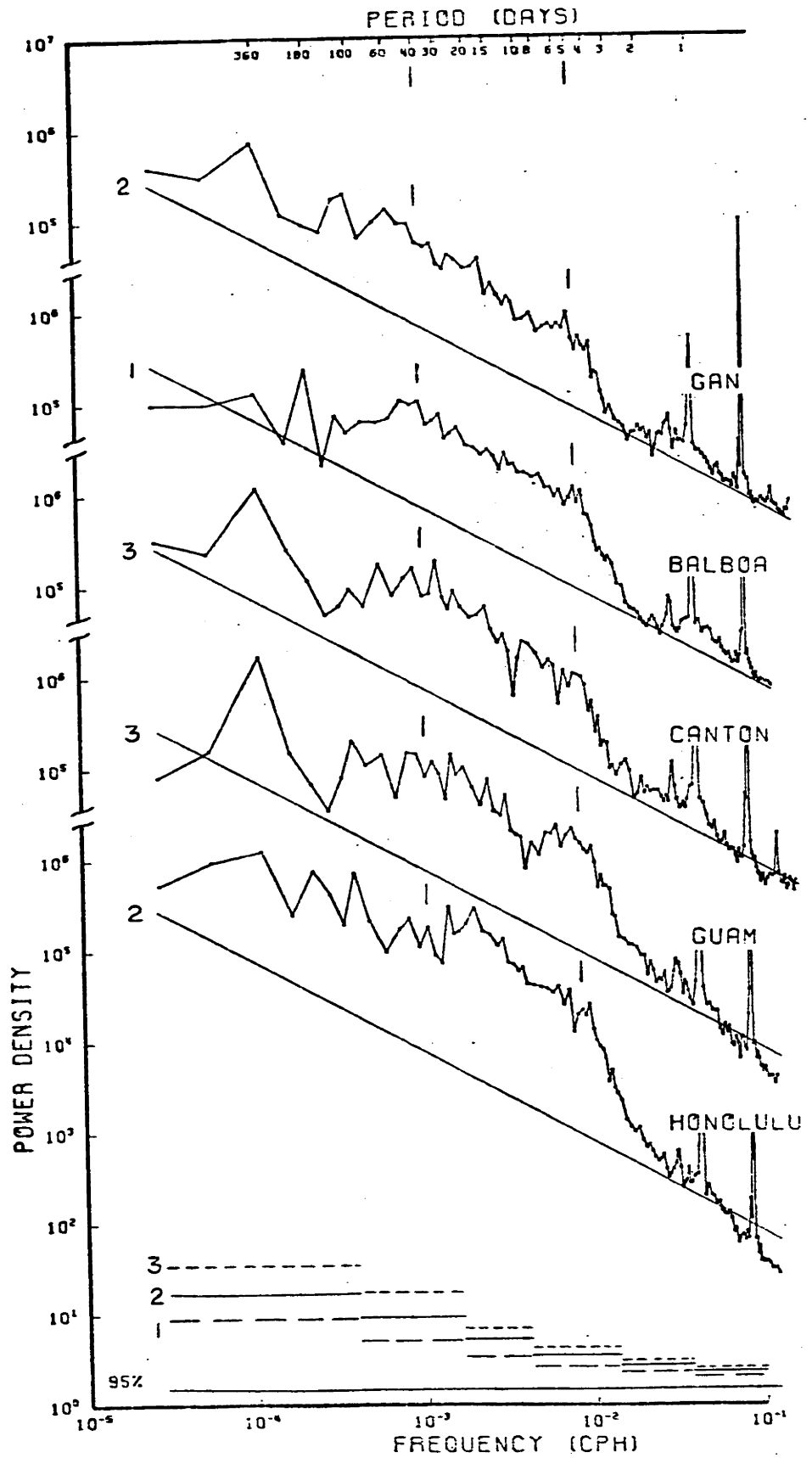


Figure 2.9 - Theoretical meridional structure of the $s'=1$, $n'=2$ planetary wave for $\epsilon \rightarrow 0$ (Example A) and $\epsilon=10$ (Example B).

Figure 2.10 - Power density spectra of air pressure from selected Pacific and Indian Ocean stations. Ordinate is power density in $(.1 \text{ mb})^2/\text{cph}$. Reference lines have a -1 slope. Otherwise, plotted as in Figure 2.3.



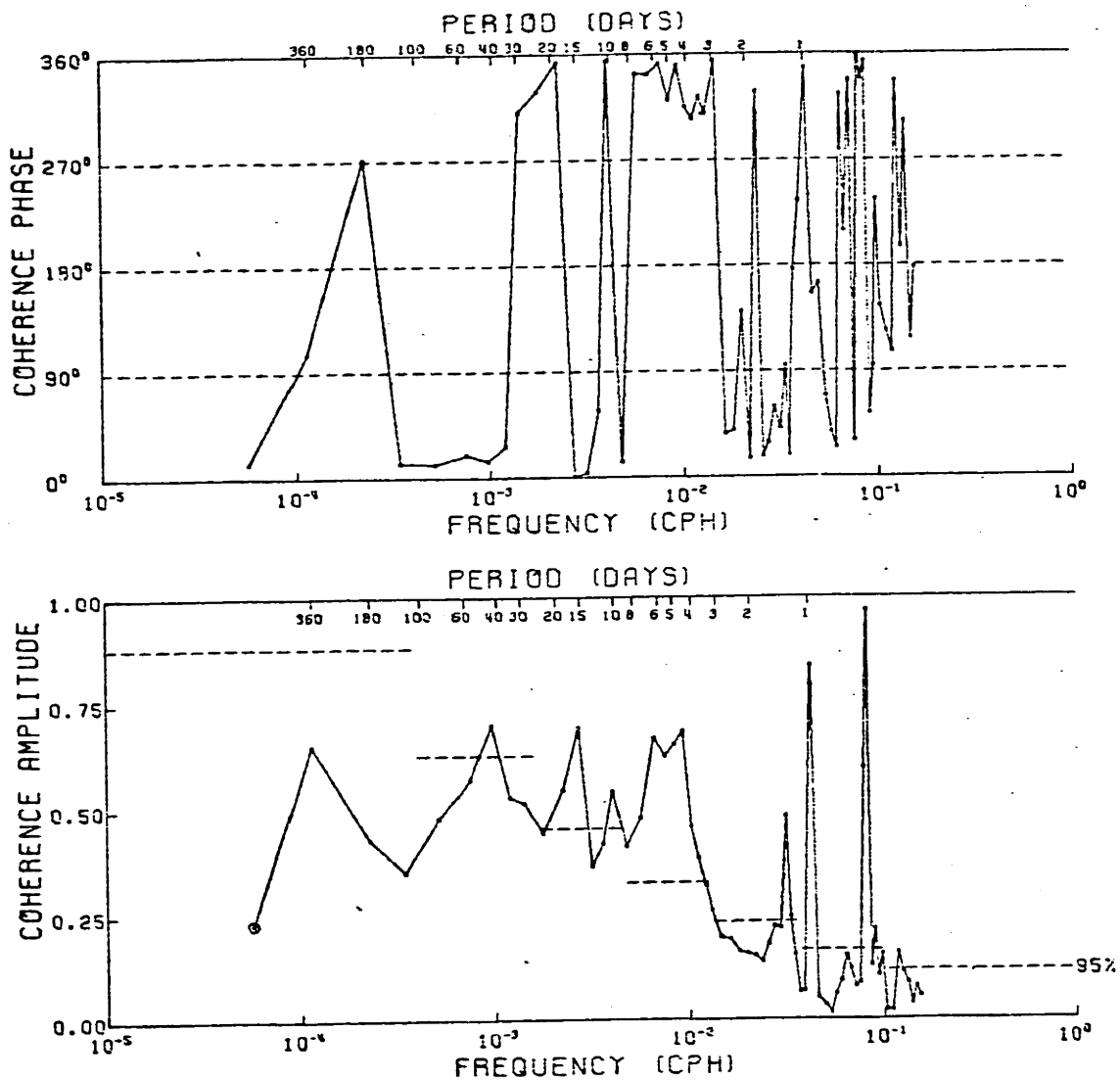


Figure 2.11 - Coherence of air pressure between Wake and Canton using 4 years of data. Positive phase indicates Wake leads. Plotted as in Figure 2.5.

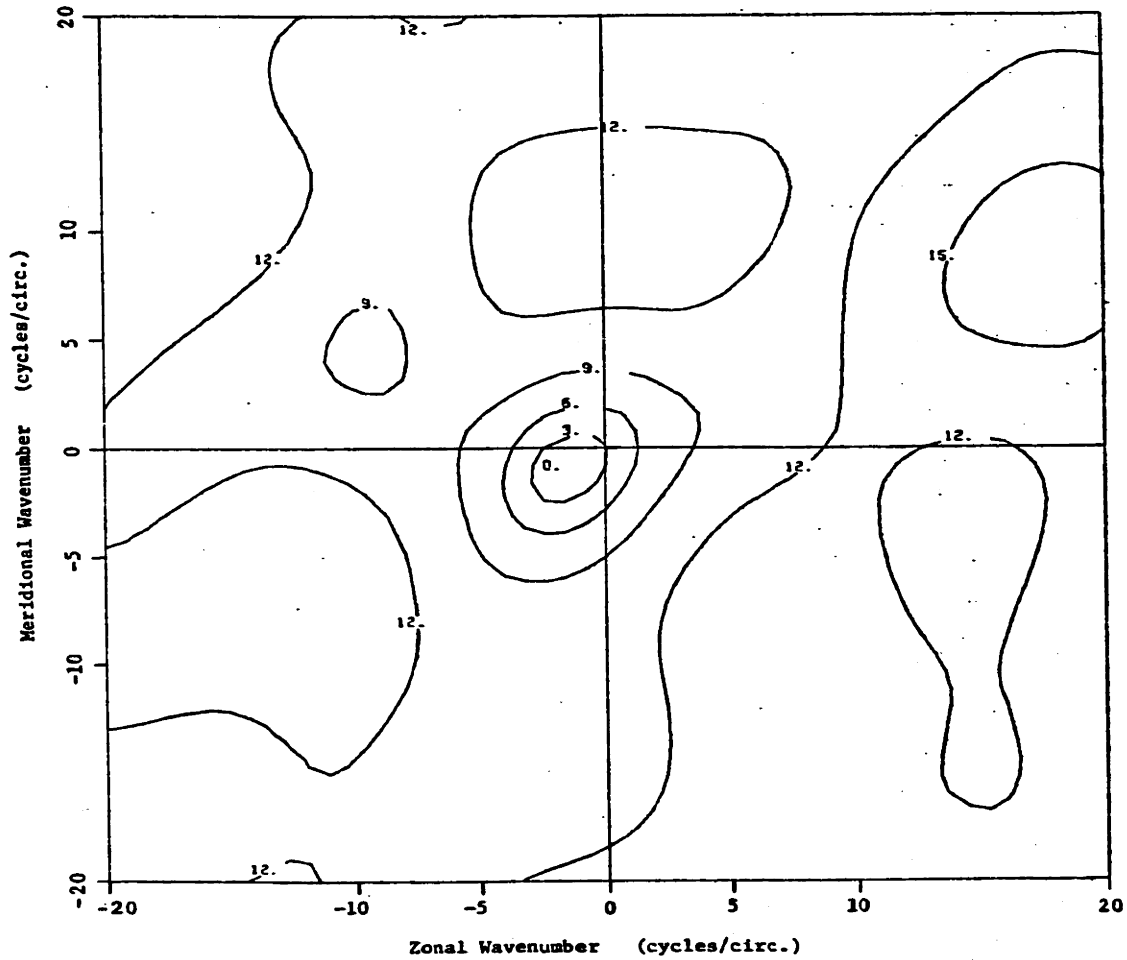


Figure 2.12 - Wavenumber spectrum of air pressure in the 4.6-6.0 day band using 2 years of data from Canton, Johnston, Wake, Guam, Kwajalein and Eniwetok. Contours indicate power relative to maximum at peak, in negative decibels with the minus sign dropped. Peak is indicated by 0.

have been used. The zonal wavenumber at the peak is $s \sim -1.6$, with 95% confidence interval $-3.2 < s < 0$, in agreement with previous estimates (Madden and Julian (1972b, 1973) and Burpee (1976,1977)) and half-power bandwidth $\Delta s \sim 2.9$. The peak meridional wavenumber is not significantly different from zero at the 95% level, as expected. From seven coherences between station pairs separated by more than 28° of longitude, the mean s is almost exactly -1 (latitudinal separations of the station pairs were ignored, since the meridional wavenumber is zero).

The peak in Figure 2.12 accounts for approximately 70% of the energy in the 4.3-6.0 day band, yielding an estimate of 30% for the noise energy.

The maximum amplitude of pressure occurs at mid-latitudes (Figure 2.9c) where it probably averages 1 mb at the surface (Madden and Julian (1973), Misra (1975)). The corresponding winds are too weak to be detected at sea level.

No annual modulation is detectable in the power of the five-day wave (Madden and Stokes (1975) and this investigation).

C. 7- to 20-Day Periods

Many investigators have found evidence for a variety of wave types in the Pacific in this frequency band, both in the troposphere and stratosphere (Yanai (1975)). Only a stratospheric 10-15 day period Kelvin wave has been observed consistently, however. In the equatorial zones of the Atlantic and Indian Oceans, oscillations of the surface winds at 7-20 day periods have also been observed, but there is not enough information to indicate whether descriptions of these oscillations in terms of equatorial waves is adequate or useful. Two of the observed oscillations are (1) in-phase, 14-day oscillations of the Atlantic equatorial tradewinds (Krishnamurti et al. (1975)), and (2) a 12-day oscillation of Indian Ocean monsoon

characteristics, such as the low-level jet over East Africa (Krishnamurti and Halme (1976)).

The dataset studied here suggests the presence of several baroclinic, equatorial waves in the 7-20 day band in the central Pacific, including (possibly) a 7-9 day Rossby-gravity wave and an 8-10 day Kelvin wave. None of the oscillations is a distinctive feature in the equatorial power spectra of surface winds, and only the 7-9 day Rossby-gravity wave is strong enough in the cross-spectra (see Figure 2.5) to yield significant wavenumber estimates.

The maximum-likelihood (MLM) wavenumber spectrum of meridional wind in the 7.4-8.8 day band from Canton, Arorae, Betio and Ocean is shown in Figure 2.13. The peak zonal wavenumber is -6 with a 95% confidence range of $-12.5 < s < 0$. The meridional wavenumber is not distinguishable from zero. The peak accounts for 60% of the energy in the frequency band.

In the period band of 7 to 20 days, Yanai and Murakami (1970) observed vertical wavelengths of 3 to 14 km, corresponding to equivalent depths of 3 to 63 meters (Holton (1970)). The only equatorial wave with a -6 zonal wavenumber at 8 days period, which yields equivalent depths in this range, is a Rossby-gravity wave (using the dispersion relations (1.33a and b)). The required equatorial trapping is deduced from the lack of meridional wind coherence between equatorial (within 3° of the equator) and non-equatorial stations in the 7-9 day band.

Although the 7-9 day Rossby-gravity wave is not distinct in the equatorial meridional wind power spectra (Figure 2.3a), the oscillation is suggested in the power spectrum of Canton north wind using only August to January data (Figure 2.8a). In the 7.1- to 9.5-day band, the August to January power density is $690 \text{ (m/s)}^2/\text{cph}$, and the February to July power

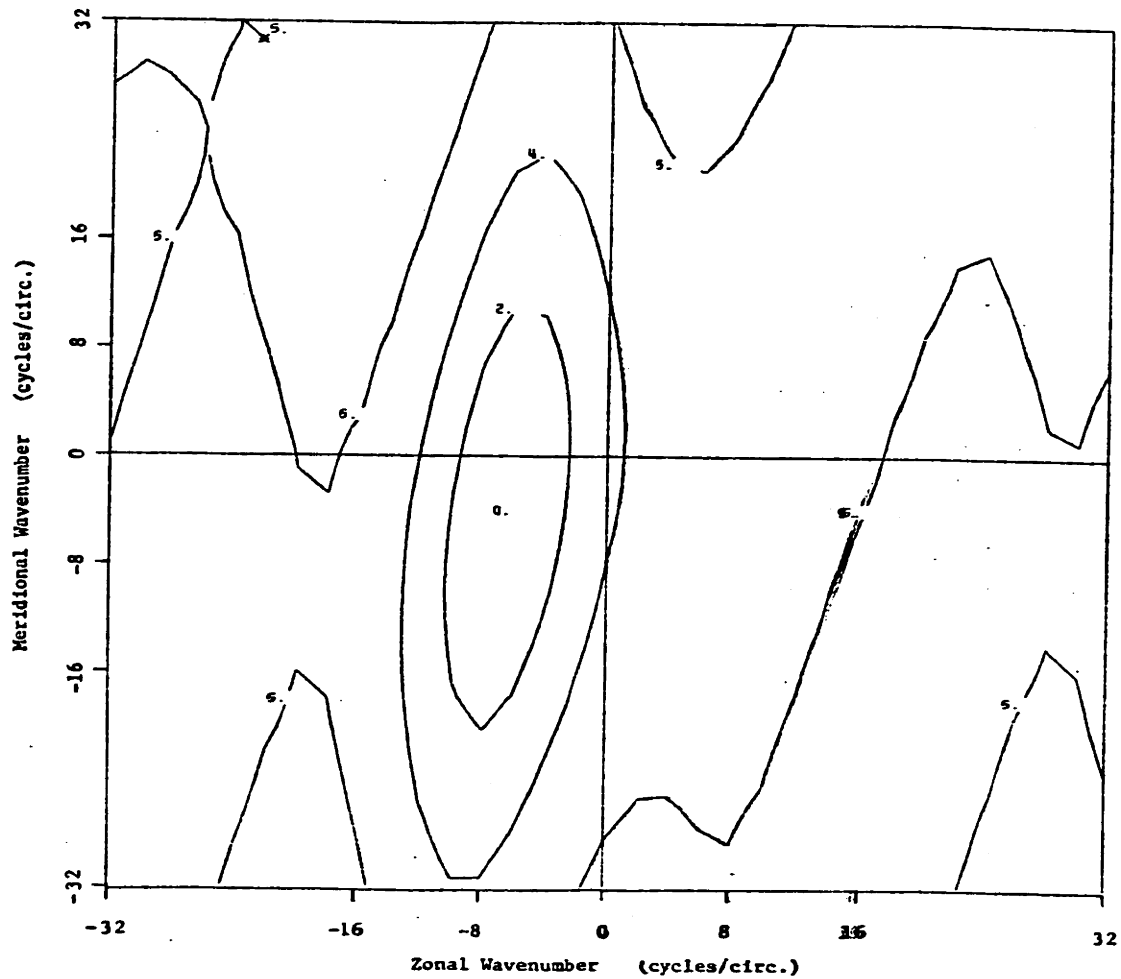


Figure 2.13 - Wavenumber spectrum of north wind in the 7.4-8.8 day band, using 3.6 years of data from Canton, Arorae, Betio and Ocean. Plotted as in Figure 2.12.

density is $350 \text{ (m/s)}^2/\text{cph}$. These numbers are significantly different at the 9% level. This annual variation is seen at Arorae, Betio and Ocean, but not at Galapagos or in the Indian Ocean. The Q of the 8-day meridional wind peak in Figure 2.8a is 3-4, so the August to January rms amplitude is $\sim 50 \text{ cm/s}$.

D. 20- to 90-Day Periods

The only atmospheric oscillation in this period band that is consistently detected is an oscillation discovered by Madden and Julian (1971), and independently by Parker (1973), that has been modelled as a damped Kelvin wave (Chang (1977)) with a period most often between 40 and 50 days (hereafter the oscillation will be referred to as the 40-50 day Kelvin wave). The 40-50 day Kelvin wave is a conspicuous feature in the zonal wind power density spectra from equatorial stations in the western Pacific Ocean (e.g., Canton, Arorae, Betio and Ocean in Figure 2.14a) and the Indian Ocean (e.g., Gan in Figure 2.15), and is less distinctly present in the equatorial power density spectra of surface air pressure (Figure 2.10).

Madden and Julian (1972a; hereafter MJ72) found that the 40-50 day Kelvin wave was globe-girdling in the upper troposphere, but that in the lower troposphere it was strongest in the western Pacific and undetectable over Africa and the Atlantic. In agreement with their results, the oscillation is not obviously present in the zonal wind power density from the Galapagos Islands (Figure 2.14a). However, Picaut and Verstraete (1976) found peaks at 40-50 day periods in the surface air pressure and winds at Abidjan on the Gulf of Guinea. It is possible that this 40-50 day Kelvin wave forces oceanic oscillations in all three equatorial oceans. Picaut and Verstraete (1976) document 40-50 day oscillations in sea level and sea surface temperature along the north coast of the Gulf of Guinea, and,

Figure 2.14 - Power density spectra of east wind from Pacific Ocean stations within 12° of the equator. Plotted as in Figure 2.3.

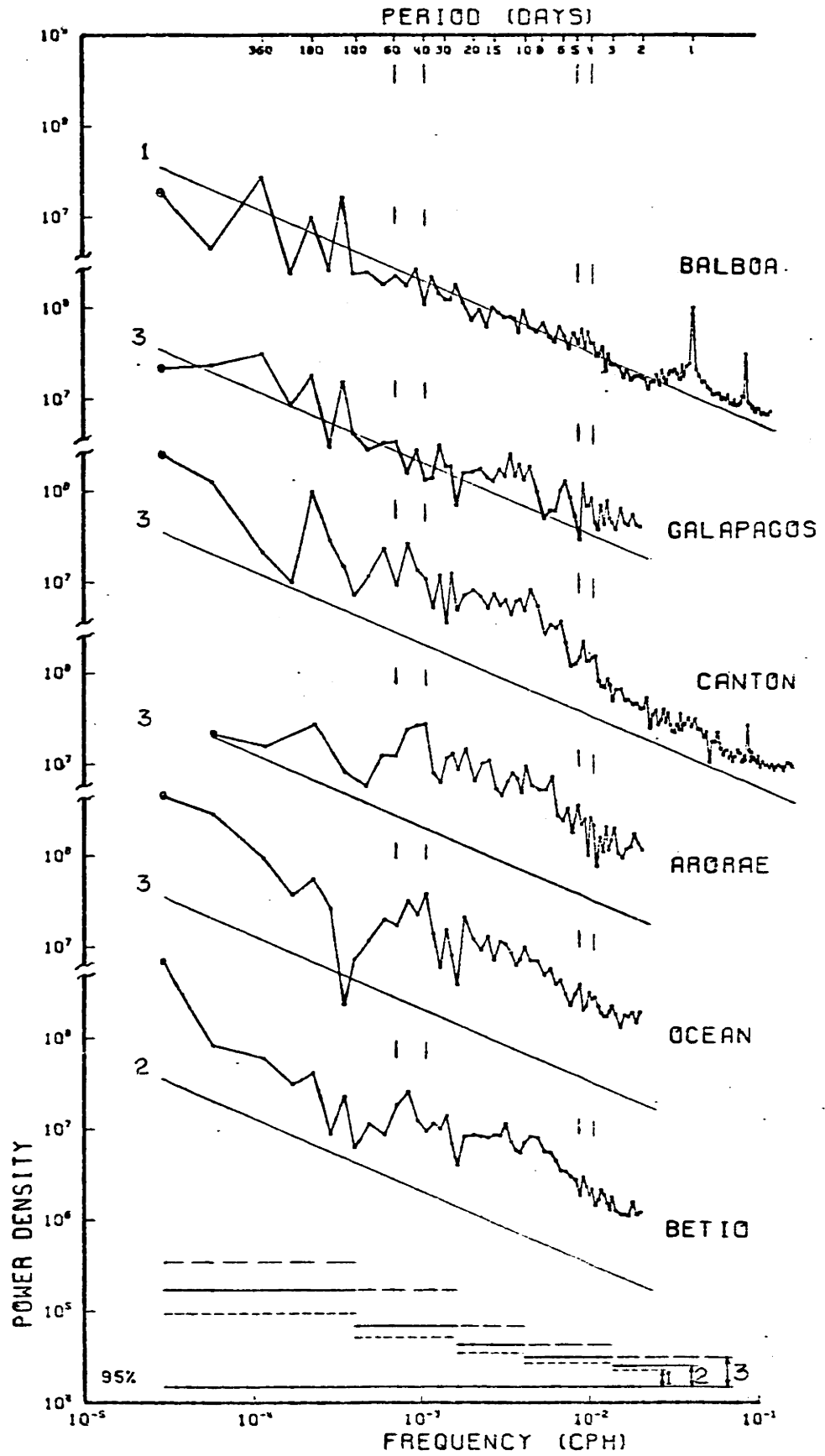


Figure 2.14a

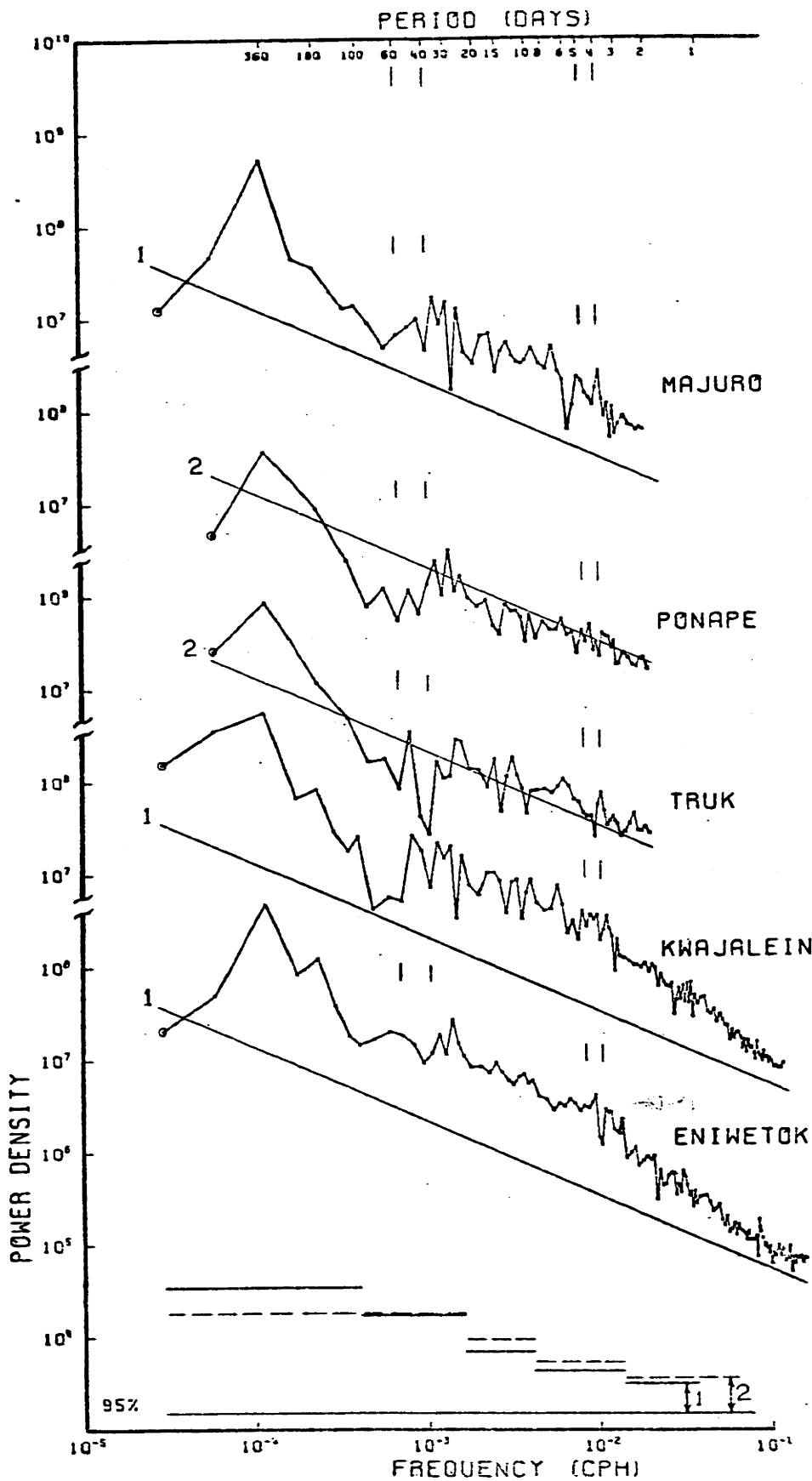


Figure 2.14b

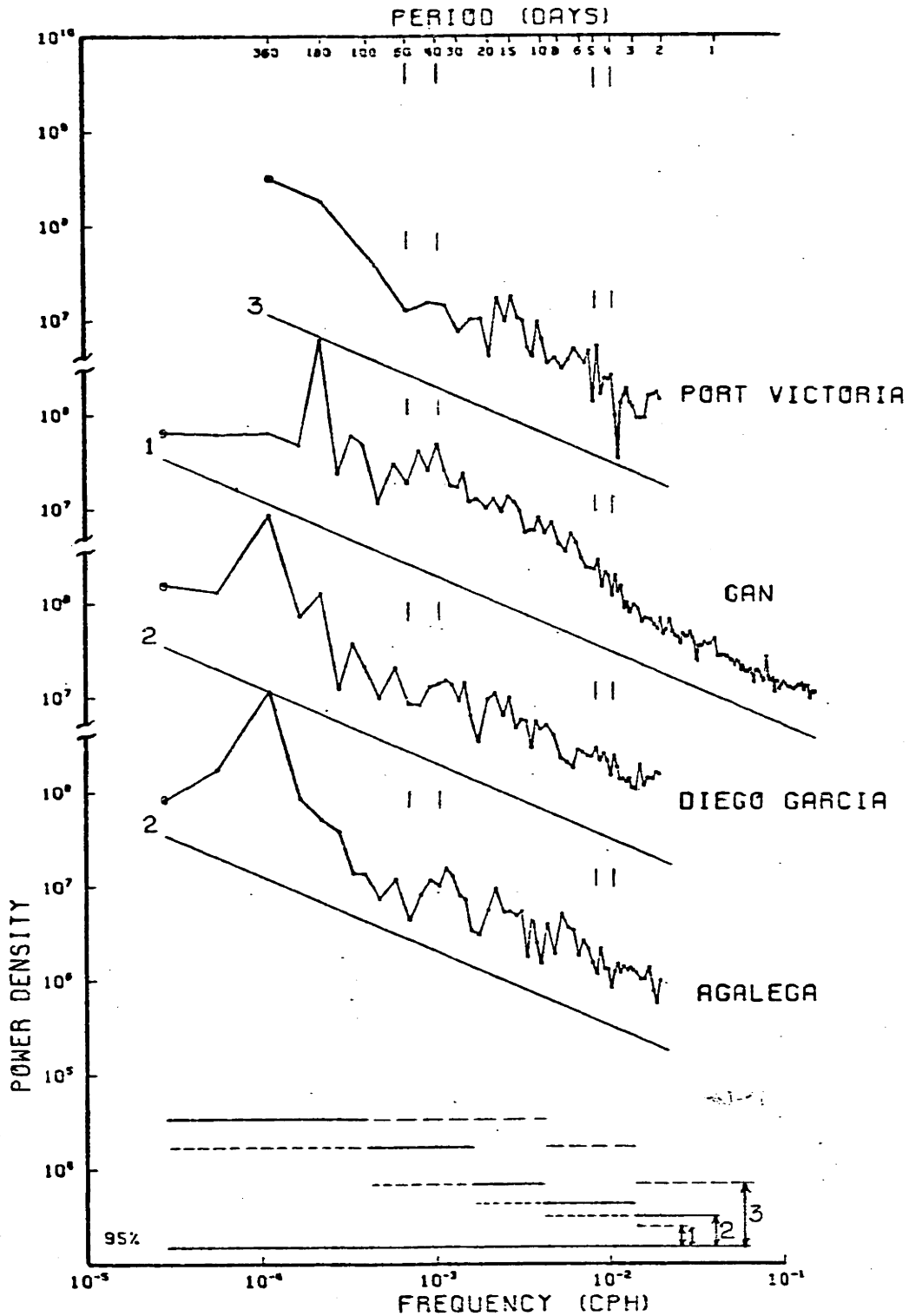


Figure 2.15 - Power density spectra of east wind from Indian Ocean stations. Plotted as in Figure 2.3.

in the next chapter, evidence is presented of a ~50-day oscillation in sea level in the Pacific Ocean.

MJ72 have described the 40-50 day Kelvin wave in more detail than any other authors. They analyzed 5-10 years of tropical surface pressure (from 25 stations) and tropospheric zonal winds (from 6 stations). The data studied here is not of sufficient temporal or spatial coverage to produce a statistically convincing description of the 40-50 day Kelvin wave. However, the results of the data analysis are shown to be generally consistent with MJ72. Distinctive features of the oscillation as it exists at sea level are suggested. Note that our data from the central-western Pacific antedates (pre-1958) the data studied by MJ72 (post-1957).

An example of the coherence of the zonal wind in the western Pacific is given in Figure 2.16. The largest zonal wind coherence amplitudes in the 20-90 day band occur near the equator in the central-western Pacific around 40 days period. The period of the coherence amplitude peak varies somewhat as might be expected from the variable noise levels at each station and the differing time spans of each station pair. In fact, MJ72 noted that between 1957 and 1962 the average period of the 40-50 day Kelvin wave was 48 days, whereas between 1962 and 1968 it was 33 days. Parker (1973) found that the period range was 28-45 days in his 1960 to 1969 dataset, and Picaut and Verstraete (1976) found the oscillation at 40-50 days in 1969-1974. The power density spectra and coherences presented here suggest a period range of 30-60 days in 1950-1957.

The propagation direction implied by the coherence phases is generally eastward in the 30-60 day band near the equator in the western Pacific, assuming the oscillation is in small wavenumbers. However, eastward propagation is not indicated for all the station pairs, in agreement with

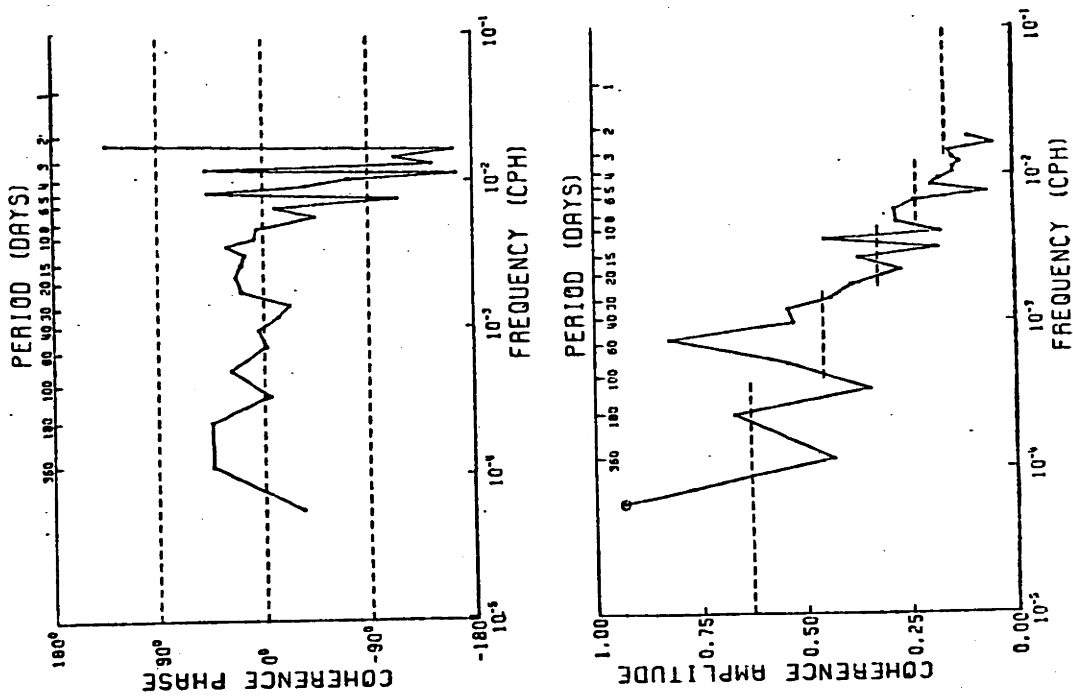


Figure 2.16 - Coherence of east wind between Canton and Betio using 8 years of data. Plotted as in Figure 2.5.

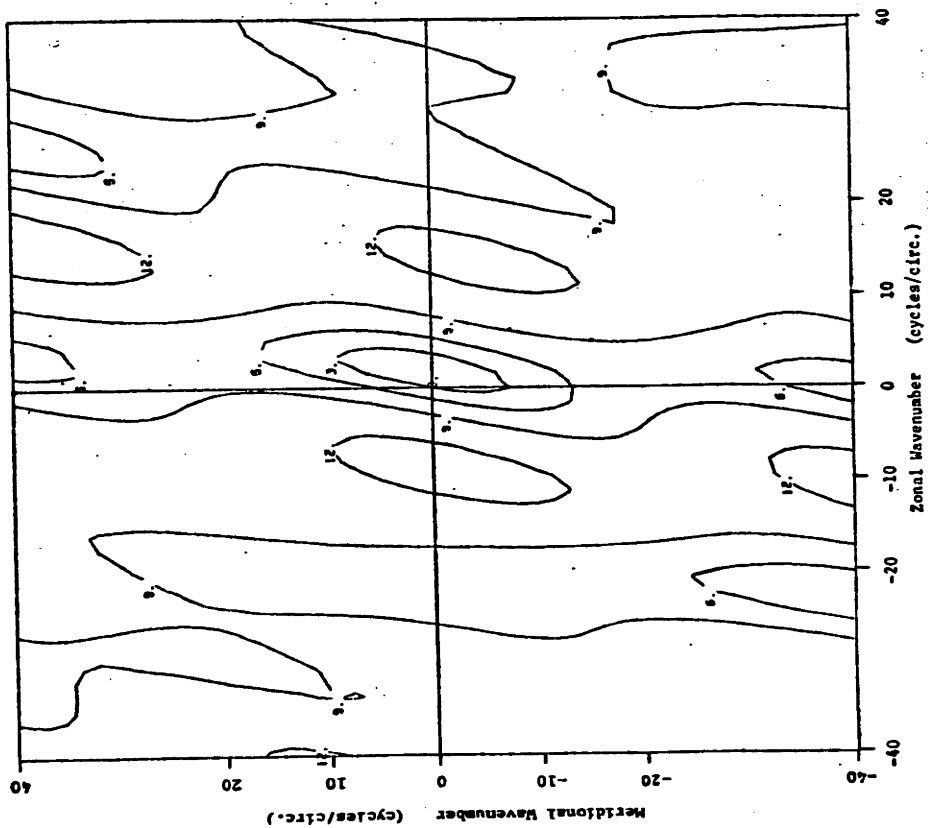


Figure 2.17 - Wavenumber spectrum of east wind in the 40-55 day band, using 3 years of data from Canton, Arorae, Betio and Ocean. Plotted as in Figure 2.12.

MJ72's (see their Figure 4*) discovery of poleward, as well as westward, propagation north of 5°N and west of 170°E in the Pacific. Those central-western Pacific station pairs separated by more than 800 km, which have at least one member within 3° of the equator, yield coherence phases consistent with the hypothesis of eastward and poleward propagation in the 30-60 day band.

An estimate of the wavenumbers of the 40-50 day Kelvin wave was obtained from the maximum-likelihood wavenumber spectrum of zonal wind using 3 years of data from Canton, Ocean, Majuro and Ponape. The peak (Figure 2.17) occurred at zonal wavenumber $s \sim 1.6$ and meridional wavenumber $q \sim 0$, with zonal wavenumber half-power bandwidth of $\Delta s \sim 3.6$. Although the peak accounts for 73% of the power in the 40-55 day band, the degrees of freedom are low so that the peak is significantly different from zero zonal wavenumber not at the 95% level, but only at the 55% level. MJ72 and Parker (1973) stated that the eastward propagation of the 40-50 day Kelvin wave was quite irregular. Parker (1973) establishes the mean zonal wavenumber as $s \sim 1$, but MJ72 estimate $s \sim 1$ east of 150°E and $s \sim 2$ west of 150°E .

The surface air pressure coherence is found to have large amplitude over large distances for the entire 20-90 day band, within 10° of the equator in the Pacific Ocean. For example, Figure 2.18 displays the coherences for the near-equatorial Kwajalein-Canton pair and the sub-tropical (20° - 30°N) Wake-Midway pair. Wake and Midway are closer to each other (~ 1900 km) than Kwajalein and Canton (~ 2600 km). The phases corresponding to the large tropical coherence amplitudes are invariably small and do not indicate any preferred propagation direction. This phenomenon

*MJ72 used sea level air pressure coherences to construct their model of the propagation of the 40-50 day Kelvin wave. The air pressure coherences are discussed shortly.

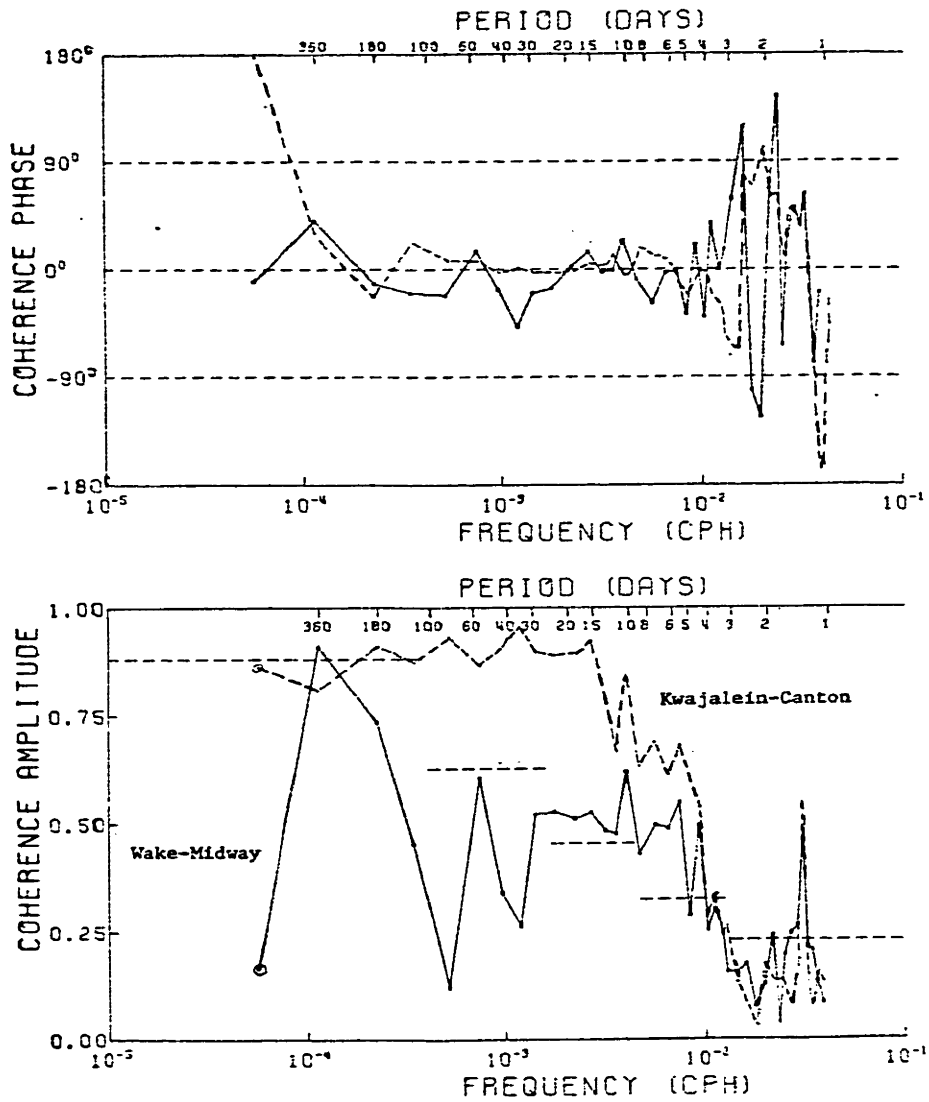


Figure 2.18 - Superimposed coherences of air pressure between Kwajalein and Canton (dashed), and between Wake and Midway, using four years of data for each coherence function. Plotted as in Figure 2.5.

of nearly synchronous pressure fluctuations in the tropical Pacific, first noted by Palmer and Ohmstede (1956), precludes identification of the 40-50 day Kelvin wave.

The coherences between meridional wind and both zonal wind and air pressure suggest that the 40-50 day Kelvin wave has a surface meridional wind component, probably a boundary layer product (see Lindzen and Forbes (1978)). The meridional wind is approximately in-phase (out-of-phase) with both the zonal wind and air pressure north (south) of the equator.

The amplitude of the 40-50 day Kelvin wave has been obtained from the power density spectra of zonal wind from Gan (Figure 2.15) in the Indian Ocean, and from Canton, Arorae, Betio and Ocean (Figure 2.14a) in the Pacific Ocean. The rms zonal wind amplitude is 0.4 - 0.6 m/s, using the observed bandwidth of 3.5×10^{-4} cph (hence $Q \sim 2-3$).

The oscillation has an annual modulation as well as large interannual variability (Madden and Julian (1971, 1972b), Parker (1973)). (MJ72 report finding 40-50 day peaks in the power density of surface pressure from the 1890's for two tropical stations.) The data analyzed here suggest the oscillation is stronger in the northern winter months, but in other years this may not be true (MJ72 and Parker (1973)). Maximum amplitudes of the oscillation can reach 2 mb and 2 m/s at the surface on the equator.

E. Frequency-Wavenumber Spectra of Equatorial Surface Winds and Pressure.

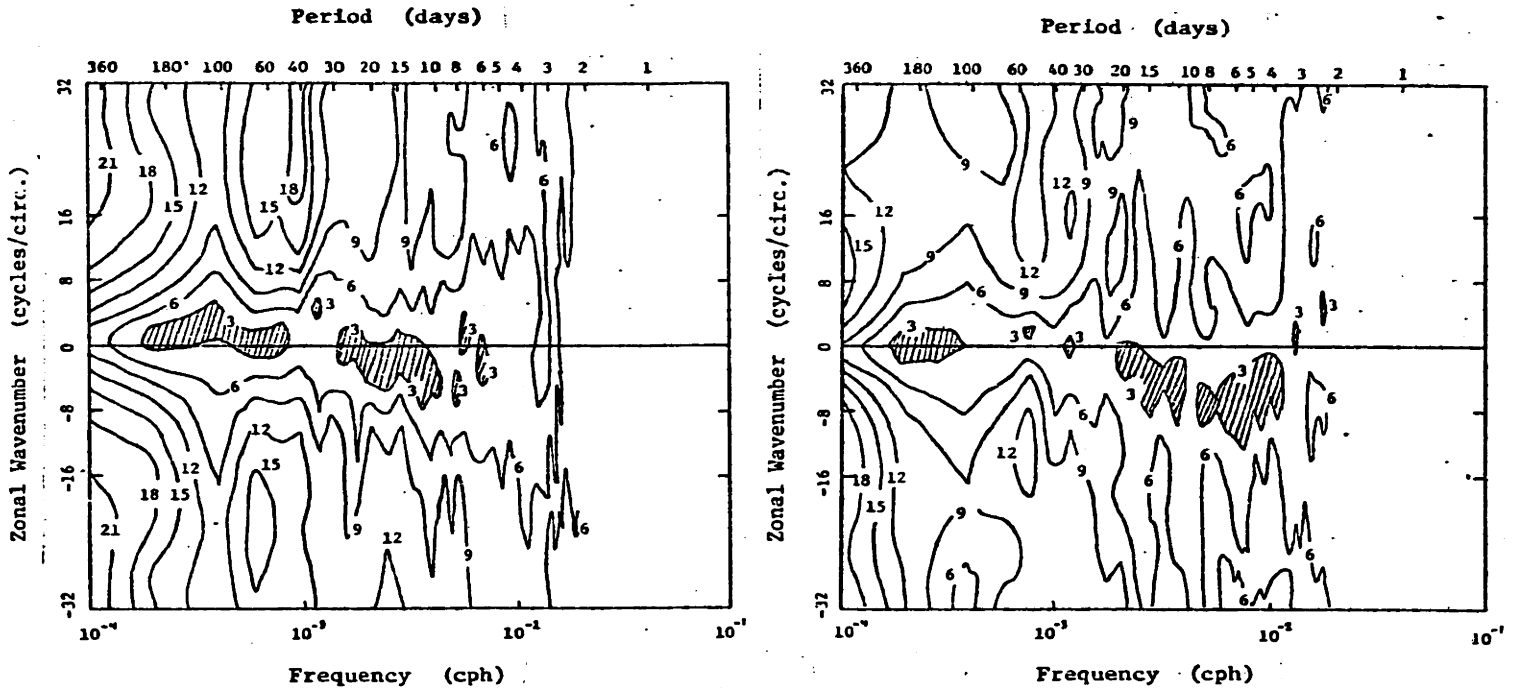
Zonal wavenumber spectra for periods from 2 to 90 days have been computed for surface winds and air pressure in the equatorial, central-western Pacific, but before presenting these spectra a few cautionary remarks are in order. First, earlier in this chapter, wavenumber spectra have been examined for the frequency bands where statistically non-zero wavenumber estimates could be made. Therefore, in the following wave-

number spectra, peaks indicating non-zero wavenumbers are statistically significant, at the 95% level*, only if they occur at frequencies associated with the previously discussed equatorial waves. The spectra nevertheless indicate possible asymmetries in wavenumber space, which need to be corroborated with additional data. Second, the maximum-likelihood estimator is known to produce inaccurate estimates of wide-band (in wavenumber) spectra (Davis and Regier (1977)), so it is not possible to obtain meaningful estimates of the slope of the spectral decay as wavenumber magnitude increases.

Another drawback to the usefulness of the frequency-zonal wavenumber spectra presented in this section is that we only have coarse information on the meridional variation of the spectra. Yet the following wavenumber spectra are important contributions, because virtually nothing is known about the frequency-wavenumber structure of atmospheric fields at the tropical sea surface, aside from a few published power spectra (e.g., Groves and Hannan (1968) and Wunsch and Gill (1976)).

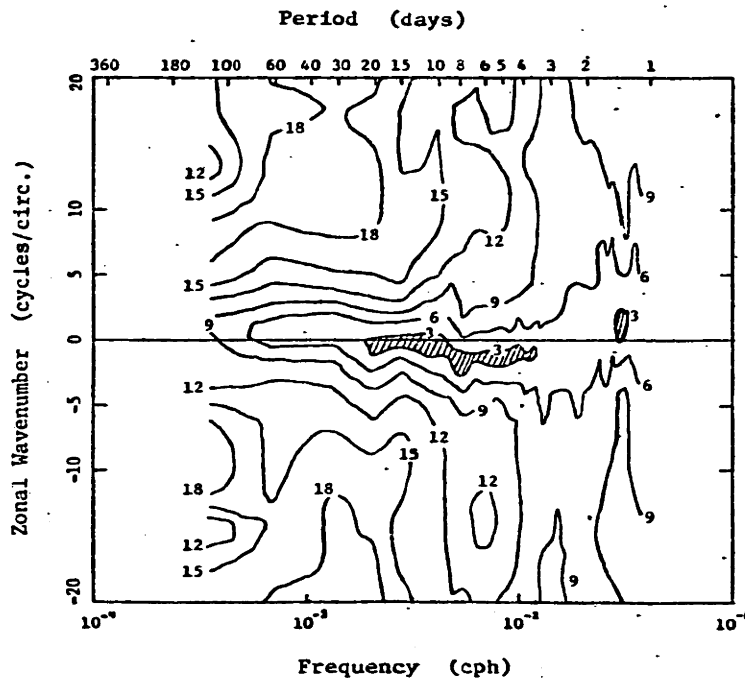
Figure 2.19a presents the zonal wavenumber versus frequency spectrum of surface atmospheric pressure, using 4 years of data from Canton, Johnston, Wake, Guam, Kwajalein and Eniwetok. The zonal wavenumber estimates are estimates at zero meridional wavenumber, rather than estimates obtained from integration over all significant meridional wavenumbers. Such integration is an objectionable procedure, because the nonuniform beam patterns require integration limits that are a function of zonal wavenumber, to avoid aliasing. The actual peak meridional wavenumbers are probably not distinguishable from zero.

*McWilliams (1979, personal communication) notes that the Capon and Goodman (1970) statistics are not accurate for irregularly-spaced arrays, such as those used here. However, a more accurate formalism is not known to the author.



(b) east wind

(c) north wind



(a) air pressure

Figure 2.19 - (a) Zonal wavenumber versus frequency contour plots of air pressure power density. Contours are decreasing power (in negative decibels with the minus sign dropped) relative to the peak power in each frequency band. The peaks are shaded. Abscissa is frequency in cycles/hour. Ordinate is wavenumber s , in cycles/circumference. Stations used include Canton, Johnston, Wake, Guam, Kwajalein and Eniwetok. (b) As in (a) but for zonal wind using Canton, Arorae, Betio and Ocean data. (c) As in (b) but for meridional wind.

The spectrum is displayed using contours of decreasing power (in negative decibels with the minus sign dropped) relative to the peak in each frequency band. The peaks are shaded for easier identification.

Figure 2.19a indicates westward propagation at 5 days in accordance with the observed propagation of the 5-day barotropic oscillation (Section 2.B.2). Westward propagation is suggested for periods as long as 9 days. At periods greater than 9 days, no directional preference is detectable, and at periods less than 3 days (excluding a barotropic oscillation at 1.4 days*) the wavenumber spectrum is inadequately estimated, probably because of increased bandwidths.

The size of the array (i.e., distance between elements) used to compute Figure 2.19a is remarkable, and was made possible by the narrow wavenumber bandwidths of the tropical air pressure field at periods greater than 3 days. Decreasing the array size decreases the low-wavenumber resolution.

The spectrum of zonal wavenumber versus frequency for north wind using 3.6 years of data from Canton, Arorae, Betio and Ocean is displayed in Figure 2.19c. The Rossby-gravity waves at 4-5 days and 8 days (Sections 2.B.1 and 2.C) are evident, with the proper westward propagation. Furthermore, westward propagation occurs for periods of 10-20 days. There is a hint of eastward propagation at 60 days, but elsewhere the spectrum is approximately symmetric and peaked at zero wavenumber, or else indeterminate.

Figure 2.19b displays the wavenumber-frequency spectrum of east wind using the same 3.6 years of data from Canton, Arorae, Betio and Ocean. As in the north wind spectrum, westward propagation is indicated at 8-20 days. Eastward propagation weakly appears at the Kelvin wave periods of 30-60 days. The Kelvin wave propagation is more accurately resolved by a larger array (Section 2.D). Eastward propagation is also suggested at

*See the footnote on page 33.

120-180 days.

The spectra in Figures 2.19b and 2.19c are representative of the central equatorial Pacific surface wind field as far north as 7° . The spectra for stations between 10°N and 20°N are quite different, but will not be discussed here.

As a graphic, but simplistic, illustration of the value of frequency-wavenumber spectra of surface winds, the spectra of Figures 2.19b and 2.19c are superimposed on the dispersion diagram (Figure 1.1) for the first-baroclinic mode, equatorially-trapped waves, in Figure 2.20. The equivalent depth is assumed to be $h_1 \approx .92\text{m}$, so $c_1 \approx 3.0 \text{ m/s}$ and $\sqrt{\epsilon_1} \approx 309$. Only the smoothed 4 db contours of the wavenumber spectra are plotted. Where the dispersion lines coincide with the maximum power of the wind spectra, one might expect those oceanic waves to be excited, and if conditions are right, the ocean may resonate. Note the occurrence of wind power around the zero zonal group velocity points of the low-mode inertia-gravity waves. Evidence of the excitation of the low-mode inertia-gravity waves is found in sea level spectra (Wunsch and Gill (1976) and Chapter 3).

One must remember that higher-baroclinic modes may also be generated, or, depending upon the frequency, zonal wavenumber, and latitudinal distribution of the wind energy, forced waves may be generated which can not establish vertical modes. (See Philander (1978)).

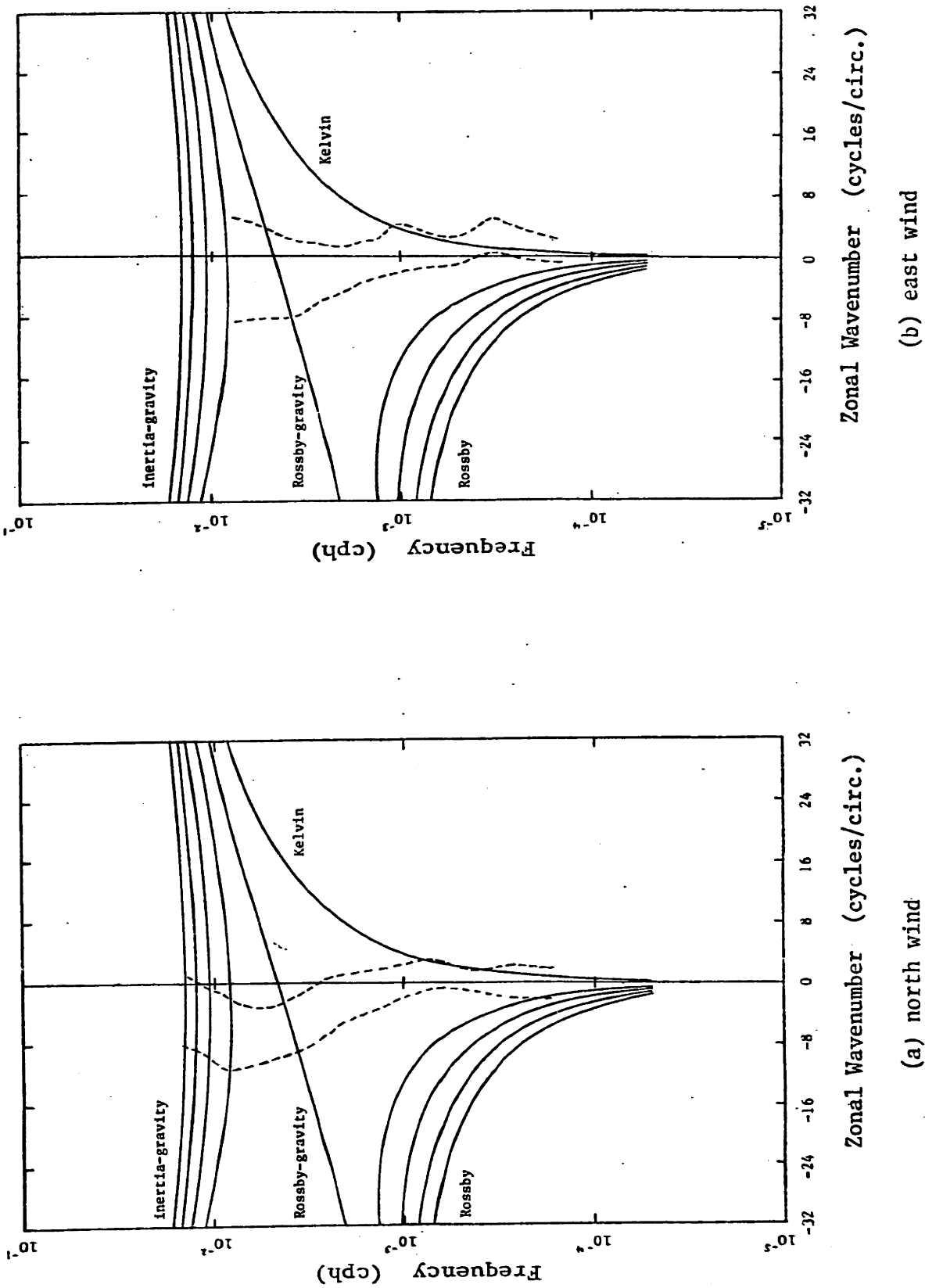


Figure 2.20 - Superposition of heavily smoothed zonal wavenumber versus frequency plots of (a) north wind and (b) east wind, and the dispersion curves of the four gravest theoretical, first-baroclinic mode equatorially-trapped waves ($c_1=3.00$ m/s so $h_1=.9174$). Only the 4 db contours (dashed) of the wavenumber spectra (Figures 2.19b and c) are presented. The abscissa is zonal wavenumber in cycles/circumference and the ordinate is frequency in cycles/hour (log scale).

CHAPTER 3

OCEANIC OSCILLATIONS AT THE TROPICAL SEA SURFACE

A. Introduction

The power density spectrum of twelve years of sea level measurements from Christmas Island (2°N , $157^{\circ}30'\text{W}$) is presented in Figure 3.1. The heart of this dissertation is the investigation of the dynamics of the large-scale oceanic oscillations responsible for the prominent spectral features of the tropical sea level auto-spectra (as in Figure 3.1) and cross-spectra. The motivation of this work was outlined in Chapter 1, and the emphasis is on understanding the dynamics of equatorially-trapped waves in the oceans.

The investigation is pursued here through spectral analyses of unique, long time series of sea level measurements from islands in the Pacific and Indian Oceans, in conjunction with the spectral descriptions of the surface atmospheric fields just obtained. It should be emphasized that atmospheric oscillations at the sea surface need not be prominent features in the auto-spectra to force identifiable oceanic oscillations, but rather need only dominate the cross-spectra.

Any study of sea level oscillations in the tropical oceans at periods greater than one day must acknowledge the presence of comparatively strong long-period tides. The tides at 28, 14 and 9 day periods (Figure 3.1) are located in the frequency band where only Kelvin and mixed Rossby-gravity waves exist for the lowest-baroclinic mode equatorially-trapped waves (refer to Figure 1.1). The problem of the long-period tides as "noise" is important enough to warrant a detailed study in the tropical

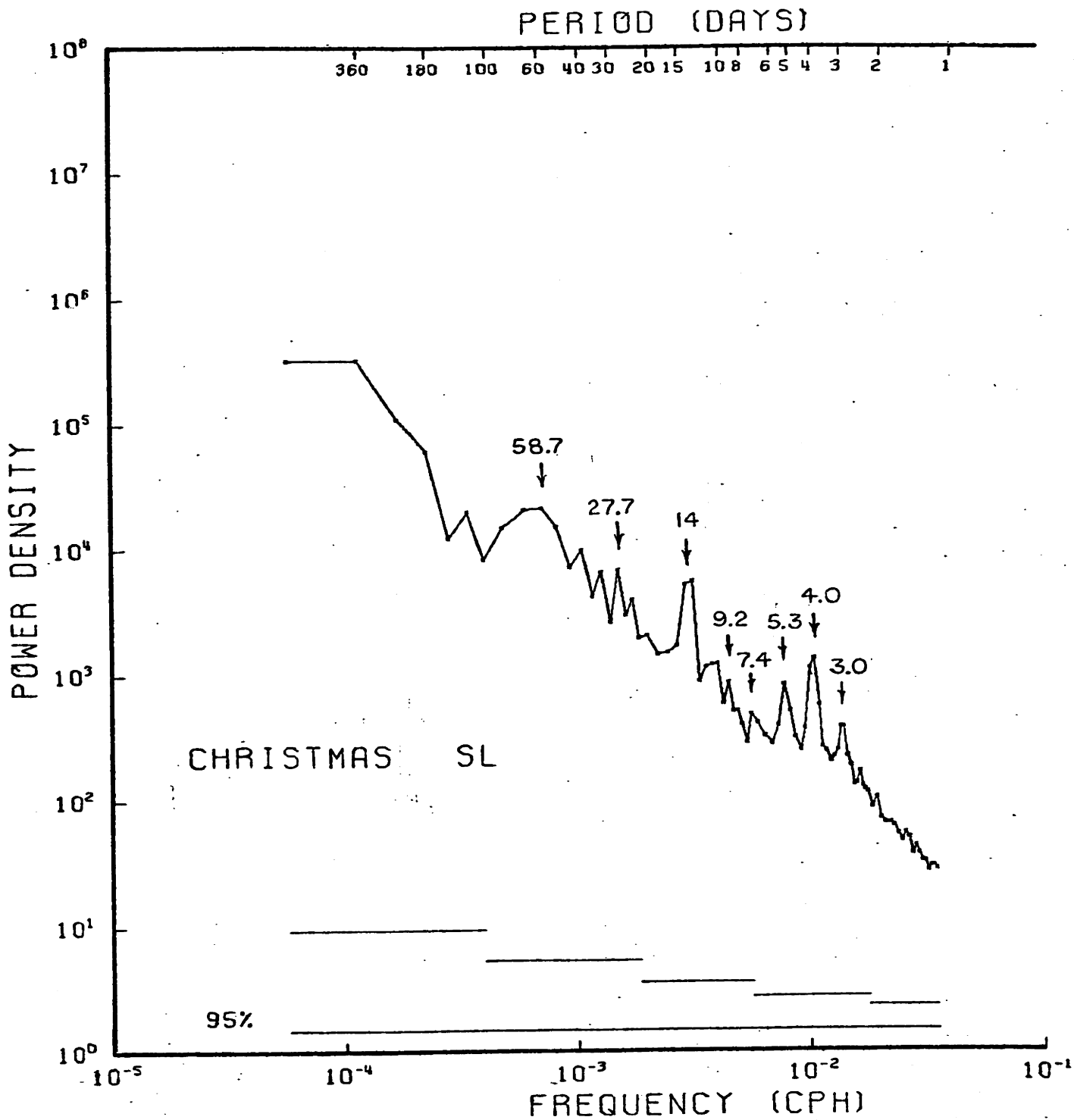


Figure 3.1 - Sea level power density spectrum of 12 years of data from Christmas (2°N, 157°30'W). Ordinate is power density in cm²/cph. Otherwise, plotted as in Figure 2.1. The periods (in days) of the prominent peaks are indicated.

Pacific and Indian Oceans (Section 3.B). The short zonal scales of planetary modes studied by Wunsch (1967) are not observed above the noise.

Among the important observational questions is whether equatorial waves can be detected near the meridional boundaries, and if detected, whether they propagate from the equatorial waveguide into the coastal waveguide, or vice versa, or not at all. Judging from the coherence functions between sea level records, oscillations at 4-6 days are present throughout the Pacific, independent of latitude. Since the presence of "global" oscillations at 4-6 days can contaminate interpretation of inertia-gravity wave propagation along the equatorial waveguide, the nature of the 4-6 day "global" oscillations is examined in Section 3.C. Intriguing evidence of a barotropic, planetary mode at 4-6 days is found. The mode is probably forced by the 5-day barotropic atmospheric oscillation documented in Section 2.B.2.

The evidence for equatorially-trapped inertia-gravity waves in the Pacific and Indian Oceans is reviewed and extended in Section 3.D. The meridional structures of the lowest meridional modes in the Pacific Ocean are clarified. Higher modes are responsible for both discrete peaks in the power density spectra (e.g., at 3 days in Figure 3.1) and the slope of the sea level spectra at 1-2.5 days, for stations near the equator in the Pacific. The spectra of the scattered and short Indian Ocean sea level records suggest an inertia-gravity wave field that is similar to that found in the equatorial mid-Pacific. The longitudinal extent of the lowest meridional modes in the Pacific is traced with the sea level spectra and sea level-weather cross-spectra. Zonal wavenumbers and bandwidths of the strongest inertia-gravity waves are estimated, and the annual and inter-

annual variability of the strongest modes is discussed. Although sea level acts as a low-pass filter on baroclinic modes, the lowest meridional, second-baroclinic mode is detectable in the auto-spectra and cross-spectra. The strong arguments for inertia-gravity wave resonance are summarized.

The study of equatorially-trapped waves continues in Section 3.E with evidence for waves at periods longer than 7 days being presented, including evidence of a 9-10 day mixed Rossby-gravity wave (distinct from the 9-day tide) and 35-80 day Kelvin waves (see Figure 3.1). These oscillations are apparently forced by atmospheric oscillations (studied in Chapter 2) with similar periods. The Kelvin wave is an especially exciting discovery since it apparently exists at the eastern shore of the Pacific and may be directly useful for understanding the equatorial ocean's response to long time-scale changes in the surface wind field.

A.1 Sea Level Dataset. The tide gauge records have been collected from a variety of sources over the past 15 years. Much of the data was obtained under the direction of Carl Wunsch at the Massachusetts Institute of Technology.

The sea level time series range in length from less than one year to over twenty years (Table 3.1) and are scattered, not very uniformly, across the Pacific (Figure 3.2) and Indian (Figure 3.3) Oceans. The temporal overlap is seen (Table 3.1) to be quite irregular, limiting the possible cross-spectra that can be computed. In fact, the sea level records from the Indian Ocean have practically no overlap in time, severely limiting what we can learn about the large-scale fluctuations in that ocean.

All records were sampled hourly and rounded to the nearest 0.1 foot, at worst, with some records rounded to the nearest 0.1 cm. Errors due to this "least count" roundoff and errors due to instrumental frequency

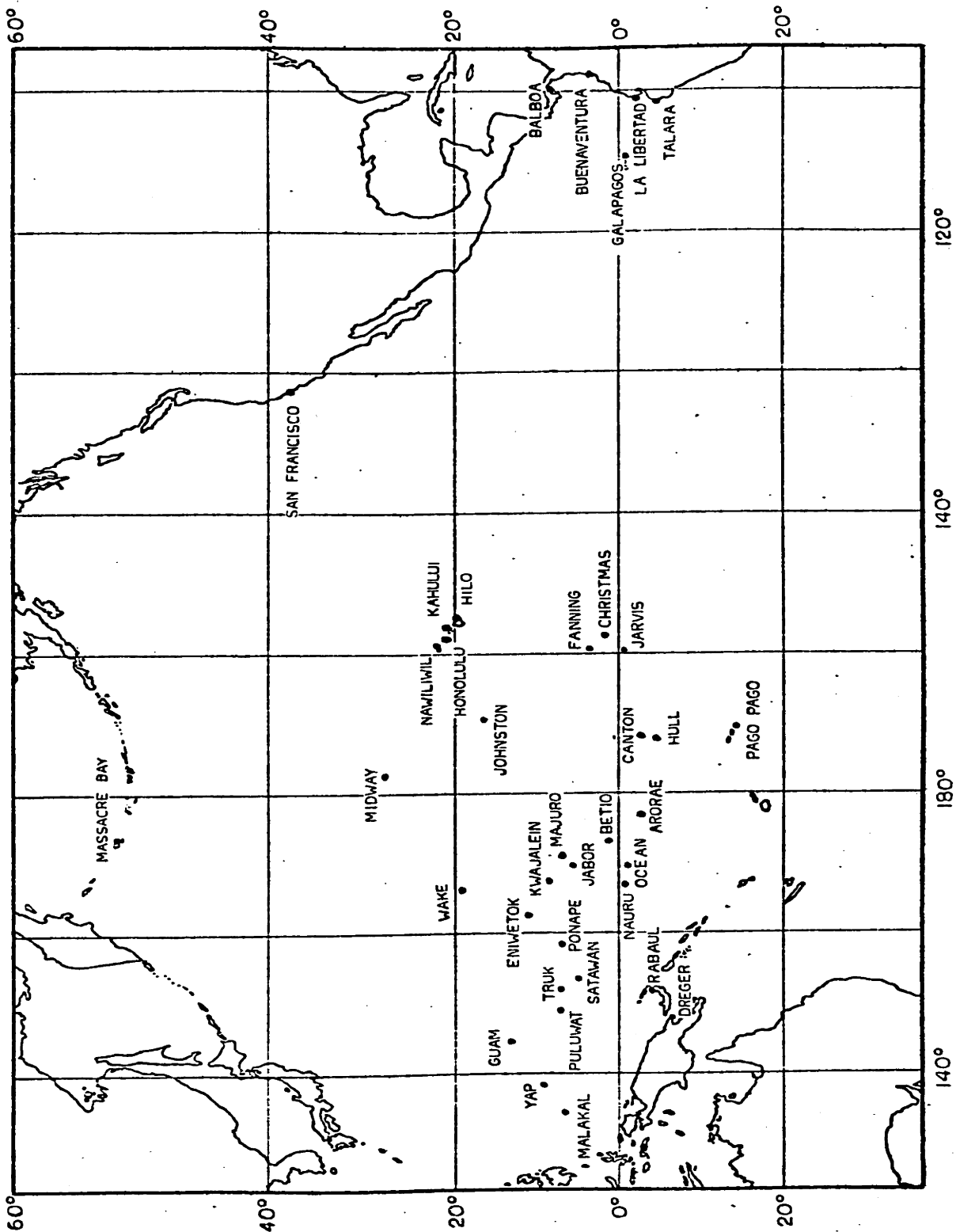


Figure 3.2a

Figure 3.2 - Maps showing locations of the tide gauge stations supplying data for use in this study. (a) Entire Pacific Ocean. (b) Central-western Pacific.

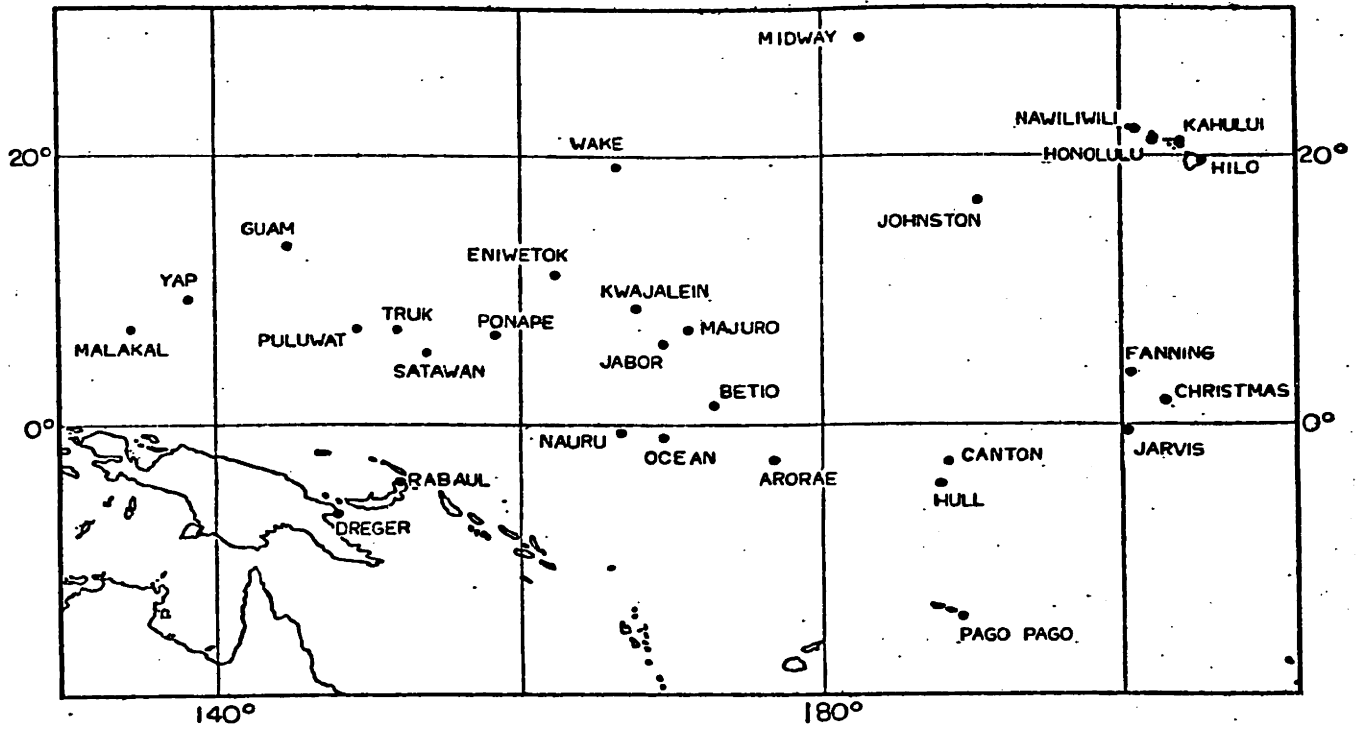


Figure 3.2b

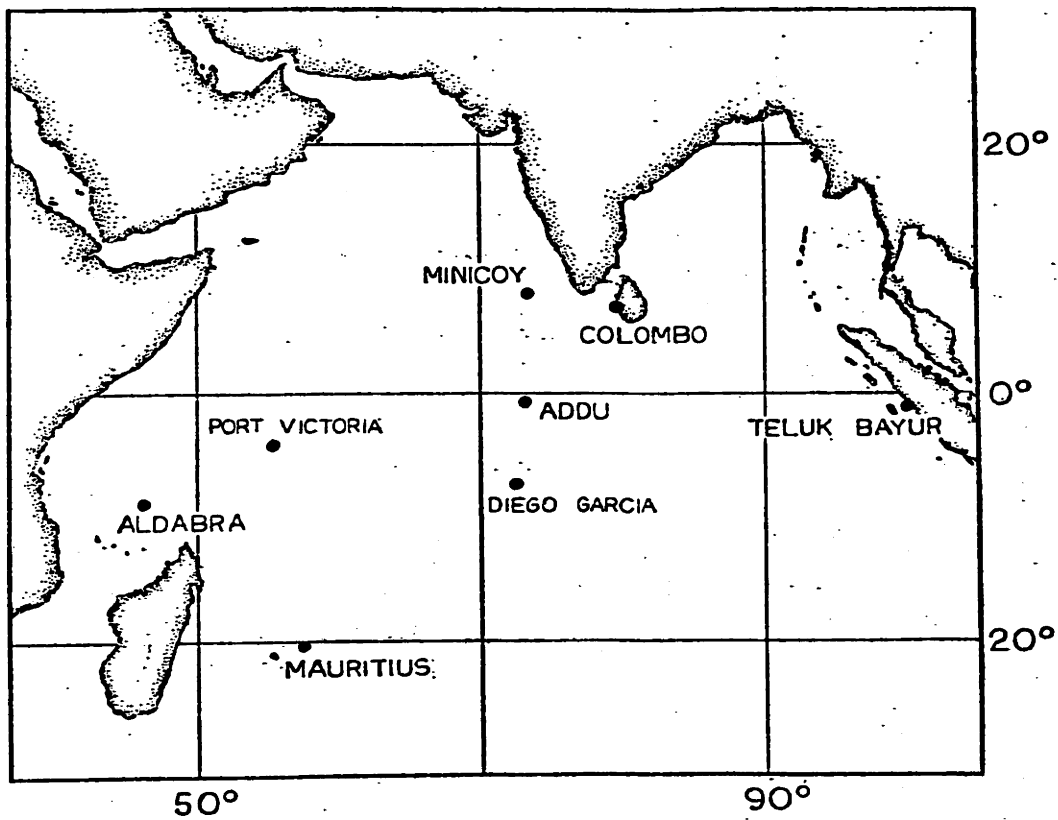


Figure 3.3 - Map showing locations of tide gauge stations in the Indian Ocean.

response characteristics and drift have been discussed by Wunsch (1966, pp. 27-28) for a subset of the data used here. The possible errors are negligible in the period band of interest here, 1-90 days.

Some of the records have been edited with rather sophisticated error detection and replacement schemes (Wunsch (1966, Appendix 1)), but most have simply been subjectively scanned for obviously "bad" points and gaps. Single "bad" points and gaps of 1-2 points were filled by linear interpolation of neighboring values. For larger gaps (at most several days), the tidal signal was predicted by the harmonic method and adjusted for the long-period trends surrounding the gap. Gaps larger than several days were not filled, just flagged.

Further detection of errors occurred during the actual data analysis. For instance, tidal harmonic constants were computed for all sea level records and compared with previous analyses (e.g., Luther and Wunsch, (1975) and the International Hydrographic Bureau published constants). The harmonic constants are sensitive to subtle errors in the timing of the records. Also, gaps and large least count errors have distinctive signatures in the power density spectra when the spectra are computed to frequencies greater than 2 cycles/day. At worst, errors that have escaped detection will degrade the cross-spectra, so we have erred on the side of caution.

The question of whether island sea level measurements are representative of open ocean conditions has been addressed by Wunsch (1972), Luther and Wunsch (1975) and others. For instance, positioning a tide gauge within a lagoon that has restricted communication with the open ocean can produce sea level records that differ substantially from the sea level fluctuations of the surrounding ocean due to increased steric effects in

the lagoon, surf set-up and slow response time of the lagoon water level to changes in the surrounding sea level. In addition, real and important differences in sea level measured on opposite sides of an island can occur due to diffraction of long ocean waves by island arcs (Larsen (1977)). For the period band studied here, only the latter effect may be important in the interpretation of the following analyses.

B. The Long-Period Tides

The long-period tides are intrinsically interesting, aside from the motivations discussed above. The behavior of the ocean in response to the well-known tidal forcing is relevant for understanding the ocean's response to meteorological forcing at the same periods. An elegant example of this point is provided by the data (Miller and Wunsch (1973)) and model (Wunsch (1974)) of the 14-month "Pole tide" in the North Sea, where it appears that the atmospherically-forced sea level continuum around the "Pole tide" is amplified topographically, as the "Pole tide" is.

Since the inception of dynamical tidal theory in 1775 by Laplace, the most pressing question concerning the long-period ocean tides has been whether these tides are equilibrium or not, that is, whether the sea surface fluctuates exactly in phase and with the same amplitude as the imposed gravitational potential. Theoretically, Wunsch (1967) demonstrated (in a mid-latitude basin) that the long-period tidal forcing may excite standing Rossby modes. If friction is strong enough, these free oscillations are damped, leaving only an equilibrium tide in the model. Topography and basin geometry are also expected to produce non-equilibrium fluctuations, as suggested by Kagan et al.'s (1976) global numerical model of the fortnightly tide, although the governing dynamics in their model are not obvious.

The measurement of the long-period tides is so intricately related

to the movement of the surface of the solid earth that until the "self-consistent" calculation of the static tide (that is, the equilibrium tide with oceanic self-attraction and loading accounted for in realistic basins) by Agnew and Farrell (1978), the dynamical portion of the long-period sea level tides could not be accurately determined. The sea level amplitudes associated with the astronomical tides at 28, 14 and 9 days are estimated in this section for the tropical Pacific and Indian Oceans and compared with the self-consistent equilibrium tides. The ocean tides are found to be slightly non-equilibrium with large zonal scale in the Pacific.

Wunsch's (1967) succinct review of the origin of the long-period tidal forcing and of previous theoretical and observational work is a necessary introduction to the rest of this section and has been assumed to be familiar to the reader.

The seven strongest linear, long-period, astronomical tides between 1 and 90 days are listed in Table 3.2. The form of the potentials for these tides is given by

$$V_i = \frac{G}{2} A_i (1 - 3 \sin^2 \theta) \cos(\omega_i t + \alpha_i) \quad , \quad (3.1)$$

where A_i and α_i are listed in Table 3.2, α_i is phase relative to a common start time, and $G \approx 26.8 \times g$ cm, where g is the gravitational acceleration (see Doodson (1921) or Godin (1972)).

Table 3.2: Selected Linear Long-Period Tides

<u>Period</u> (Mean Solar Days)	<u>$\omega_i (10^{-6} s^{-1})$</u>	<u>A_i</u>	<u>Darwin Symbol</u> (if any)	<u>Doodson No.</u>
31.812	2.286	.01578	—	063 655
27.555	2.639	.08254	Mm	065 455
14.765	4.925	.01370	MSf	073 555
13.661	5.323	.15642	Mf	075 555
13.633	5.334	.06481	—	075 565
9.133	7.963	.02995	—	085 455
9.121	7.973	.01241	—	085 465

The equilibrium tide (without considering self-attraction and the solid earth deflections) is then

$$\bar{\eta}_i^{eq} \equiv \frac{V_i}{g} = \frac{G A_i}{2g} (1 - 3 \sin^2 \theta) \cos(\omega_i t + \alpha_i^{eq}) \quad (3.2a)$$

$$\equiv H_i^{eq}(\theta) \cos(\omega_i t + \alpha_i^{eq}) \quad (3.2b)$$

The coefficient of the largest equilibrium tide, Mf, is $\frac{G A_{Mf}}{2g} \approx 2.1 \text{ cm}$.

B.1. Data Analysis. Estimates of the long-period tidal admittances and phases were obtained from fast Fourier transforms of the sea level records listed in the introduction (Table 3.1). The data were not tapered before transforming, and only occasionally was a record long enough to require "low-pass" filtering and decimation (the "low-pass" filter used in this case was a box average of two hourly samples).

The actual measured form of the sea level response to the tidal potential (3.1) includes a multiplicative constant and phase shift not present in (3.1), such that

$$\mathcal{Y}_i^{SL} = \nu_i H_i^{SL}(\theta, \phi) \cos(\omega_i t + \alpha_i^{SL} + \mu_i), \quad (3.3)$$

where H_i^{SL} and α_i^{SL} are the amplitude and phase of the true tide at frequency ω_i , and $\nu_i H_i^{SL}$ and $(\alpha_i^{SL} + \mu_i)$ are the amplitude and phase obtained from the Fourier transform at ω_i . The terms ν_i and μ_i arise from the practical constraint that with short (a few years) record lengths it is impossible to resolve tides, by Fourier analysis, that differ in frequency by only 1 cycle per 18.6 years, such as the two 13.6 day tides in Table 3.2. These neighboring tidal constituents beat against each other (analogous to the spring-neap beat of the semidiurnal tides) producing years with larger 13.6 day tides than others. For example, the 13.6 day tide is nearly twice as strong in 1951 and 1969 as it is in 1960. Practical measurement of the tide is subsequently more difficult in 1960 if the noise level is high. The frequency splitting of the tides that gives rise to the 18.6 year beat is due to the regression of the lunar nodes (see Smart (1971, p.121)), hence the name "lunar nodal factors" for ν_i and μ_i . (See Godin (1972, pp. 165-170) for a discussion of the calculation of the nodal factors.)

A simple measure of the non-equilibrium nature of the tides is obtained from the "driving point admittance". If the equilibrium and observed tides are represented as complex exponentials such that

$$\mathcal{Y}_i^{SL} = \nu_i H_i^{SL}(\theta, \phi) e^{i(\omega_i t + \alpha_i^{SL} + \mu_i)}, \quad (3.4a)$$

and

$$\mathcal{Y}_i^{eq} = \nu_i H_i^{eq}(\theta, \phi) e^{i(\omega_i t + \alpha_i^{eq} + \mu_i)}, \quad (3.4b)$$

then the admittance at ω_i is defined as

$$Y_i(\theta, \phi) \equiv \frac{\mathcal{Y}_i^{SL}}{\mathcal{Y}_i^{eq}} = \frac{H_i^{SL}}{H_i^{eq}} e^{i(\alpha_i^{SL} - \alpha_i^{eq})} \equiv |Y_i| e^{-i\psi_i}. \quad (3.5)$$

For calculation of the admittance, the equilibrium tide is numerically generated from the orbital motions of the earth and the moon, following the treatment by Munk and Cartwright (1966, Appendix A), for the same time period and sampling interval as the observed sea level record. The calculated equilibrium tide is analyzed in the same manner as the sea level record, so the resultant Fourier coefficients are subject to the same nodal factor corrections as for measured sea level. The admittance, then, is clearly independent of the nodal factor corrections. Also, to lowest order, spurious effects of the transformation process cancel.

In addition, the equilibrium tide has been corrected for the effects of ocean self-attraction and yielding of the earth due to the external potential and change in ocean load, with the real distribution of the oceans taken into account (Agnew and Farrell (1978)). The ocean self-attraction and loading factors, etc., are all computed assuming the sea level response to the imposed potential is static (mass is conserved), hence the admittance is a true measure of how much the real ocean tides deviate from the static, equilibrium limit, which would give $|Y_i| = 1$ and $\psi_i = 0$. Numerical values of the static tide computed by Agnew and Farrell were generously provided by Agnew (private communication). Very roughly, the yielding of the earth due to the external potential reduces the equilibrium tide by about 30%, ocean loading and self attraction on a completely water-covered earth increase the equilibrium tide by about 25%, and consideration of the true distribution of the water mass generally reduces the equilibrium tide by 0-15% in a spatially dependent manner (thus the longitude dependence explicit in (3.4b)).

The most critical problem in estimating the amplitudes of the long-period tides is contamination by "noise", or rather, the background

continuum level around the tidal frequencies. The continuum level in power density, which is generally related to atmospheric forcing, is a strong function of frequency, rising with increasing period, and is also a strong function of position, in accordance with geographical changes in the atmospheric forcing and oceanic response. Cartwright (1968) successfully obtained estimates of the long-period tides around Great Britain from the residual sea level remaining after removal of meteorological effects (the tides were buried in the continuum of the raw sea level).

The tides are deterministic signals so the stochastic noise contaminating the Fourier transform estimates can be reduced by increasing the record length (see Wunsch (1967)). But if the record length is too long, twelve years for instance, the logic behind the application of the nodal factor correction breaks down as tides separated in frequency by only 1 cycle per 18.6 years begin to be resolved. Ideally, one would like to analyze a continuous 18.6 year record and completely resolve the tides, bypassing the inelegant nodal factor correction, as well as drastically reducing the noise content of the estimates. In practice, such long records are rare, especially in the Pacific. Four to eight year record lengths were found to be adequate for reducing the noise level, at least for the Mf tide, while not obviating the usefulness of the nodal factor correction. Assuming the admittance is a slowly varying function of frequency, such that tides separated by 1 cycle/18.6 years have the same admittance (a good assumption; see Munk and Cartwright (1966)), estimates of the admittance are not hindered by consideration of the nodal modulation, (3.5), hence longer records are always better.

Nearly as important as noise in estimating H_i^{SL} and the admittance is the subject of alignment. If the frequency of a tidal line falls between

the harmonics of the Fourier transform its energy is divided among them, reducing the estimated amplitude of the tide at the harmonic with frequency nearest the tidal component. Since the equilibrium tide is analyzed in a manner identical to the sea level, to lowest order the effect of the transform misalignment is cancelled out in the computation of the admittance, with one important exception. If the tidal line is already weak, the misalignment increases the effect of noise and the accuracy of the resultant admittance estimate is substantially reduced. Alignment error, unlike noise error, is not a function of record length. The analyses completed here have always aligned the tide under consideration so that the expected error from misalignment is less than 2%. Occasionally, this required different Fourier transformations for estimating the different tidal lines. For those tide pairs separated by only 1 cycle/18.6 years (Table 3.2), the larger component was aligned, although an argument can be made for locating the Fourier harmonic between the two tides.

Error bars are essential to the interpretation of the estimates of tidal amplitude, phase and admittance. Assuming the noise has approximately a normal probability distribution and has constant variance, σ_N^2 , in a small frequency band about the tidal line under consideration, then the probability distributions for $\nu_i^{SL} H_i$, $|Y_i|$ and ψ_i are easily determined following the analysis of Munk and Cartwright (1966, Appendix B). In general, these three quantities are normally distributed only in the limit of very large signal-to-noise ratio. This error estimation procedure suffers from the assumption that σ_N is known exactly, whereas it is actually estimated here from the Fourier transform coefficients surrounding each tidal line. For this reason, we have opted to calculate the 95% confidence limits for the tidal estimates, rather than the smaller one-standard-deviation confidence

limits employed by Wunsch (1967) (note that Wunsch estimated the error bars using a procedure that takes into account the uncertainty of σ_N , see Wunsch (1966, p. 49)).

B.2. Observed Fortnightly (Mf) Tide. Estimates of the amplitude, H_i^{SL} , admittance amplitude, $|Y_i|$, and admittance phase, ψ_i , for the Mf tide are listed in Table 3.3 for stations in the Pacific and Indian Oceans. Latitude and longitude for each station are listed as are the total number of years of hourly sea level data used to obtain the estimates. Frequently, more than one record of sea level, from separate time periods, was available for a particular station, so the vector-averaged estimates of tidal amplitude and admittance from each piece are presented in Table 3.3.

The amplitude H_i^{SL} , and consequently Y_i , have been corrected for a small bias due to noise (see Wunsch (1967)). A positive admittance phase, ψ_i , indicates that sea level lags behind the equilibrium tide. Note that ψ_i is equivalent to the classical Greenwich epoch, G , equatorward of the node in the potential (3.1) ($+35^\circ 16'$ latitude) and is $G + 180^\circ$ poleward of the node.

The 95% error bars are indicated in Table 3.3, but note that the estimates are not centered within the confidence interval, as implied by the form of presentation. If no error bars are indicated, the estimate has 95% error bars greater than $\pm 100\%$ of amplitude and $\pm 90^\circ$ of phase. The confidence interval decreases in magnitude as the signal-to-noise ratio (SNR) increases, where $SNR = \nu_i H_i^{SL} / \sigma_N$. The mean signal-to-noise ratio is indicated in the table. When $SNR \lesssim 1.5$ the 95% error bars on $\nu_i H_i^{SL}$ are larger than $\pm 100\%$. This fact, combined with observations of the amplitudes of the immediate neighbors (within 3 harmonics) of the tidal line in the Fourier transform, has led us to create a grading system to indicate subjectively the reliability of each estimate:

TABLE 3.3 Mf Tide - Pacific Ocean

STATION	LATITUDE (In Degrees & Minutes)	LONGITUDE	YEARS of Data	AMPLITUDE	MEAN	ADMITTANCE*	ADMITTANCE*	REMARKS & "Grades"
				H _{SL} (cm)	SNR ⁺	Amplitude γ	Phase ψ (deg)	
Balboa	8 57 N	79 34 W	8.0	1.24 ± .20	4.0	.91 ± .13	20 ± 7	A
Buenaventura	3 54 N	77 5 W	4.0	2.10 ± 1.21	3.8	1.38 ± .53	17 ± 23	A
La Libertad	2 12 S	80 55 W	4.0	.70 ± .68	2.0	.45 ± .30	44 ± 46	C; misaligned
Talara	4 35 S	81 17 W	4.0	1.22 ± .29	4.0	.83 ± .13	-4 ± 9	A
Galapagos	0 54 S	89 34 W	6.7	1.27 ± .20	5.7	.79 ± .10	19 ± 7	A
Christmas Is.	2 00 N	157 30 W	11.9	1.32 ± .14	9.3	.80 ± .05	9 ± 3	A **
Fanning Is.	3 54 N	159 24 W	1.9	1.52 ± .60	2.5	.86 ± .25	25 ± 17	A
Canton Is.	2 49 S	171 40 W	17.0	1.31 ± .07	7.5	.80 ± .02	18 ± 2	A **
Hull Is.	4 30 S	172 07 W	0.8	1.22 ± 1.00	2.3	.74 ± .39	17 ± 34	A
Arorae Is.	2 37 S	176 50 E	1.4	1.74 ± .63	3.3	1.06 ± .23	10 ± 12	A **
Betio Is.	1 22 N	172 56 E	1.9	1.02 ± .29	3.5	.60 ± .12	12 ± 11	A
Ocean Is.	0 53 S	169 35 E	1.1	1.55 ± 1.27	2.5	.91 ± .46	17 ± 31	A
Nauru Is.	0 32 S	166 55 E	0.8	1.76 ± 1.00	3.4	1.05 ± .37	9 ± 20	A
Rabaul	4 12 S	152 11 E	2.0	1.20 ± .51	4.3	.74 ± .20	-18 ± 15	A **
Dreger Hbr.	6 39 S	147 52 E	1.1	1.38 ± .25	5.6	.93 ± .11	21 ± 7	A
Majuro At.	7 10 N	171 05 E	2.0	1.19 ± .10	11.7	.78 ± .04	10 ± 3	A
Kwajalein	8 44 N	167 44 E	8.0	1.06 ± .18	6.1	.69 ± .08	15 ± 6	A **
Eniwetok	11 21 N	162 21 E	6.0	1.11 ± .17	5.6	.80 ± .10	9 ± 7	A
Ponape Is.	7 00 N	158 15 E	1.5	1.14 ± .14	8.1	.75 ± .06	8 ± 4	A
Satawan	5 16 N	153 39 E	0.5	1.37 ± .27	5.2	.87 ± .10	22 ± 7	A
Truk	7 27 N	151 52 E	4.6	1.10 ± .14	6.1	.72 ± .07	7 ± 5	A **
Puluwat Is.	7 22 N	149 13 E	0.5	1.05 ± .34	3.3	.69 ± .14	9 ± 11	A
Yap Is.	9 30 N	138 10 E	1.5	1.01 ± .23	4.1	.72 ± .13	9 ± 10	A
Malakal Hbr.	7 19 N	134 27 E	0.8	.98 ± .43	3.2	.67 ± .21	3 ± 18	A
Guam	13 27 N	144 39 E	4.0	1.00 ± .42	4.1	.74 ± .24	-6 ± 18	A
Wake Is.	19 17 N	166 39 E	4.0	.59 ± .38	2.7	.57 ± .35	31 ± 42	B
Johnston Is.	16 45 N	169 32 W	5.0	.90 ± .18	3.6	.76 ± .15	27 ± 11	A
Pago Pago Hbr.	14 17 S	170 40 W	2.0	.91 ± .13	7.2	.71 ± .08	0 ± 6	A
Hilo	19 42 N	155 04 W	7.9	.57 ± .06	3.5	.55 ± .06	40 ± 5	A
Kahului	20 56 N	156 29 W	4.0	.58 ± .14	4.2	.60 ± .15	50 ± 14	A
Honolulu	21 19 N	157 52 W	27.0	.61 ± .04	5.0	.61 ± .04	39 ± 4	A
Nawiliwili	21 57 N	159 21 W	2.0	.57 ± .38	2.2	.67 ± .54	18 ± 59	B
Midway Is.	28 12 N	177 22 W	5.0	.37	1.3	.75	44	C
San Francisco	37 48 N	122 28 W	12.0	1.22 ± .31	3.1	4.35 ± 4.30	-38 ± 25	A
Massacre Bay	52 50 N	173 12 E	8.5	1.83 ± .70	3.7	1.12 ± .26	17 ± 34	A

*Signal-to-Noise Ratio (see text).

*Relative to the "self-consistent" equilibrium tide (see text).

**The weighted vector-average of these stations gives $|\gamma| = .77 \pm .01$ and $\psi = 12^\circ \pm 1^\circ$ (to compare with Mm tide).

TABLE 3.3 Mf Tide - Indian Ocean

STATION	LATITUDE (In Degrees & Minutes)	LONGITUDE	YEARS of Data	AMPLITUDE	MEAN	ADMITTANCE*	ADMITTANCE*	REMARKS & "Grades"
				H _{SL} (cm)	SNR ⁺	Amplitude γ	Phase ψ (deg)	
Minicoy	8 17 N	73 03 E	4.0	1.45 ± .15	9.6	1.01 ± .07	8 ± 4	A
Diego Garcia	7 14 S	72 26 E	2.0	1.80 ± 1.06	3.2	1.15 ± .44	0 ± 23	A
Teluk Bayur	1 00 S	100 20 E	0.6	.25	1.1	.17	-25	C
Colombo	6 57 N	79 51 E	0.7	1.08	1.4	.65	13	C
Port Victoria	4 37 S	55 27 E	1.0	1.80 ± .83	3.0	1.21 ± .39	8 ± 18	A
Aldabra	9 18 S	46 24 E	0.4	1.75 ± 1.55	2.2	1.28 ± .86	-20 ± 45	B
Mauritius	20 09 S	57 29 E	3.0	.78 ± .29	2.3	.86 ± .46	16 ± 34	A

*Signal-to-Noise Ratio (see text).

*Relative to the "self-consistent" equilibrium tide (see text).

- A - Strong Signal - $\text{SNR} \geq 2$ and no immediate neighbor with amplitude $\geq \sqrt{H_i^{\text{SL}}}$;
- B - Clear Signal - $\text{SNR} > 1.5$ and no immediate neighbor with amplitude $> \sqrt{H_i^{\text{SL}}}$ and only one immediate neighbor with amplitude $\approx \sqrt{H_i^{\text{SL}}}$;
- C - Possible Signal - $1.0 \leq \text{SNR} \leq 1.5$, or no more than two immediate neighbors have amplitudes $\geq \sqrt{H_i^{\text{SL}}}$, or the tidal line appears to be misaligned;
- D - No Signal - $\text{SNR} < 1.0$ or more than two immediate neighbors have amplitudes $\geq \sqrt{H_i^{\text{SL}}}$.

These "grades" are indicated in Table 3.3. In calculating the vector-averaged estimates from several pieces of data, only "A" and "B" estimates were used.

It is well-known that hydrodynamical nonlinearities may produce large tidal fluctuations at the sum and difference frequencies of two or more of the strong diurnal and semidiurnal tides. Since several of the difference frequencies exactly equal the frequencies of the long-period tides studied here, it is necessary to investigate the possibility that the long-period tides are actually due to nonlinear tides. The strongest nonlinear long-period tide is theoretically the tide due to the interaction of the strongest daily tides, usually the semidiurnal M_2 (12.42 hours period) and S_2 (12 hours period) which have a difference frequency exactly equal to the weak linear long-period tide with Doodson Number 073 555 (MSf in Table 3.2). Each linear tide in Table 3.2 corresponds to the difference frequency of at least one pair of daily tides that are weaker than M_2 and S_2 , so the argument is that if the nonlinear MSf tide is small then the rest of the nonlinear long-period tides must be small. The MSf tide has been sought at

all the islands listed in Table 3.3. Of the non-continental stations, only at Christmas Island, Canton Island and Pago Pago Harbor was a tide measureable, but even there the tides were so small that nonlinear contamination of Mf and the other strong, linear, long-period tides seems unlikely. Of the coastal stations, two, Balboa and Buenaventura, have strong MSf tides, greater than 1.2 cm. (The Gulf of Panama, where these stations are located, has unusually large semidiurnal tides.) Table 3.3 shows that Buenaventura has an enhanced Mf admittance but not Balboa. In addition, coherence calculations between Balboa and non-coastal stations invariably have a peak at Mf, but this is not true for Buenaventura. The conclusion is that the Mf measured at Buenaventura is largely due to the nonlinear tide at that frequency, but that at Balboa, although MSf is large, Mf appears to be primarily linear (compare Balboa and Galapagos in Table 3.3).

The admittances (Table 3.3) are compared with previous measurements by Wunsch (1967) and Cartwright (1968) in Table 3.4. All admittance amplitudes are relative to the self-consistent equilibrium tide of Agnew and Farrell (1978). The admittances are equal*, within the error bars (recall that the error bars are computed differently by Wunsch than here), except for discrepancies in phase at Canton and Eniwetok and the absence of a tide at Balboa in Wunsch's (1967) measurements. With regard to the latter, and in light of the possible nonlinear contamination discussed above, the Balboa Mf tide in Table 3.3 should be viewed with caution.

A cursory examination of Table 3.3 reveals a statistically significant non-equilibrium Mf tide in the tropical Pacific Ocean that is dependent upon latitude (as noticed by Wunsch (1966)) and perhaps weakly dependent upon longitude. To isolate the dependences of the Mf tide on latitude and longitude, admittances from stations equatorward of 10° are plotted versus

*Note that Wunsch's data is generally a subset of that used here.

TABLE 3.4 Comparison of Mf Admittances

STATION	YEARS of Data	ADMITTANCE*	ADMITTANCE*	SOURCE	REMARKS
		Amplitude $ Y $	Phase ψ (deg)		
Balboa	8.0	.91 ± .13	20 ± 7	Table 3.3 Wunsch (1967)	No Visible Tide
	7.6	---	---		
Christmas Is.	11.9	.80 ± .05	9 ± 3	Table 3.3 Wunsch (1967)	
	2.8	.84 ± .10	18 ± 10		
Canton Is.	17.0	.80 ± .02	18 ± 2	Table 3.3 Wunsch (1967)	
	3.8	.76 ± .11	47 ± 12		
Hull Is.	0.8	.74 ± .39	17 ± 34	Table 3.3 Wunsch (1967)	
	0.7	.58 ± .27	28 ± 34		
Arorae Is.	1.4	1.06 ± .23	10 ± 12	Table 3.3 Wunsch (1967)	
	0.7	1.20 ± .28	-1 ± 18		
Ocean Is.	1.1	.91 ± .46	17 ± 31	Table 3.3 Wunsch (1967)	
	0.9	1.16 ± .32	18 ± 21		
Kwajalein	8.0	.69 ± .08	15 ± 6	Table 3.3 Wunsch (1967)	
	2.3	.72 ± .10	6 ± 11		
Eniwetok	6.0	.80 ± .10	9 ± 7	Table 3.3 Wunsch (1967)	
	3.8	.66 ± .08	34 ± 10		
Guam	4.0	.74 ± .24	-6 ± 18	Table 3.3 Wunsch (1967)	
	3.8	.65 ± .11	-6 ± 14		
Wake Is.	4.0	.57 ± .35	31 ± 42	Table 3.3 Wunsch (1967)	
	3.8	.54 ± .11	31 ± 14		
Johnston Is.	5.0	.76 ± .15	27 ± 11	Table 3.3 Wunsch (1967)	
	3.8	.62 ± .45	25 ± 46		
Hilo	7.9	.55 ± .06	40 ± 5	Table 3.3 Wunsch (1967)	
	3.8	.64 ± .10	52 ± 13		
Kahului	4.0	.60 ± .15	50 ± 14	Table 3.3 Wunsch (1967)	
	3.8	.59 ± .09	49 ± 13		
Honolulu	27.0	.61 ± .04	39 ± 4	Table 3.3 Wunsch (1967) Munk and Cartwright (1966)	
	3.8	.59 ± .16	51 ± 19		
	20.0	.66 ± .09	38 ± 6		
San Francisco	12.0	4.35 ± 4.30	-38 ± 25	Table 3.3 Wunsch (1967)	
	7.6	2.00 ± .70	-19 ± 26		

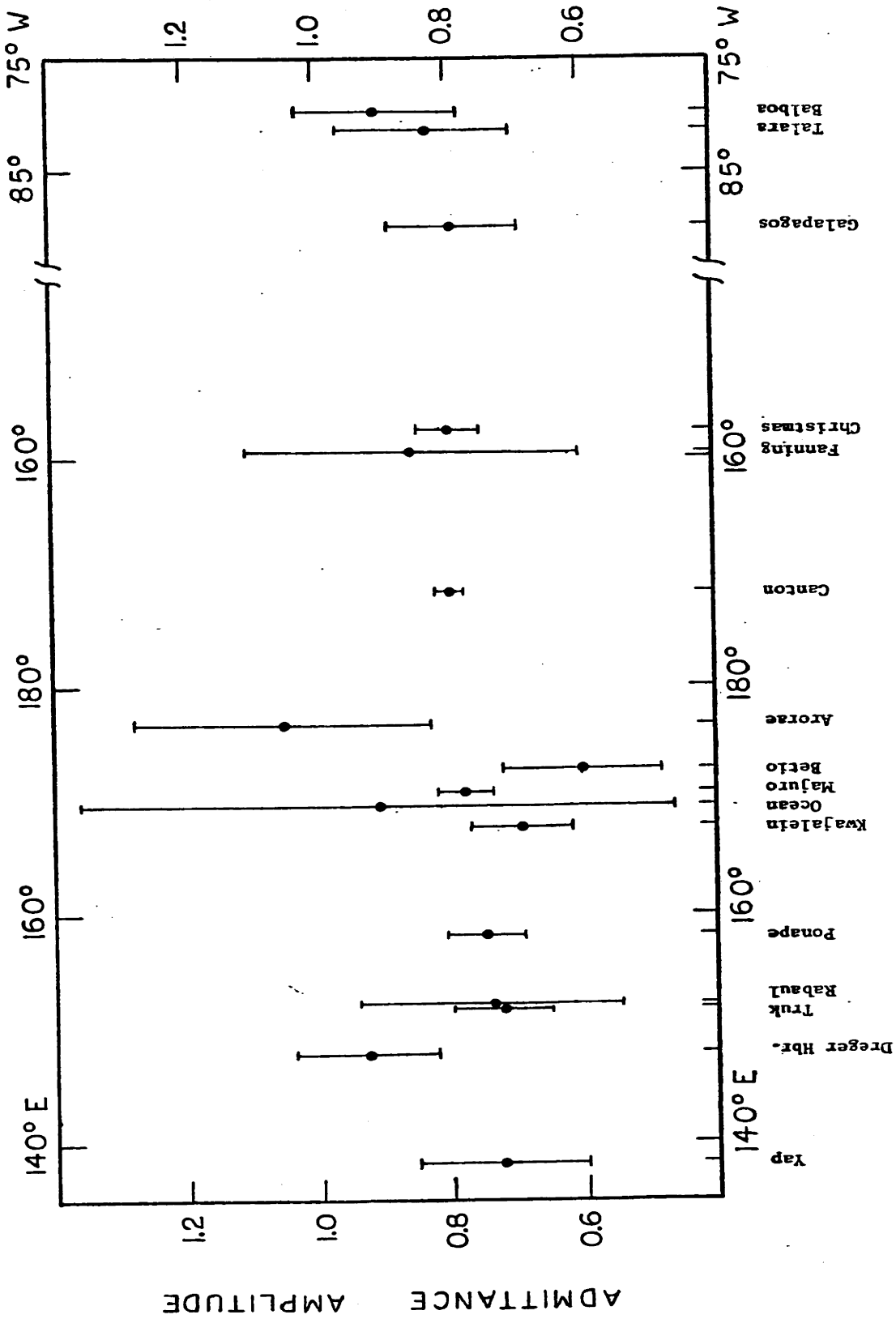
*Relative to the "self-consistent" equilibrium tide (see text).

longitude in Figure 3.4 , and admittances from stations between 150°W and 160°E are plotted versus latitude in Figure 3.5. Only admittances calculated from more than one year of data are plotted. The nonlinear Buena-ventura, the anomalous La Libertad, and the statistically uncertain Midway admittances are also omitted.

The only indication of significant variation in admittance amplitude over short distances comes from the stations with the shortest data lengths and largest error bars, such as Arorae, Betio and Ocean. As a graphic demonstration of the variation in the admittance due to random fluctuations of the background noise (a common problem with short record lengths), successive year-long segments of data from Canton have been analyzed for the Mf tide. The results are listed in Table 3.5.

Large admittances at Arorae and Ocean (from a subset of the data used here) helped motivate Wunsch (1967) to model the apparent small-scale (O(1000 km)) variations in the admittance in terms of standing Rossby waves in a mid-latitude basin. Considering the large error bars, it is impossible to conclude from the data presented here that small scale variations of the admittance amplitude, or phase, exist. On the other hand, Wunsch's model predicts the strongest non-equilibrium variations to be in the immediate neighborhood of the nodes of the forcing ($+35^{\circ}16'$ of latitude for the potential (3.1)), so the tropical data analyzed here are insufficient for testing the theory. Conversely, the theory cannot explain the ocean-wide non-equilibrium behavior of the Mf tide shown in Figures 3.4 and 3.5.

There is a slight suggestion (not significant at the 95% level) that the admittance amplitude and phase decrease slowly westward across the Pacific. The zonal uniformity, mirroring the zonal independence of the



LONGITUDE

Figure 3.4 - Admittance amplitude (a), and phase (b), of the fortnightly (Mf) tide plotted vs. longitude for all stations in the Pacific within 10° degrees of the equator and with more than one year of data. Exceptions are that Buenaventura and La Libertad are not plotted (see text). 95% error bars are indicated.

Figure 3.4a

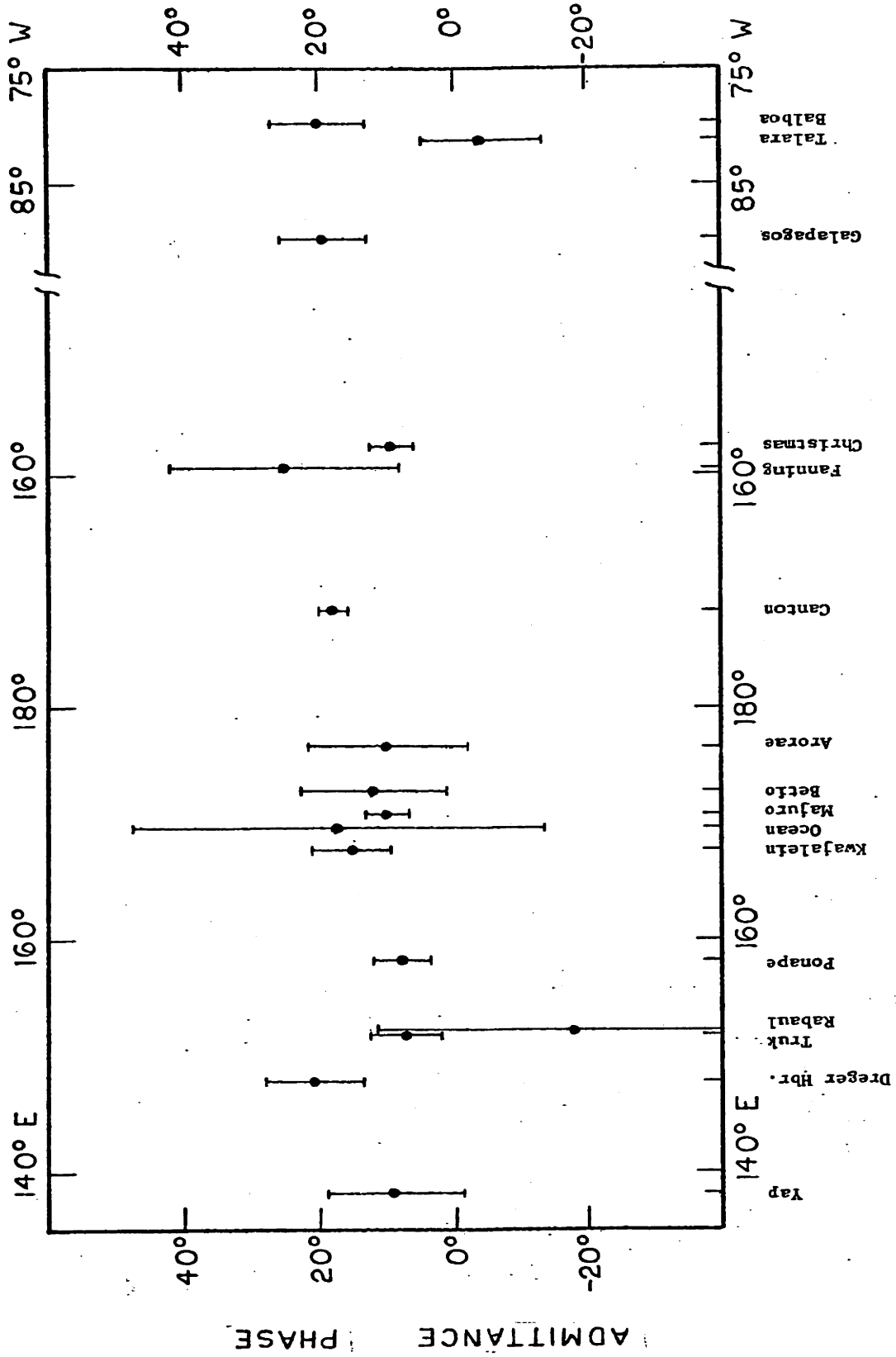


Figure 3.4b

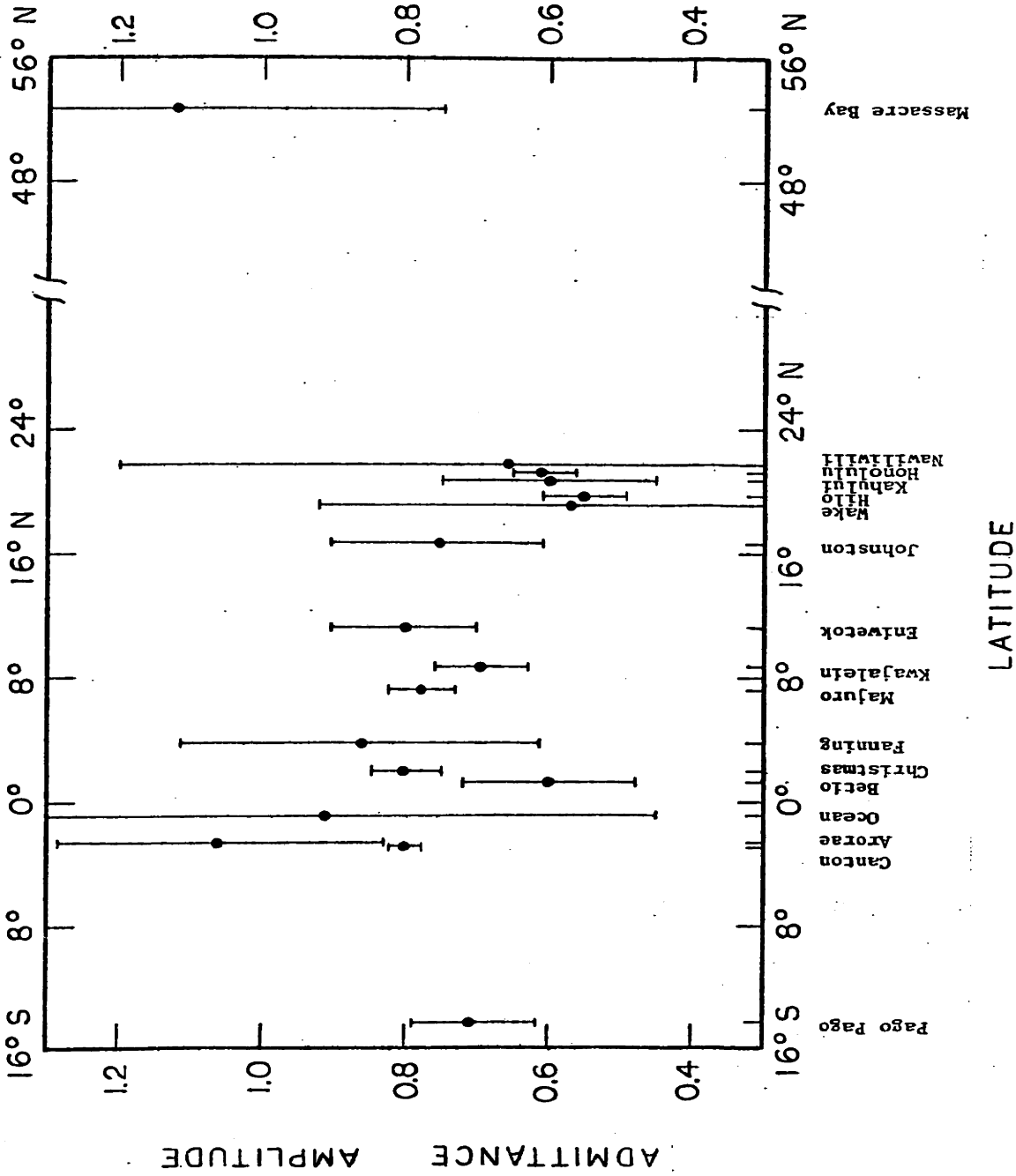


Figure 3.5a

Figure 3.5 - Admittance amplitude (a), and phase (b), of the fortnightly (Mf) tide plotted vs. latitude for all stations between 160° E and 150° W having more than one year of data, with the exception that Midway is omitted. 95% error bars are indicated.

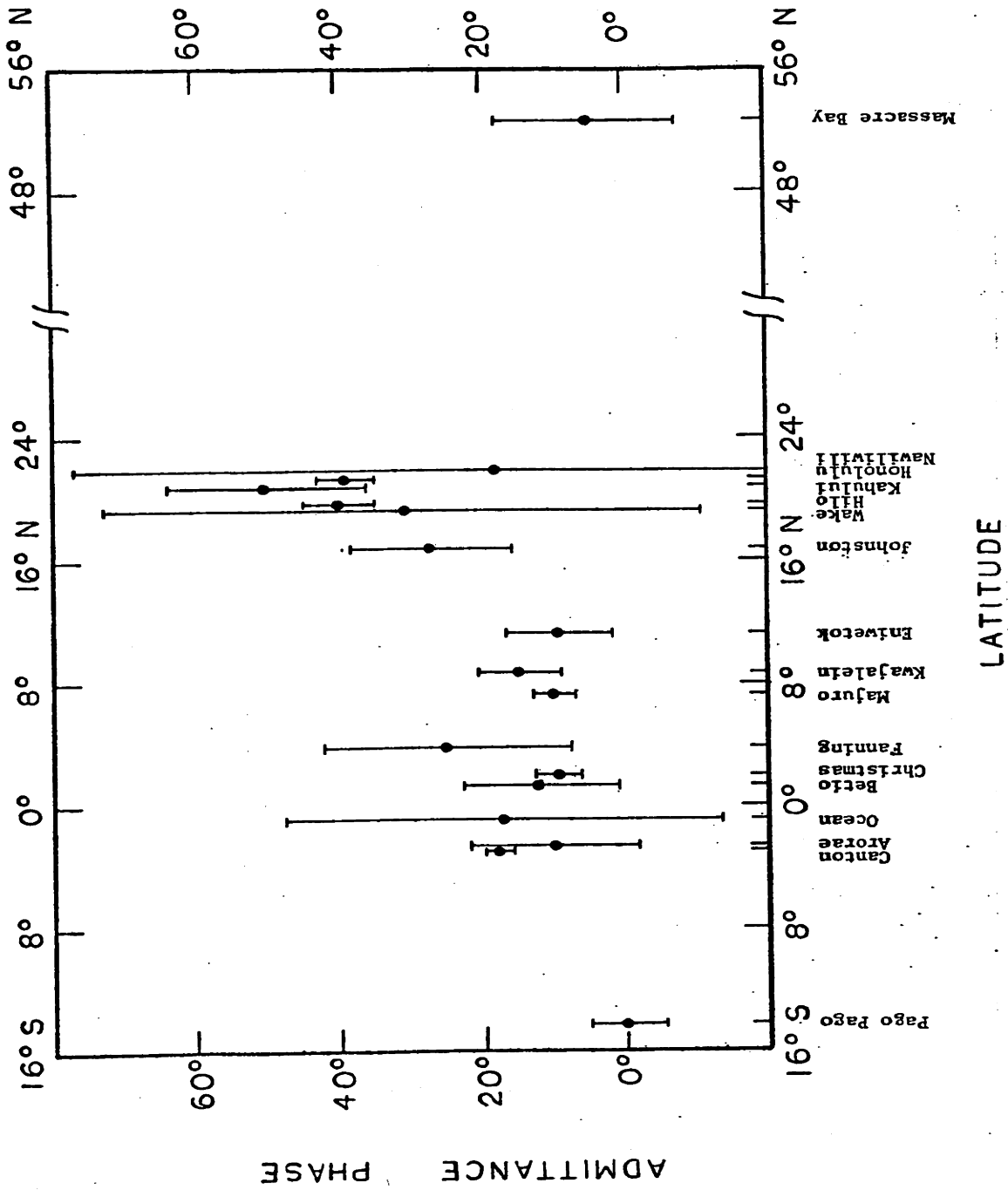


Figure 3.5b

TABLE 3.5 Mf Tide at Canton Is. (2°49'S, 171°40'W) for Successive

One Year Records

TIME ORIGIN (GMT)	AMPLITUDE ⁺⁺ H _{SL} (cm)		SIGNAL-TO- Noise Ratio (SNR)	ADMITTANCE ⁺ Amplitude		ADMITTANCE ⁺ Phase ψ (Deg)	REMARKS
	Y	Y		Y	Y		
5/28/49 2100	1.16 ± .38		3.0	.73 ± .16		5 ± 6	} Corresponds to } Time of Arorae } and Ocean Data } misaligned
5/28/50 2100	1.29 ± .28		4.5	.83 ± .12		20 ± 8	
5/28/51 2100	1.36 ± .19		7.2	.87 ± .08		7 ± 5	
5/27/52 2100	1.20 ± .29		4.2	.74 ± .12		30 ± 9	
5/27/53 2100	1.26 ± .29		5.0	.78 ± .11		19 ± 8	
5/27/54 2100	1.16 ± .37		4.1	.74 ± .15		1 ± 11	
5/27/55 2100	1.54 ± .57		4.1	1.01 ± .23		16 ± 13	
4/16/57 2000	1.35 ± 1.23		2.1	.80 ± .47		18 ± 38	
4/16/58 2000	1.57 ± 1.11		3.0	.94 ± .41		25 ± 27	
4/16/59 2000**	1.96 ± 1.27		3.4	1.27 ± .56		23 ± 27	
4/15/60 2000**	-----		0.9	-----		-----	
7/2/61 0200**	1.44 ± .60		4.5	.87 ± .21		13 ± 13	
7/2/62 0200	1.63 ± .47		5.7	.97 ± .17		25 ± 10	
7/12/63 0200	.94 ± .56		2.5	.59 ± .22		16 ± 23	
7/21/64 0200	1.21 ± .40		3.9	.79 ± .17		22 ± 12	
7/31/65 0200	.97 ± .43		2.7	.61 ± .16		27 ± 15	
8/10/66 0200	1.52 ± .18		8.7	.93 ± .07		23 ± 4	
5/22/75 0500	1.43 ± .63		4.0	.84 ± .23		13 ± 15	

* The data length for these estimates is always 9216 hours (384 days).

+ Relative to the "self-consistent" equilibrium tide (see text).

** These segments have interpolated gaps.

++ The noise variance is estimated from the six Fourier harmonics nearest the Mf tidal line.

95% error bars are computed from this estimate of the noise variance.

forcing (3.1), is the most striking feature of the non-equilibrium tide. The northward decrease of the admittance amplitude, and increase of the admittance phase, is significant at the 95% level, but the significance is gained solely on the basis of data from the Hawaiian Islands. The close agreement between the admittances from the four Hawaiian stations is surprising considering the possible excitation of topographic waves (Rhines (1969)) and the diffraction of the daily tides around Hawaii (Larsen (1977)). It is hard to imagine, however, that all four stations have uniformly small admittance amplitudes and large phases as the result of a purely topographic phenomenon. South of the equator, the admittance amplitude and phase both appear to be decreasing, based on the single station, Pago Pago. Poleward of the node (at $35^{\circ}16'N$) in the Mf forcing potential, both Massacre Bay and San Francisco (Table 3.3) have measurable tides with admittance phases close to zero, indicating the node exists in the ocean tide as well as the forcing. Neither station has a significantly non-equilibrium tide.

The admittances from four coastal stations, Balboa and Talara in the east and Rabaul and Dreger Harbor in the west, are included in Figure 3.4. Although none of the admittance amplitudes are significantly different from 1.0 at the 95% level, their average, 0.82, is. Both Dreger Harbor and Balboa have distinctly non-equilibrium phases (significant at the 95% level), in agreement with the mid-ocean observations. More data are necessary to ascertain coastal influences on the Mf tide.

In contrast to the Pacific Ocean, the Mf tide in the tropical Indian Ocean is not significantly non-equilibrium, at the 95% level (Table 3.3). There is a suggestion that the admittance amplitude increases westward, but much more data are needed to accurately determine the form of the Mf

tide in the Indian Ocean.

3.3. Brief Remarks on the Dynamics of the Fortnightly Tide. Kagan et al. (1976) have numerically solved the vertically-integrated Laplace Tidal Equations for the Mf tide in the world oceans, with topography and friction (horizontal and vertical) included. The model reproduces the major features of the Mf tide that have been observed in each ocean to date*, but the most important dynamical terms are not obvious. The small Q of the 5-day barotropic oscillation studied in the next section (3.C) suggests that dissipation may play an important role in large-scale barotropic oscillations. The possibility that the observed long-period tides are strongly-damped waves needs to be re-examined analytically since large-scale, slightly non-equilibrium solutions were excluded from Wunsch's (1967) model by his choice of boundary conditions, i.e., the tide was required to be equilibrium at the margins of the basin.

The existence of Rossby and topographic waves has not been completely excluded by the data analysis above. One has to wonder whether the two zones of high admittance amplitude off Brazil and Madagascar in Kagan et al.'s (1976) numerical solution are indications of westward intensification due to Rossby waves (à la Wunsch (1967)), or are local resonances dependent upon the particular basin geometry, similar to the amplification of the semidiurnal tides in the Gulf of Panama.

*Note that Kagan et al.'s admittance amplitude is relative to the equilibrium tide corrected for the yielding of the earth due to the potential (3.1) only, i.e., their equilibrium tide is 0.67 times (3.2). Hence their direct comparison of the model admittances with Wunsch's (1967) observations is erroneous, since Wunsch calculated the admittance amplitudes with (3.2). Also, the lack of small-scale (O(1000 km)) variations near the nodes of the forcing in Kagan et al.'s model is not necessarily proof that Wunsch's (1967) standing Rossby waves are not established, as Kagan et al. state. The model's grid-scale (5° of latitude and longitude) ensures that numerical friction will damp the small-scale waves (Harrison, personal communication, 1979).

B.4. Observed Monthly (Mm) Tide. Estimates of the amplitude and admittance of the Mm tide are listed in Table 3.6. Due to the larger background noise level at this longer period (see Figure 3.1), the error bars are much larger than for the Mf tide. Frequently, the monthly tide did not stand above the background. Estimates without error bars in Table 3.6 have 95% error bars greater than $\pm 100\%$ of the amplitude and $\pm 90^\circ$ of phase. Estimates in parentheses give the root-mean-square background level when no tide was discernible. If we take an average of estimates from stations in the central-western Pacific within 10° of the equator using only estimates where the tide was clearly present (grades of "A" or "B" only), then the mean admittance is $|Y| = .87 \pm .04$ and $\psi = 27^\circ \pm 2^\circ$. The same stations give $|Y| = .77 \pm .01$ and $\psi = 12^\circ \pm 1^\circ$, for the Mf tide (Table 3.3). Therefore, the Mm tide is closer to equilibrium in amplitude, but not in phase, than the Mf tide.

The meridional variations of the Mf admittance shown in Figure 3.5 are not clearly evident for the Mm tide, particularly since the error bars are so large. Unlike the Mf tide, the Mm tide in the eastern tropical Pacific may be significantly different from the central-western Pacific tide. Buena Ventura (Table 3.6) has a very large Mm admittance amplitude which, like the Mf tide there, is probably due to the nonlinear tides, so Buena Ventura is not considered further. Of the remaining four eastern Pacific stations, two, Galapagos and Balboa, do not have a clear Mm tide even though the background levels are low enough so that a near-equilibrium tide, as in the central Pacific, would stand out clearly above the background. The final two stations, La Libertad and Talara on the coast of South America, have clear Mm tidal signals, but with phases indicating that the sea level tide may lead the forcing. Better measurements are necessary to confirm

TABLE 3.6 Mm Tide - Pacific Ocean

STATION	LATITUDE (In Degrees & Minutes)	LONGITUDE	YEARS of Data	AMPLITUDE ⁺⁺	MEAN	ADMITTANCE*	ADMITTANCE*	REMARKS & "Grades"
				H ^{SL} (cm)	SNR ⁺	Amplitude ⁺⁺ Y	Phase ψ (deg)	
Balboa	8 57 N	79 34 W	8.0	.35	1.3	.48	45	C
Buenaventura	3 54 N	77 05 W	4.0	2.00 ± .46	5.2	2.61 ± .84	40 ± 18	A
La Libertad	2 12 S	80 55 W	4.0	.90 ± .34	3.3	1.15 ± .58	-50 ± 31	A
Talara	4 35 S	81 17 W	4.5	.55 ± .22	1.9	.71 ± .37	-14 ± 32	B
Galapagos	0 54 S	81 17 W	4.0	.19	1.2	.24	1	C
Christmas Is.	2 00 N	157 30 W	7.0	.99 ± .16	4.7	1.17 ± .23	21 ± 11	A **
Fanning Is.	3 54 N	159 24 W	1.5	.26	1.1	.32	9	C
Canton Is.	2 49 S	171 40 W	15.7	.73 ± .12	2.9	.84 ± .18	32 ± 12	A **
Hull Is.	4 30 S	172 07 W	0.8	.67 ± .49	1.9	.82 ± .71	42 ± 69	B
Arorae Is.	2 37 S	176 50 E	1.4	.71 ± .24	2.3	.82 ± .31	52 ± 23	B **
Betio Is.	1 22 N	172 56 E	1.1	.43 ± .22	2.7	.51 ± .30	-34 ± 38	C; misaligned
Ocean Is.	0 53 S	169 35 E	0.9	1.08 ± .52	2.7	1.24 ± .68	47 ± 35	A
Nauru Is.	0 32 S	166 55 E	0.8	(.80)	<1.0	(1.01)	--	D
Rabaul	4 12 S	152 11 E	2.0	.44 ± .36	1.8	.58 ± .57	35 ± 85	B **
Dreger Hbr.	6 39 S	147 52 E	1.1	.23	1.2	.33	-8	D
Majuro At.	7 10 N	171 05 E	2.0	(.50)	<1.0	(.63)	--	C; misaligned
Kwajalein	8 44 N	167 44 E	8.0	.75 ± .14	3.9	.95 ± .22	23 ± 13	A **
Eniwetok	11 21 N	162 21 E	4.0	.57 ± .36	2.1	.79 ± .66	19 ± 66	B
Ponape Is.	7 00 N	158 15 E	1.5	.51 ± .43	2.0	.66 ± .67	28 ± 89	C
Truk	7 27 N	151 52 E	2.8	.35 ± .23	2.1	.43 ± .34	2 ± 57	B **
Yap Is.	9 30 N	138 10 E	1.5	(.25)	<1.0	(.34)	--	D
Malakal Hbr.	7 19 N	134 27 E	0.8	.77 ± .72	1.8	1.01 ± 1.13	143 ± 107	C
Guam	13 27 N	144 39 E	4.0	.53 ± .40	1.9	.74 ± .73	20 ± 82	B
Wake Is.	19 17 N	166 39 E	4.0	(.40)	<1.0	(.67)	--	D; misaligned
Johnston Is.	16 45 N	169 32 W	3.0	.27	1.2	.41	114	D
Pago Pago Hbr.	14 17 S	170 40 W	2.0	.32	1.2	.41	-41	C
Hilo	19 42 N	154 04 W	5.9	.64 ± .29	1.9	1.15 ± .93	-15 ± 59	B
Kahului	20 56 N	156 29 W	4.0	.52 ± .31	2.7	1.04 ± 1.08	-17 ± 93	B
Honolulu	21 19 N	157 52 W	23.0	.41 ± .08	2.2	.81 ± .32	21 ± 24	B
Nawiliwili	21 57 N	159 21 W	2.0	.49	1.4	.95	3	C
Midway Is.	28 12 N	177 22 W	5.0	.19	1.1	.64	83	C
San Francisco	37 48 N	122 28 W	4.0	1.09	2.1	4.99	47	B
Massacre Bay	52 50 N	173 12 E	8.5	<.74	---	<.86	--	D; misaligned

⁺Signal-to-Noise Ratio (see text).

^{*}Relative to the "self-consistent" equilibrium tide (see text).

⁺⁺Values in parentheses are root-mean-square background levels.

^{**}The weighted vector-average of these stations gives $|Y| = .87 \pm .04$ and $\psi = 27^\circ \pm 2^\circ$. The stations were chosen to be within 10° of the equator in central Pacific with more than a year of data and "grades" A or B. A total of 36.9 years went into average. See text.

TABLE 3.6 Mm Tide - Indian Ocean

STATION	LATITUDE (In Degrees & Minutes)	LONGITUDE	YEARS of Data	AMPLITUDE	MEAN	ADMITTANCE*	ADMITTANCE*	REMARKS & "Grades"
				H ^{SL} (cm)	SNR ⁺	Amplitude Y	Phase ψ (deg)	
Minicoy	8 17 N	73 03 E	4.0	.44	1.6	.55	52	C; misaligned
Diego Garcia	7 14 S	72 26 E	2.3	.93 ± .43	2.9	1.20 ± .71	-5 ± 38	A
Port Victoria	4 37 S	55 27 E	1.0	.92 ± .77	1.8	1.17 ± 1.19	-4 ± 89	C; misaligned
Mauritius	20 09 S	57 29 E	1.5	1.23 ± .73	2.3	2.15 ± 2.00	27 ± 77	B

⁺Signal-to-Noise Ratio (see text).

^{*}Relative to the "self-consistent" equilibrium tide (see text).

the non-equilibrium character of the Mm tide in the eastern Pacific before speculation on the origin of the variability becomes meaningful.

Observations of variations in the length of day (l.o.d.) make the above analysis of the oceanic Mm tide more intriguing. Agnew and Farrell (1976) point out that the l.o.d. observations suggest the integrated oceanic Mf tide is slightly below equilibrium and the oceanic Mm tide is nonexistent or in quadrature with the forcing. We have confirmed that an Mm tide does exist in the ocean (in agreement with previous observations by Wunsch (1967)), but with perhaps a larger non-equilibrium phase than Mf and perhaps greater spatial variability than Mf, so that the integrated oceanic Mm tide in phase with the forcing may be much smaller than for the Mf tide, in agreement with the l.o.d. observations. But without more accurate measurements of the Mm tide this remains a speculation.

B.5. Observed Nine-Day Tide. The nine-day tide (Table 3.2), with only 20% of the forcing of the Mf tide, has received little attention.* If the tide is near-equilibrium in amplitude, it will be barely visible above the sea level continuum unless many years of data are analyzed. However, some spectra, and numerous cross-spectra, signal the presence of the nine-day tide, especially in the western Pacific where the sea level power density spectrum from Truk Atoll (Figure 3.6) clearly shows the nine-day tide, as well as Mf and Mm. Strong peaks in the coherence between sea level measured at Kwajalein and Eniwetok (Groves and Hannan (1968, Fig. 7a)) can be attributed to the nine-day and fortnightly tides.

Estimates of the amplitude and admittance of the nine-day tide (Doodson No. 085 455) are listed in Table 3.7. When no clear tide was present and the root-mean-square background level was larger than the equilibrium nine-day tide, no entry was made in the table. Estimates

*Maksimov et al. (1967) studied the nine-day tide with Arctic sea level data, but their work leaves some perplexing questions unanswered.

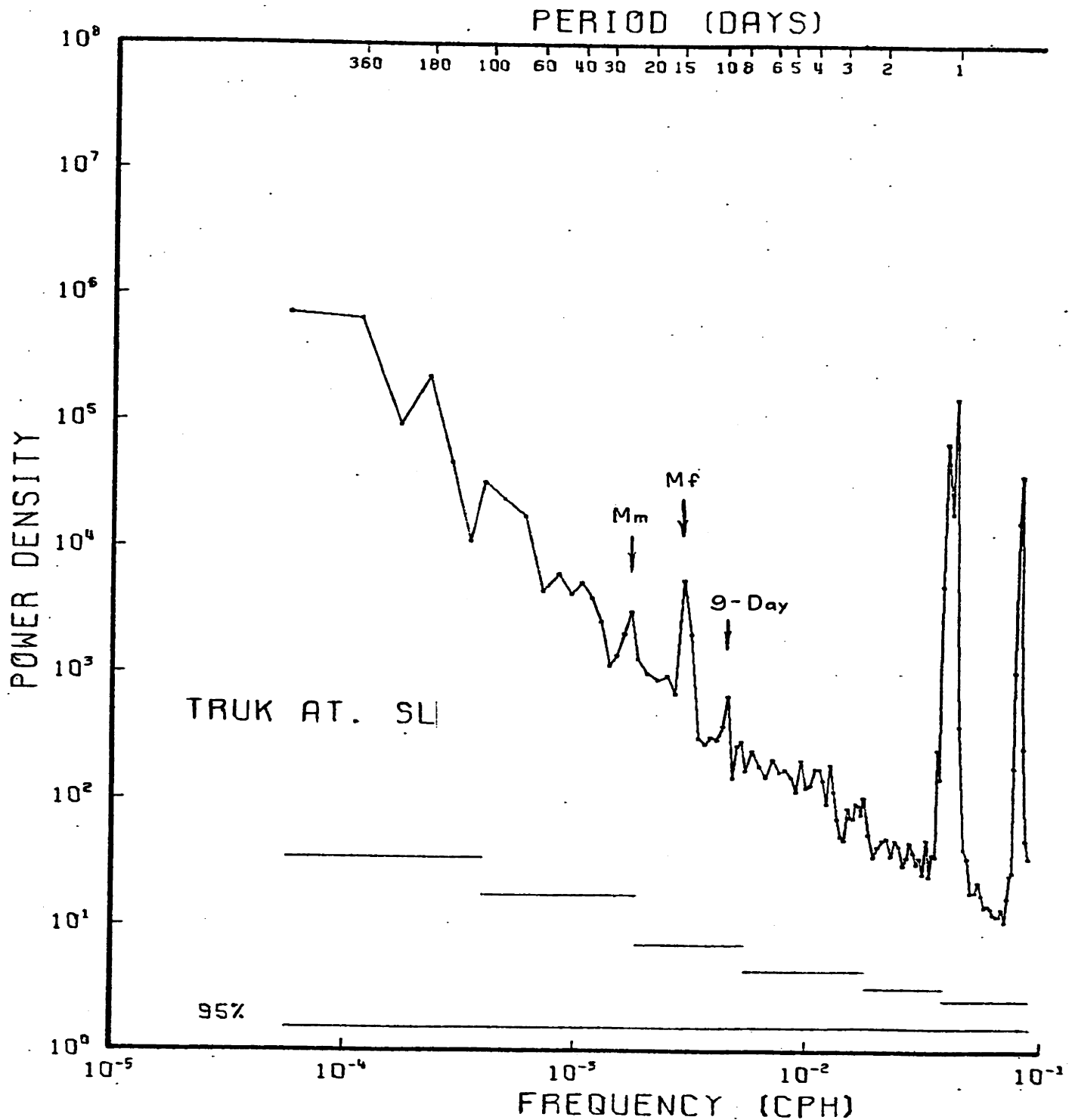


Figure 3.6 - Power density spectrum of 4 years of sea level data from Truk ($7^{\circ}27'n$, $151^{\circ}52'E$), clearly showing the three strongest long-period tides (as marked). The 95% confidence interval plotted does not pertain to the deterministic tidal signals. Otherwise, the spectrum is plotted as in Figure 3.1.

TABLE 3.7 Nine-Day Tide

STATION	LATITUDE (In Degrees & Minutes)	LONGITUDE & Minutes)	YEARS of Data	AMPLITUDE ⁺⁺		MEAN SNR ⁺	ADMITTANCE* ⁺⁺		ADMITTANCE* Phase ψ (deg)	REMARKS & "Grades"
				H ^{SL} (cm)	Y		Y	Y		
Balboa	8 57 N	79 34 W	8.0	.15		1.4	.61	-21	C;misaligned	
Buenaventura	3 54 N	77 05 W	4.0	.42		1.6	1.44	20	C;misaligned	
Galapagos	0 54 S	89 34 W	5.0	(.19)		<1.0	(.61)	--	D	
Christmas Is.	2 00 N	157 30 W	9.0	.27 ± .10		2.6	.84 ± .76	4 ± 74	B **	
Canton Is.	2 49 S	171 40 W	7.7	.20 ± .09		2.5	.69 ± .86	35 ± 122	B **	
Rabaul	4 12 S	152 11 E	2.0	.16		1.3	.55	-80	C	
Majuro At.	7 10 N	171 05 E	2.0	.24 ± .12		2.2	.83 ± 1.08	12 ± 120	B **	
Kwajalein	8 44 N	167 44 E	7.7	.25 ± .17		2.8	.83 ± 1.33	2 ± 150	A	
Eniwetok	11 21 N	162 21 E	4.0	.24		1.7	.84	-1	B	
Ponape Is.	7 00 N	158 15 E	1.5	.27 ± .11		2.6	.93 ± 1.02	23 ± 106	A **	
Truk	7 27 N	151 52 E	4.8	.33 ± .08		3.0	1.37 ± 1.51	11 ± 104	B **	
Yap Is.	9 30 N	138 10 E	1.5	.18		1.6	.65	-34	C;misaligned	
Guam	13 27 N	144 39 E	4.0	.22 ± .17		2.0	.87	23	B	
Wake Is.	19 17 N	166 39 E	4.0	(.13)		<1.0	(.62)	--	D	
Hilo	19 42 N	155 04 W	3.0	.23		1.9	1.10	115	B	
Kahului	20 56 N	156 29 W	4.0	.18 ± .11		1.9	1.00	63	B	
Honolulu	21 19 N	157 52 W	8.0	.25 ± .09		3.3	1.47 ± 2.21	43 ± 142	B	
Minicoy	8 17 N	73 03 E	4.0	.41 ± .12		3.6	1.55 ± 1.50	27 ± 80	A	
Diego Garcia	7 14 S	72 26 E	1.5	.42		1.7	1.41	-32	B	

⁺ Signal-to-Noise Ratio (see text).

⁺⁺ Values in parentheses are root-mean-square background levels.

**The weighted vector-average of these stations (representing the most reliable estimates above) yield $|Y| = .87 \pm .25$ and $\psi = 12^\circ \pm 14^\circ$.

*Relative to the "self-consistent" equilibrium tide (see text).

with error bars have 95% error greater than $\pm 100\%$ of amplitude and $\pm 90^\circ$ of phase. Values in parentheses are root-mean-square estimates of the background level at 9.1 days period. The six most reliable estimates of the nine-day tide admittance in the Pacific (Table 3.7) have been vector-averaged, weighted by data length, to give $|Y| = .87 \pm .25$ and $\psi = 12^\circ \pm 14^\circ$. This is to be compared with $|Y| = .77 \pm .01$ and $\psi = 12^\circ \pm 1^\circ$ for the average fortnightly tide from the same six stations (Table 3.3). Although we cannot accurately describe the structure of the nine-day tide from the observations, the tide is clearly measurable from sea level records in the tropical Pacific and Indian Oceans, and hence must be reckoned with in later studies of equatorially-trapped waves.

B.6. Conclusions and Discussion on the Long-Period Tides. We have found that the long-period tides* are slightly non-equilibrium in the Pacific Ocean, and have suggested that the dynamics of the tides are dominated by frictional forces. The existence of these tides, especially the nine-day tide, is crucial to the interpretation of sea-level cross-spectra in the equatorial waveguide. No free oscillations at the tidal periods are clearly present, although the spatial coverage of the dataset is not adequate for detecting the standing Rossby modes described by Wunsch (1967). Certainly, the gravest, "circulating" Kelvin modes of an equatorial basin (postulated by Philander (1978)) are not evident. (Indeed, the dynamical Mf tide component in the Pacific increases in amplitude away from the equator, which is decidedly un-Kelvin-like behavior.)

No propagating coastal tides, as Picaut and Verstraete (1979) found along the Gulf of Guinea at the MSf tide period (14.765 days), are clearly present in the eastern Pacific, although the nonlinear MSf tide does have

*The work on long-period tides by Maksimov (1966 and others) has not been discussed in relation to our results due to the unreliability of his estimates and the lack of error analysis (see comments by Wunsch (1966, p. 26)).

a northward phase lag between Buenaventura and Balboa in the Gulf of Panama.

It is reasonable to assume that all the long-period tides in the 2-90 day band* are approximately equilibrium. Since the equilibrium amplitudes of all the tides not discussed above (i.e., excluding the Mm, MSf, Mf and nine-day tides) are well below the background levels of the sea level spectra, we do not expect these other tides will contaminate the sea level analyses discussed in subsequent sections of this chapter. In support of this claim, note that Miyata (1970) computed the sea level power density at Canton ($2^{\circ}49'S$, $171^{\circ}40'W$) that was coherent with the astronomical tidal forcing, and found that, aside from the four tides above, only the five- and seven-day tides accounted for even one-tenth of the raw sea level power at their tidal periods.

Further steps in the investigation of the long-period tides are suggested by this work. Simple theoretical models can examine the sensitivity of the tides to friction in its various forms for simple basin geometries. Future observational studies can take advantage of the relationships between sea level and weather (by removing the effects of weather on sea level), thereby reducing the "noise" level and improving the estimates of the long-period tides (Cartwright (1968)).

C. Barotropic Normal Modes

The theory of equatorially-trapped inertia-gravity waves defines a narrow zonal band about the equator, poleward of which the oscillations decay as a Gaussian of latitude (see equations (1.25) and (1.27)). For the 4- and 5-day peaks in Figure 3.1, which have been identified as the signature of inertia-gravity waves (Wunsch and Gill (1976) and the next section), the theory predicts that the power in the sea-surface displacement

*See Godin (1972; pp. 220-222) for a listing of the tides.

of these modes at $\pm 10^\circ$ of latitude will be less than 1% of the maximum power near the equator. It is surprising, therefore, to find strong coherence amplitude at 4-6 day periods between sea level stations far from the equator, for instance between Kwajalein ($8^\circ 44'N$, $167^\circ 44'E$) and Wake ($19^\circ 17'N$, $166^\circ 39'E$) (Figure 3.7). Also, it is plausible to expect that the simple horizontal and vertical mode structure responsible for the 4- and 5-day peaks in Figure 3.1 will be altered in the presence of rough topography and convoluted horizontal boundaries, such as near the eastern and western edges of the equatorial Pacific. Yet strong sea level coherence at 4-6 days occurs near both coasts, and not just near the equator (Figure 3.8). In fact, almost every sea level coherence computed between Pacific stations, coastal and island, has significant (at the 95% level) amplitude in the 4-6 day band, even for large (5000 km) horizontal separations.

The possible presence of a forced or free oscillation in the Pacific Ocean at 4-6 days period, which is not equatorially-trapped and would obscure the study of equatorial waves at the same periods, has led us to examine the 4-6 day band more closely. The dynamics of the large-scale oscillation and its impact on our study of equatorial waves are discussed.

C.1. Test for a Static Response to Atmospheric Pressure

The first hypothesis to be tested is that the sea level oscillation is simply the static response to the global, 5-day, barotropic atmospheric oscillation studied in Chapter 2 (section B.2). The coherences between sea level and atmospheric pressure at Truk and Galapagos are plotted in Figure 3.9. If the sea level response is static, the phase should be 180° , which it clearly is not at 4-6 days. The vector-averaged coherences between sea level and atmospheric pressure in the 4-6 day band, for all

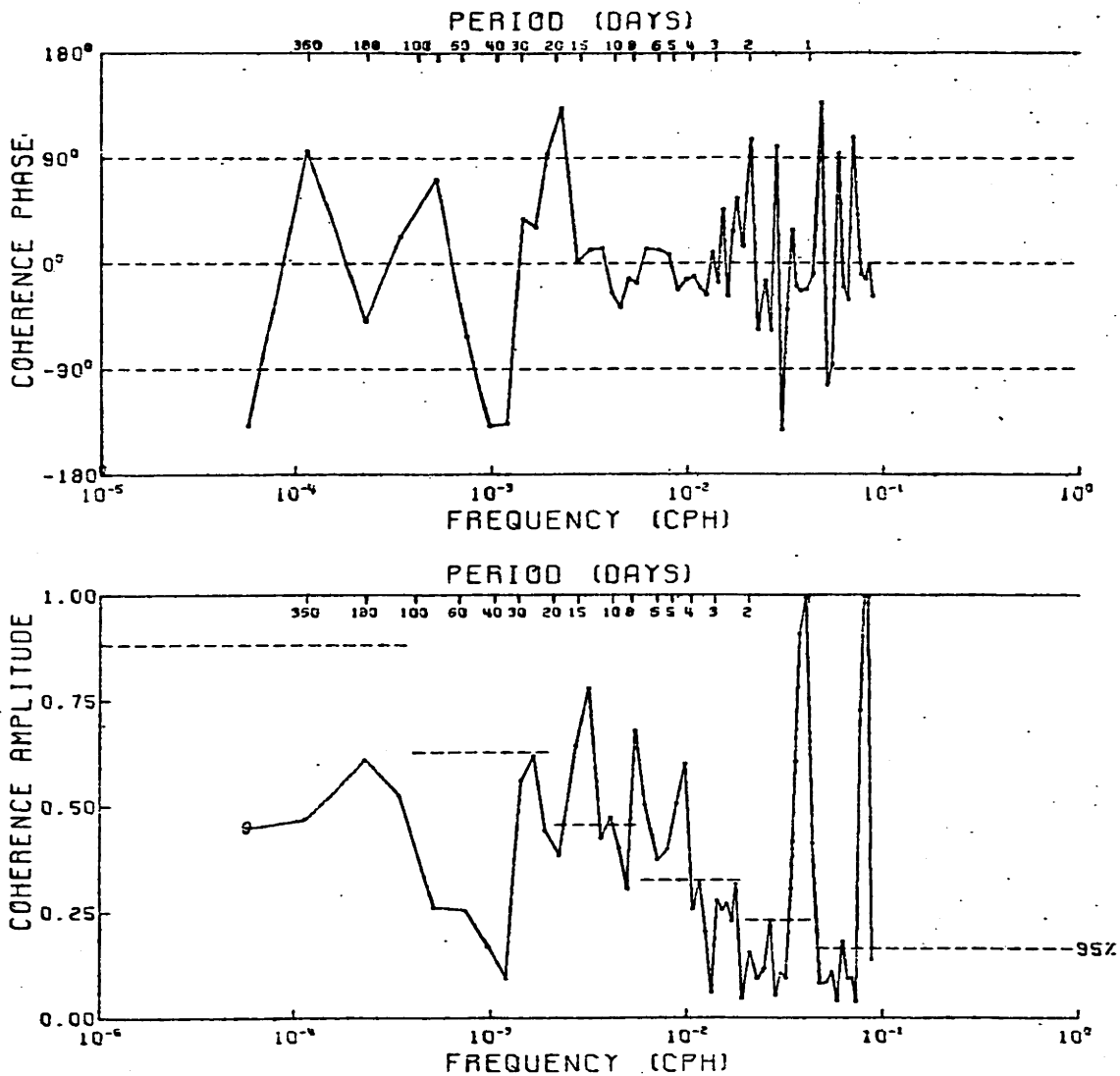
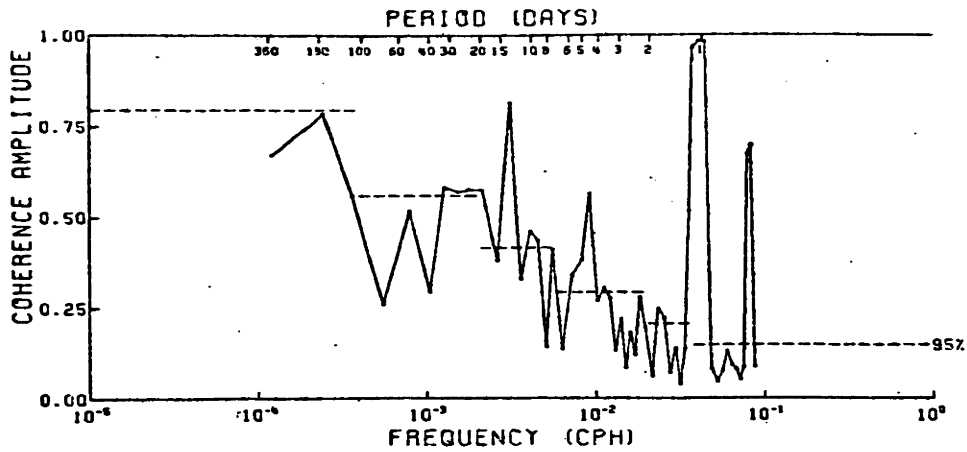
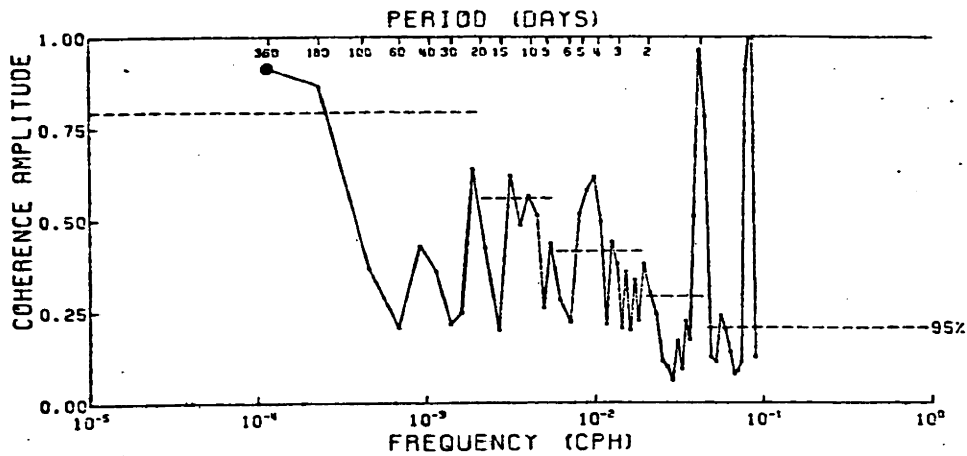


Figure 3.7 - Coherence amplitude and phase between 4 years of sea level data from Kwajalein ($8^\circ 44'N$, $167^\circ 44'E$) and Wake ($19^\circ 17'N$, $166^\circ 39'E$), showing unusually strong amplitude at 4-6 days period. The semidiurnal, diurnal and fortnightly tides produce the strong coherence amplitudes at .5, 1. and 14 days. The origin of the strong amplitude at 8 days is not known. The 95% level of no significance is indicated. The lowest-frequency point plotted is the "zerth"-harmonic estimate, which is circled to indicate that its 95% level of no significance is higher than that plotted.



(a)



(b)

Figure 3.8 - Coherence amplitude between sea level records, showing large 4-6 day amplitude. (a) 4.7 years from Guam ($13^{\circ}27'N$, $144^{\circ}39'E$) and Truk ($7^{\circ}27'N$, $151^{\circ}52'E$). (b) 2.5 years from Balboa ($8^{\circ}57'N$, $79^{\circ}34'W$) and Talara ($4^{\circ}35'S$, $81^{\circ}17'W$). Plotted as in Figure 3.7.

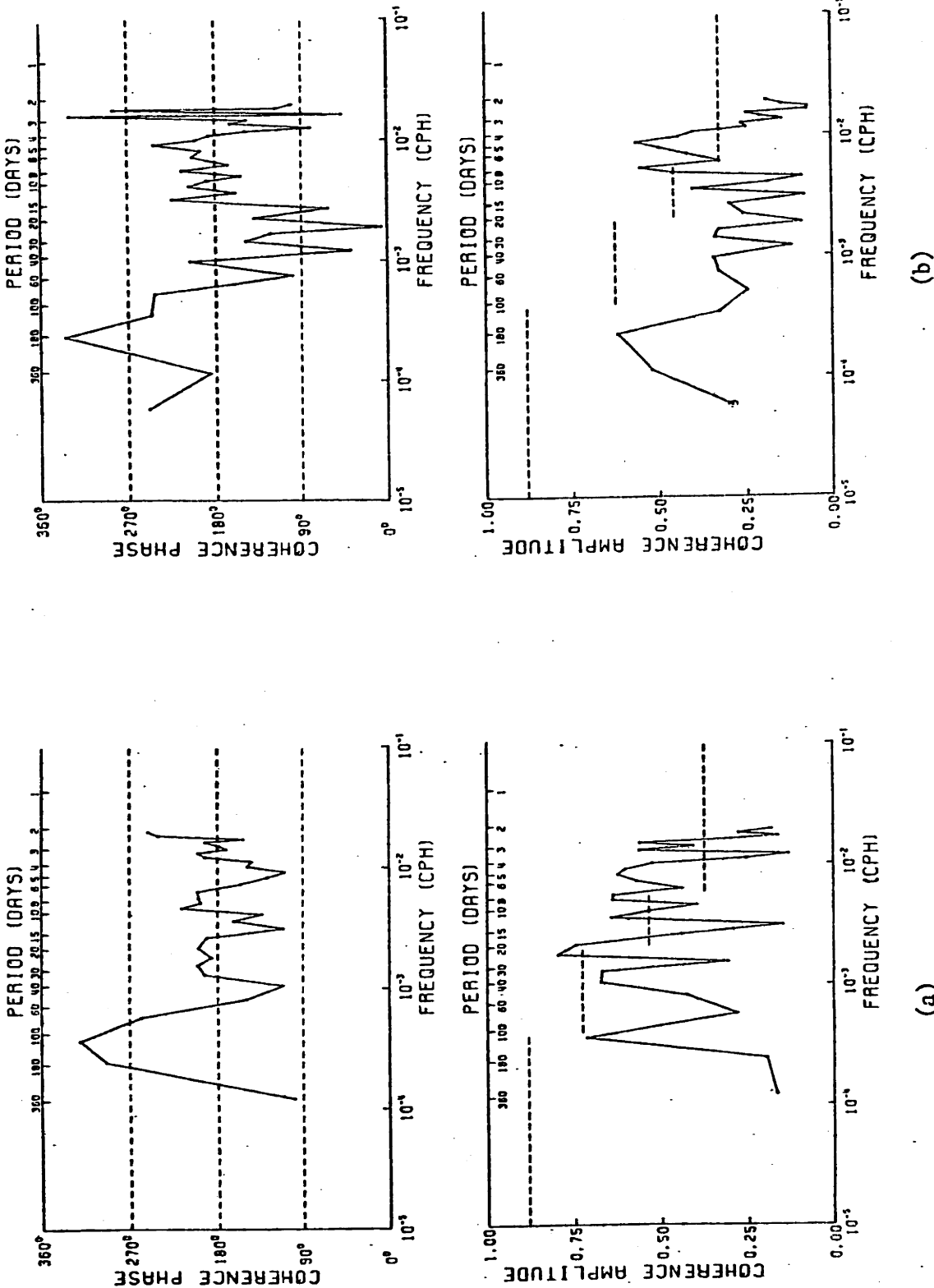


Figure 3.9 - Coherence amplitude and phase between sea level and surface atmospheric pressure for (a) 2.8 years of data from Truk (7°27'N, 151°52'E), and (b) 4 years of data from Galapagos (0°54'S, 89°34'W). The coherence amplitudes are strong in the 4-6 day band while the phase is not 180°, so sea level is not responding statically to the air pressure. Positive phase specifies that sea level leads.

the stations with cotemporal sea level and weather records, are tabulated in Table 3.8. A positive phase indicates sea level leads air pressure.

Table 3.8

Coherence Amplitude and Phase Between Sea Level
and Surface Air Pressure in the 4-6 Day Band

<u>Station</u>	<u>Latitude</u>	<u>Longitude</u>	<u>Amplitude</u>	<u>Phase (deg)⁺</u>
Balboa	8°57'N	79°34'W	.46	-173 ± 11
Galapagos	0°54'S	89°34'W	.44	-152 ± 15
Canton*	2°49'S	171°40'W	—	—
Kwajalein	8°44'N	167°44'E	.33	114 ± 21
Eniwetok	11°21'N	162°21'E	.32	133 ± 32
Truk	7°27'N	151°52'E	.56	127 ± 14
Guam	13°27'N	144°39'E	.45	139 ± 14
Wake	19°17'N	166°32'W	.42	129 ± 18
Johnston*	16°45'N	169°32'W	—	—
Hilo	19°42'N	155°4'W	.59	162 ± 10
Honolulu	21°18'N	157°52'W	.45	163 ± 9
Midway	28°12'N	177°22'W	.66	159 ± 8

*Coherence amplitude below the 95% level of no significance.

⁺Error bars are the 95% confidence limits.

The coherences for Kwajalein, Eniwetok and Hilo in Table 3.8 are in excellent agreement with the sea level - weather regressions computed by Groves and Hannon (1968) and Miyata and Groves (1971) using datasets that do not temporally overlap those used here. Both papers indicate the 4-6 day band is unusual in that sea level is coherent with atmospheric

pressure and does not respond statically, like an "inverted barometer". Note that the multiple regression of sea level on atmospheric winds and pressure at Kwajalein and Eniwetok (Groves and Hannan (1968)) yielded a modulus for both islands of ~ 0.5 cm/mb for the amplitude response of sea level to air pressure at 4-6 days. This modulus is significantly different from the static 1 cm/mb with 95% confidence.

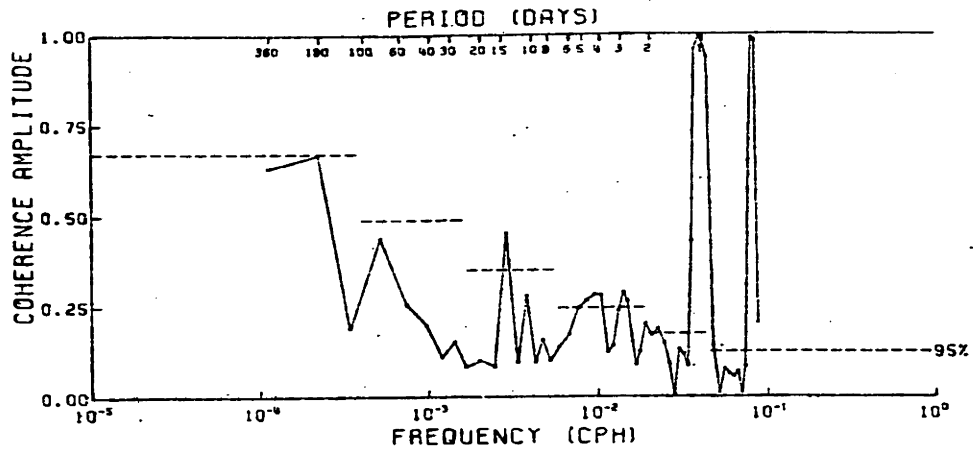
C.2. Possible Planetary Basin Modes.

Since sea level is coherent in the 4-6 day band over large distances (Figure 3.10), the oceanic oscillation must be narrow-band in wavenumber, and since the oscillation extends into mid-latitudes (Figure 3.10a), the only plausible explanation is that the oscillation is a barotropic normal mode of the Pacific basin, probably a planetary (Rossby) mode*.

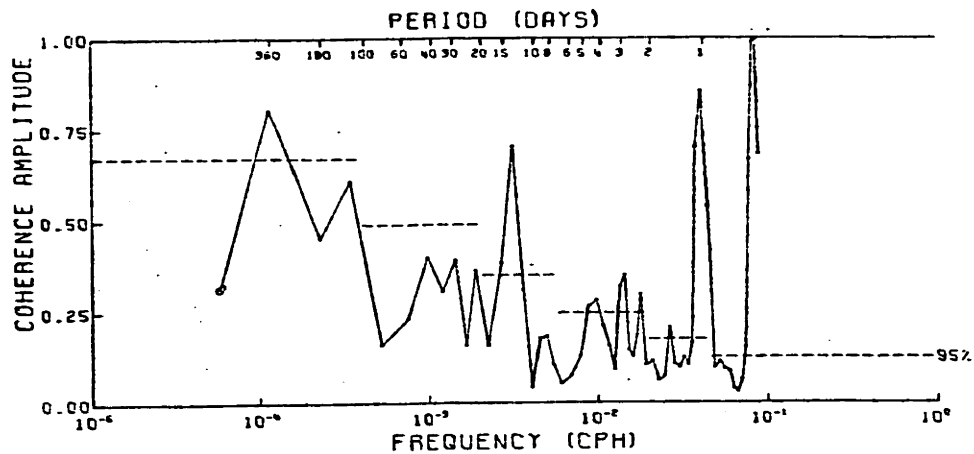
The search for planetary waves in the Pacific began with Groves and Zetler's (1964) calculation of the coherence between sea level measured at Honolulu and San Francisco. Their results are in excellent agreement with Figure 3.10a, but without further evidence they could not prove that the coherence in the 4-6 day band indicated the presence of a large-scale ocean wave. Groves and Hannan (1968) made a more determined attempt to find planetary waves in sea level measurements from Kwajalein and Eniwetok. After removing the effects of local weather on sea level, they concluded that a small amount of planetary wave energy was present in the 5-10 day band.

Longuet-Higgins (1966), in a study of the planetary modes of a hemispherical basin centered at the equator, suggested that a small peak at 2

*On the basis of a single sea level-atmospheric pressure coherence function (from Canton), Wunsch and Gill (1976) postulated a "resonant barotropic response" at 5.4 days period.



(a)



(b)

Figure 3.10 - Coherence amplitude between sea level records, showing significant amplitude in the 4-5 day band. (a) 7 years from Honolulu ($21^{\circ}19'N$, $157^{\circ}52'W$) and San Francisco ($37^{\circ}48'N$, $122^{\circ}28'W$). (b) 7 years from Canton ($2^{\circ}49'S$, $171^{\circ}40'W$) and Balboa ($8^{\circ}57'N$, $79^{\circ}34'W$). Plotted as in Figure 3.7.

days period in the power spectrum of sea level at Honolulu (computed by Munk and Cartwright (1966)) was an indication of the gravest planetary mode of the Pacific Ocean. In a later note, referring to the sea level coherence between Honolulu and Mokuoloe on the island of Oahu (computed by Miyata and Groves (1968)), Longuet-Higgins (1971) retracted this initial suggestion, but argued that peaks in the coherence at 0.35 and 0.23 cpd were possibly manifestations of the gravest planetary modes of the Pacific. The peaks could also be due to island-trapped waves, he noted. Surprisingly, LeBlond and Mysak (1977; p. 164) recently stated that the 0.23 cpd peak is due to the inertia-gravity waves observed by Wunsch and Gill (1976); this is incorrect since the inertia-gravity waves at that period are miniscule at 10°N ., let alone 21°N , the latitude of Honolulu.

Several investigators have computed the gravest planetary eigenfrequencies and eigenmodes for geometries idealizing the Pacific basin. The eigenfrequencies for the lowest modes, from the most thorough analyses, are listed in Table 3.9. The gross differences in the model dynamics are indicated in the table. The frequency-spacing between modes is small, even for the gravest modes, and decreases for the higher modes so that the modal spectrum approaches a continuum as the frequency decreases if a small amount of friction is included (see, for example, Harrison (1979)).

Identification of the real ocean mode(s) responsible for the 4-6 day coherences in Figures 3.7-3.10, solely by matching the observed and theoretical frequencies, is impossible without a complete numerical solution with realistic geometry and topography, since the theoretical frequencies are strong functions of basin dimensions, depth and bottom slope. Longuet-Higgins (1965) found that for a mid-latitude rectangular basin the frequency increased as any basin dimension increased. Therefore, in a later

TABLE 3.9 Eigenfrequencies of the Gravest Planetary Modes in a Homogeneous, Flat-Bottomed Ocean with Dimensions on the Order of the Pacific

Basin Geometry	Longuet-Higgins (1966)		Longuet-Higgins & Pond (1970)		Rattray & Charnell (1966)		Mofjeld & Rattray (1971)	
	Hemisphere	Circle (c)	Hemisphere	Rectangle (e)	Hemisphere	Rectangle (e)	Hemisphere	Rectangle (f)
Rotational Terms	$\vec{\Omega} \times \hat{k}$	β -plane	$\vec{\Omega} \times \hat{k}$	β -plane	$\vec{\Omega} \times \hat{k}$	β -plane	β -plane	β -plane
$\epsilon = (2\Omega a)^2 / gD$	0	0	22	(a) (d)	22	22	22	22
Periods (days) of Gravest Modes (b)								
Symmetrical								
1	3.3	2.4	4.5	4.1	4.2			
2	4.1	3.3	5.0	4.9	5.0			
3	5.0	4.5	5.6	6.0	6.1			
Antisymmetrical								
1	1.6	1.5	2.0	2.7	2.6			
2	2.6	2.4	2.9	3.8	3.8			
3	3.6	3.5	3.8	5.1	5.2			
4	4.6	4.5	4.7	5.3	5.6			

Notes: (a) $\epsilon=22$ corresponds to $D=4$ km.

(b) Symmetry describes the structure of the surface displacement with respect to the equator. Ordering of the modes is on the basis of period.

(c) The basin is centered on the equator with radius = $\frac{7}{4}$ times the radius of the earth.

(d) Longuet-Higgins & Pond computed the frequencies for nearly all values of ϵ . We have chosen only the one value here for comparison with the other models.

(e) Zonal dimension is 1.3×10^4 km. Meridional extent is 6×10^3 km north of equator to 1.1×10^4 km south of equator.

(f) Basin is centered on the equator with zonal and meridional dimensions of 1.25×10^4 km.

paper, Longuet-Higgins (1971) reduced the frequencies of the gravest modes of a hemispherical basin (computed by Longuet-Higgins and Pond (1970); see Table 3.9) by 30% to match the modes with observations from the Pacific. But Mofjeld and Rattray (1971) found that for a rectangular basin centered on the equator the frequency is actually a strong function of the ratio of the two basin dimensions. We have not attempted to adjust the mode periods in Table 3.9 for any differences between the model basin dimensions and the dimensions of the Pacific Ocean. Such an adjustment is especially futile since topography (shelves, ridges, etc.) has been found to increase strongly the frequencies of the planetary basin modes in numerical models (Christensen (1973b) and Platzman (1975)) and analytical studies (Ripa (1978)).

The models listed in Table 3.9 differ substantially in their choices of horizontal boundary conditions. Although the periods of the gravest modes are relatively insensitive to the boundary conditions (Buchwald (1973), Flierl (1977)), the improper choice of boundary conditions may arbitrarily rule out possible solutions to the quasi-geostrophic equations, leading to incorrect conclusions regarding comparison with observations. For instance, Longuet-Higgins (1971) dismisses the sea level coherence (or lack thereof) between Honolulu and San Francisco (as computed by Groves and Zetler (1964), but see Figure 3.10a) since "the vertical displacement is theoretically small" there, but this "theoretical" result was due to the too-restrictive requirement that the stream-function be zero on the horizontal boundaries (Longuet-Higgins (1965, 1966)). Larichev (1974) emphasized that since the theoretical planetary modes can

have significant displacement at the boundaries, long records of sea level at coastal stations may be useful for studying the modes in the real oceans.

C.3. Wavenumber Estimates of the Oceanic Wave.

The planetary eigenfunctions corresponding to the eigenfrequencies in Table 3.9 are characterized by the presence of a westward-propagating component (Longuet-Higgins (1965)), as well as a standing component. For the gravest planetary modes, the standing component has such a large scale that only the propagating component is likely to be detected in sea level cross-spectra. Table 3.10 lists the sea level coherence amplitude and phase in the 3.5-6.0 day band for various station pairs. The band, 3.5-6.0 days, was chosen so as to increase the degrees of freedom in the coherence estimate after it was found that the phase changed little across this band. In general, the resolution of the original coherence computation was chosen to produce 6 estimates in the 3.5-6.0 day band. The estimates with significantly nonzero amplitudes (at the 90% level) were then vector-averaged to produce a final estimate which appears in Table 3.10 if the amplitude is significantly non-zero (at the 95% level). Coherences have not been computed for all possible station pairs, but only a representative sampling. In anticipation of the large zonal scale of the oscillation, only station pairs separated by more than 10° of longitude are included in Table 3.10. And finally, only station pairs with at least one station poleward of 8° from the equator are considered, in order to avoid "contamination" by equatorially-trapped inertia-gravity waves at 4-6 day periods.

The only consistent interpretation of the phases in Table 3.10 is that the oceanic mode is westward propagating with a very large wavelength. Since the wavelengths of the propagating components of the

TABLE 3.10 Coherence Amplitude and Phase Between Sea Level Records
(3.5-6.0 Day Band)

STATION 1 (a)	STATION 2	AMPLITUDE (b)	PHASE (c) (deg)	LATITUDINAL Separation (deg)	LONGITUDINAL Separation (deg)	ZONAL (d) Separation (km)	$\frac{2\pi a}{\lambda_x}$ (e)
Honolulu	Balboa	.25	126 ± 33	12.4	78.3	8622	-3.0 ± 0.4
Canton	Balboa	.24	73 ± 26	11.8	92.1	10140	-3.2 ± 0.3
Kwajalein	Canton	.30	-13 ± 17	11.5	20.6	2294	-0.6 ± 0.8
Truk	Kwajalein	.38	-8 ± 13	1.3	15.9	1721	-0.5 ± 0.8
Eniwetok	Canton	.44	0 ± 27	14.2	26.0	2811	0.0 ± 1.1
Yap	Truk	.49	-11 ± 19	2.1	13.7	1476	-0.8 ± 1.4
Guam	Kwajalein	.40	0 ± 15	4.7	23.1	2400	0.0 ± 0.7
Guam	Eniwetok	.50	-40 ± 26	2.1	17.7	1883	-2.4 ± 1.5
Guam	Wake	.34	-26 ± 16	5.8	22.0	2487	-1.2 ± 0.7
Wake	Johnston	.35	-31 ± 22	2.5	23.8	2488	-1.4 ± 1.0
Kwajalein	Honolulu	.34	-98 ± 29	12.6	34.4	3812	-2.9 ± 0.9
Johnston	Hilo	.26	-49 ± 24	3.0	14.5	1533	-3.6 ± 1.7
Canton	Honolulu	.24	-52 ± 22	24.1	13.8	1518	-3.8 ± 1.6
Canton	Hilo	.24	-62 ± 26	22.5	16.6	1814	-3.8 ± 1.6
Kwajalein	Pago Pago	.35	-25 ± 33	23.0	21.6	2440	-1.1 ± 1.5
Pago Pago	Hilo	.33	-27 ± 36	34.0	15.6	1668	-1.8 ± 2.4
Massacre Bay	Hilo	.26	-50 ± 25	33.1	31.7	2319	-2.4 ± 1.2
Honolulu	San Francisco	.26	-127 ± 20	16.5	35.4	3080	-4.6 ± 0.7
Hilo	San Francisco	.27	-142 ± 18	18.1	32.6	2784	-5.7 ± 0.7
Massacre Bay	San Francisco	.18	123 ± 28	15.0	64.3	5103	-5.2 ± 0.6

Notes: (a) Station 1 is always westward of station 2.

(b) Coherence amplitudes have not been corrected for bias, but all are significantly non-zero at the 95% level.

(c) Positive phase indicates first station leads second. Error bars are 95% confidence limits.

(d) The distance (in km) of each station from the 160° W meridian is used for computing the zonal separation.

(e) λ_x is zonal wavelength (calculated using the zonal separation) and "a" is the radius of the earth. Error bars are 95% confidence limits. Negative values imply westward propagation.

gravest antisymmetric and symmetric planetary modes (Figures 2 and 7, respectively, in Longuet-Higgins (1966)*) are nearly independent of latitude, the phases in Table 3.10 are used to compute the zonal wavelength, λ_x , of the oscillation after first converting the position of each station into a distance east or west from the mid-basin meridian of 160° . [N.b., for β -plane models of planetary modes, the wavenumber of the propagating component is independent of latitude and mode. This is not the case for spherical basins wherein the modes may even have amphidromic points, indicating eastward propagation in some regions (Longuet-Higgins (1966)). For a 5-day period mode of an equatorial β -plane model, $\frac{2\pi a}{\lambda_x} = \frac{-\beta a}{2\omega} = -5$ cycles/circumference.]

The normalized wavenumbers, $\frac{2\pi a}{\lambda_x}$, listed in Table 3.10 are also plotted in Figure 3.11. Although the scatter is large, westward propagation is clear. There is a suggestion that the wavelength is decreasing with latitude (see Table 3.10), but it is not useful to interpret the variations in terms of existing constant-depth models because topography can be expected to alter the eigenfunctions significantly (Platzman (1975)).

The most poleward stations in our dataset, Massacre Bay (53°N) and Pàgo Pàgo (14°S), have been included in Table 3.10 in support of the hypothesis that the oscillation is basin-wide. There is no indication from the coherences of a node at the equator, so the sea-surface displacement is apparently symmetric about the equator. The periods of the gravest symmetric modes (Table 3.9) lie in the 4-6 day band.

C.4. Power Density.

The 4-6 day oceanic oscillation, which is clear in the coherences

*Note that in Longuet-Higgins (1966) symmetry properties refer to the stream-function, whereas symmetry properties here refer to sea surface displacement.

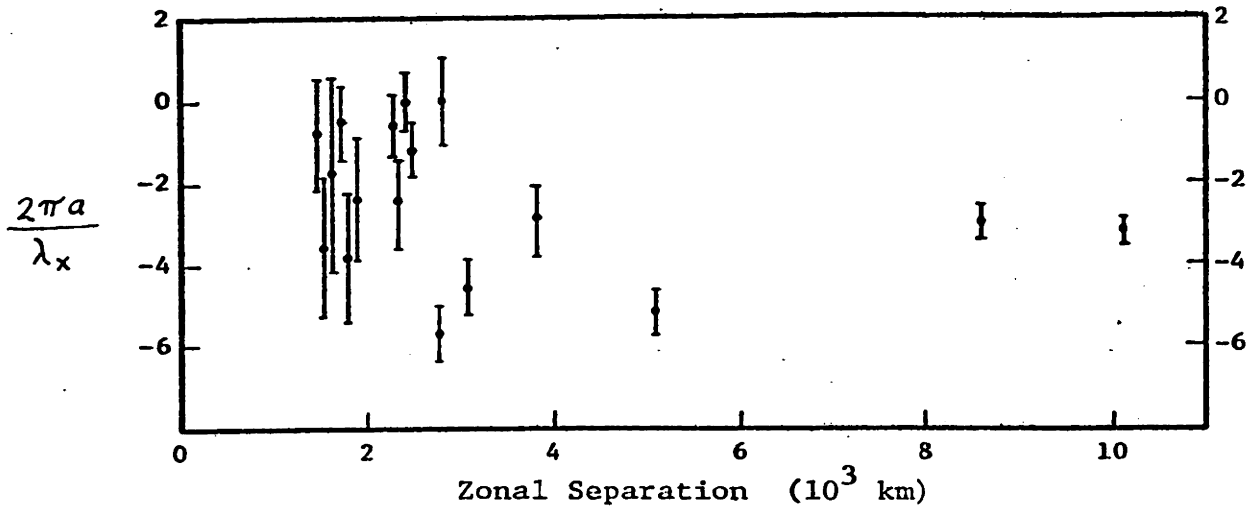
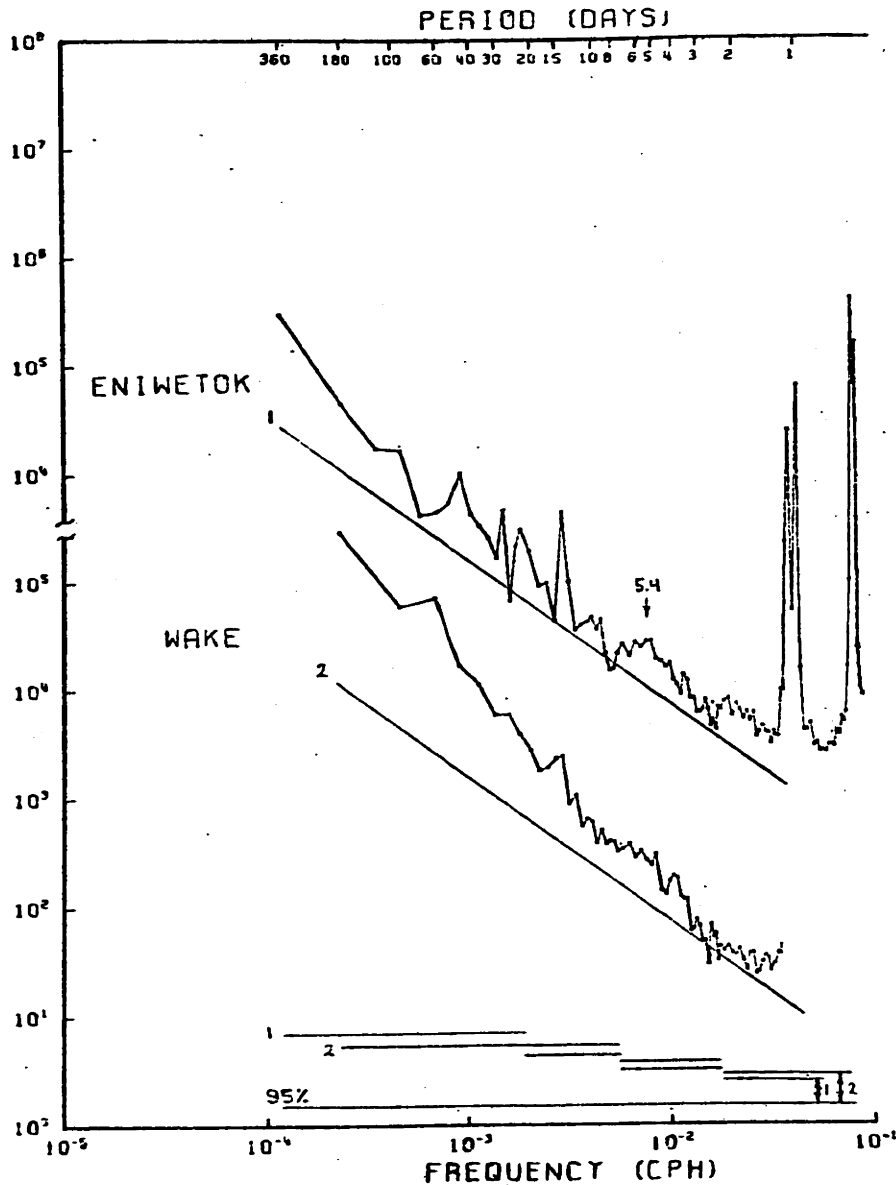


Figure 3.11 - Normalized wavenumbers, $\frac{2\pi a}{\lambda_x}$, plotted vs. zonal separation, as listed in Table 3.10. The zonal separation between two stations is defined as the difference between the station distances, measured east-west, from the 160° W meridian to the stations. The wavenumber, $\frac{2\pi}{\lambda_x}$, is computed from the sea level coherence phase in the 3.5-6.0 day band, using the zonal separation just defined.

(Figures 3.7-3.10), is difficult to detect in the power density spectra. This is an indication that dissipation has smeared the frequency response into a broader frequency range, affecting the power spectra, while the narrow-band wavenumber structure, revealed in the coherences, is unaffected. Dissipation can be expected to skew the amplitude structure so that the strongest amplitudes are in the west (Wunsch (1967)), and in fact, we find that the sea level power spectra in the West Pacific do suggest a peak around 5 days, as in Figure 3.12a, the power density spectrum of sea level from Eniwetok*. However, the sea level spectrum at nearby Wake Island (also shown in Figure 3.12a), has only a slight "plateau" at 5.4 days. Eniwetok and Wake are strongly coherent at ~5 days (Figure 3.12b).

The ~5-day "peak" at Eniwetok is not convincing evidence for the presence of oceanic waves, but, assuming it does reflect the presence of the barotropic ocean wave, the rms amplitude of the ocean wave is estimated to be 0.35 cm, using a Q of 4. (For calculating the $Q \approx \frac{\omega}{\Delta\omega}$, $\Delta\omega$ was estimated from the coherences and is certainly underestimated, so $Q=4$ is an upper bound for the oscillation.) Groves and Hannan (1968) estimated that the planetary wave energy at ~5 days period at Kwajalein and Eniwetok corresponded to an rms sea level amplitude of 0.5 cm. If we assume $\zeta = \frac{-f}{g} \Psi$ (Longuet-Higgins (1965)), where ζ is sea-level displacement and Ψ is a stream-function ($u \approx \frac{\partial \Psi}{\partial y}$ and $v \approx -\frac{\partial \Psi}{\partial x}$), then the rms current amplitude at Eniwetok associated with the planetary waves is around 0.2 cm/s, which should be detectable in kinetic energy power spectra from the deep ocean if the energy in the deep Pacific has levels similar to those found in the Atlantic during the Mid-Ocean Dynamics Experiment (Richman, Wunsch,

*It is shown in Section 3.D.12.b that the ~5-day peak at Eniwetok is definitely not due to equatorially-trapped inertia-gravity waves.



(a)

Figure 3.12 - (a) Sea level power density spectra of 7.9 years of data from Eniwetok ($11^{\circ}21'N$, $162^{\circ}21'E$) and 5.5 years of data from Wake ($19^{\circ}17'N$, $166^{\circ}39'E$). Eniwetok, with a lower background level than Wake, has a peak, albeit broad, at approximately 5.4 days, which peak is not clearly present at Wake (although there is a hump around 5 days at Wake). Plotted as in Figure 3.1.

(b) Coherence amplitude between two years of sea level data from Eniwetok and Wake, showing the expected peak at 5.4 days. The lines are drawn purely for reference with the same ordinate crossing and slope $= -4/3$. Otherwise, the plot is as in Figure 3.7.

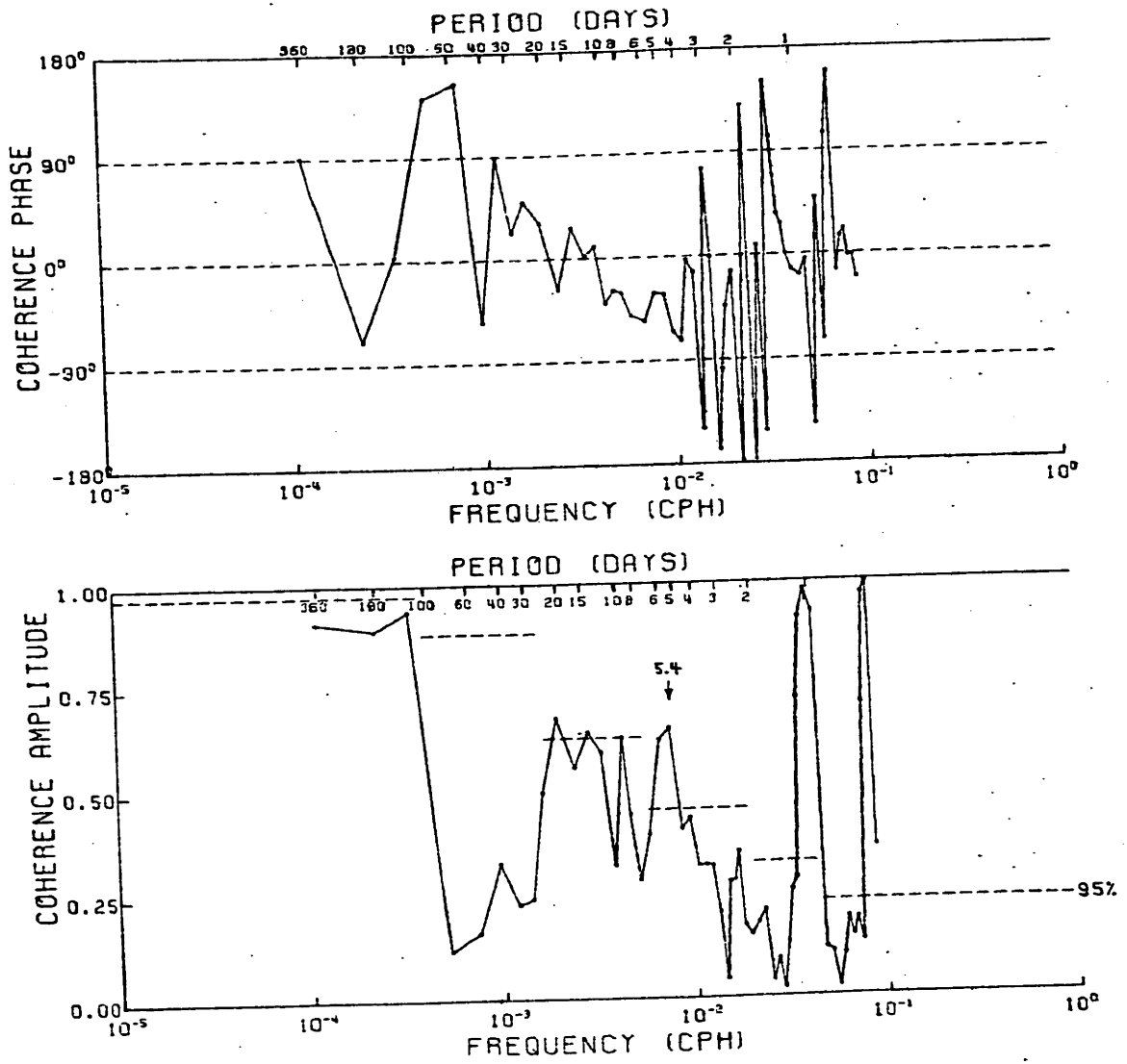


Figure 3.12b

and Hogg (1977), Figure 21b).

C.5. Conclusions and Discussion. We have shown that a 4-6 day, non-static oscillation of sea level exists in the Pacific Ocean. The basin-wide character of the oscillation implies that it is barotropic. The large coherence length of the oscillation suggests narrow wavenumber bandwidths; or, since the oscillation can be described as a summation of the normal modes of the basin, the large coherence length implies the presence of only a small number of modes. Since no nodes were found anywhere in the basin, the gravest symmetric planetary mode is probably the only basin mode that is significantly excited. The observed westward propagation further supports the suggestion that a barotropic, planetary mode of the Pacific basin is present at 4-6 days. To give the reader a rough idea of the horizontal structure of this 4-6 day oscillation, we present in Figure 3.13 the surface displacement of the gravest, symmetric planetary mode of a flat-bottomed hemispherical basin. Figure 3.13 is taken from Christensen (1973a), who computed the gravest planetary eigenfunctions for a hemispherical ocean 4 km deep, using procedures outlined by Longuet-Higgins and Pond (1970).

It seems more than coincidental that the observed 4-6 day oceanic oscillation has nearly the same theoretical meridional structure (Figure 3.13) as the ~5-day barotropic atmospheric wave (Figure 2.9c), which is clearly forcing the oceanic wave (Section C.1). We suggest that the similarity of the meridional structures of oceanic and atmospheric modes produces larger oceanic amplitudes than would occur if the forcing was completely random. (Remember that the oceanic oscillation has a low Q , i.e., that it is strongly damped.)

With regard to the study of equatorially-trapped waves, it is impor-

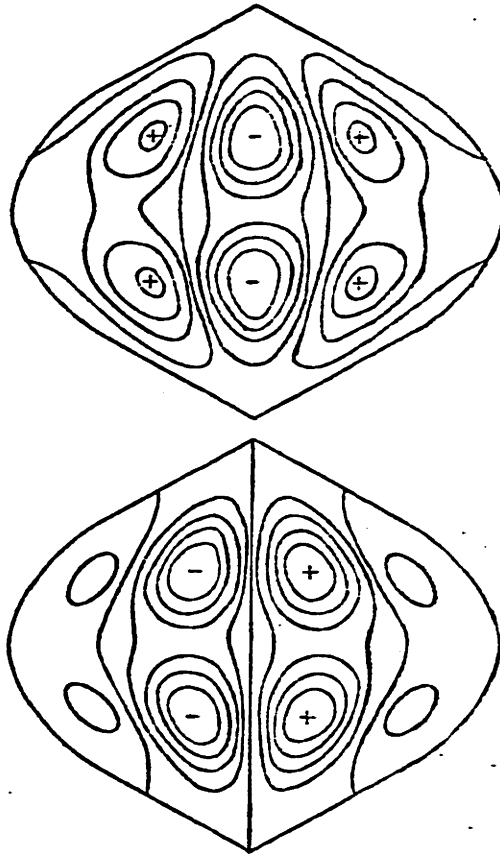


Figure 3.13 - Surface displacement eigenfunction for the gravest, symmetric planetary mode of a hemispherical basin centered on the equator. Depth= 4km. Upper: real part. Lower: imaginary part. (Taken from Christensen (1973a; Figure 1)).

tant to note that this planetary mode dominates the 4-6 day sea level coherence in the eastern equatorial Pacific (see Figures 3.8b and 3.9b) and western equatorial Pacific (see Figures 3.8a and 3.9a), and the mode may contaminate the wavenumber estimates of the equatorial inertia-gravity waves in the central Pacific.

A final point is that Figure 3.10 suggests the presence of at least one additional oscillation, at 3 days period. Although the 3-day coherence peak is not always present (Figures 3.7 and 3.8), the coherence amplitude between Midway and Johnston is so large (Figure 3.14) that the possibility of a planetary mode, perhaps topographically trapped (see Platzman (1975)), is worth further investigation.

D. Observations and Models of Equatorial Inertia-Gravity Waves

In 1976, Wunsch and Gill presented evidence demonstrating that the 3-, 4-, and 5-day peaks in equatorial Pacific sea level spectra (Figure 3.1) are manifestations of first-baroclinic inertia-gravity waves. They argued that the ocean is in resonance near the frequency where the zonal group velocity is zero for each meridional mode (that is, where $\sigma_s = -1/2$ in Figure 1.1). The validity of Wunsch and Gill's (hereafter, WG) conclusions are re-examined in this section, with a view toward extending our knowledge of the kinematics and dynamics of inertia-gravity waves near the equator. Re-examination is possible because: (1) we have a priori knowledge of the existence of a barotropic oscillation at ~5 days, which could have misled the study; (2) the temporal and spatial coverage of this dataset far exceeds that examined by WG; and (3) we have improved knowledge of the frequency-wavenumber spectra of the surface winds that directly generate at least part of the inertia-gravity wave spectrum.

The presentation of results is simplified by assuming the WG con-

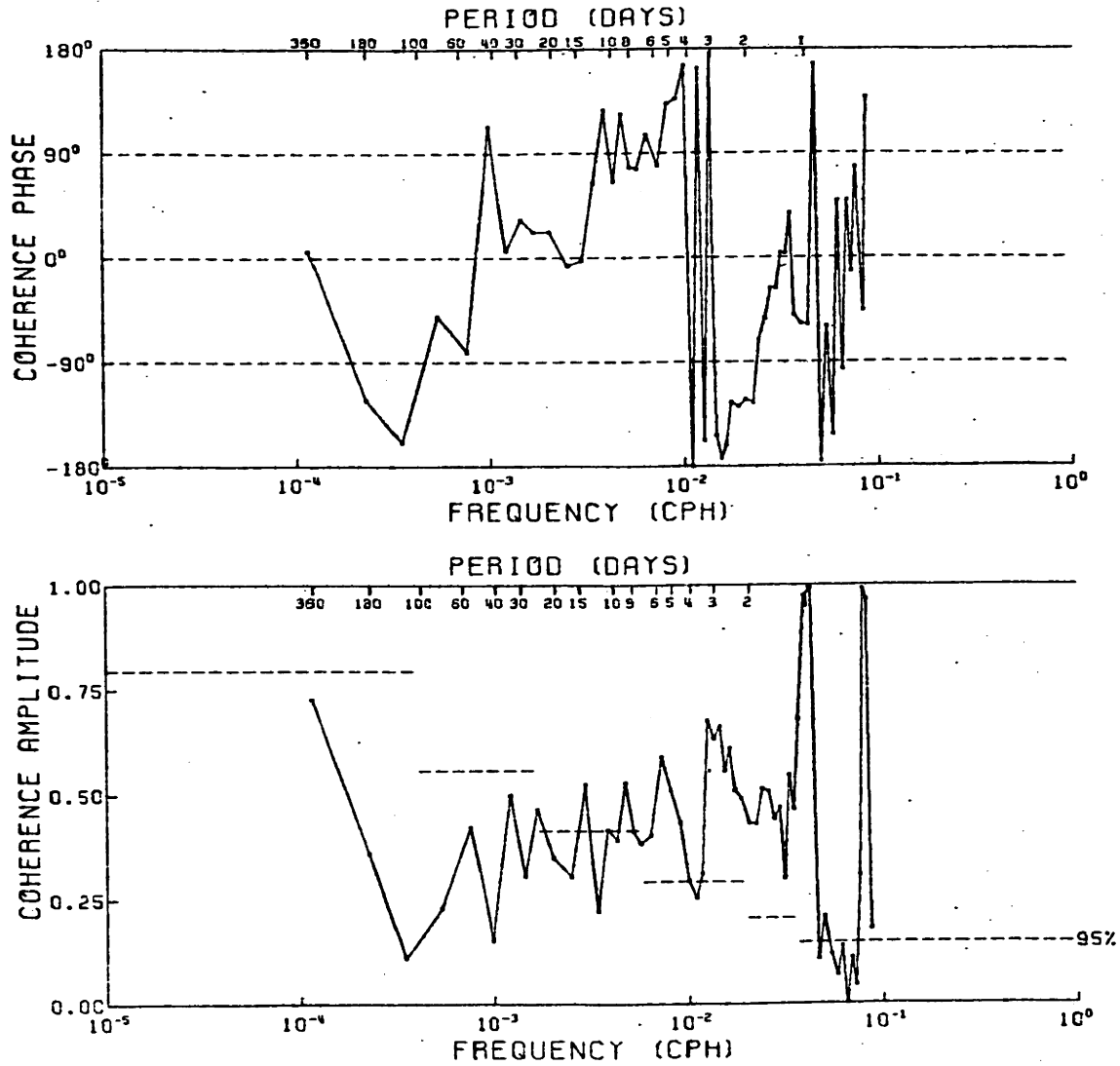


Figure 3.14 - Coherence amplitude and phase between 5 years of sea level from Midway ($28^\circ 12' N$, $177^\circ 22' W$) and Johnston ($16^\circ 45' N$, $169^\circ 32' W$), showing a rather large peak at 3 days with a phase of 180° . (The large background level between 1 and 2 days is unusual and not understood.) Positive phase indicates that Midway leads. The 95% level of no significance is indicated for the amplitude.

clusions are working hypotheses to be tested. Specifically, we consider the following hypotheses: (1) the ocean is in resonance, that is, vertical and meridional modes have been established; (2) energy is concentrated (without specification of cause) in the neighborhood of the frequency-wavenumber points where the theoretical zonal group velocity vanishes; and (3) peaks occurring in the tropical sea level spectra, in accordance with (1) and (2), are first-baroclinic modes (that is, for the moment we assume only the first baroclinic mode produces substantial sea level deflections above the background "noise" level).

The first test of the hypotheses (Section 3.D.1) is whether or not the observed peaks in Pacific sea level spectra correspond to the periods predicted from the linear theory. The theoretical predictions require knowledge of the baroclinic "equivalent depths", which are obtained numerically using vertical profiles of mean buoyancy frequency. The agreement between theory and observations is good. However, in Section 3.D.2, we demonstrate that inertia-gravity wave energy is not uniformly distributed along the equator in the Pacific, indicating the importance of processes ignored in the simple theory, such as topographic dispersion, reflections from meridional boundaries and/or longitudinal variations in the forcing. This zonal variability precludes the possibility that a "universal" spectrum might describe the energy distribution of low-mode equatorial inertia-gravity waves.

Testing the hypotheses further, the observed meridional variation of the power density for the two gravest meridional modes in the Pacific is compared with theory (Section 3.D.3). Given the success of this comparison and that in Section 3.D.1, higher modes can be identified in the most energetic subsets of the Pacific data (Section 3.D.4). It is sug-

geste that the Pacific equatorial sea level spectra, from periods slightly longer than the diurnal tides to the three day period, are dominated by baroclinic inertia-gravity waves. The scanty Indian Ocean observations are examined for inertia-gravity waves in Section 3.D.5.

Unlike measurements of current and vertical displacement below the sea surface, the filtering effect of the sea level observations enables the estimation of zonal wavenumber bandwidths (Section 3.D.7) from sea-level cross-spectra without substantial contamination from the higher vertical modes. Before computing the wavenumber bandwidths, the possible sea level expressions of the higher vertical modes are computed in Section 3.D.6 for an exponential Brunt-Väisälä profile underlying a homogeneous mixed-layer.

Inertia-gravity wave energy is stationary over a long period of time, but typical stochastic fluctuations of the wave field can produce disturbingly dissimilar spectra from consecutive years (Section 3.D.8).

Frequency bandwidths of the sea level peaks for each meridional mode are estimated in Section 3.D.9. One of the possible explanations of the bandwidths is that the width mirrors atmospheric forcing (a non-oceanic-resonance hypothesis). This possibility is examined in detail in Section 3.D.10, where evidence of atmospheric forcing (or lack thereof) for each mode is presented and the dynamics of the air-sea coupling are briefly discussed.

The properties of inertia-gravity waves in the Pacific, as found in this study, are summarized in Section 3.D.11, where the arguments for and against oceanic resonance are explicitly enumerated. As further evidence that the simple linear theory of inertia-gravity waves explains the observed spectra, an energy spectral model is created, using the

sea-level spectrum from a single island, to predict the sea-level spectra at other islands (Section 3.D.12). The arbitrariness of choices of frequency-wavenumber dependences in the model is emphasized, as are the differing dynamical arguments underlying the specification of the "low"-frequency equatorial internal wave spectrum versus the "high"-frequency mid-latitude internal wave spectrum. It would be useful to take the modelling a step further and attempt to produce the sea level spectra from the forced linear equations using the observed frequency-wavenumber spectra (Chapter 2) of the surface atmospheric fields. To do this would require including both dissipation and some model of the boundary-layer coupling between surface wind stress and the oceanic waves, a more extensive effort than is feasible for the present investigation.

D.1. Identification of Pacific Sea Level Spectra Peaks as Inertia-Gravity Waves by Comparing Observed and Predicted Periods. The Pacific sea-level spectra that exhibit peaks in the 3-5 day range, which are suspected to be due to inertia-gravity waves, are shown in Figures 3.15a and 3.15b. The spectra have been arranged according to the volume of data available at each station, as indicated. The straight lines have slopes of $-4/3$ and identical y-intercepts and are intended as references for comparing spectral levels and shapes. Frequency-band averaging has been adjusted so that the resolution in the inertia-gravity wave band is nearly identical for each spectrum.

Whether a peak occurs for a given meridional mode at any island should depend upon the energy in the mode and the latitudinal structure of the mode (see equations (1.27b) and (1.28)). [Remember that at this point we are assuming only the first baroclinic mode will substantially affect the sea level observations.] Consequently, meridional mode identification

Figure 3.15 - Sea level power density spectra with probable inertia-gravity peaks. Numbers in parentheses beneath the station names are the data lengths in years. The straight lines are solely intended to aid intercomparison. The inclined lines have a $-4/3$ slope. The long-period tides, Mf and Mm, are indicated for Canton. Otherwise, plotted as in Figure 3.1.

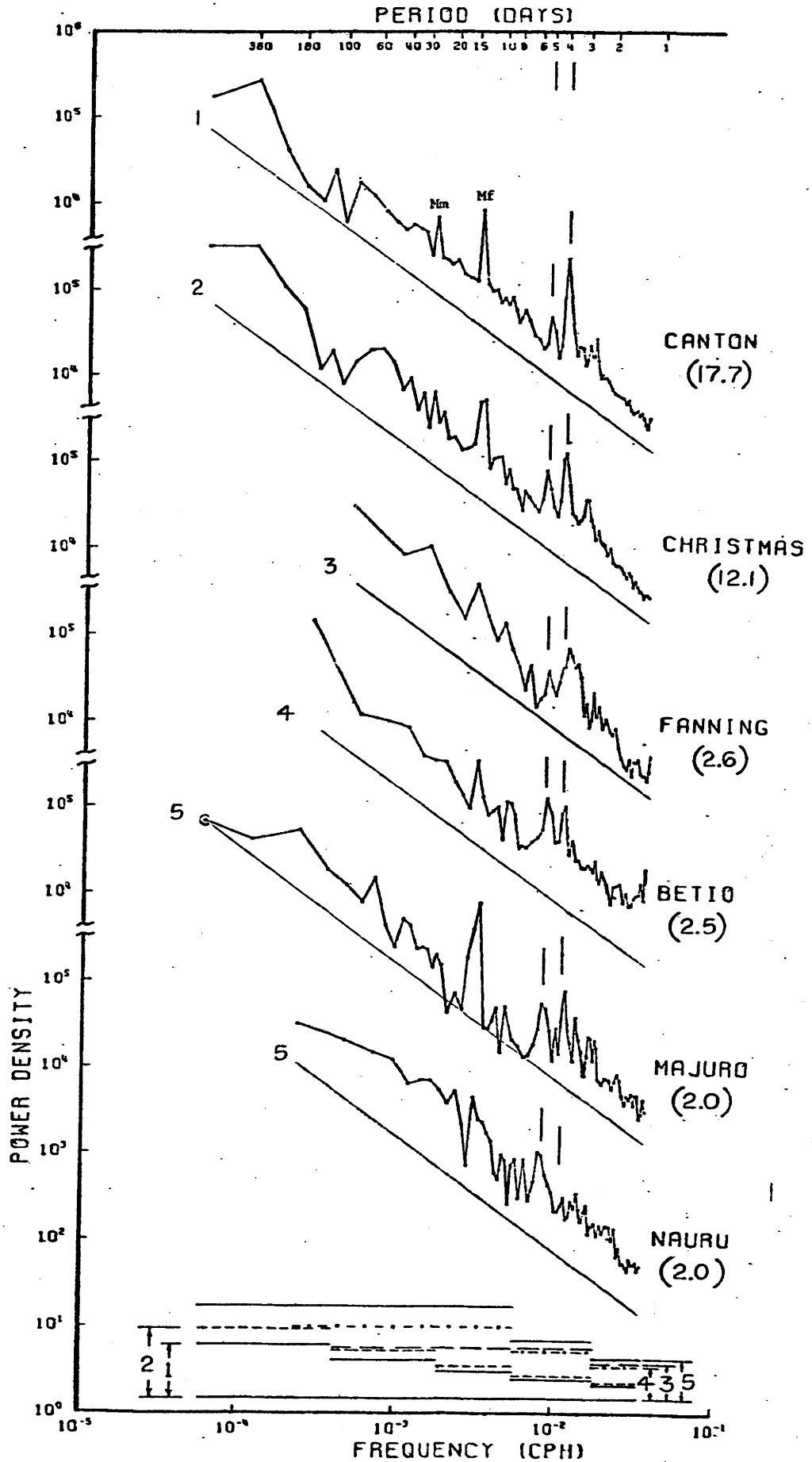


Figure 3.15a

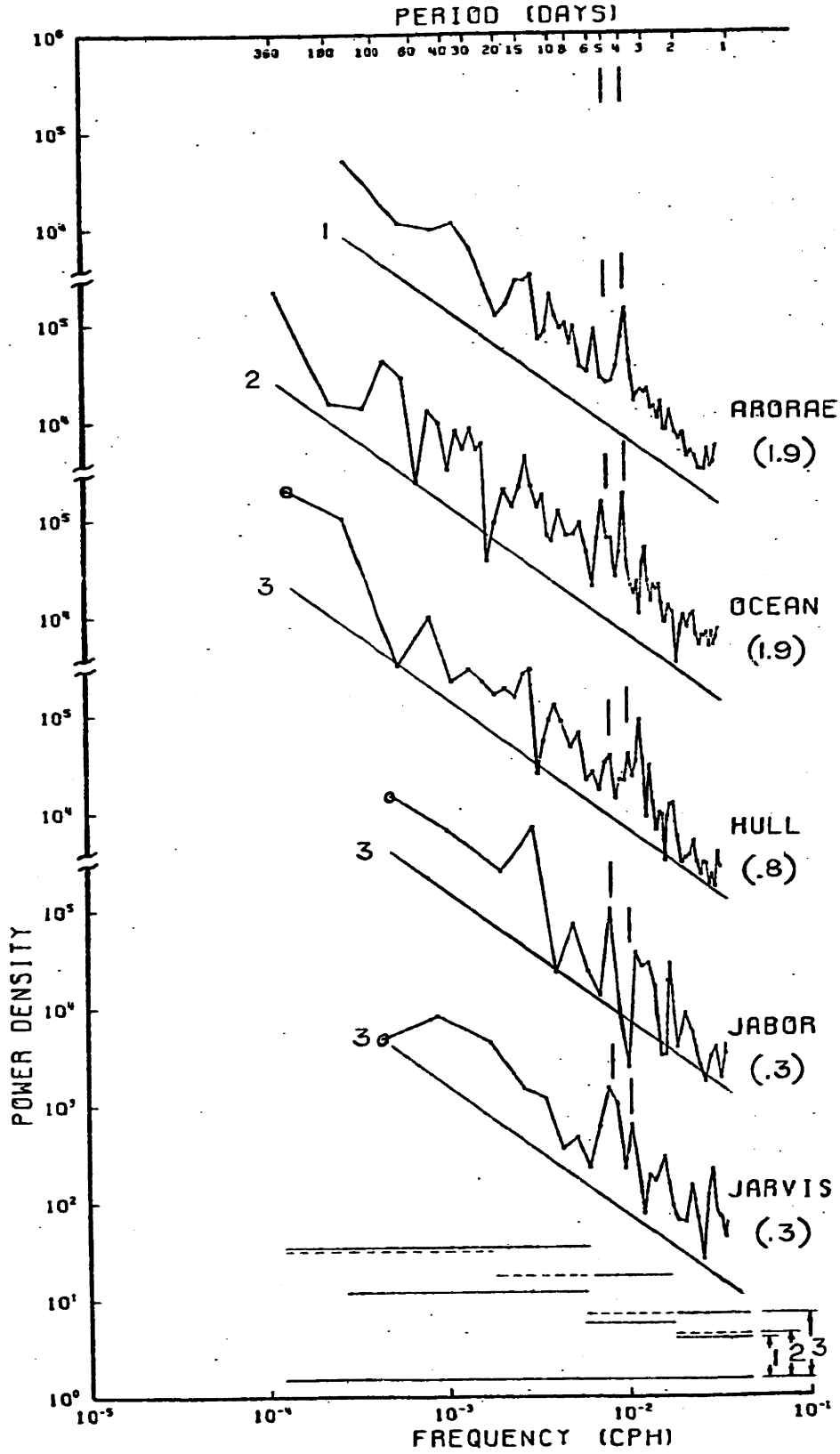


Figure 3.15b

may seem arbitrary, since a peak may be strong at one island and not exist at another. The criterion used is the rather obvious one (for the gravest modes) of identifying the mode number of a peak by its proximity in frequency to a predicted peak.

The predicted peak periods are hypothesized to occur where the zonal group velocity (c_{gx}) is zero for each meridional mode; that is, where $\sigma_s = -1/2$ (Figure 1.1). Using (1.33b), the predicted periods (in days) are, for baroclinic mode r and meridional mode n ,

$$T_{r,n} = \frac{\epsilon_r^{1/4}}{2} \left[n + 1/2 + \sqrt{n^2 + n} \right]^{1/2}, \quad \begin{matrix} n=1,2,\dots \\ r=1,2,\dots \end{matrix} \quad (3.6)$$

where $\epsilon_r = \frac{4\Omega^2 a^2}{gh_r}$ and is determined from the vertical structure equation (1.17). We could arbitrarily choose ϵ_1 to match one predicted peak with one observed peak at each island, then determine whether the remaining observed peaks correspond to prediction (à la WG). However, if ϵ_1 can be estimated independently we will have a more meaningful test of the simple linear theory, since it has been shown (McPhaden and Knox (1979)) that strong shears in the equatorial currents can alter the periods of the group velocity zeros (as well as the meridional structures) of the inertia-gravity waves.

Estimates of ϵ_1 have been obtained by a method that is sufficiently novel, and perhaps controversial, that it deserves a few comments here. Bell, Mays and deWitt (1974) have produced profiles of the Brunt-Väisälä frequency at standard depths to 500 meters, using σ_t observations from the NODC archives, averaged over 5° squares for each of the four seasons. An exponential tail was appended to these Brunt-Väisälä profiles and h_1 (and ϵ_1) were computed using a numerical solution to the Boussinesq form of (1.17) (the program was written by James Richman). Ocean depths for each

5° squares were estimated from topographic charts and the e-folding depth was always 1.3 km (à la Garrett and Munk (1972)). The assumption here is that by far the most important horizontal variations in density, those which will cause horizontal variations in ϵ_1 , occur in the top 500 meters, which includes the entire thermocline near the equator. The computations showed an increase of c_1 ($c_1 = \sqrt{gh_1} = \frac{2\Omega a}{\sqrt{\epsilon_1}}$) near the equator from ~ 2.30 m/s at 90°W to a maximum of ~ 3.00 m/s at 180°, declining to ~ 2.60 m/s at 140°E. The speed c_1 increases poleward from the equator, in accordance with the deepening of the thermocline, which slightly strengthens the equatorial trapping of the inertia-gravity waves. [From Richman et al. (1977), $c_1 \approx 3.27$ m/s in the MODE region of the Atlantic.]

The estimates of ϵ_1 for the 5° squares containing each of the island stations were used in the computation of the inertia-gravity peak periods. More sophisticated schemes of weighting the density field with the meridional structure functions are not warranted with the coarsely-sampled density field at hand.

One can imagine that this scheme of estimating ϵ_1 is subject to several sources of error. Many 5° squares had no observations at all, others had all their observations concentrated in one season (collected by one ship during one year?). Little can be done about the sampling density except to note the number of observations used to compute each buoyancy profile. The computation is not very sensitive to either the e-folding distance or the ocean depth.

Table 3.11 lists the observed periods of the suspected inertia-gravity peaks for the islands in Figure 3.15, with more than six months of data. The predicted periods found from (3.6), using Bell et al.'s (1974) data to obtain ϵ_1 for each island, are also listed. The comparison identifies

TABLE 3.11 - Observed and Predicted* Periods of Inertia-Gravity
Sea Level Peaks

		NPTS**	Periods ⁺ (days) for Mode No. n					Eigenvalues [#]	
			1	2	3	4	5	$\sqrt{\epsilon_1}$	c.
Canton	Sea Level	17.7	5.06 ±.15	3.95 ±.10	3.30 ±.06	2.92 ±.05	2.66 ±.04	306	3.03
	Density	28	5.24	4.02	3.39	2.99	2.70	320	2.90
Christmas	Sea Level	12.1	5.33 ±.15	4.04 ±.10	NP	2.99 ±.05	NP	325	2.85
	Density	42	5.35	4.11		3.05		334	2.78
Fanning	Sea Level	2.6	5.12 ±.15	##	##	NP	NP	306	3.03
	Density	42	5.35					334	2.78
Betio	Sea Level	2.5	5.08 ±.15	3.92 ±.10	NP	NP	NP	303	3.06
	Density	146	5.17	3.96				311	2.98
Majuro	Sea Level	2.0	5.33 ±.15	3.78 ±.08	3.24 ±.05	2.75 ±.04	2.53 ±.04	294	3.16
	Density	63	5.40	4.14	3.49	3.08	2.78	340	2.73
Nauru	Sea Level	2.0	5.23 ±.15	NP	NP	NP	NP	319	2.91
	Density	87	5.22					318	2.92
Arorae	Sea Level	1.9	5.76 ±.22	3.87 ±.10	NP	NP	NP	297 [@]	3.12
	Density	21	5.15	3.95				309	3.00
Ocean	Sea Level	1.9	5.27 ±.15	4.04 ±.10	NP	3.04 ±.06	NP	326	2.85
	Density	87	5.22	4.01		2.98		318	2.92
Hull	Sea Level	0.8	5.09 ±.15	3.90 ±.10	3.37 ±.07	2.97 ±.05	NP	309	3.00
	Density	28	5.24	4.01	3.39	2.99		320	2.90

* Predicted periods are calculated using equivalent depths from numerical solutions to the vertical structure equation, with the observed density field to 500 meters (see text).

** NPTS is number of years for sea level data and number of profiles for density data.

+ Periods for sea level data are approximate (center) periods of observed peaks. NP = No Peak observed.

$\sqrt{\epsilon_1} = 2\Omega a/c$, where $\Omega = 7.2722 \times 10^{-5} \text{ s}^{-1}$, $a = 6.378 \times 10^6 \text{ m}$, $c = \sqrt{gH}$, $g = 9.81 \text{ m/s}^2$.

Second and third mode peaks at Fanning appear smeared together.

@ The period of the n=1 mode is abnormally high and is excluded from the calculation of $\sqrt{\epsilon_1}$.

the suspected meridional mode number for each observed peak thus allowing computation of an average ϵ_1 , also listed, from the observed peaks. Considering the rough approximation to the density field, the agreement between the periods of the observed peaks and the periods predicted from (3.6) is remarkably good. The serious disagreements are at Fanning, Majuro and Arorae. The Fanning observations are surprising, considering the results for nearby Christmas. It is possible that the density field during the Fanning sea level observations differed substantially from the density field estimate used here. The same may be true for Majuro and Arorae, although for these islands topography may also be a factor. Notice, however, that Betio, which is between Majuro and Arorae, shows no significant discrepancy between observed and predicted periods.

It is worth mentioning that, independent of modal interpretation, the shortest period peaks in the Canton and Christmas spectra, 2.66 and 2.99 days, respectively, are significant at the 95% level, as first found by Groves and Grivel (1962) at Canton.

D.2 Zonal Variations of Inertia-Gravity Wave Energy in the Pacific.

Figure 3.16 shows the sea level spectra from three islands near 7°N and three islands near the equator. The spectra demonstrate a reduction in the amplitudes of the low-mode inertia-gravity waves in the east Pacific and west of the Marshall Islands. Each group of stations was chosen to minimize amplitude variations due to the meridional structures of the inertia-gravity waves. In addition, the Majuro and Ponape, and Christmas and Galapagos, datasets used to construct Figure 3.16 were chosen to be cotemporal to avoid amplitude variations that might be expected for a stochastic process over short periods of time. Note that the background levels are nearly identical for all the spectra in the inertia-gravity

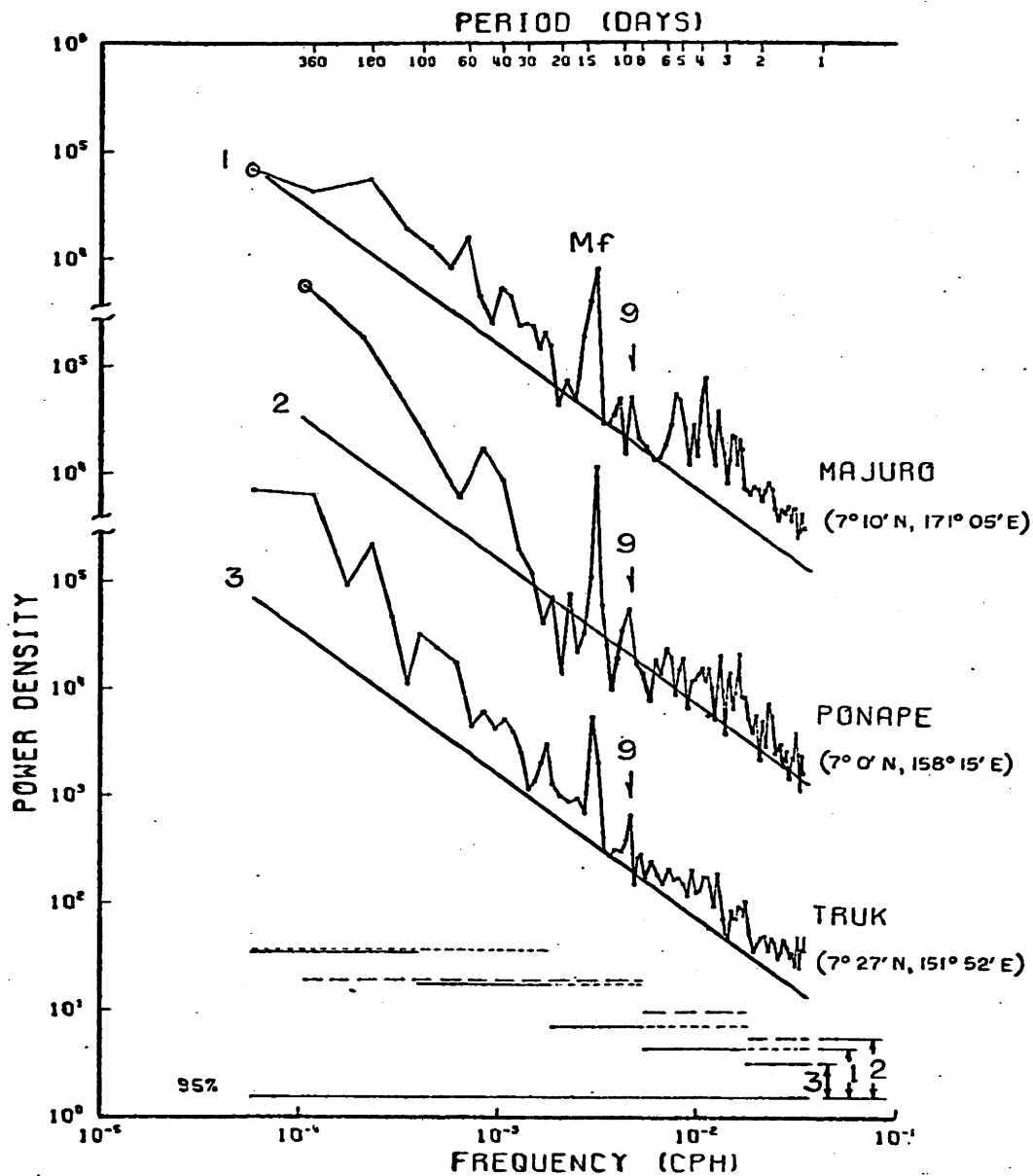


Figure 3.16a

Figure 3.16 - Sea level power density spectra from selected stations showing zonal variation in inertia-gravity wave energy. The Christmas record is edited to correspond with the time of the Galapagos data. Reference lines have a $-4/3$ slope. The 9-day tide is indicated in (a) with an arrow. Otherwise, plotted as in Figure 3.1.

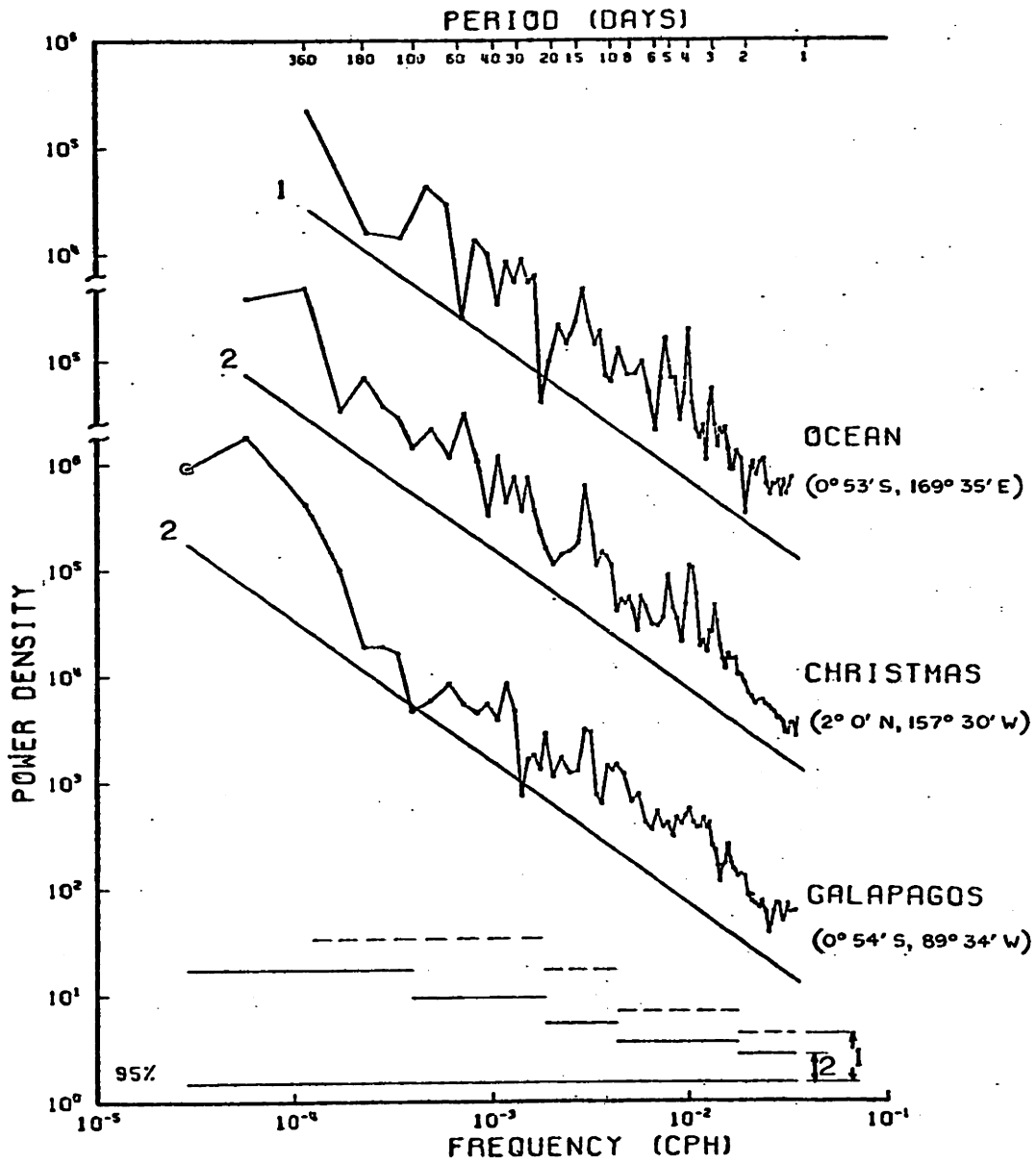


Figure 3.16b

band, removing the possibility that fluctuations in the "noise" level account for the lack of peaks at Galapagos, Ponape and Truk.*

On the other hand, kinetic energy spectra computed from observations by Harvey and Patzert (1976), taken 500 km due west of the Galapagos Islands, have "peaks" in the 4-5 day band (Patzert, personal communication, 1978). The records are too few (2 current meters) and too short (~2 months) to identify first-baroclinic inertia-gravity waves.

Additional evidence of the absence of a strong 4-5 day inertia-gravity signal at Truk and Galapagos was found in Section 3.C, where it was shown that sea level at both islands is coherent with atmospheric pressure at 4-6 days. We concluded that the sea level energy at both islands at 4-6 days is probably due to a barotropic planetary mode of the Pacific basin.

The zonal variability of inertia-gravity wave energy, found above for the Pacific, indicates that a "universal" spectrum of equatorial inertia-gravity waves does not exist for the lowest modes. More important, the zonal variability suggests a significant change in the dynamics of equatorial inertia-gravity waves as a function of longitude. Topography, meridional boundaries and zonal variations of the atmospheric forcing functions may each contribute to the observed variability. For instance, the East Pacific Rise and the Solomon Rise may inhibit vertical mode formation and/or efficiently scatter low-mode energy into higher vertical modes.

*The Majuro spectrum exhibits an excess of energy in the $n=1$ (~5-day) and $n=2$ (~4-day) modes when compared with a simple model spectrum (Section 3.D.12). This does not alter our conclusions about zonal variations of inertia-gravity wave energy.

D.3 Meridional Structure of the Gravest Inertia-Gravity Modes in the Pacific. Following WG, we will compare the meridional distribution of power obtained from the sea level spectra for the two lowest meridional modes with the theoretical expressions, from (1.27) and (1.28):

$$|\mathcal{J}|_{r,n}^2 = \frac{c_r^2 \epsilon_r^{1/2} |V_c Z(0)|^2}{g^2 \bar{\rho}^2(0)} \left[\frac{H_{n+1}/2}{\sqrt{\epsilon_r} \sigma - s} - \frac{n H_{n-1}}{\sqrt{\epsilon_r} \sigma + s} \right]^2 e^{-\epsilon_r^{1/2} \theta^2}, \quad (3.7a)$$

where r equals 1 for the first baroclinic mode. The appearance of the factor $c_r^2 (=gh_r)$ in (3.7a) indicates that the sea level power is more dependent upon the equivalent depth than $|u|^2$ or $|v|^2$, which, using (1.22), (1.25) and (1.27a), are:

$$|u|_{r,n}^2 = \frac{\epsilon_r^{1/2} |V_c Z(z)|^2}{\bar{\rho}^2(z)} \left[\frac{H_{n+1}/2}{\sqrt{\epsilon_r} \sigma - s} + \frac{n H_{n-1}}{\sqrt{\epsilon_r} \sigma + s} \right]^2 e^{-\epsilon_r^{1/2} \theta^2}, \quad (3.7b)$$

$$\text{and } |v|_{r,n}^2 = \frac{|V_c Z(z)|^2}{\bar{\rho}^2(z)} H_n^2 e^{-\epsilon_r^{1/2} \theta^2}. \quad (3.7c)$$

To demonstrate this point, $|\mathcal{J}|_{1,2}^2$, $|u|_{1,2}^2$ and $|v|_{1,2}^2$ are plotted in Figure 3.17 for two values of c_1 (ϵ_1), where the currents have been evaluated at $z=0$, $Z(0) \equiv \bar{\rho}(0)$, and σ and s correspond to the zonal group-velocity zero point. Because of the strong dependence of $|\mathcal{J}|_{1,2}^2$ on c_1 , the sea level observations are normalized using the observed eigenvalues in Table 3.11 before comparison with the theoretical structure functions computed using $c_1 = 3.00$ m/s.

Due to the existence of a 5-day barotropic planetary mode in the Pacific (Section 3.C), and since we have shown that the lowest-mode inertia-gravity wave energy is weak in the East Pacific and west of the Marshall Islands, only those stations with more than four months of data

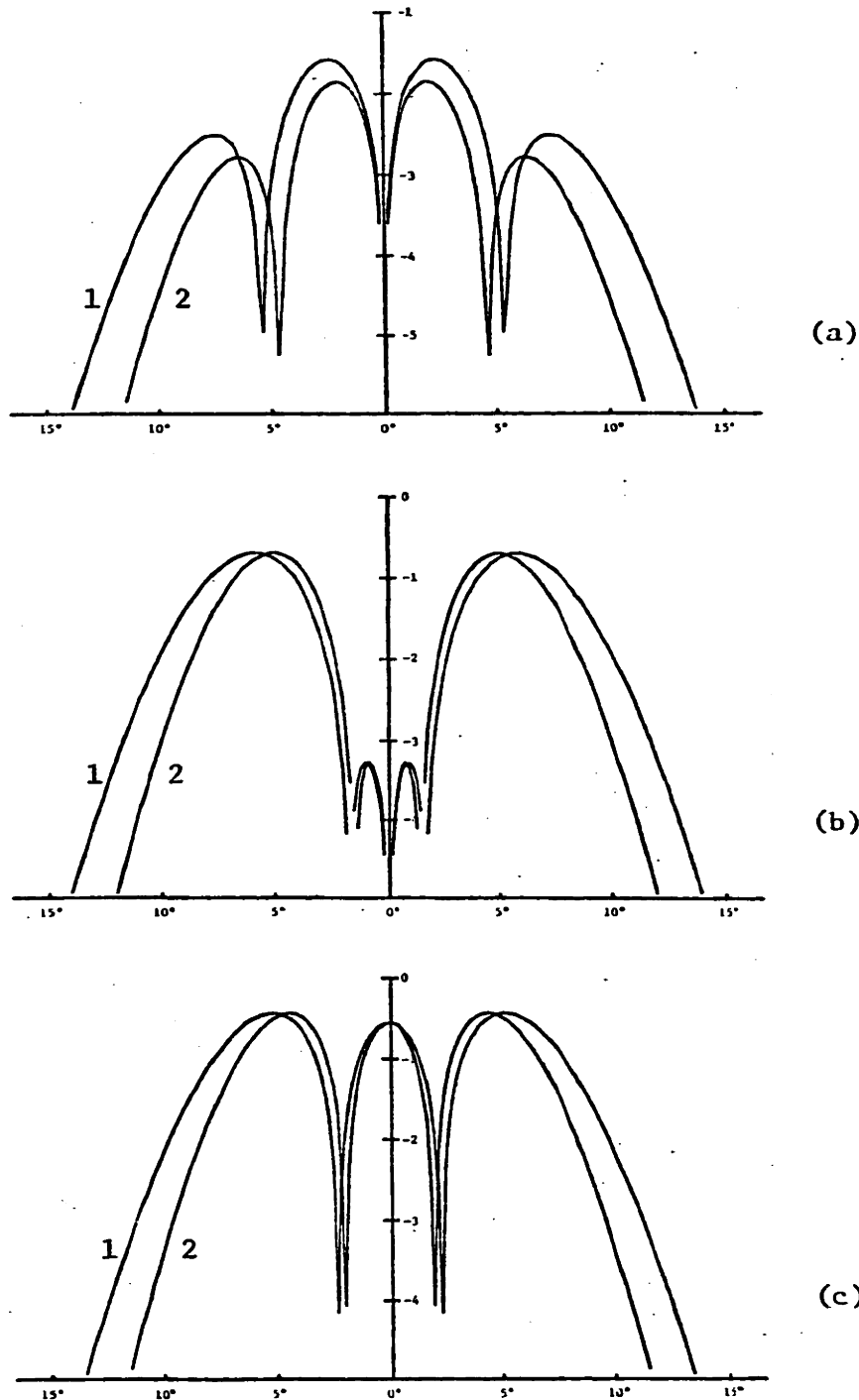


Figure 3.17 - Theoretical meridional structures of (a) J^2 , (b) $u^2|_{z=0}$, (c) $v^2|_{z=0}$ for the second-meridional, first-baroclinic inertia-gravity mode, using two values of the first-baroclinic equivalent depth. The larger value, $h_1 = .92$ m (#1 in figures), is typical of the central equatorial Pacific, and the smaller value, $h_1 = .49$ m, is typical of the eastern equatorial Pacific. The abscissa is latitude and the ordinate is $\log(\text{cm}^2)$ for (a) and $\log((\text{cm/s})^2)$ for (b) and (c).

in the "mid-Pacific", defined as the zone within 10° of the equator between 150°W and 160°E , are used in the present comparison with theory. This "mid-Pacific" region includes Kwajalein and the stations in Figure 3.15 except that Jarvis is excluded for lack of data. The inclusion of Kwajalein sea level, already shown to be influenced by the 5-day barotropic oscillation, serves to emphasize the large amplitudes of the equatorial inertia-gravity waves.

To obtain estimates of the sea level power in the inertia-gravity modes, some statement about the background continuum is necessary. The background level between 1 and 14 days is fairly uniform across the "mid-Pacific", with some slight regional differences, such as the weakening of the background in the Marshall Islands seen in Figure 3.18a where the sea level spectrum of Majuro is superimposed on Canton's spectrum. The remarkably similar spectra from Canton and Christmas (Figure 3.18b), which have by far the longest datasets, led to a choice of representation of the background level in the "mid-Pacific" of the form $A\omega^{-3/2}$, where ω is frequency in cycles/hour. The function $A\omega^{-3/2}$ is plotted in Figure 3.18b for $A=.17$. This background level is subtracted from each of the "mid-Pacific" sea level spectra before estimating the power in the inertia-gravity modes, to avoid the introduction of "spurious" meridional structure due to differences in the background levels from station to station, as pointed out by WG. It should be noted that there are significant variations in the background levels of tropical sea level spectra outside the "mid-Pacific" regions, as can be seen in Figure 3.18c where the sea level spectrum from Johnston (see Figure 3.2b) is superimposed on Canton's spectrum. The variability in Figure 3.18c is not the result of stronger atmospheric pressure fluctuations, which dominate sea level at mid-latitudes (Wunsch

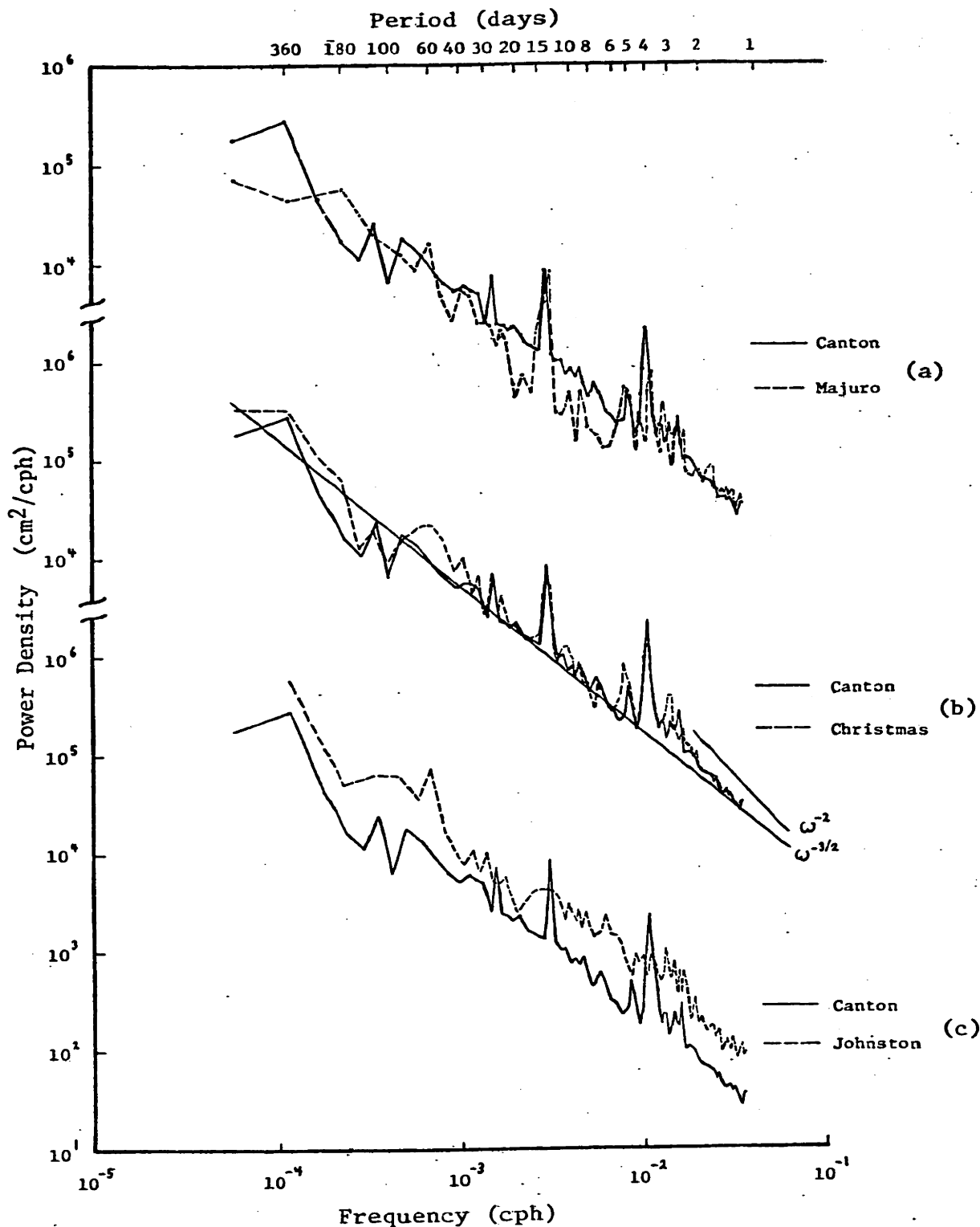


Figure 3.18 - (a) Comparison of sea level spectra from Canton and Majuro illustrating the lower background level typical of the Marshall-Caroline Islands region. (b) Comparison of sea level spectra from Canton and Christmas showing remarkable similarity even though the stations are over 1500 km apart. Straight lines are discussed in text. (c) Comparison of sea level spectra from Canton (2°14'S, 171°40'W) and Johnston (16°45'N, 169°32'W) showing that large variations in the sea level spectra can occur over distance 0(2000 km) in the tropics. Spectra are plotted as in Figure 3.1.

(1972)), but can be shown to be due to fluctuations in the surface wind.

The theoretical structures (equation (3.7a)) of the two gravest meridional modes for the first baroclinic mode are plotted in Figure 3.19, where $c_1=3.00$ m/s and σ and s correspond to the zero zonal group-velocity point. Superimposed on the theoretical curves are normalized estimates of the power obtained from sea level spectra of stations in the "mid-Pacific" with more than four months of data. The choice of the amplitude, V_c , of each theoretical mode is somewhat arbitrary. Emphasis was placed on matching the most reliable observations, that is, Canton and Christmas, with the theoretical curves. The results are satisfactory since there are few observations which differ from the theoretical curves by more

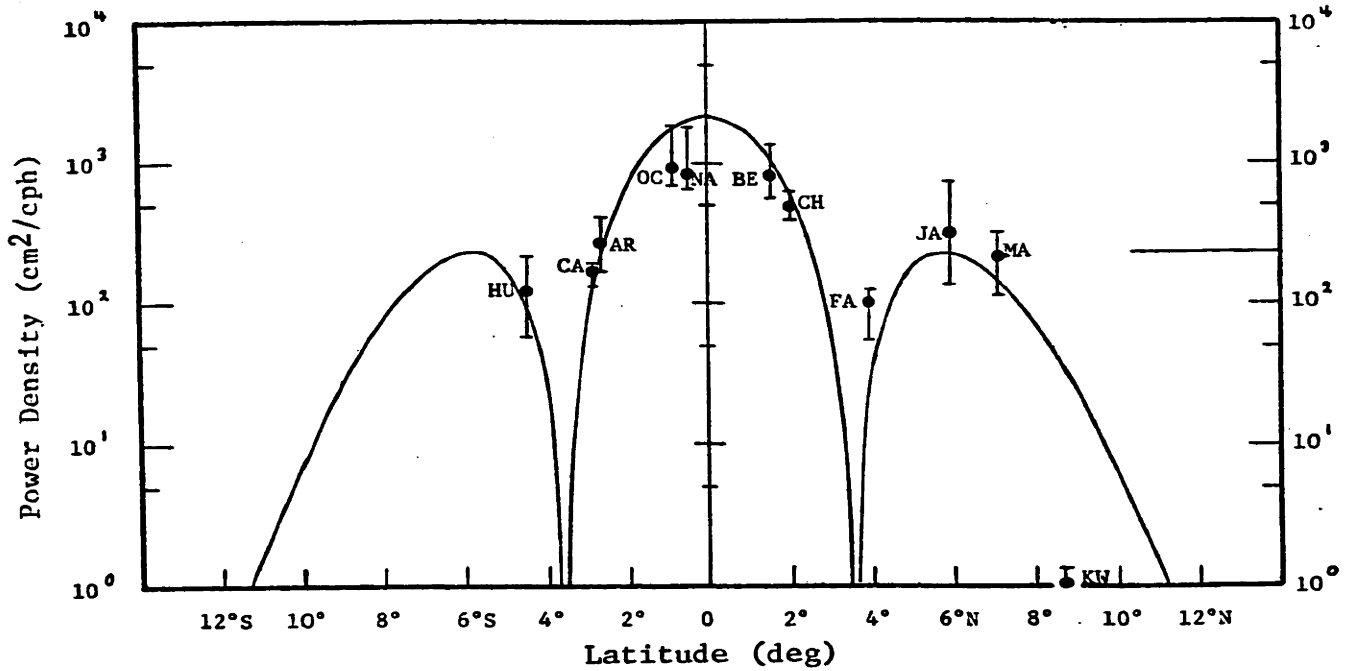
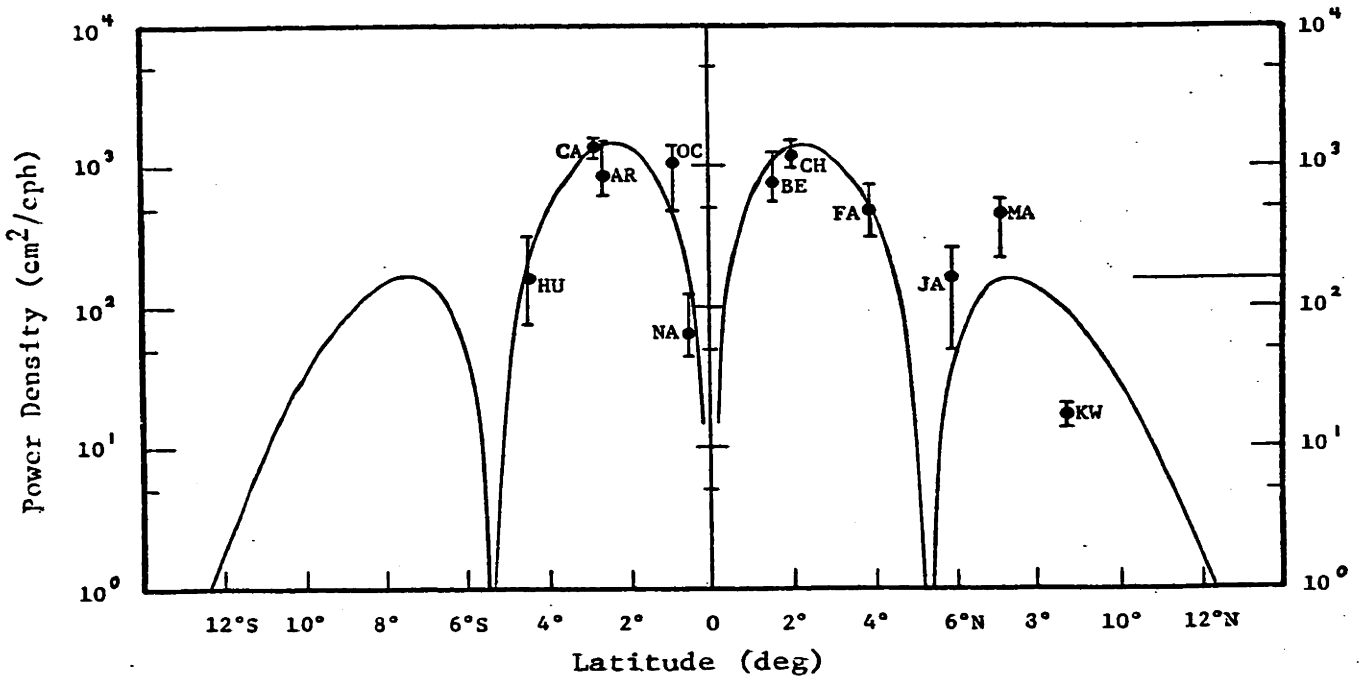
(a) $n=1$ mode(b) $n=2$ mode

Figure 3.19 - Comparison of the observed spatial distribution of sea level power, at 4 and 5 days, with theory. Power density estimates are averages over peak-centered bands of width $\Delta\omega \sim 9.1 \times 10^6$ cph. $c_1 = 3.00$ m/s for the theoretical construction. (a) $n=1$ mode at 5.2 days. (b) $n=2$ mode at 4.0 days. The background level, averaged over all the stations, is indicated by the straight line to the right of each figure.

than the 95% confidence bands (i.e., Fanning in Figure 3.19a, Majuro in Figure 3.19b, and Kwajalein in Figures 3.19a and b). The power density estimates are averages over the bandwidth $\Delta\omega=9.1 \times 10^{-4}$ cph centered on the peaks. For the plotted curves, $v_c^2 = 1.57 (.39) (\text{m/s})^2/\text{cph}$ for $n=1(2)$.

Figure 3.19 displays slightly better agreement between theory and observations than the similar Figures 9 and 10 of WG. (Note that WG use confidence intervals that are one standard deviation of chi-squared wide.) The major improvement is in the fit for mode $n = 2$, where in WG the "KU" data point at 5°N , supposedly Kusaie Is., was accidentally obtained from an analysis of Majuro data (at 7°N). There is not enough continuous sea level data from Kusaie to compute a power density spectrum that resolves the inertia-gravity waves. Also, with two years of data from Nauru ($0^\circ 32'\text{S}$) the equatorial node for mode $n = 2$ is well-determined, whereas only three months of data from Jarvis ($0^\circ 23'\text{S}$) was available to WG. We have not included the Jarvis data in Figure 3.19 since the 95% error bars are so large they obviate its usefulness (but compare Jarvis and Nauru in Figure 3.15). The improved fit for $n = 2$ argues against the existence of a non-resonant, forced $n=1$ mode at 4 days period, as was suggested by Philander ((1978); p. 39).

Without an objective criterion for goodness-of-fit, and without more stations to resolve the meridional structure, it is not enlightening to construct comparisons like Figure 3.19 for the higher meridional modes.

D.4. Identification of Higher Meridional Modes, $n>2$. It has already been shown in Section 3.D.1 that peaks in the sea level spectra (Figure 3.15) apparently correspond to modes as high as $n = 5$. Identification was dependent upon assuming that a given peak is associated with the mode that has a predicted period nearest to the observed peak. This results in the

occasional identification of a high mode, such as $n = 4$ at Christmas (Figure 3.15), without finding all the lower modes, i.e., $n = 3$ is missing at Christmas. In Section 3.D.12 the consistency of the previous identification of meridional modes will be confirmed by a spectral model of equatorial inertia-gravity waves, a model which demonstrates that the particular "peak" pattern at each island is a simple consequence of the meridional structures of the modes. In this section we present an additional spectrum that suggests the occasional existence of meridional modes with $n > 5$.

The power density spectrum for the two years when the $n = 2$ mode (4.04 days period) was strongest at Christmas is shown in Figure 3.20a. Several peaks at frequencies higher than that of the $n = 2$ mode are clearly present, suggesting a relationship between the strengths of these peaks and the $n = 2$ mode. Perhaps the forcing function was stronger across the whole inertia-gravity band during these two years or perhaps the high energy in the $n = 2$ mode is leaked to higher frequencies by nonlinear or topographic interactions. Using the phase speed $c_1 = 2.85$ m/s (from Table 3.11) and the theoretical equation (3.6) for the periods of the meridional modes we can compare the periods of the observed peaks in Figure 3.20a with theory (Table 3.12).

Table 3.12

Mode Number	<u>Period (days)</u>								
	1	2	3	4	5	6	7	8	9
Computed for $c_1 = 2.85$ m/s	5.28	4.05	3.42	3.01	2.72	2.50	2.33	2.19	2.07
Observed-Christmas (Fig. 3.20a)	5.30	4.04		3.07		2.50			2.09
Observed-Christmas (Fig. 3.20b)	5.30	4.04		3.07				2.18	

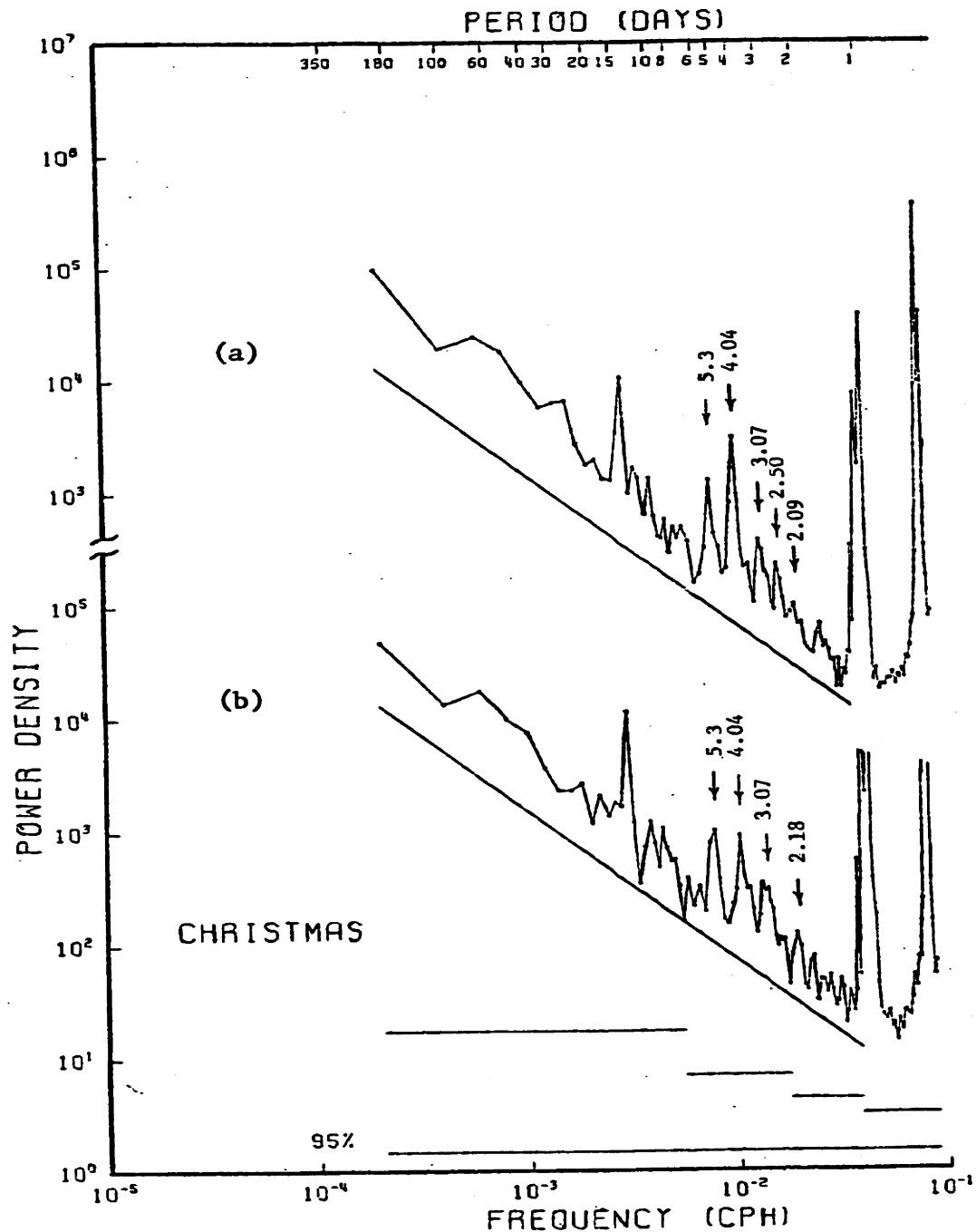


Figure 3.20 - Sea level spectra from Christmas using the two years wherein the power in the $n=2$ (4.04 days) mode was (a) strongest (10/60-10/61 and 12/66-12/67), (b) weakest (12/67-12/68 and 11/70-11/71). Reference lines have a $-4/3$ slope. Otherwise plotted as in Figure 3.1.

For comparison, the power density spectrum of sea level at Christmas for the two years when the $n = 2$ mode was weakest is shown in Figure 3.20b. The periods of the observed peaks in Figure 3.20b are also included in Table 3.12. The major differences between Figures 3.20a and 3.20b are that the $n = 2$ (4.04 days) and $n = 6$ (2.50 days) modes are noticeably weaker in Figure 3.20b. None of the variations exceed the 95% confidence intervals, hence they may simply be random fluctuations of the wave field.

When the complete Christmas record is used to compute the power density (Figure 3.15) no mode higher than $n = 4$ is clearly visible, as noted in Section 3.D.1. Similarly, the long Canton record produces a spectrum (Figure 3.15) in which no modes higher than $n = 5$ are clearly detectable. Yet Figure 3.20a suggests that the inertia-gravity waves of higher mode number may be strong enough to dominate the sea level spectra in the "mid-Pacific" for periods from the longest diurnal tide to 2.5 days. The lack of peaks between 1 and 2.5 days at Canton and Christmas (Figure 3.15) indicates that over long periods of time the higher modes, which must have some nonzero frequency bandwidth, smear together as a result of the compaction of modes in frequency-space as n increases (Table 3.12).

D.5 Inertia-Gravity Wave Signals in Indian Ocean Sea Level Data.

Four near-equatorial sea level spectra from the Indian Ocean are presented in Figure 3.21. Two other stations, more "coastal" than "open ocean," have been excluded from Figure 3.21 (see Figure 3.3 and Table 3.1). Subsets of the data from three of the stations (all but Minicoy) have been previously examined by Wunsch (1976) for inertia-gravity waves, but we can slightly improve upon his observations.

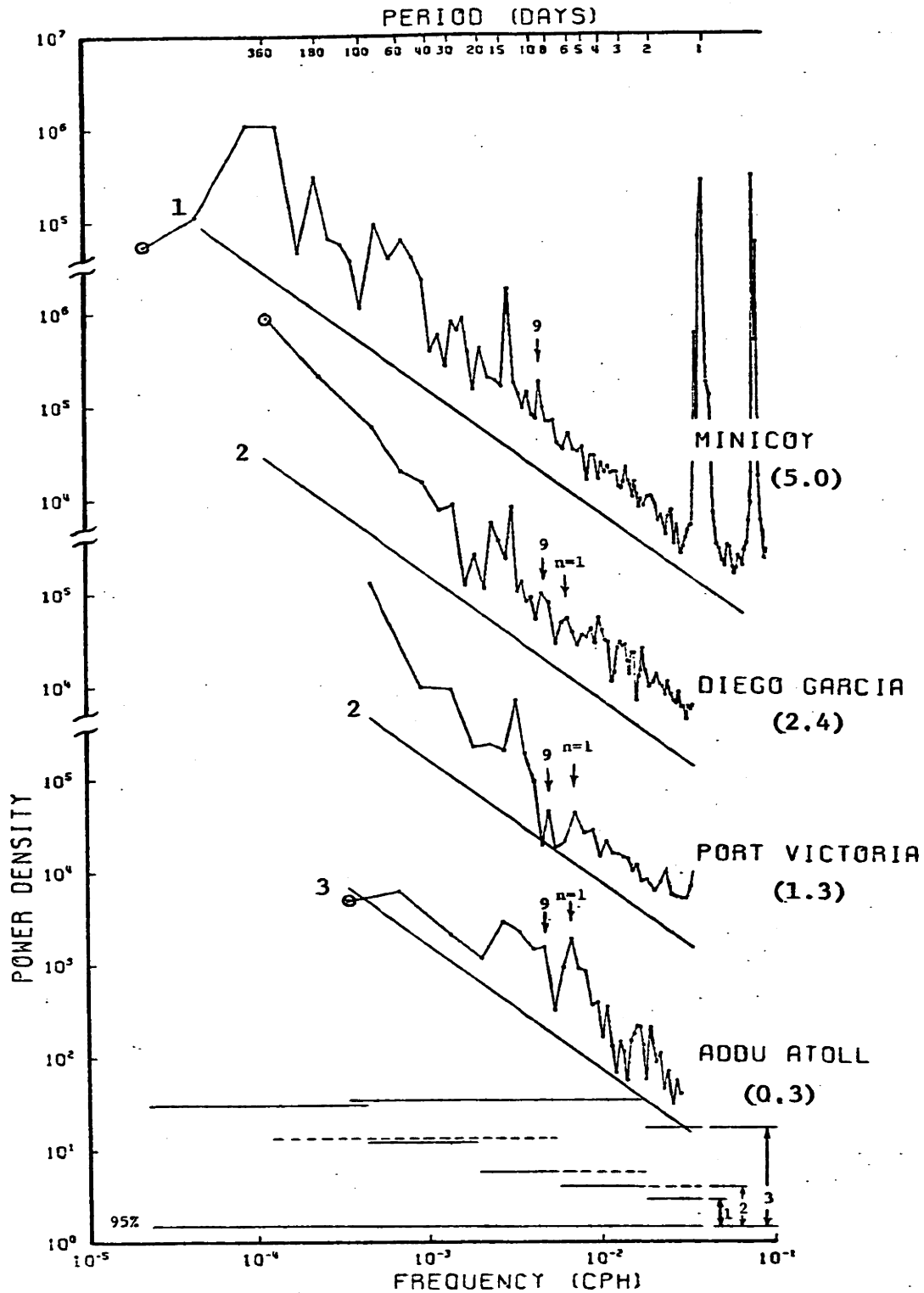


Figure 3.21 - Sea level spectra from four near-equatorial stations in the Indian Ocean. Possible $n=1$ mode inertia-gravity peaks are indicated with arrows. The nine-day tide is also indicated with an arrow labeled "9". Reference lines have $-4/3$ slopes. Numbers in parentheses are data lengths in years. Otherwise, plotted as in Figure 3.1.

here is good reason to believe that the distinct peaks in the "mid-Pacific" sea level spectra, which we have argued are due to equatorial inertia-gravity waves, will not be present in the Indian Ocean sea level spectra. The Indian Ocean is narrower in longitude* with rough topography in half the basin. Therefore, one might expect that vertical normal modes will not be established and that resonance near the zero zonal group velocity points will not occur. However, there is as much energy in the equatorial surface winds at 4-5 days in the Indian Ocean (Figures 2.4 and 2.15) as in the Pacific (Figures 2.3 and 2.14), although the wavenumber spectra of the Indian Ocean winds is not known.

The spectra from both Addu Atoll ($0^{\circ}34'S$) and Port Victoria ($4^{\circ}37'S$) have an apparent peak at about 6 days period (although neither peak is statistically significant at the 95% level). If the peak is identified as due to the $n = 1$ meridional mode then $c_1 (= \sqrt{gh_1})$ must be ~ 2.2 m/s. Using three hydrographic stations from the equatorial Indian Ocean, Wunsch (1976) estimated c_1 to be between 2.3 and 2.7 m/s. Using Bell et al.'s (1974) data (as in Section 3.D.1) we find $c_1 \approx 2.4$ m/s near Port Victoria and $c_1 \approx 2.5$ m/s near Addu Atoll. The difference between the required $c_1 \approx 2.2$ m/s and $c_1 \approx 2.4 - 2.5$ m/s is not significant considering the paucity of data. In subsequent discussions of the Indian Ocean sea level spectra we'll use $c_1 = 2.5$ m/s.

Additional suggestions of low-mode inertia-gravity wave energy in Indian Ocean sea level spectra are provided by the superpositions of Indian and Pacific Ocean spectra from similar latitudes. The sea level

*The width of the Indian Ocean at the equator is actually less than any wavelength of the first-baroclinic mode inertia-gravity waves near the zero zonal group velocity points.

spectra from Addu Atoll (0°34'S), Port Victoria (4°37'S) and Diego Garcia (7°14'S) are superimposed on the Pacific sea level spectra from Nauru (0°32'S), Hull (4°30'S) and Majuro (7°10'N), respectively, in Figure 3.22. Since the theoretical periods of the inertia-gravity peaks (presumed to be at the zero zonal group velocity points) are proportional to $\sqrt{c_1}$, the Indian Ocean sea level spectra have been displaced to higher frequencies, relative to the Pacific spectra, by an amount (using 3.6):

$$\Delta x = \log \left[\frac{(\omega_{1,n})_{\text{PACIFIC}}}{(\omega_{1,n})_{\text{INDIAN}}} \right] = \log \left[\frac{(\sqrt{c_1})_{\text{PAC}}}{(\sqrt{c_1})_{\text{IND}}} \right] = \log \left[\frac{\sqrt{3.0}}{\sqrt{2.5}} \right] = .0396$$

The frequency scales for both Indian and Pacific spectra are shown. The single ordinate scale applies for both oceans.

The Addu Atoll spectrum is seen to be remarkably similar to the Pacific's Nauru spectrum (in the inertia-gravity band). The Port Victoria spectrum is similar to the Pacific's Hull spectrum in the inertia-gravity band, except that Port Victoria is apparently missing its $n = 3$ peak. This is possibly the result of the smaller c_1 in the Indian Ocean: whereas Hull is at a maximum of the $n = 3$ function in the Pacific, Port Victoria is closer to an $n = 3$ node than an $n = 3$ maximum. (See Figure 3.17a). The Diego Garcia spectrum is seen to be as energetic as the Pacific's Majuro spectrum, in the inertia-gravity band, with possible inertia-gravity peaks. Clearly, the Diego Garcia spectrum is more difficult to interpret owing to a larger background level and the proximity of the $n = 1$ mode to the strong 9-day tide (Figure 3.21).

Figure 3.22 suggests that the first-baroclinic inertia-gravity wave field in the Indian Ocean may be as strong as in the Pacific, and that energy may also be concentrated near the zero zonal group velocity points in that ocean. Could resonance occur in the Eastern Indian Ocean over the relatively smooth Ceylon Abyssal Plain, even though the basin width is less than any zonal wavelength of the inertia-gravity waves near the zero

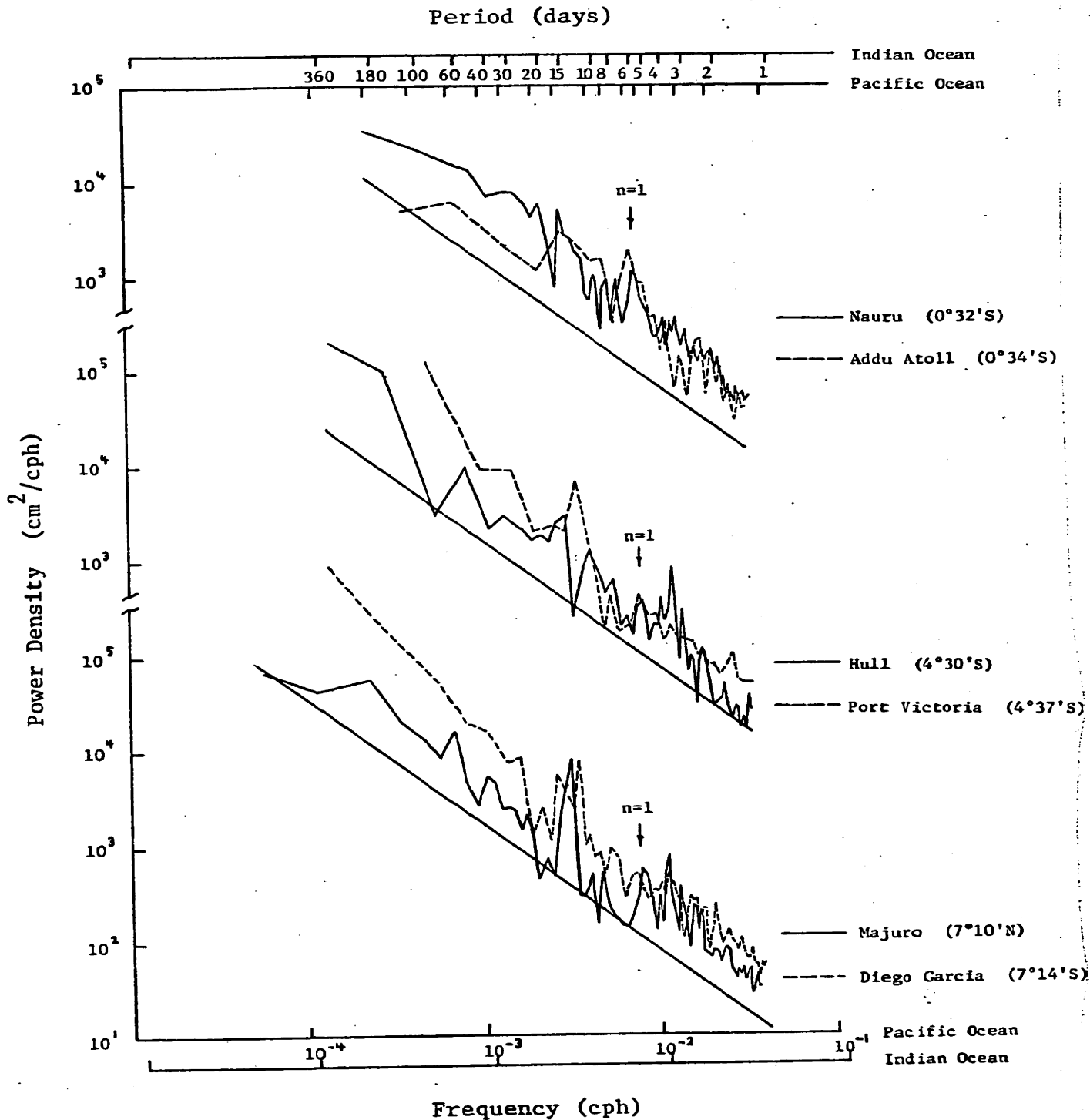


Figure 3.22 - Superposition of sea level spectra from islands in the Pacific and Indian Oceans. The pairs of islands are at nearly identical distances from the equator. Latitudes are given. Reference lines have $-4/3$ slope. Abscissae for the Pacific and Indian stations are indicated (see text). Otherwise, plotted as in Figure 3.1.

zonal group velocity points?

We will re-examine the Indian Ocean spectra, and the points made above, in Section 3.D.12 when we construct a spectral model of the equatorial inertia-gravity wave field.

D.6 Sea Level Deflection Due to Higher Vertical Modes. Until this point it has been assumed that only the first baroclinic mode will produce fluctuations that can be detected in sea level datasets. However, a peak at about 7 days, corresponding to the period* of the second-baroclinic, first-meridional mode, occurs in the spectra at Christmas and Canton (Figures 3.1 and 3.18b). Yet both stations are near nodes in the meridional structure function of this mode. The second-baroclinic mode would seem to be excluded as the cause of the 7.4-day peak, unless the mode contains much more energy than the first-baroclinic modes at 4 and 5 days.

To get an idea of the possible strengths of the sea level fluctuations due to the higher vertical modes, we have calculated the ratio of sea level to maximum internal displacement, $\frac{|\zeta_r|}{|\zeta_r|_{\max}}$, for the first few baroclinic modes, using simple profiles of $N(z)$. For constant N , it is easy to show that $\frac{|\zeta_r|}{|\zeta_r|_{\max}} \propto \frac{1}{r}$, but this only crudely represents oceanic conditions. A more realistic profile of $N(z)$, although still flawed, is the exponential decay model with a surface mixed-layer:

$$N(z) = \begin{cases} 0 & , 0 < z < H , \\ N_0 e^{\lambda z} & , -D < z < 0 . \end{cases} \quad (3.8)$$

With (3.8) one can study how sensitive the ratio $\frac{|\zeta_r|}{|\zeta_r|_{\max}}$ is to details of the stratification, such as mixed-layer depth and vertical stratification scale ($\equiv L = \lambda^{-1}$).

*The period is calculated from (3.6) using $h_2 = .28\text{m}$ ($\sqrt{\epsilon_2} = 562$) obtained from a numerical analysis of Bell et al.'s (1974) data near Christmas.

If, instead of the definition (1.22), we let

$$\{u, v, p\} = \text{Re} \left[\hat{q} \{U(\sigma), V, zP\} Q'(z) e^{is\phi - i2\alpha\sigma t} \right] \quad , \quad (3.9a)$$

and

$$\{p, w\} = \text{Re} \left[\hat{q} \left\{ \frac{zN^2R}{g}, W \right\} Q(z) e^{is\phi - i2\alpha\sigma t} \right] \quad , \quad (3.9b)$$

where \hat{q} is an amplitude constant, then the Boussinesq form of equations (1.4) - (1.6) can be separated into the horizontal structure equation (1.23) and a vertical structure equation that is simpler than (1.17), that is,

$$\frac{d^2 Q(z)}{dz^2} + \frac{N^2(z)}{c_r^2} Q(z) = 0 \quad , \quad (3.10)$$

with the boundary conditions from (1.19):

$$\text{and} \quad Q(z) = 0 \quad \text{at} \quad z = -D \quad , \quad (3.11a)$$

$$Q' - \frac{g}{c_r^2} Q = 0 \quad \text{at} \quad z = H \quad , \quad (3.11b)$$

where the origin is at the base of the mixed layer.

Equation (3.10) is simpler than the vertical structure equation for mid-latitude internal waves (see Garrett and Munk (1972)), a simplification resulting from the reasonable neglect of vertical acceleration in the momentum equations. The solutions to (3.10) for $z < 0$, using the $N(z)$ profile in (3.8), are combinations of Bessel functions, but, unlike the mid-latitude case (Garrett and Munk (1972)), the order is constant and not a function of frequency. After application of the boundary conditions (3.11), the solution to (3.10) is $Q(z) = \sum_r Q_r(z)$,

$$\text{with} \quad Q_r(z) = B_r \frac{N_0}{c_r} (H - z - h_r) J_1(q_r) \quad , \quad 0 < z < H \quad , \quad (3.12a)$$

$$Q_r(z) = B_r J_0(q_r e^{\lambda z}) \quad , \quad -D < z < 0 \quad , \quad (3.12b)$$

where $J_m(x) \equiv J_m(x) Y_0(q_r e^{-\lambda D}) - Y_m(x) J_0(q_r e^{-\lambda D})$, $q_r = \frac{N_0}{\lambda c_r}$, $c_r^2 = gh_r$,

and B_r is an amplitude function of r .

The eigenvalues c_r are solutions to

$$\frac{N_0}{c_r} (H - h_r) = \frac{J_0(q_r)}{J_1(q_r)} \quad (3.13a)$$

If $q_r e^{-\lambda D} > 1$, then the Bessel functions can be replaced with their asymptotic expansions (Abramovitz and Stegun (1972, p. 364)), and (3.13a), for example, becomes

$$\frac{N_0}{c_r} (H - h_r) = \tan [q_r (e^{-\lambda D} - 1)] \quad (3.13b)$$

The asymptotic forms are in fact very accurate (for reasonable parameter values) except for the two gravest vertical modes. Note that as $\lambda \rightarrow 0$, the constant N ocean (beneath a homogeneous mixed-layer) case is readily obtained (e.g., Munk and Phillips (1968), for $H = 0$). After choosing $L = 1.3$ km (à la Garrett and Munk (1972)), $D = 4$ km, $H = 100$ m and $N_0 = .0065$, (3.13a) was solved numerically for h_r , $r = 1$ to 4. These eigenvalues are compared in Table 3.13 with eigenvalues for a constant N ocean and with numerical solutions (Section 3.D.1) of (3.10) using Bell et al.'s (1974) data from the Gilbert Islands.

Table 3.13

Solution	Stratification	Model Information				Equivalent Depths, h_r (m)			
		D (km)	$\frac{N}{\rho_0}$ (rad/s)	L (km)	H (m)	<u>1</u>	<u>2</u>	<u>3</u>	<u>4</u>
A	Bell et al. (1974)	4.4	-----	1.3	---	.91	.29	.098	.053
B	Exponential N(z)	4.0	.0065	1.3	100	.92	.21	.089	.049
C	Constant N	4.1	.0023	∞	0	.92	.23	.102	.058

Table 3.13 demonstrates the major inaccuracy of the exponential N(z) model, which is that the second and third mode eigenvalues are not even reproduced as well as with the constant N model (assuming Solution A yields the most

realistic eigenvalues).

Further numerical and asymptotic solutions to (3.13a) showed that the equivalent depths, for all r , increase when D , L , N_0 or H increase.

$$\text{Since } \frac{\partial \eta}{\partial t} = w, \quad \frac{\mathcal{I}_r}{\mathcal{I}_r(z)} = \frac{\mathcal{I}_r(H)}{\mathcal{I}_r(z)} = \frac{Q_r(H)}{Q_r(z)}, \quad \text{which from (3.12)}$$

gives

$$\mathcal{I}_r/\mathcal{I}_r(z) = N_0 \sqrt{h_r/g} \mathcal{J}_1(q_r)/\mathcal{J}_0(q_r e^{\lambda z}),$$

and

$$\therefore \frac{|\mathcal{I}_r|}{|\mathcal{I}_r|_{\max}} = N_0 \sqrt{\frac{h_r}{g}} \frac{|\mathcal{J}_1(q_r)|}{|\mathcal{J}_0(q_r e^{\lambda z})|_{\max}} \quad (3.14)$$

Numerical solution of (3.14) with the parameters of Table 3.13 indicates that to get a 1 cm sea level displacement requires maximum internal displacements of ~ 7 , ~ 22 , ~ 43 , and ~ 72 meters for the first, second, third and fourth baroclinic modes, respectively. These required displacements grow much faster than r , the growth rate for a constant N ocean: as $\lambda \rightarrow 0$, (3.14) gives $\frac{|\mathcal{I}_r|}{|\mathcal{I}_r|_{\max}} = \frac{N_0^2 D}{g \pi r}$. Furthermore, the total modal energy must increase approximately as fast as r^2 to maintain a 1 cm sea level displacement. (This last calculation has been made only for small zonal wavenumber.)

The effect of various mixed-layer depths on the ratio of sea level displacement to maximum internal displacement is summarized in Figure 3.23 for several vertical modes. For high modes, the ratio decreases as H is increased from zero. For low modes, the ratio first increases then decreases. The general result is that as the mixed-layer depth increases the sea level expressions of the higher modes decrease while the sea level effect of the first baroclinic mode increases, for realistic equatorial values of H . This suppression of the higher vertical modes is not strong unless $r > 3$.

Changes in the vertical stratification scale, L , lead to predictable results. As $L \rightarrow \infty$, the constant N case is obtained. As $L \rightarrow 0$, the

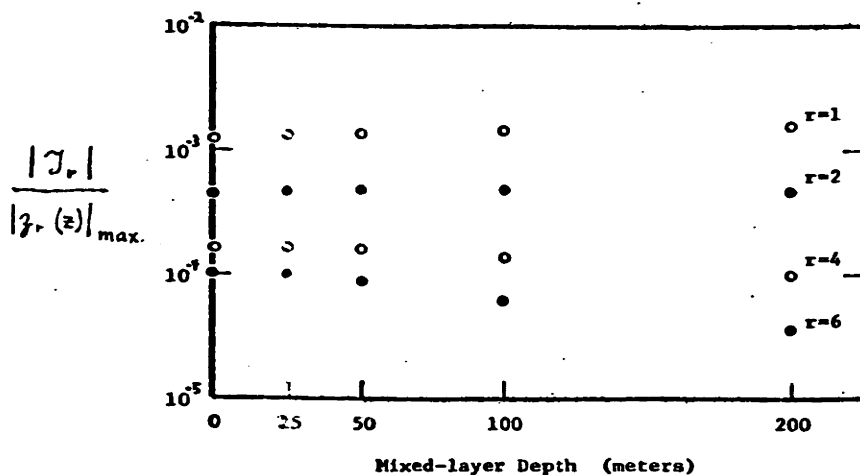


Figure 3.23 - Plot of the magnitude of the sea surface displacement divided by the maximum internal displacement for several mixed-layer depths, assuming the stratification is the exponential decay from a mixed-layer given by (3.8). The vertical mode numbers are shown.

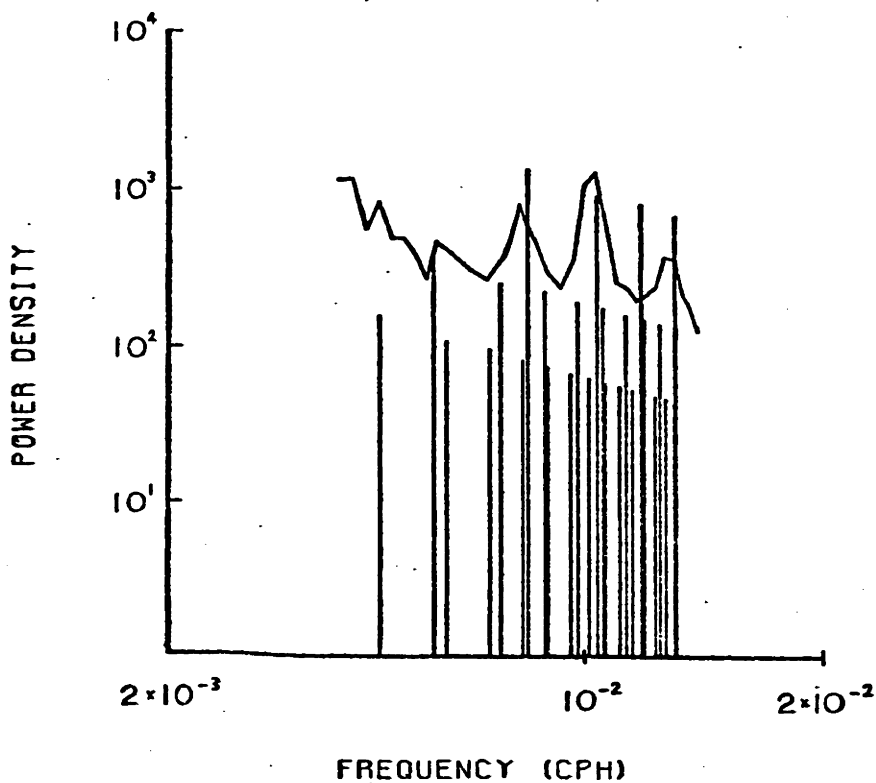


Figure 3.24 - Line spectrum of sea level displacement for the first three baroclinic modes, assuming equal amounts of energy are concentrated at the zero zonal group velocity points and assuming the stratification is given by (3.8). Four, nine and 14 meridional modes are plotted for the first, second and third baroclinic modes, respectively. Also shown is a segment of the sea level spectrum from Christmas Island (Figure 3.15).

stratification approaches the two-homogeneous-layer limit so that higher modes are rapidly suppressed (see Gill (1975)).

Keeping the total energy of each mode constant, sea level power falls roughly as r^{-2} . Considering the maximum sea level power evident for $r = 1$ in Figure 3.15, this rate of decrease is almost sufficient to rule out the possible detection of second-baroclinic modes. As a graphic example of this point, a line spectrum of sea level power is shown in Figure 3.24 for the first three baroclinic modes up to a frequency of 1/3 cycle/day. Constant total energy for each mode is assumed, with the energy in each meridional mode concentrated at the zero zonal group velocity point. Superimposed on the line spectrum is the sea level power spectrum from Christmas. Whether any of the modes in Figure 3.23 is actually present in the sea level spectrum from a particular island depends, of course, on the latitudinal structure functions. In Section 3.D.12, we return to this question when the sea level power spectra at each island are constructed given several assumed distributions of energy among the modes and explicitly accounting for the latitudinal structures.

Finally, note that spatial (along the Pacific equator) and temporal (at the Indian Ocean equator (Colborn (1975))) changes in the mixed-layer depth can change $\frac{|T_v|}{|z^*|_{\max}}$ by as much as 20% (Figure 3.23).

D.7 Zonal Wavenumbers and Bandwidths. Horizontal coherences of inertia-gravity temperature and current fluctuations beneath the sea surface are strongly dependent upon the zonal and vertical wavenumber bandwidths. Since sea level is primarily responding to the first baroclinic mode, coherence between sea level stations at the meridional-mode frequencies can be interpreted solely in terms of the zonal wavenumber and zonal wavenumber bandwidth. Insofar as one can assume that the distribution

of energy in σ -s space for each meridional mode is not a strong function of vertical mode number, the sea level coherences will help determine the energy spectrum for all vertical modes and not only for the first baroclinic mode. In other words, if the first baroclinic mode energy is not anomalously distributed in σ -s space, any spectral description of the internal inertia-gravity wave field at the equator must be able to reproduce the observed sea level coherences and power density spectra.

Perhaps the most important discovery made by Groves and Grivel (1962) in their study of equatorial sea level fluctuations was that sea level is strongly coherent at the 4-day period over large distances (O(2000 km)) near the equator. Such strong coherence usually occurs only at tidal frequencies. If the 4-day inertia-gravity oscillation were not coherent over large distances one could not, of course, estimate the zonal wavenumber or bandwidth from the existing sea level stations.

Even with the rather large sea level dataset used here, we are hindered by lack of data in attempts to estimate the wavenumbers and bandwidths. The problem is a general lack of long-duration cotemporal data. One cannot even begin to compute sea level frequency-wavenumber spectra as was done for surface weather variables in Chapter 2. Figure 3.25 displays the sea level coherences for the two station pairs with the most cotemporal data in the "mid-Pacific" region defined earlier. All three stations in Figure 3.25 have strong 4-day ($n = 2$ mode) power density peaks, but only Canton and Christmas have $n = 1$ power density peaks at the same period (we found in Section 3.D.1 that the apparent period of the $n = 1$ mode at Arorae was anomalously large). Both coherences in Figure 3.25 have large amplitude peaks at 4 days and the Christmas-Canton coherence amplitude is significantly non-zero at 5 days ($n = 1$ mode). In general, although we

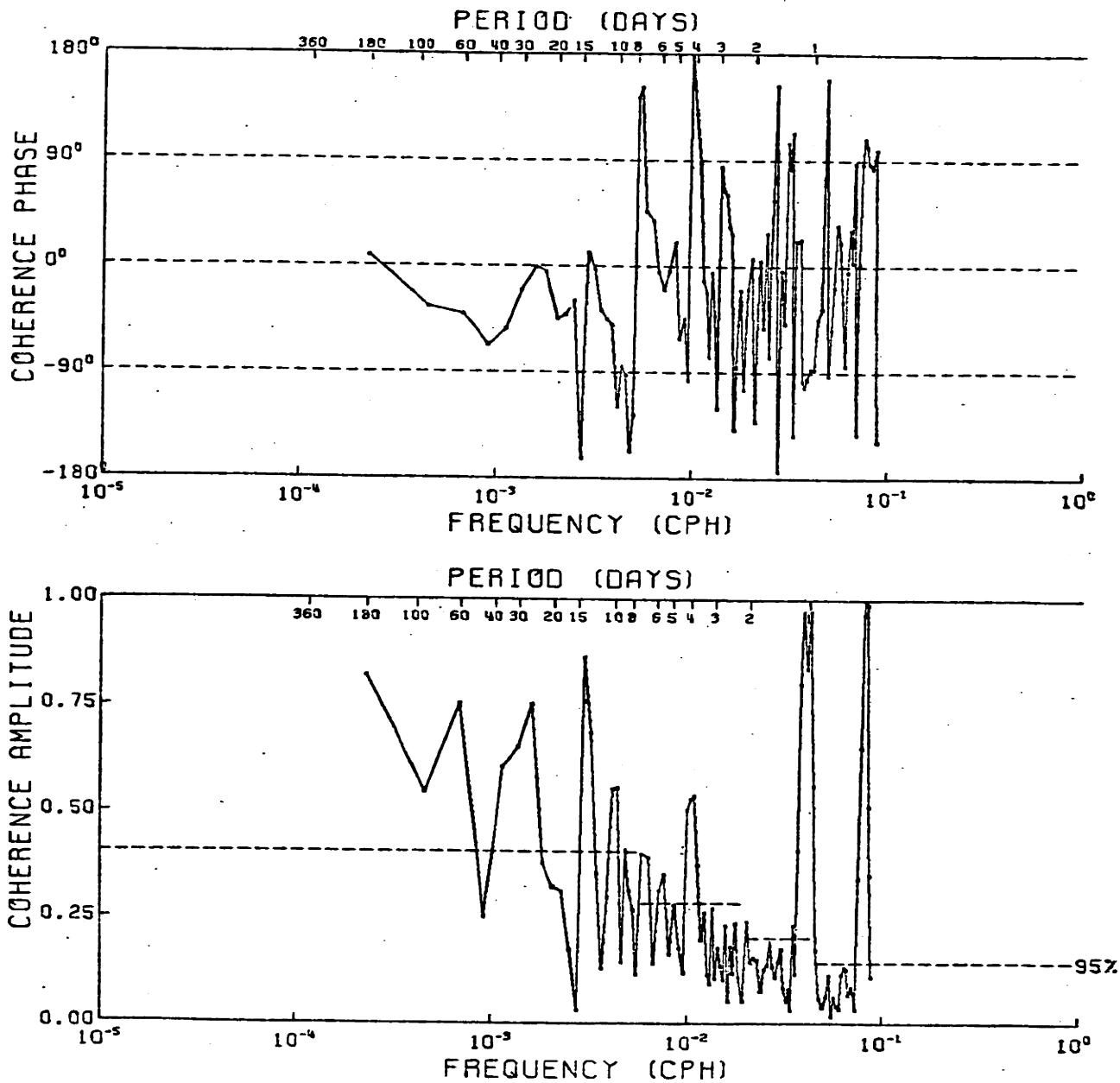


Figure 3.25a

Figure 3.25 - Sea level coherence amplitudes and phases between (a) Christmas and Canton, (b) Canton and Arorae. Positive phase indicates that the first station leads the second. The 95% level of no significance for the amplitude is shown.

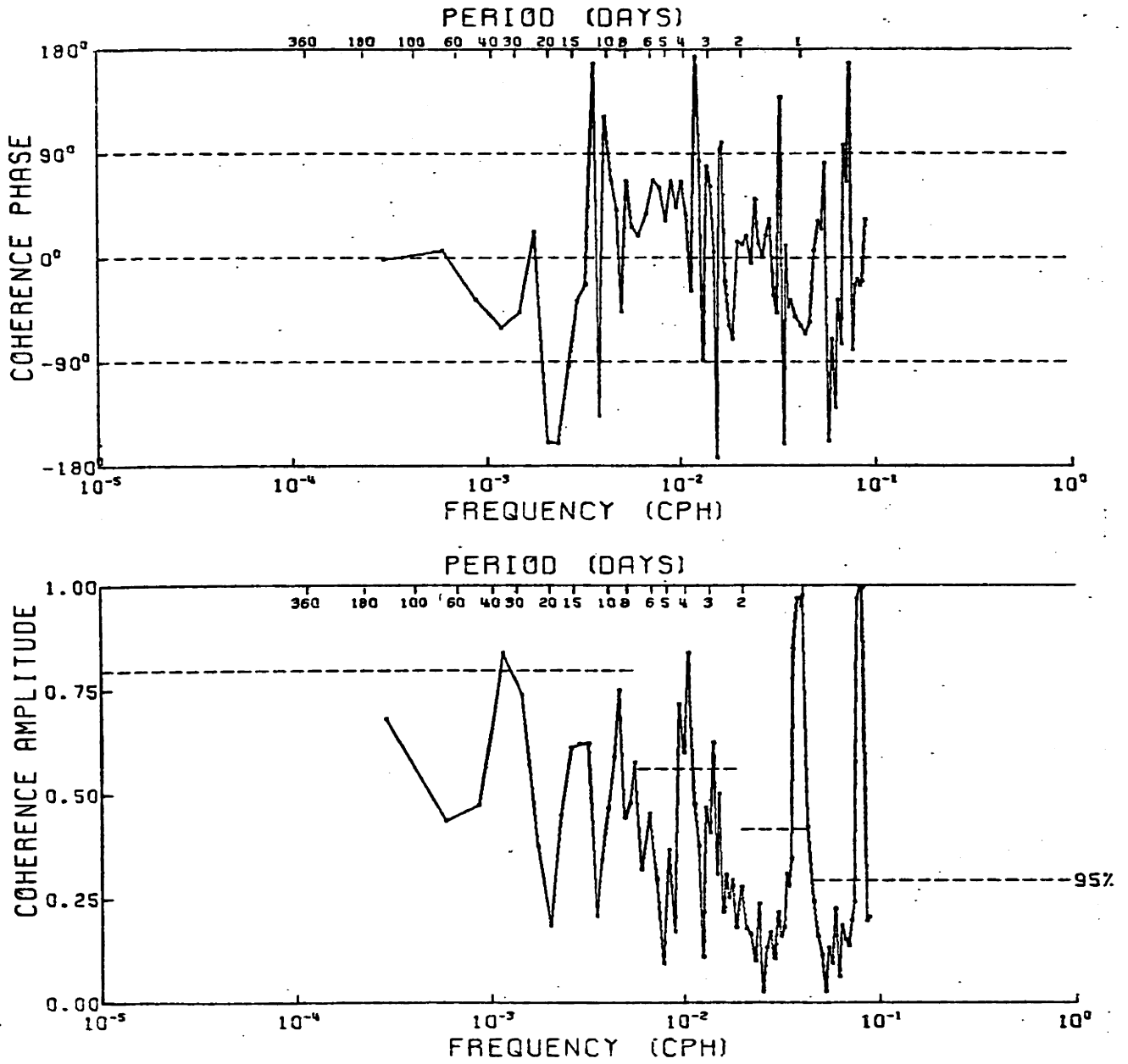


Figure 3.25b

have hypothesized that the whole 1-3 day band is dominated by inertia-gravity waves, the coherence amplitude in Figure 3.25 does not rise above the 95% level of no significance. This is not surprising since the meridional modes are more closely spaced in this frequency band, and since, because of the different meridional structures, the mix of modes is expected to be different at each island.

The "mid-Pacific" sea level coherences with non-zero (at 95% significance) amplitudes at 4 and 5 days are summarized in Table 3.14.

Table 3.14

<u>Station Pairs</u>	<u>No. of Years</u>	<u>Zonal Sep. (deg)</u>	<u>Coherence</u>			
			<u>3.8-4.3 days</u>		<u>5.0-5.8 days</u>	
			<u>Amp.</u>	<u>Phase*</u>	<u>Amp.</u>	<u>Phase*</u>
Christmas - Canton	10.5	14.2	.42	130±15	.33	-11±39
Canton - Arorae	2.0	11.5	.70	47±16	---	-----
Christmas - Fanning	2.0	1.9	.63	0±17	.51	5±24
Canton - Ocean	1.9	18.8	.53	206±37	---	-----
Betio - Nauru	1.5	6.1	---	-----	.64	5±32

*Error bars are 95% confidence limits.

If our original hypothesis is correct, that the inertia-gravity wave energy responsible for the 4- and 5-day sea level power peaks is concentrated near the zero zonal group velocity points, then the expected zonal wavenumbers are $s \approx -5.2$ and -4 cycles/circumference for the 5- ($n = 1$) and 4-day ($n = 2$) waves, respectively. In Table 3.14, at 4 days, only the Canton-Arorae and Christmas-Fanning coherences agree with the hypothesis, although the latter is trivial since the stations are so close.

The most important coherence occurs for the Canton-Christmas pair, because they are long records and because the 4-day ($n = 2$) mode has a node between the stations. Given the expected $s \approx -4$ at 4 days, and the

presence of the node, Christmas should lead Canton by 237° , but the observed phase lead is only 130° . Groves and Grivel (1962) and Wunsch and Gill (1976) previously found a 130° phase lead using subsets of the data used here, an observation which led Groves and Grivel to conclude that a node did not exist between Canton and Christmas, contrary to our present belief. Dividing the records into shorter pieces still yields a coherence phase of roughly 130° for each piece. If there is not a node between the stations then $-10 < s < -8$, which is also obtained from the Canton-Ocean coherence. At present we do not have a good explanation for the apparent disagreement of these coherence phases with our original hypothesis.

The 5-day ($n = 1$) coherence phases in Table 3.14 suggest a wavenumber of smaller magnitude than the hypothesized $s \approx -5.2$, but the evidence is inconclusive.

Wavenumber bandwidths, Δs , can be computed from the 4- and 5-day coherence amplitudes in Table 3.14 using a procedure described by Munk and Phillips (1968). After correction of the amplitudes for a small bias (Jenkins and Watts (1968, p. 397)), the bandwidth is estimated as roughly 5-10 for the $n = 1$ and 2 modes, the same as was found for the atmospheric, 4-5 day mixed Rossby-gravity waves in the Pacific (Section 2.B.1.a).

D.8 Temporal Variability of the 4-5 Day Inertia-Gravity Power. The stationarity and ergodicity of the inertia-gravity wave amplitudes has been implicitly assumed in many of the foregoing analyses, where we have frequently compared data from different time periods. Yet Groves (1956) found an amplitude of 3 cm for the 4-day oscillation at Canton, which is much larger than our estimate of .81 cm for the rms amplitude of the 4-day wave. We emphasize here, by example, the large variations in amplitude that can occur for a stationary random process, and we suggest the possibility of non-stationary annual fluctuations of the inertia-gravity wave energy at

the equator in the Pacific.

Figure 3.26 compares power spectra of separate one-year pieces of sea level from Canton, demonstrating the maximum variability possible in the inertia-gravity band with one-year pieces. The dataset for Figure 3.26a includes the three-month segment responsible for Groves' (1956) large amplitude estimates (above). The power densities in the 3.7-5.4 day band are $1708 \pm 600 \text{ cm}^2/\text{cph}$ and $339 \pm \text{cm}^2/\text{cph}$ in Figures 3.26a and b, respectively. The numbers are significantly different at the 95% level. This result is atypical, however, as power spectra of the remaining Canton data, and also the Christmas data, taking one year at a time, do not show significant temporal variability of the 4-5 day power, at the 95% level.

Random fluctuations of the power in the 4-5 day band sometimes produce spectra, from one-year-long segments, that are considerably "confused" in terms of identifying the gravest meridional mode peaks. These spectra, of which Figure 3.27b is an example, are, at worst, misleading. The spectrum for the year of data preceding that for Figure 3.27b is shown in Figure 3.27a.

The unwary analyst can be further misled about the presence (or absence) of inertia-gravity peaks in equatorial sea level spectra (and perhaps also in sub-surface current and temperature spectra) by heavily smoothing the spectra from short records to reduce the error bars (the emphasis here is on the word "short"). For example, the spectrum of 152 days of Christmas sea level is plotted in Figure 3.28 after box-averaging 10 (Figure 3.28a) and 3 (Figure 3.28b) adjacent periodogram estimates. The particular year (1971) had rather weak inertia-gravity amplitudes. Figure 3.28a should be compared with sub-surface current records obtained by Taft et al. (1974) for the same time period, at a location 850 km east and 330 km south of

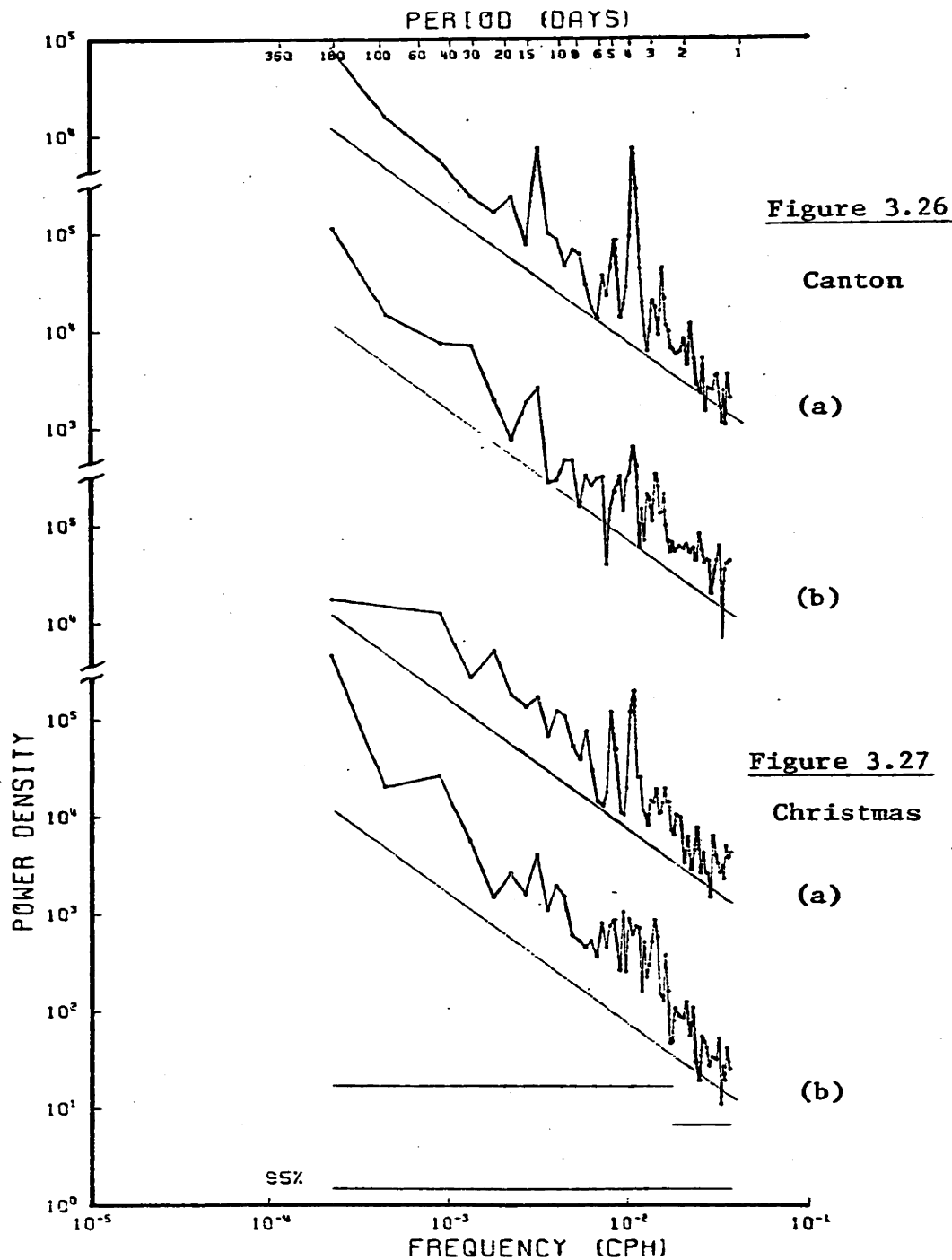


Figure 3.26 - Sea level spectra of 1-year-long records from Canton. (a) 5/52-5/53 - shows the largest 4-day power of any single 1-year spectrum. (b) 7/61-7/62 - shows the smallest 4-day power of any single 1-year spectrum. Reference lines have a $-4/3$ slope. Otherwise, plotted as in Figure 3.1.

Figure 3.27 - Sea level spectra from consecutive 1-year-long records at Christmas. (a) 8/56-8/57. (b) 8/57-8/58.

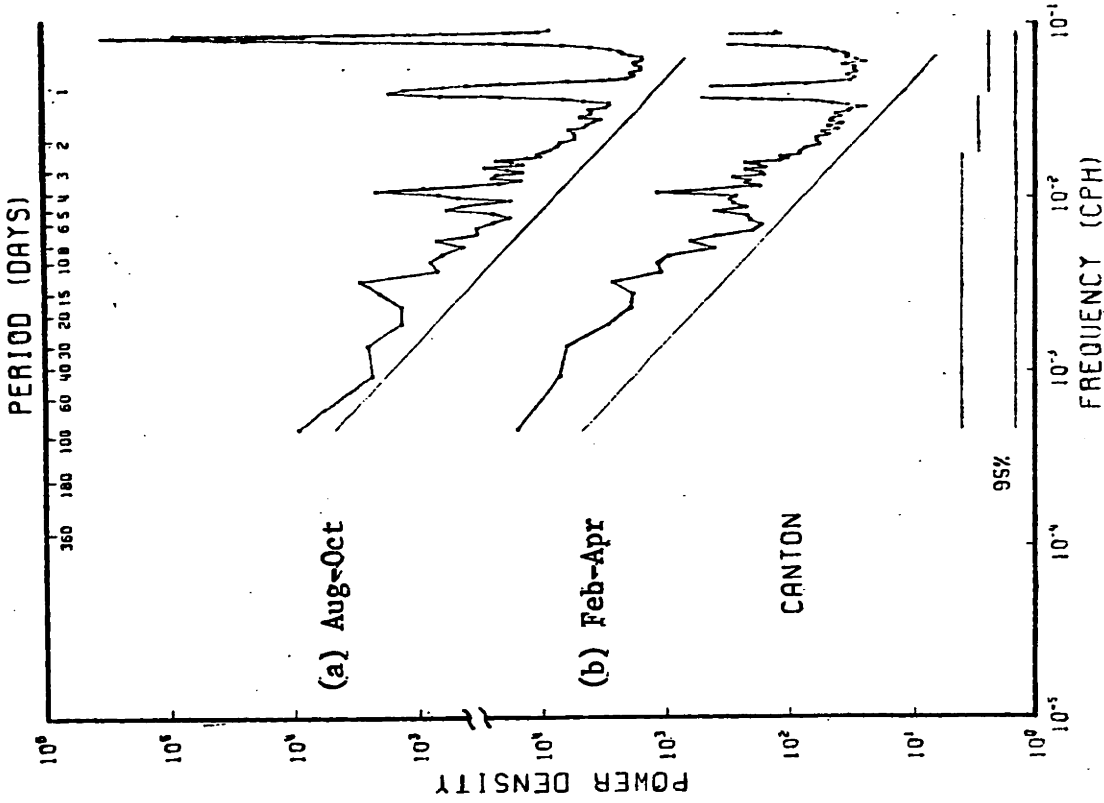


Figure 3.29

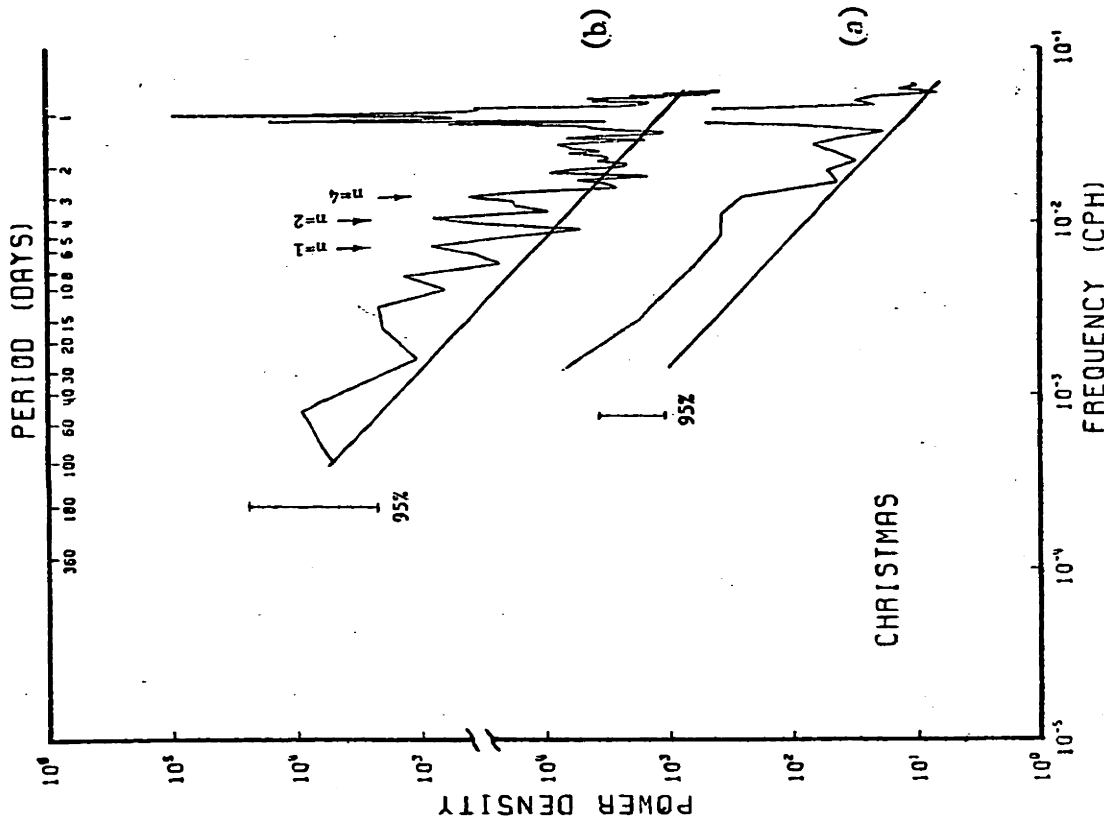


Figure 3.28

Figure 3.28 - Sea level spectra of 152 days of Christmas data (beginning 4/18/71) after box-averaging (a) 10, and (b) 3, adjacent periodogram estimates. Reference lines have a $-4/3$ slope.

Figure 3.29 - Sea level spectra from Canton for the months of (a) August through October, and (b) February through April, demonstrating the annual cycle in the strengths of the 4- and 5-day inertia-gravity waves at Canton. Reference lines have a $-4/3$ slope.

Christmas (their Figure 11). Wunsch and Gill (1976) examined the Taft et al. (1974) data in terms of inertia-gravity waves emphasizing the presence of 4- and 5-day peaks in the current spectra, but they found it impossible to construct a simple interpretation of the data in terms of low mode inertia-gravity waves.

In Section 2.B.1.b, we found a significant annual fluctuation of the 4-5 day power of north wind at Canton. As expected from the coherence between sea level and north wind at Canton (see Section 3.D.10), Canton sea level power in the 4-5 day band also has an annual fluctuation (Figure 3.29) with the proper phase, that is, strongest in the fall. The power densities in the 3.7-5.4 day band are $728 \pm 114 \text{ cm}^2/\text{cph}$ and $421 \pm 68 \text{ cm}^2/\text{cph}$ in Figure 3.29a (August through October) and Figure 3.29b (February through April), respectively. The numbers are significantly different at the 95% level. The magnitude of this annual variation of 4-5 day sea level power is identical to that for the north wind at Canton (see Section 2.B.1.b). Surprisingly, however, no similar annual fluctuation of the 4-5 day power is found at Christmas.

In view of the above results, we have come to the conclusion that, as a rule of thumb, a minimum of two years of data from a single station is necessary for studying the 4-5 day inertia-gravity waves at that station and confidently relating the observations to data from other stations in other time periods. Two years may seem rather long until one realizes that two years contains the same number of 5-day cycles as the 40-day Internal Wave Experiment (IWEX; Briscoe (1975)) contained 6-hour cycles.

D.9 Frequency Bandwidths of the Inertia-Gravity Peaks. Let $Q \left(\equiv \frac{\omega_0}{\Delta\omega} \right)$ be considered a normalized measure of bandwidth, where ω_0 is the centered peak period of a particular inertia-gravity mode (e.g., Tables 3.11 and 3.12),

and $\Delta\omega$ is the frequency bandwidth of the peak at the half-power points. Estimates of Q utilizing the Canton and Christmas spectra (Figure 3.15) yield $8 < Q < 19$ for the $n = 1$ and 2 modes, which is a slightly larger range than that found by Wunsch and Gill (1976). Q estimates for $n = 4$ and 6 (Figure 3.20a) are also well within this range. Hence, the Q does not appear to be a strong function of frequency for the inertia-gravity waves.

Typically, in analogy with simple physical systems (such as harmonic oscillators) that have discrete natural frequencies, Q is considered a measure of dissipation. (Wunsch and Gill (1976) have examined the consequences of this interpretation of Q for the inertia-gravity waves, although their conclusions are questionable because of the manner in which dissipation is incorporated into the equations of motion. See the discussion in Stevens and White (1979).) But for inertia-gravity waves there are a number of alternative interpretations for the frequency bandwidth and hence Q . For example, (1) the frequency bandwidth may reflect the distribution of energy in frequency-wavenumber space for each mode (Figure 1.1), so that narrow bandwidth implies that energy is concentrated near the zero zonal group velocity points; (2) the frequency bandwidth may simply mirror the frequency bandwidth of peaks in the atmospheric forcing fields; (3) inter-annual and seasonal fluctuations of the density field will introduce fluctuations into the values of the eigenvalue equivalent depths which directly affect the wave peak periods (equation 3.6); and (4) nonlinear interaction with the mean circulation can Doppler-shift the wave peak periods (McPhaden and Knox (1979)) so fluctuations in the mean circulation will introduce fluctuations in the peak periods.

Only the second, of the above possible explanations for the frequency

bandwidth, has been excluded by the analyses in this thesis. The Q of the 4-5 day atmospheric waves at Canton is less than the oceanic Q (see Section 2.B.1.b). In addition, no surface atmospheric variables have peaks at either 3 or 2.5 days corresponding to the peaks in the Christmas sea level spectrum (Figure 3.20a) and other sea level spectra. Therefore, at the very least, we can agree with the Wunsch and Gill (1976, p. 386) conclusion that the "observations imply that friction is small enough for the response spectrum to have more prominent peaks than the forcing spectrum."

D.10 Observations of Forcing. Of all the stations showing sea level inertia-gravity peaks (Figure 3.15), only Canton has cotemporal datasets of surface weather. The coherences between 8 years of sea level and surface wind components (positive north and east) are shown in Figure 3.30. The sea level - north wind coherence is peaked at exactly the periods of the peaks in Canton's sea level power spectrum (Figure 3.15). There is also significant coherence between sea level and east wind in the 4-5 day band, but the amplitude is not as strong as for sea level - north wind coherence. [N.b., significant coherence between east and north wind at Canton occurs only at a shorter period (3.5 days) than the peaks in Figure 3.30.]

Figure 3.30 is in good agreement with the sea level wind coherences computed by Groves and Miyata (1967). In fact, Groves and Miyata employed 13 years (compared to our 8) of cotemporal sea level and surface weather observations in their computations, but they lacked a formalism (i.e., equatorially trapped waves) within which to interpret their analyses.

Figure 3.30, and Groves and Miyata's (1967) analysis, suggest that both the $n = 1$ and $n = 2$ modes are predominantly driven by the north wind, with contributions from the east wind. Contrary to these observations, the forced, inertia-gravity wave model advanced by Wunsch and Gill (1976)

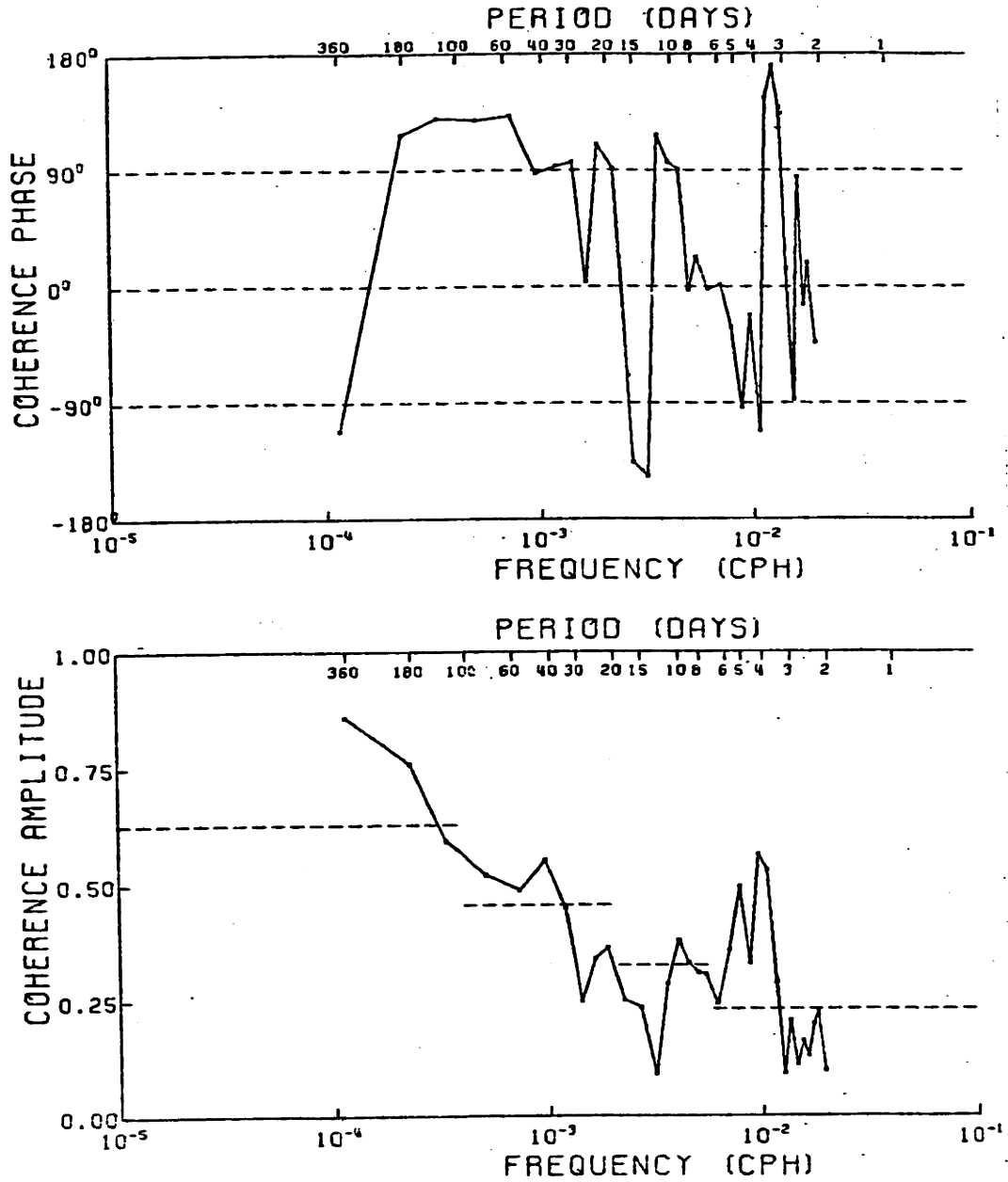


Figure 3.30a

Figure 3.30 - Coherence amplitudes and phases between (a) sea level and north wind, (b) sea level and east wind, at Canton. Positive phase indicates that sea level leads the wind. The 95% level of no significance for the amplitude is shown.

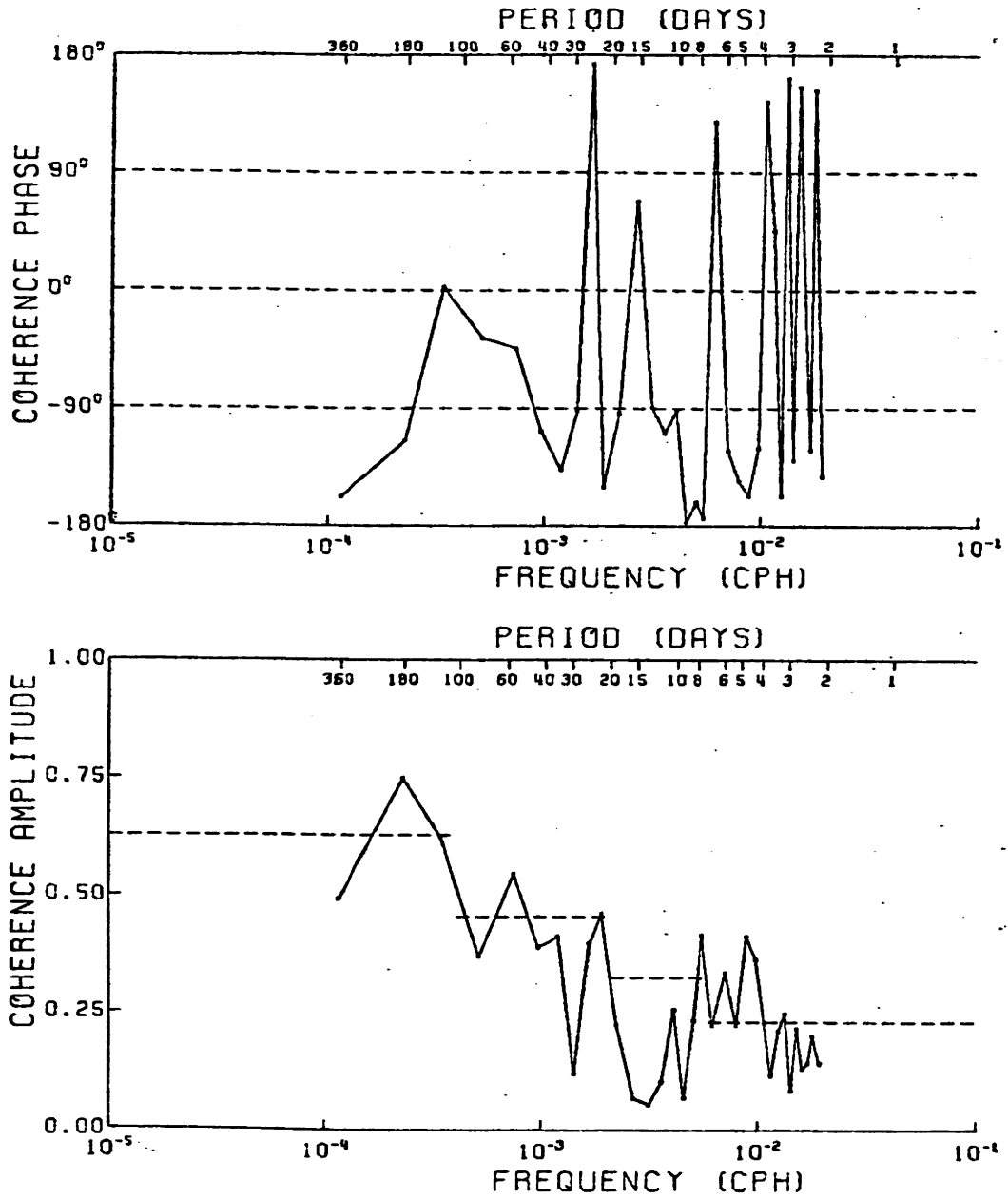


Figure 3.30b

requires that symmetric (n even) modes are only excited by the meridional wind and antisymmetric (n odd) modes are only excited by the zonal wind*. The problem is that WG's parameterization of the surface wind stress as a body force, $\vec{\tau}/H$, in the mixed-layer of depth H, is valid only if variations in the Coriolis parameter, $f (= 2\Omega \sin \theta)$, and mixed-layer depth can be ignored (Charney (1955)). Certainly, f cannot be considered a constant near the equator, except at frequencies high enough so that rotation is negligible throughout the region of interest. The body force parameterization is frequently used in studies of the wind-driven equatorial oceans, yet the validity of the parameterization is never addressed.

Figure 3.30 provides further evidence supporting the hypothesis that the ocean is resonating. The figure suggests that both the 4 and 5 day inertia-gravity waves are forced by the wind. But in Section 2.B.1 we showed that the meridional structure of the wind field is not a function of frequency in the 4-5 day band; consequently, insofar as we have established that the 4 and 5 day oceanic waves correspond to different meridional structures, those structures must be due to the establishment of oceanic normal modes.

The coherence amplitudes and phases for the 3.5-7 day band, from Figure 3.30, are summarized in Table 3.15. Positive phase indicates that sea level leads the wind component. The phase estimates in Table 3.15 suggest that sea level in the 4-5 day band lags north wind by 20° - 120° and lags east wind by 120° - 160° . The rapid phase variation in the sea level-wind coherences in Table 3.15 is suggestive of a resonant response (WG).

Since there is no indication in Figure 3.30 that wind and sea level are coherent at higher frequencies, we have no evidence that higher

*Moore and Philander (1977), studying the time-dependent response of the equatorial ocean to abrupt changes in the surface wind stress, obtained the same relationships between the symmetries of the wind forcing and the oceanic response.

meridional modes are directly excited by the wind.

Table 3.15

<u>Period (days)</u>	<u>Sea Level-North Wind</u>		<u>Sea Level-East Wind</u>	
	<u>Amp.</u>	<u>Phase</u>	<u>Amp.</u>	<u>Phase</u>
3.61	.29	146+ 35	(.12)	(45)
3.91	.53	-112+16	.23	144+48
4.28	.56	- 22+15	.36	-120+27
4.72	.33	- 94+30	.41	-157+23
5.27	.49	- 31+18	.22	-146+51
5.95	.36	2+27	.34	-123+29
6.84	.24	- 2+45	.22	129+51

*Values in parentheses have amplitudes below the 95% level of no significance. Error bars on phase are 95% confidence limits.

D.11 Summary and Discussion. We hypothesized at the beginning of this section that, in accordance with the linear theory of equatorially-trapped inertia-gravity waves: (1) the ocean is in resonance, that is, vertical and meridional modes have been established; (2) energy is concentrated (without specifying why) in the neighborhood of the frequency-wavenumber points where the theoretical zonal group velocity vanishes; and (3) peaks occurring in the tropical sea level spectra, as per (1) and (2), are first-baroclinic modes. In support of these hypotheses in the Pacific, we found the following:

- (1) the periods of the zero zonal group velocity points ($c_{gx} = 0$) for the first few meridional modes of the first baroclinic mode, computed with the aid of observed density data, correspond to the periods of observed sea level peaks at most "mid-Pacific" stations;
- (2) the theoretical meridional structures of the $n = 1$ and 2 meridional modes, at $c_{gx} = 0$ for $r = 1$, easily account for the observed distribution of sea level power;

- (3) the surface atmospheric fields do not have meridional dependences that are strong functions of frequency, whereas the meridional structure of sea level at 5 days ($n = 1$ mode) is very different from the 4-day ($n = 2$ mode) structure;
- (4) the surface atmospheric spectra do not have peaks corresponding to the higher meridional mode ($n > 2$) peaks observed in the sea level spectra;
- (5) the 4- and 5-day sea level peaks in the "mid-Pacific" have higher Q than corresponding peaks in the surface winds; and
- (6) the least convincing piece of evidence, due to the proximity of modes in frequency space: the coherence phase between sea level records, and between sea level and north wind, varied rapidly near the 4-day ($n = 2$) period as expected for normal modes of a linear system.

On the other hand, the observed sea level-sea level coherence phases produced ambiguous estimates of the zonal wavenumber for $n = 1$ and 2.

In addition, the lack of inertia-gravity peaks in the sea level spectra, and the occurrence of sea level-air pressure coherence in the 4-5 day band, at Galapagos and Truk suggest that resonance is not occurring in the eastern and far-west Pacific. The evidence for low-mode resonance in the Indian Ocean is also weak.

We now consider why energy is concentrated at zero zonal group velocity ($c_{gx} = 0$) points. The idea that energy accumulates where $c_{gx} = 0$ for equatorially-trapped waves can be traced at least as far back as Blandford (1966), but physical explanations of the causes of the energy accumulation have rarely been presented. There are at least three possible explanations, representing different dynamical situations, for the observed accumulation of low-mode inertia-gravity wave energy at $c_{gx} = 0$ in the "mid-Pacific":

- (1) The forcing is localized in physical space. Waves for which $c_{gx} \neq 0$

propagate away from the region of forcing leaving only waves near $c_{gx} = 0$ to be observed. (2) The forcing is the same strength across the basin, but, because of the distribution of rough topography and/or the presence of meridional boundaries, low-vertical-mode resonance occurs only in central portions of the basin where there is smooth topography. Low-vertical-mode waves generated over smooth topography that have $c_{gx} \neq 0$ will propagate into regions of rough topography, and be scattered into higher vertical modes, or will propagate into the side-wall boundary layers and be more quickly dissipated or scattered into other meridional modes (e.g., Moore (1968)). The low-vertical-mode energy lost from the smooth topography regions in this manner is not replaced since low-vertical-mode waves are not strong in the regions of rough topography even though the assumed forcing function is independent of position. Therefore, of all the low-vertical-mode waves, only those near $c_{gx} = 0$ are left to be observed in the smooth topography regions away from the boundaries. (3) The forcing is concentrated in small negative wavenumbers corresponding to the wavenumbers of the oceanic waves near $c_{gx} = 0$.

The 3rd case above is relevant for the two gravest meridional modes in the "mid-Pacific", given the wavenumber spectra of the surface meridional wind found in Section 2.B.1 (see also Section 2.E). However, the wavenumber distribution of the surface winds is broader at the frequencies corresponding to the higher meridional modes in the ocean, and no direct wind forcing of these higher modes has been detected. (N.b., case 3 is not excluded by the fact that the oceanic waves have a higher Q than the atmospheric forcing.)

The 1st case above (forcing localized in central-western Pacific), and possibly elements of the 2nd case (increasingly rough topography and/or proximity to a side-wall boundary), may explain the reduction of

low-vertical-mode inertia-gravity wave energy from the "mid-Pacific" to the Galapagos Islands. Only the 2nd case can explain the reduction of low-vertical-mode inertia-gravity wave energy from the "mid-Pacific" to the west.

For the benefit of those investigators worried about aliasing by the low-mode 4-5 day inertia-gravity waves, the amplitudes depicted in Figure 3.19 correspond to maximum surface current velocities of 4 cm/s, decreasing towards the bottom in accordance with the first-baroclinic mode structure function. Of course, at times the amplitude could be much larger.

D.12 Spectral Models of Equatorial Inertia-Gravity Waves. A simple spectral model, based upon the hypothesis of resonant, linear, inertia-gravity waves near the equator, is constructed and compared with the observed sea level spectra (Section D.12.a). At each island, the relative amplitudes of the peaks associated with the gravest meridional modes are reproduced, a natural consequence of the different meridional structures. Computation of the inertia-gravity model spectrum slightly poleward of the turning latitudes of the gravest meridional modes suggests the presence of "inertial" peaks in some sea level spectra (Section D.12.b).

Eriksen's (1979) recent extension of the "Garrett and Munk" internal wave spectrum to the equatorial oceans is compared with sea level observations in Section D.12.c.

The two spectral models studied in this section, which take different approaches to the specification of the energy spectrum, emphasize the arbitrariness of the spectral forms. Indeed, there are more degrees of freedom in choosing the form of the equatorial internal wave spectrum than the form of the mid-latitude spectrum, yet much less data. Some of the unique dynamics and kinematics of the equatorial inertia-gravity waves, which may lead to a better understanding of the characteristics of the

equatorial spectra, are discussed in Section D.12.d.

D.12.a. Simple Model to Explain Observed Sea Level Spectra. The expression for the sea-surface displacement energy, obtained using the definitions (3.9) and the corresponding solutions to (1.23), is

$$\mathcal{J}^2(n, r, \sigma) = \hat{q}^2 \left(\frac{dQ_r(z)}{dz} \right) A^2 \frac{h_r \epsilon_r^{1/2}}{g} e^{-\sqrt{\epsilon_r} \theta^2} \left[\frac{H_{n+1}/2}{\sqrt{\epsilon_r} \sigma - s} - \frac{n H_{n-1}}{\sqrt{\epsilon_r} \sigma + s} \right]^2, \quad \begin{matrix} r=1,2,\dots \\ n=1,2,\dots \end{matrix} \quad (3.15)$$

A^2 is a normalization constant which is chosen, following Eriksen (1979), so that \hat{q}^2 is only a function of $\bar{E}_H(n, r, \sigma)$, the total average energy/unit surface area/unit frequency; that is, \bar{E}_H is defined by

$$\bar{E}_H \equiv \left[\frac{\rho_0}{2} \int_{-D}^H \int_{-\infty}^{\infty} \left(u^2 + v^2 + \frac{g^2 \rho^2}{N^2 \bar{\rho}^2} \right) d\theta dz \right] / \left[\frac{2\sqrt{2n+1}}{\epsilon_r^{1/4}} \right], \quad (3.16)$$

where $\left[\frac{2\sqrt{2n+1}}{\epsilon_r^{1/4}} \right]$ is the width of the equatorial waveguide for meridional mode n of baroclinic mode r .

With the Brunt-Väisälä profile (3.8), $Q_r(z)$ is given by (3.12).

Separating the vertical structure functions from the horizontal functions in (3.16), B_r in (3.12) is determined by normalizing the Q_r , such that

$$\int_{-D}^H \frac{N^2 Q_r^2}{c_r^2} dz \approx \int_{-D}^H \left(\frac{dQ_r}{dz} \right)^2 dz = 1, \quad (3.17a)$$

so that

$$B_r = \frac{c_r}{N_0} \sqrt{2\lambda} \left\{ \mathcal{J}_i^2(q_r) \cdot \left[1 + \lambda^2 q_r^2 (H-h_r)^2 \right] - \frac{4}{\pi^2 q_r^2} \right\}^{-1/2}, \quad (3.17b)$$

Evaluation of the second integral in (3.16), over θ , finally yields

$$A^2 = 2\sqrt{2n+1} \left[2^n n! \sqrt{\pi} \right]^{-1} \cdot \left[1 - \frac{\sqrt{\epsilon_r} (n+1)}{(\sqrt{\epsilon_r} \sigma - s)^2} + \frac{\sqrt{\epsilon_r} n}{(\sqrt{\epsilon_r} \sigma + s)^2} \right]^{-1}, \quad (3.18)$$

so

$$\bar{E}_H(n, r, \sigma) = \frac{\rho_0}{2} \hat{q}^2(n, r, \sigma) \quad (3.19)$$

Relationships analogous to (3.15) and (3.18) for the inertia-gravity waves can also be obtained for the mixed Rossby-gravity and Kelvin waves, the

former being obtained by setting $n = 0$ in (3.15) and (3.18).

With the normalization above, the observed $\hat{q}^2 = 2030$ (1550) $(\text{m/s})^2/\text{cph}$ for $n = 1(2)$ (from Figure 3.19), where $N_0 = .0065$ rad/s, $\lambda = (1.3 \text{ km})^{-1}$, $D = 4 \text{ km}$ and $H = 100 \text{ m}$ have been used in (3.12), (3.13), and (3.17).*

A spectral model constructed from the observed inertia-gravity characteristics, summarized in the previous subsection, can only be a function of frequency, since no information on baroclinic modes other than the first has been obtained here, and since the horizontal wavenumber information (Section 3.D.7) is ambiguous. Therefore, we assume that, after integration over the zonal wavenumber, the energy for each meridional mode, n , is distributed as a Gaussian function of frequency centered at the frequency σ_{0n} , corresponding to the zero zonal group velocity point for n . In accordance with the results of Section 3.D.9, the Q ($= \frac{\sigma_{0n}}{\Delta\sigma}$) of each Gaussian is assumed independent of mode number. The full form of the model spectrum is given by

$$\bar{E}_H = K A(r) B(\sigma, n) \quad , \quad (3.20a)$$

where

$$A(r) = \sqrt{h_r} \left(1 + \sqrt{\frac{h_r^*}{h_r}}\right)^{-2} / \sum_{r=1}^{r_{\max}} \sqrt{h_r} \left(1 + \sqrt{\frac{h_r^*}{h_r}}\right)^{-2} \quad , \quad (3.20b)$$

and

$$B(\sigma, n) = \sigma_{0n}^{-4} \frac{1.67Q}{\sqrt{\pi}} \exp \left[-2.78 Q^2 \left(1 - \frac{\sigma}{\sigma_{0n}}\right)^2 \right] \quad , \quad (3.20c)$$

where the symbols are as previously defined.

The vertical wavenumber dependence, $A(r)$, is included in the spectrum so we can test whether the second and/or third baroclinic modes will produce a measurable deflection of sea level. The form of $A(r)$ was chosen

*If we had instead assumed that \hat{q}^2 is only a function of E_x , the total energy/unit zonal distance/unit frequency (i.e., $E_x = \bar{E}_H \cdot 2\epsilon_r^{-1/4} / \sqrt{2n+1}^x$), then $\hat{q}^2 = 400$ (391) $(\text{m/s})^2/\text{cph}$ for $n = 1(2)$.

so that, like Eriksen's (1979) spectrum, the vertical dependence asymptotes to a -2 power law at high frequency and high baroclinic mode number (after summation over the meridional modes), thus matching the slope of the mid-latitude internal wave spectrum. $A(r)$ weights the lowest vertical modes more heavily at all frequencies than the vertical wavenumber dependence used by Eriksen (1979) (see Equation 3.21).

The exponent of σ_{0n} in (3.20c) is chosen so that the spectrum asymptotes to a σ^{-2} dependence as σ increases, in agreement with the observed sea level slope between 1 and 2.5 days in the "mid-Pacific" (Figure 3.18b). The observed frequency-dependence of internal wave displacement spectra at mid-latitude is also σ^{-2} (Cairns (1975)).

It must be emphasized that the spectrum (3.20) is highly contrived and not unique. The spectrum, in conjunction with (3.15), is meant only to test (1) whether the particular relative amplitudes of the inertia-gravity peaks at each island are the direct consequence of the meridional structure functions for each mode, n ; (2) whether the spectral levels between 1 and 2.5 days observed in Canton and Christmas sea level (Section 3.D.4) can be reproduced; and (3) whether the second and/or third baroclinic modes are necessary to achieve (1) and (2).

After numerous tests, in which the forms of $A(r)$ and $B(\sigma, n)$ were varied somewhat, we found that (1) only the first meridional mode of each baroclinic mode, other than $r = 1$, produces a clearly identifiable peak in the model sea level spectra; (2) the second baroclinic mode, but not higher modes, significantly affects the sea level spectrum (mainly by contributing to the spectral level in the one- to three-day band); and (3) the second meridional mode of the first-baroclinic mode (~ 4 -day period) has slightly more observed energy than the model spectrum (3.20) allows.

With these points in mind, the spectrum (3.20) in conjunction with (3.15) was computed for the islands in Figure 3.15 using $r_{\max} = 2$, $Q = 11$, $h_r^* = h_6$, and $K = 2.82 \times 10^5 \text{ ((m/s)}^2\text{/cph)(kg/m}^2\text{)}$, (except that $K = 4.5 \times 10^5$ for the $n = 2$, $r = 1$ mode), where K was chosen to provide the best match for Christmas. Without loss of generality, $s = 0$ in (3.15) and (3.18) to simplify the computation. The computation of $\frac{dQ_r}{dz}$ from (3.12) and (3.17) employs $\lambda = (1.3 \text{ km})^{-1}$, D and H from topographic and density data (see Section 3.D.1), and an N_0 adjusted so that h_1 agrees with observed values (Table 3.11). Varying Q does no more than change the widths of the distinguishable peaks in the model spectra.

The computed spectra are superimposed on the observed sea level spectra of the "mid-Pacific" islands in Figure 3.31. The observed Canton spectrum is nearly identical to the computed spectrum*, with Canton showing slightly stronger $n = 1$ and 2 amplitudes than Christmas. The comparisons between the computed and observed spectra for the remaining islands in Figure 3.31 are not bad, but are certainly not flawless. The broad observed peak at ~ 3.5 days at Fanning is seen to be due to a combination of the $n = 2$ and 3 modes, but the observed peak at ~ 5 days (the period of the $n = 1$ mode at Fanning) is not obtained from the model since Fanning is near a node of the $n = 1$ mode (see Figure 3.19a). The observed Majuro spectrum has an unexplained excess of energy in the $n = 1, 2$, and 3 modes, but is nicely matched by the model spectrum in the 1-3 day band. The stations nearest the equator (Nauru, Ocean and Jarvis) do not have as much $n = 1$ energy as computed from the model (this is clear from Figure 3.19 also). The strongest observed peak at Hull, at ~ 3.5 days, is shown to be the $n = 3$

*Remember that some background "noise" is present in the observed spectra that is not included in the computed spectra, e.g., the 4-5 day barotropic oscillation of Section 3.C.

Figure 3.31 - Computed inertia-gravity wave sea level spectra (dashed lines), from the model (3.20), superimposed on observed sea level spectra (as in Figure 3.15).

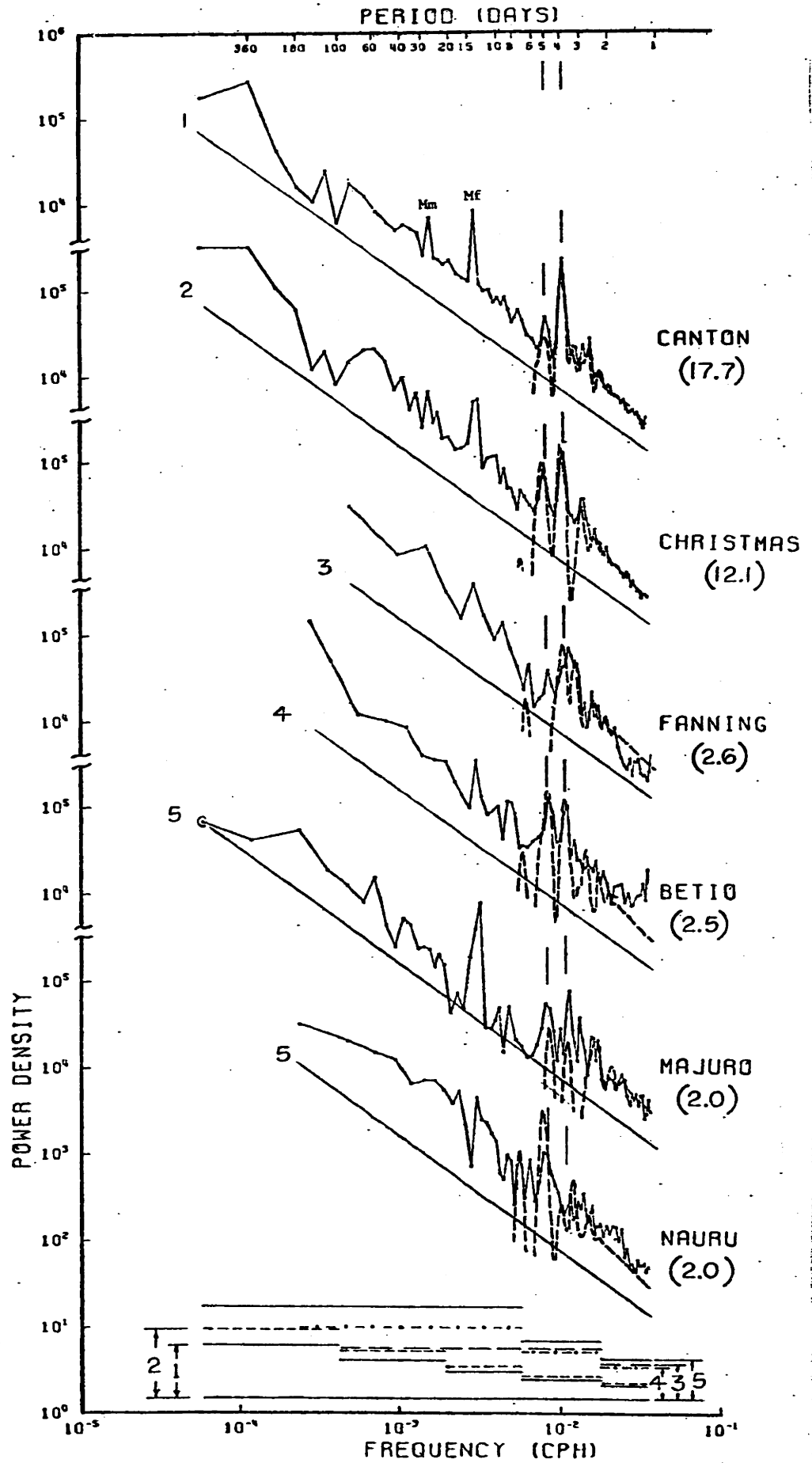


Figure 3.31a

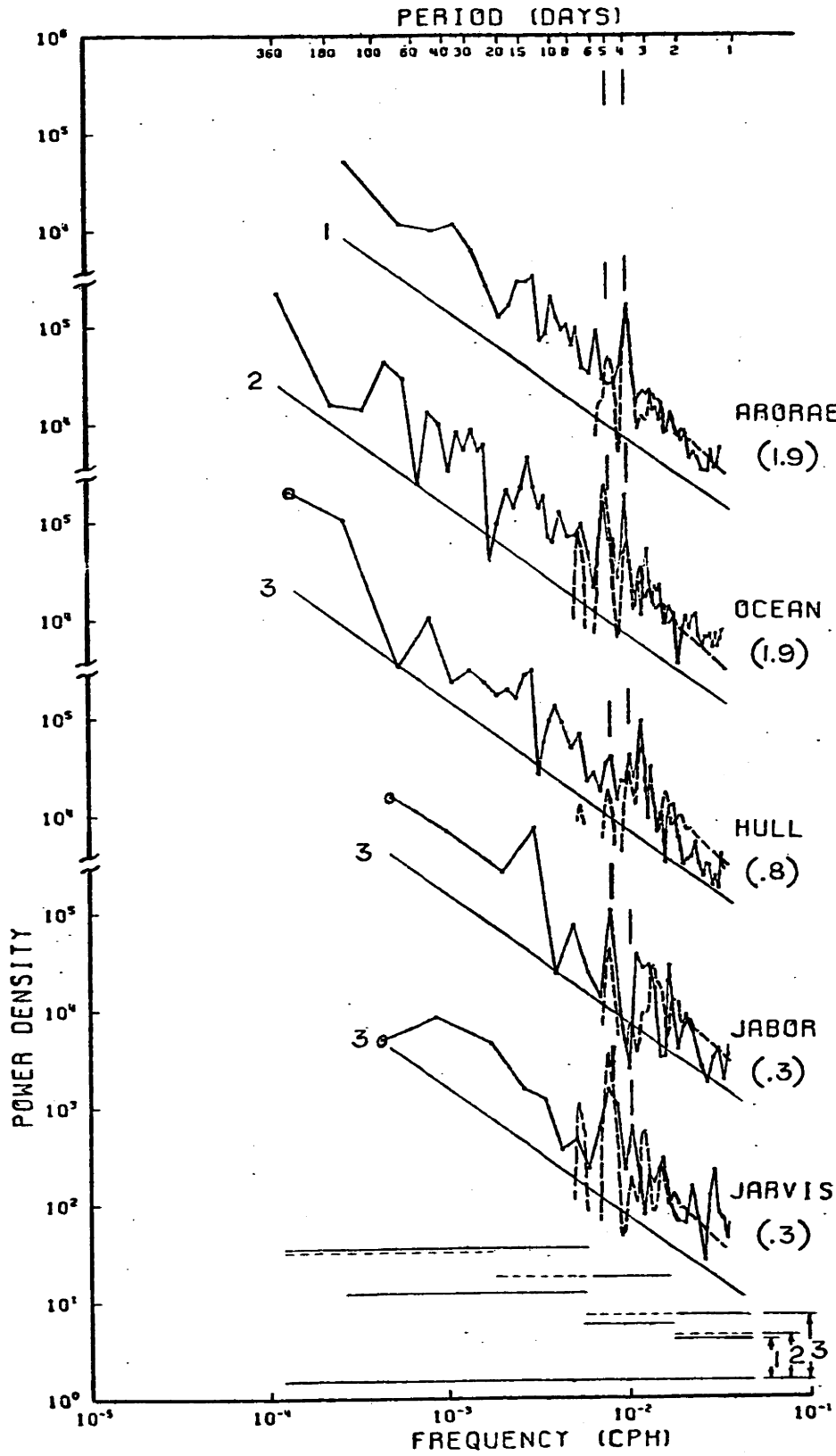


Figure 3.31b

mode, but otherwise Hull's spectrum is not well-matched by the model. A glaring discrepancy occurs at Arorae where the apparent $n = 1$ peak in the observed spectrum is clearly displaced in frequency relative to the model peak.

Much of the disagreement between the observed and model spectra is probably a consequence of the relatively short data lengths (see Section 3.D.8 and especially Figures 3.26 and 3.27). Nonlinear interaction with the mean equatorial currents (McPhaden and Knox (1979)) and diffraction may produce some of the discrepancies noted above.

The computed first-meridional, second-baroclinic mode apparently accounts for observed peaks at Fanning, Nauru, Ocean and Jarvis, but is clearly not strong enough to explain the observed peaks at Canton and Christmas which occur at the period of the $n = 1$, $r = 2$ mode (see Section 3.D.6).

D.12.b Off-Equatorial Sea Level Inertial Peaks. The model spectra for Kwajalein ($8^{\circ}44'N$, $167^{\circ}44'E$) and Eniwetok ($11^{\circ}21'N$, $162^{\circ}21'E$) are superimposed on the observed sea level spectra for these islands in Figure 3.32a. The inertial frequencies for both islands are indicated. The model spectra have apparent "blue-shifted" inertial peaks (a consequence of the equatorial inertia-gravity model, noted by Eriksen (1979)). These correspond, although not exactly, to peaks in the observed sea level spectra, thus solving a puzzle dating back to the work by Groves and Hannan (1968). Superposition of the observed sea level spectra from the two islands (Figure 3.32b) further enhances the suggestion of inertial peaks.

The "blue" shift of the model inertial peak can be shown to be a direct consequence of the shapes of the meridional structure functions, in this case the Hermite functions. The amount of the frequency shift at a

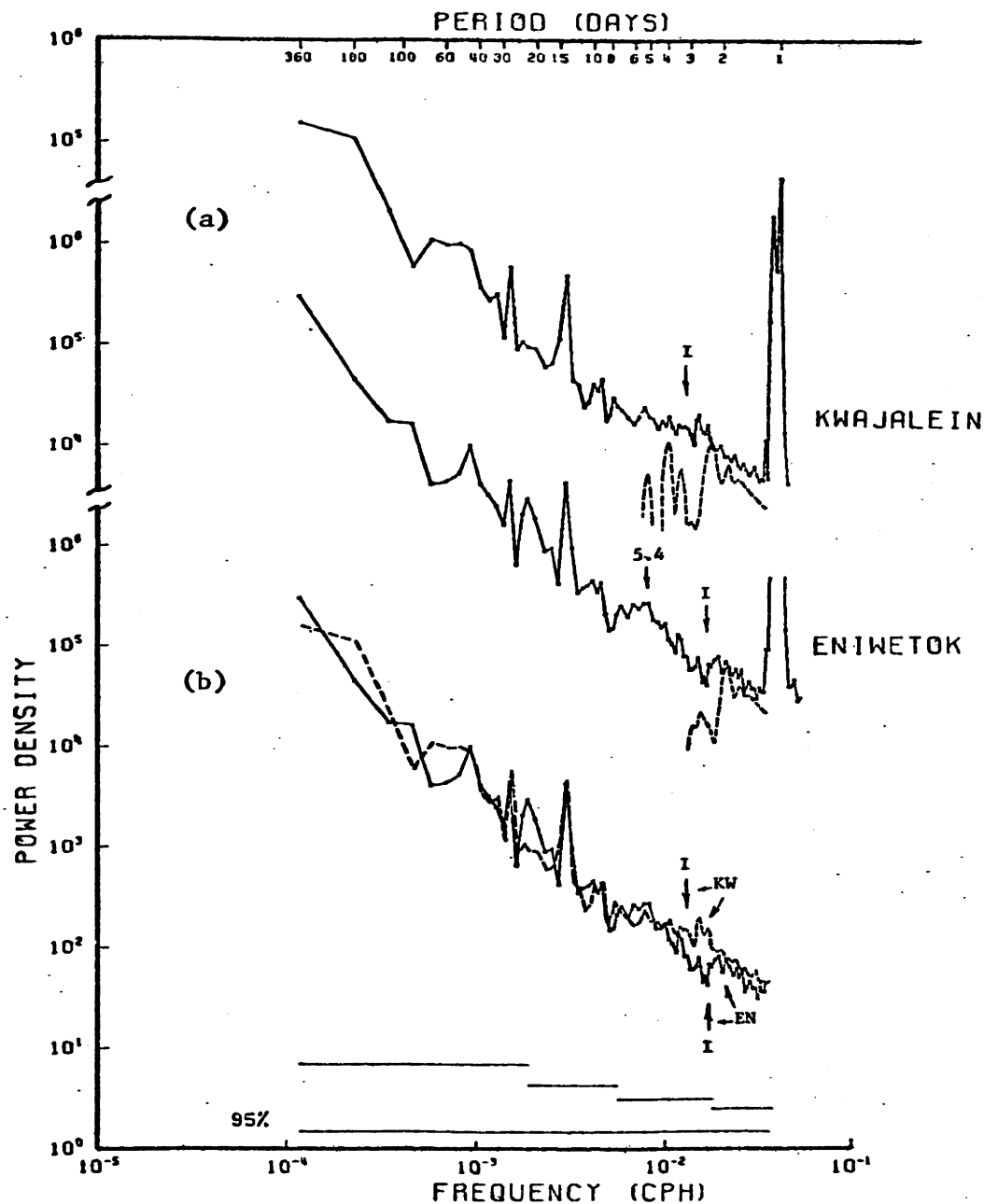


Figure 3.32 - (a) Computed inertia-gravity wave sea level spectra, from the model (3.20), superimposed on observed sea level spectra from Kwajalein ($8^{\circ}44'N$, $167^{\circ}44'E$) and Eniwetok ($11^{\circ}21'N$, $162^{\circ}21'E$). The inertial frequencies for each island are indicated. Plotted as in Figure 3.1. (b) Superposition of the observed sea level spectra from Kwajalein and Eniwetok. Inertial frequencies are indicated. Plotted as in Figure 3.1.

particular latitude depends upon the distribution of energy in zonal and vertical wavenumber space. However, the differences between the frequencies of the observed peaks (~15% above inertial) and the model peaks (~30% above inertial), in Figure 3.32, are probably due to the inaccuracy of the equatorial β -plane approximation for studying inertial waves at 10°N.

D.12.c. Comparison of Eriksen's (1979) Model Spectrum with Observed Sea Level Spectra. Eriksen (1979) made the first attempt at constructing a model spectrum of inertia-gravity waves near the equator, using moored current and temperature measurements from the western Indian Ocean. Although his model is not unique and does not explain the upper ocean observations, it is a significant contribution and deserves examination with regard to the sea level spectra studied here.

Eriksen's model is, in our notation,

$$\bar{E}_H(n, r, \sigma) = \frac{K}{\epsilon_1} \frac{(1 + \sqrt{h_r^*/h_r})^{-3}}{\sum_{r=1}^{m(n)} (1 + \sqrt{h_r^*/h_r})^{-3}} \left(\sigma^2 - \frac{s}{\epsilon_r \sigma}\right)^{-1/2} \sigma^{-3}, \quad \begin{matrix} r = 1, 2, \dots \\ n = 0, 1, 2, \dots \end{matrix}, \quad (3.21)$$

where s is uniquely determined from the dispersion relations, given n , r and σ . For Kelvin waves, K is replaced with $K/3$, and $(\sigma^2 - \frac{s}{\epsilon_r \sigma})^{-1/2}$ is replaced with σ^{-1} . Also, following Eriksen (1979), $N(z)$ is assumed to be constant so, after normalization by (3.23a),

$$Q_r(z) = \sqrt{\frac{2}{D}} \sin m(z+D), \quad (3.22a)$$

where

$$m = \frac{N_0}{\sqrt{g h_r}} \quad \text{and} \quad \sqrt{h_r} = \frac{N_0 D}{\sqrt{g} \pi r} \left(1 - \frac{D N_0^2}{r^2 \pi^2 g}\right). \quad (3.22b)$$

The model (3.21) is more sophisticated than (3.20) since the distribution of energy in zonal wavenumber space is explicitly specified.

Equation (3.21) is based on the observation of isotropy at high frequencies and the requirement that the spectrum asymptote to the slopes of the mid-latitude internal wave spectrum at high frequency and vertical wavenumber.

After a number of tests, we found that the form of $N(z)$, either exponential or constant, does not affect the computed sea level spectra of either model more than a few percent. The only way sea level is sensitive to the density field is through changes in the eigenvalues, h_r . As mentioned before, the vertical mode dependence in (3.21) weights the higher modes more heavily than our model (3.20). We still find that for computation of the sea level spectra only the first two baroclinic modes are important.

The spectra (excluding Kelvin and mixed Rossby-gravity waves) computed from (3.15), with (3.18), (3.19), (3.21) and (3.22), for Canton and Christmas are superimposed on the observed spectra in Figure 3.33, using $r_{\max} = 2$ and $h_r^* = h_6$, $D = 4$ (5.1) km and $N_0 = .00230$ (.00187) rad/s for Christmas (Canton). The model spectrum for Christmas, including Kelvin and Yanai waves, is also shown in Figure 3.33. K has been chosen so that the -2 slope at Christmas, between 1 and 2.5 days, is well-matched by the model. Figure 3.33 clearly indicates that Eriksen's model does not contain enough low-meridional-mode energy, relative to the higher meridional modes, to reproduce the observed sea level spectra in the mid-Pacific. It is also clear from Figure 3.33 that for the first-baroclinic mode the Kelvin and mixed Rossby-gravity waves are weighted too heavily relative to the inertia-gravity waves.

Eriksen's (1979) model was constructed using exclusively Indian Ocean data so it is more relevant to compare his model with observed Indian Ocean sea level spectra than with Pacific Ocean spectra. In Figure 3.34a

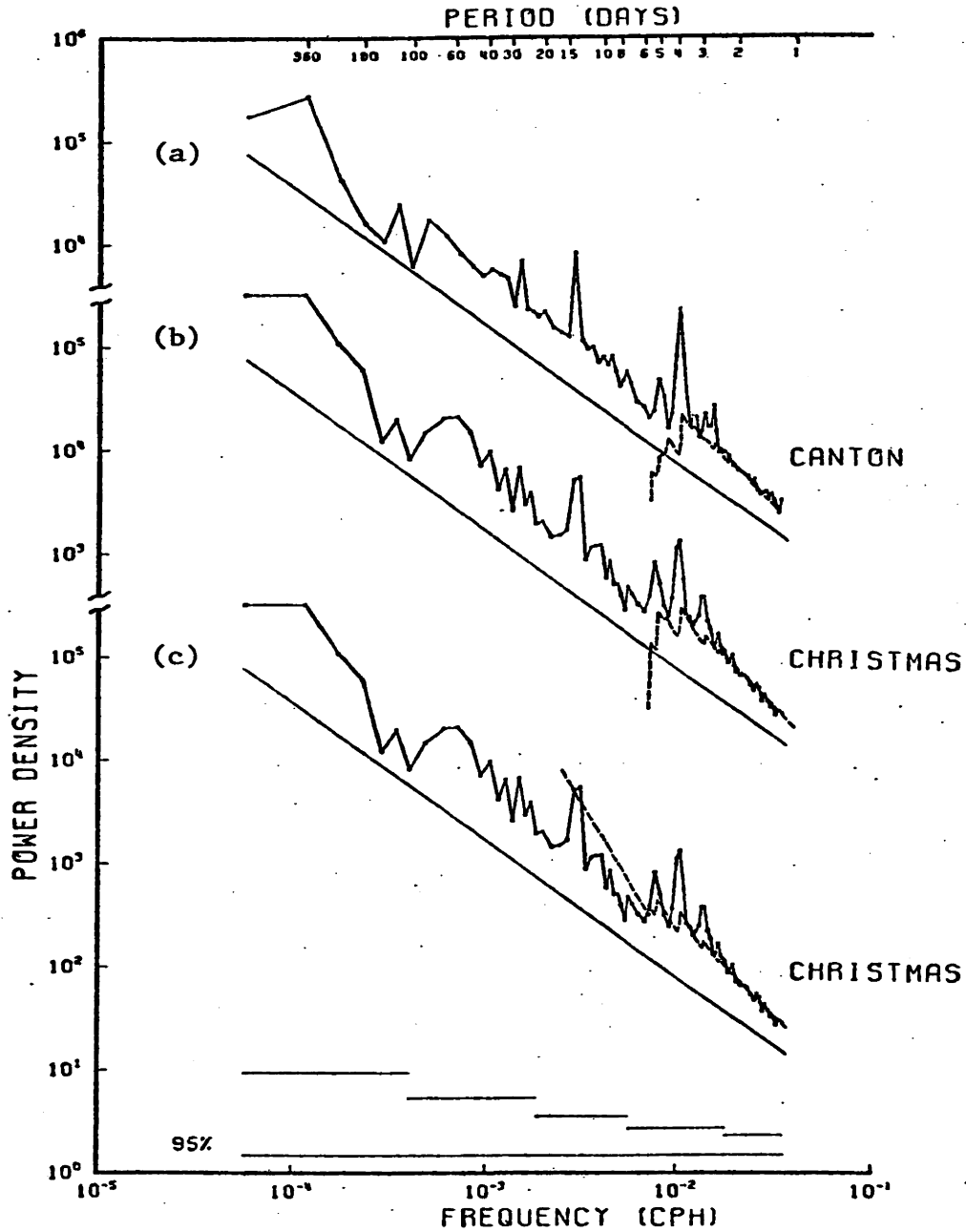


Figure 3.33 - Computed inertia-gravity wave sea level spectra (dashed) from Eriksen's model, superimposed on observed sea level spectra from (a) Canton, (b) and (c) Christmas. The model Kelvin and Yanai waves are included in (c) only. Reference lines have a $-4/3$ slope. Otherwise, as in Figure 3.1.

Eriksen's model spectra (with and without Kelvin and mixed Rossby-gravity waves) for Addu Atoll and Port Victoria are superimposed on the observed spectra, with $r_{\max} = 2$ and $h_r^* = h_6$. (Again the relevant equations are (3.15), (3.18), (3.19), (3.21), and (3.22). $D = 4$ km and $N_0 = .00196$ rad/s, so that $c_1 = 2.5$ m/s for both stations. The simple model spectrum devised in the present study, (3.20), has also been computed*, in conjunction with (3.15), (3.18), (3.19), (3.12), and (3.17), for Addu Atoll and Port Victoria and is superimposed on the observed spectra in Figure 3.34b. We have used $Q = 11$, $h_r^* = h_6$, $D = 4$ km, $H = 25$ m, $\lambda = (1.3 \text{ km})^{-1}$, and $N_0 = .00573$ rad/s for both stations. To match the Indian Ocean sea level spectra, in both models K is greater than the value used in the Pacific, which is not so much a statement that there is more inertia-gravity energy in the Indian Ocean as it is a statement that the eigenvalues are smaller in the Indian Ocean for each vertical mode (see Section 3.D.5).

We leave it to the reader to decide which model most satisfactorily corresponds to the observed sea level spectra. Neither model is a perfect match. The paucity of data is a paramount problem.

D.12.d. Caveats. This is a good time to reiterate that the spectral models discussed above are only preliminary attempts at modelling the equatorial inertia-gravity wave fields. Eriksen's (1979) model, constructed on the basis of isotropy, ignores the dispersion characteristics of the equatorial waves, i.e., the existence of zero zonal group velocity ($c_{gx} = 0$) points near which energy may accumulate. It is curious that, although the notion of energy accumulation near zero group velocity points is readily accepted (Blandford (1966), Munk and Phillips (1968)), rigorous physical explanations for this phenomenon do not exist. Some plausible explanations

*The $n = 2$, $r = 1$ mode is not given the extra energy that it was for the Pacific Ocean.

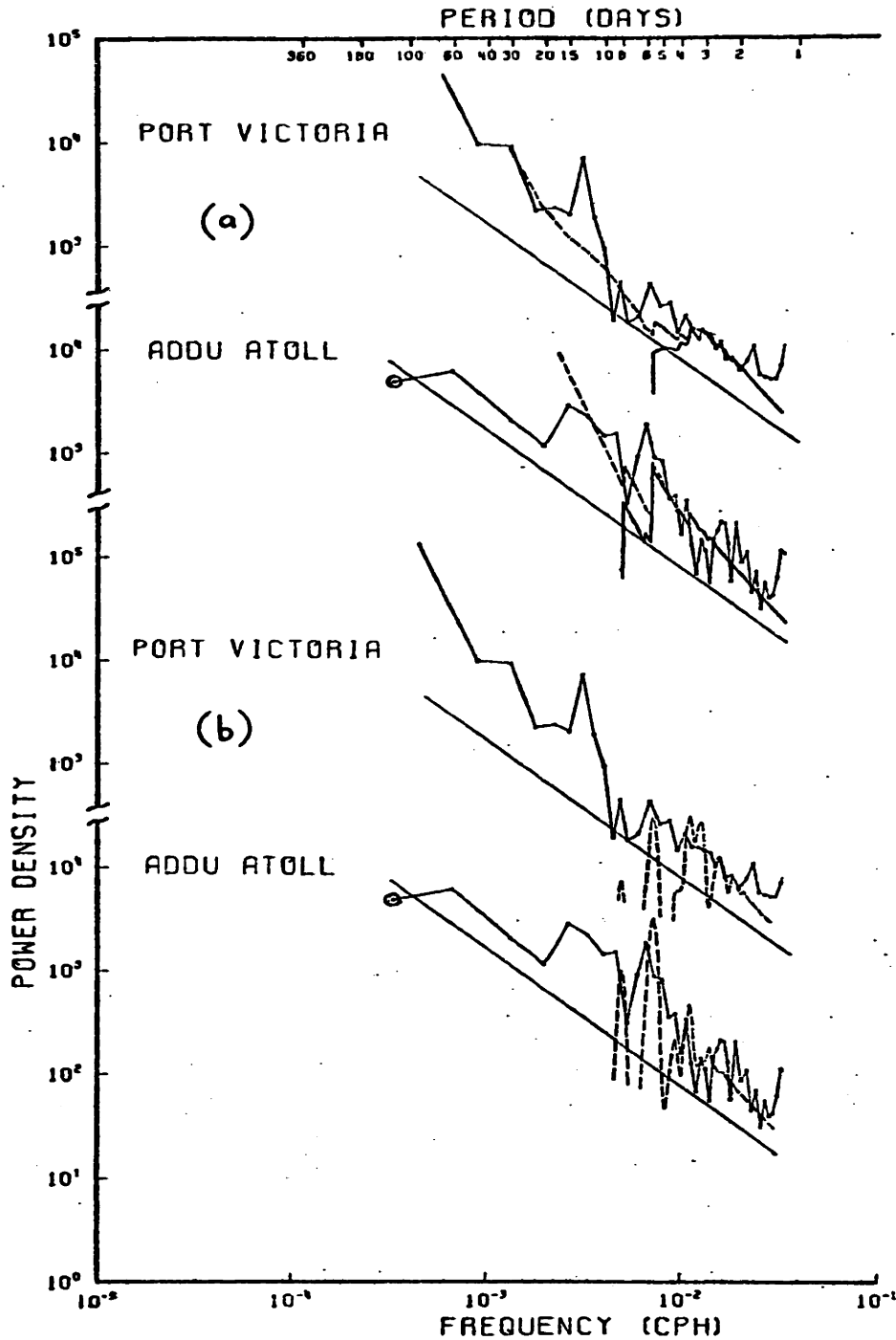


Figure 3.34 - Computed inertia-gravity wave sea level spectra, using (a) Eriksen's model, and (b) the model of equation (3.20), superimposed on observed sea level spectra from Port Victoria and Addu Atoll. The observed spectra are the solid lines with dots marking the spectrum points. Eriksen's model is computed with (dashed lines) and without (solid lines) Kelvin and Yanai waves. All the model spectra were computed assuming $c_1 = 2.5$ m/s. Otherwise, plotted as in Figure 3.1.

for accumulation of energy near the $c_{gx} = 0$ points of equatorial inertia-gravity waves were discussed in Section 3.D.11.

The model (3.20) we constructed to explain the equatorial inertia-gravity sea level spectra can not, of course, be used to compute coherence and has not been tested for compatibility with Eriksen's (1979) observations. It remains to be seen whether a frequency-wavenumber spectrum incorporating the concept of energy accumulation near $c_{gx} = 0$ points will provide a demonstrably better description of the equatorial inertia-gravity fields for vertical modes other than the first-baroclinic mode than Eriksen's (1979) model.

E. Equatorially-Trapped Waves at Periods of 7-80 Days in the Pacific

E.1 6.5-7.5 Day Inertia-Gravity Wave? We have already presented evidence regarding the existence of the first-meridional, second-baroclinic mode inertia-gravity wave (~ 7 -day period) in the "Mid-Pacific" sea level spectra (Section 3.D.6 and 3.D.12; see especially Figures 3.1 and 3.2 and Figure 3.31). The problem with the interpretation of the ~ 7 -day peak at Christmas and Canton as due to the $n = 1, r = 2$ mode is that the theoretical, linear meridional structure of this mode has nodes close to these islands, as is clear from the model summation in Figure 3.31.

The coherence between Canton and Christmas sea level (Figure 3.30a) is significantly non-zero at ~ 7 days with westward phase propagation (as required for the $n = 1, r = 2$ mode), but the estimated wavenumber is $\sim -3 \pm 1.5$ (95% error bars) does not match the theoretical $s \sim -7$.

There is coherence between sea level and east wind at ~ 7 days at Canton (Figure 3.30b), and a high-resolution calculation (not shown) indicates coherence between sea level and north wind at ~ 7 days at (

Perhaps the 7-day oscillation is simply a nonresonant, forced oscillation responding to the previously mentioned (Section 2.C) atmospheric Rossby-gravity wave at 7-9 days period.

E.2 9-10 Day Rossby-gravity Wave? Wunsch and Gill (1976) argued that if the surface atmospheric fields at the equator at ~ 9 days were dominated by small zonal wavenumbers, one might expect the first-baroclinic mixed Rossby-gravity wave to be excited and thence detected in sea level spectra in the Pacific, since the $r = 1$, mixed Rossby-gravity dispersion curve crosses the $s = 0$ axis at ~ 9 days (see Figure 1.1).

We found in Section 2.E that at ~ 9 days the equatorial Pacific surface wind wavenumber spectra are peaked at small negative wavenumbers, so in accordance with Wunsch and Gill's argument it is no surprise to find strong coherence between Canton and Christmas sea level at 9-10 days (Figure 3.25a). The coherence is stronger than occurs in the surface wind field over a comparable distance, suggesting oceanic resonance, and there is no confusion with the 9-day tide discussed earlier.

The coherence phases at 9-10 days in Figure 3.25a suggest either eastward propagation at $s \sim 6-11$, or westward propagation (assuming an equatorial node) with $s \sim -1.6$ to -6.7 . Averaging the coherence estimates from 8.5 to 10.4 days, after excluding the estimate at the 9-day tide period, yields $s \sim -4.5 \pm 1.5$. With this wavenumber estimate and the first-baroclinic mode eigenvalue, $\sqrt{\epsilon_1} \sim 306$ (Table 3.11) for Canton, the dispersion relation (1.33a) gives the mixed Rossby-gravity period $T \sim 9.9 \pm 0.4$ days, in excellent agreement with the observed period.

The coherences between Canton and Arorae sea level, and Canton and Fanning sea level, are consistent with the above Rossby-gravity wave interpretation at 9-10 days. None of the other sea level coherence pairs have

significant amplitude at 9-10 days. Also, the 9-10 day sea level power is not particularly robust compared to the background (see Figure 3.15) so we cannot test whether an equatorial minimum in the power exists, as expected for a Rossby-gravity wave. (We would also have to eliminate the 9-day tide power before attempting this test). Consequently, there is not yet enough evidence to identify unequivocally the presence of a resonant, mixed Rossby-gravity wave at 9-10 days in the Pacific.

Note that there is some coherence between sea level and surface wind at Canton at 9-10 day periods (Figure 3.30). Sea level leads north wind by 90° .

E.3. 35-80 Day Kelvin Waves. Tropospheric waves with periods of 30-60 days have been identified in the surface wind fields of the equatorial Pacific and Indian Oceans (see Section 2.D). The waves have characteristics similar to Kelvin waves and have been modeled as viscous Kelvin waves by Chang (1977). Gill (1974) was the first investigator to suggest that excess energy in Canton's sea level spectrum at 35-80 days corresponds to the excess zonal wind energy due to the atmospheric Kelvin wave.

The power density spectra of the longest equatorial sea level records (Canton and Christmas in Figure 3.35) suggest the occurrence of excess energy (broad "peaks") in the 35-80 day band. Similar "peaks", however, also occur in the 35-80 day band of sea level spectra farther from the equator, e.g., Kwajalein ($8^\circ 44' N$) and Eniwetok ($11^\circ 21' N$) in Figure 3.32. What makes the equatorial sea level "peaks" more interesting is that the fluctuations are coherent over large zonal distances, whereas away from the equator there is no coherence in the 35-80 day band over even relatively short distances. Kwajalein and Eniwetok are not coherent in the 35-80 day band although the stations are only about 650 km apart.

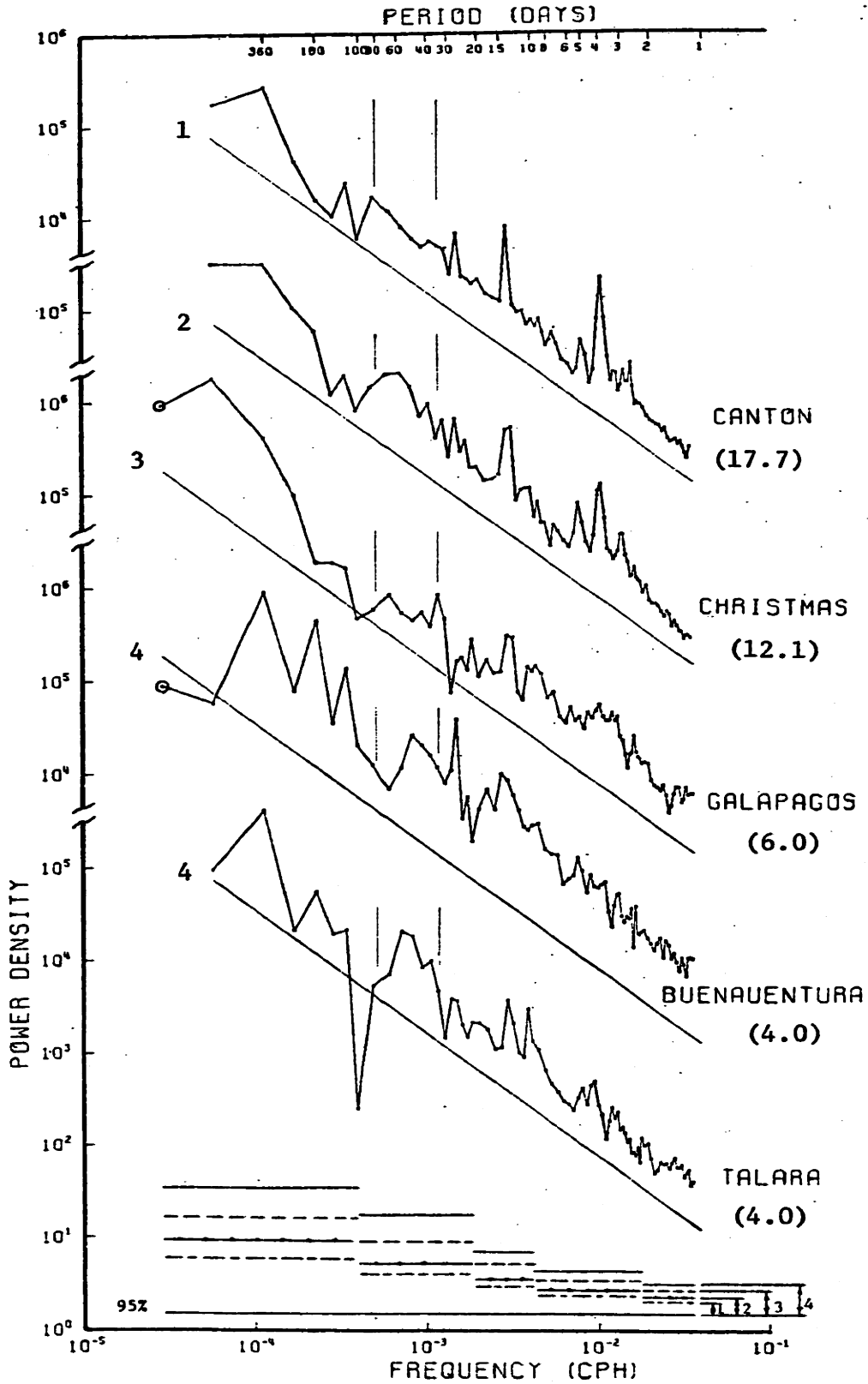
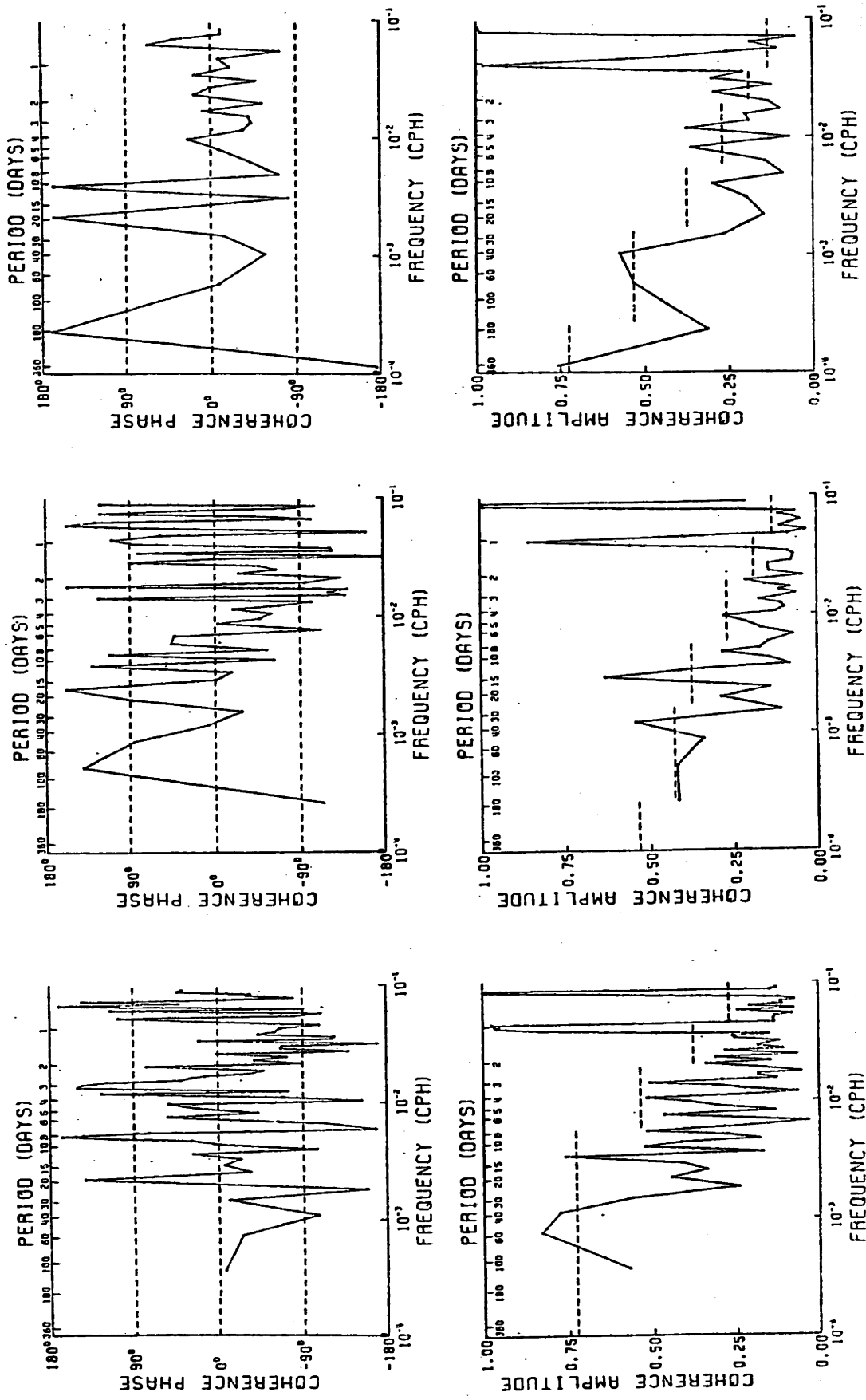


Figure 3.35 - Sea level spectra from Canton, Christmas and eastern Pacific stations exhibiting broad "peaks" in the 35-80 day band. Reference lines have a $-4/3$ slope. Otherwise plotted as in Figure 3.1.

It will be shown in this section that the equatorial ocean's response to the tropospheric Kelvin wave is also a long-wavelength Kelvin wave which can be traced from the Gilbert Islands ($\sim 170^\circ\text{E}$) to South America. This is the first time that propagation along the Pacific equatorial waveguide has been observed.

Figure 3.35 displays near-equatorial sea level spectra from the eastern Pacific, including coastal stations, along with the "mid-Pacific" Canton and Christmas spectra. All stations have at least four years of data, as indicated. Each spectrum has a "peak" (or, rather, "hump") of energy in the 35-80 day band, although only the "humps" at Christmas and Talara are significant features (at the 95% level).

More indicative than the individual power spectra, the coherences between the stations are strong in the 35-80 day band. Figure 3.36 demonstrates coherence in the 35-80 day band from Ocean Island ($169^\circ 35'\text{E}$) to Buenaventura ($77^\circ 5'\text{W}$). (See also the coherence between Canton and Christmas in Figure 3.25). Table 3.16 summarizes the coherences between equatorial Pacific stations in the 35-80 day band that are significantly non-zero at the 95% level. The only interpretation consistent with all of the phases in Table 3.16 is that of eastward propagation at small wavenumber. Estimates of the zonal wavenumber are also given in Table 3.16. The weighted average of the wavenumber estimates is 3.6 (excluding those estimates obtained from station pairs involving South America stations). Propagation along the South American coast is not indicated from the last two station pairs in Table 3.16, but then they are not separated by very large distances and are not very far from the equator.



(a) Canton-Ocean

(b) Galapagos-Canton

(c) Buenaventura-Galapagos

Figure 3.36 - Coherence amplitudes and phases between selected equatorial Pacific stations. Positive phase indicates the first station leads the second. The 95% level of no significance for the amplitude is shown. (a) Canton-Ocean. (b) Galapagos-Canton. (c) Buenaventura-Galapagos.

Table 3.16 - Sea Level-Sea Level Coherences in the 35-80 Day Band

<u>Station Pair</u> ⁺	<u>Number of Years</u>	<u>Zonal Separation (degrees)</u>	<u>Coherence</u>		<u>Zonal Wavenumber</u>
			<u>Ampl.</u>	<u>Phase*</u>	
Nauru-Betio	1.5	6.0	.81	32 _± 19	5.3 _± 3.2
Ocean-Canton	1.9	18.8	.61	64 _± 35	3.4 _± 1.9
Arorae-Canton	2.0	11.5	.52	38 _± 39	3.3 _± 3.4
Canton-Christmas	10.5	14.2	.53	50 _± 17	3.5 _± 1.2
Canton-Galapagos	6.0	82.1	.41	321 _± 32	3.9 _± 0.4
Christmas-Galapagos	5.0	67.9	.32	209 _± 42	3.1 _± 0.6
Galapagos-La Libertad	4.0	8.7	.52	64 _± 38	7.4 _± 4.4
Galapagos-Buenaventura	3.0	12.5	.50	35 _± 37	2.8 _± 3.0
Buenaven.-La Libertad	3.0	-	.66	17 _± 30	-
La Libertad-Talara	2.0	-	.69	-3 _± 37	-

⁺Westernmost station is listed first.

*Positive phase indicates that first station leads second. Error bars are 95% confidence limits.

Using the dispersion relation (1.32) for Kelvin waves, the estimate of $S = 3.6$, and the center-frequency $\sigma = .010268$ ($T \approx 49$ days), we obtain an estimate $\sqrt{\epsilon} \approx 351$, and therefore $h \approx .71$ m ($\sqrt{gh} \approx 2.65$ m/s). This value of the equivalent depth is within the bounds of our estimates of the equivalent depth for the first-baroclinic mode in the equatorial Pacific (Section 3.D.1), suggesting that the first-baroclinic mode is established and the ocean is resonating. The vertical group velocity for this oscillation (assuming a constant N ocean with $N \approx .0023$ s⁻¹; see Philander (1978)) is large enough that a vertical mode could be established in ~ 60 -80 days.

We must reiterate that the only evidence of the existence of an equatorially-trapped Kelvin wave is (1) eastward propagation, and (2) no coherence in the 35-80 day band between stations within 3° of the equator and off-equatorial stations. The only other possible equatorial waves that could explain the eastward propagation are inertia-gravity waves, in which case $\sqrt{\epsilon}$ would have to be greater than 3.4×10^4 (hence $h < 7.5 \times 10^{-5} \text{ m}$) and the sea level deflection ($\propto \sqrt{h}$) would be undetectable. Given that the 35-80 day oscillation is a Kelvin wave, the rms amplitude of its sea level deflection at Christmas (where the observed $Q \sim 2$)* is $\sim 2 \text{ cm}$. The corresponding rms surface zonal current is $\sim 8 \text{ cm/s}$.

The significantly non-zero coherence between sea level and surface wind components in the 35-80 day band at Canton (Figure 3.30) is evidence that the oceanic Kelvin wave is atmospherically forced. This forcing does not occur in the eastern Pacific, however, since Galapagos sea level is not coherent with the surface winds. The "40-50 day" atmospheric Kelvin wave which dominates the surface zonal wind power spectra in the central-western Pacific (Section 2.D), and also has a surface meridional wind component, is probably an important factor for the existence of the oceanic Kelvin wave, because the energy of the atmospheric wave is concentrated in small positive wavenumbers.

Considering the strength of the atmospheric Kelvin wave in the Indian Ocean (Section 2.D), it seems likely that energetic equatorial waves may also be generated in that ocean. We don't have enough data to test this hypothesis; however, the sea level spectrum from Minicoy (Figure 3.21) is suggestive, having excess energy in the 35-80 day band. It was mentioned

*The smaller Q ($= \frac{\omega_0}{\Delta\omega}$), compared with the inertia-gravity wave Q range of 8-19, is the result of smaller ω_0 , since $\Delta\omega$ is about half the $\Delta\omega$ in the inertia-gravity peaks (ω_0 is the peak-frequency and $\Delta\omega$ is the half-power bandwidth).

in Section 2.D. that Picaut and Verstraete (1976) suspect that the 40-50 day oscillations detected along the coast of the Gulf of Guinea are also generated by the atmospheric Kelvin wave, even though the surface expression of the atmospheric wave is supposed to be weak in the Atlantic Ocean (Madden and Julian (1972a)).

CHAPTER 4

CONCLUSIONS

Over twenty years ago, Groves (1956) postulated that the 4-day peak in the sea level spectrum from Canton was due to oceanic fluctuations that

are coupled to progressive waves in the easterly winds. The greater regularity of the sea level oscillation may be the result of a free period (as yet undiscovered) in this region of the ocean very near four days, which is in forced resonance with the wind wave.

Not until the work of Wunsch and Gill (1976) was Groves' "free period" identified as a baroclinic, equatorially-trapped inertia-gravity wave, and not until this work was it realized that Groves' "progressive waves in the easterly winds" were actually the surface expression of previously-discovered Rossby-gravity waves. We have confirmed the existence of resonant inertia-gravity waves in the mid-Pacific and have moved toward understanding the dynamics and kinematics of these, and other, baroclinic tropical waves.

The zonal variation of the energy of the low-mode inertia-gravity waves that was found in the Pacific (Section 3.D.2) probably indicates a lack of resonance in the far eastern and western equatorial Pacific. Plausible explanations for this zonal variation, utilizing the specific dispersive characteristics of the equatorial waves, (i.e., group velocity zero points) and the zonal amplitude structure of the forcing function, were presented in Section 3.D.11. The discussion emphasizes the gaps in theories which rely upon the assumption of energy concentration near group velocity zero points. The possible role of topography in the observed zonal distribution of energy is relevant to studies of mid-latitude internal waves, which may also have vertical wavenumber spectra dependent upon the local

topography.

A simple spectral model, based on the assumption that the inertia-gravity wave energy is concentrated near zero zonal group velocity points and incorporating the first two baroclinic modes, reproduces the observed mid-Pacific sea level spectra in the 1-6 day band (Section 3.D.12). A comparison was made with a model that specifies the distribution of energy in frequency-wavenumber space without regard for the dispersive properties of the equatorial inertia-gravity waves (Eriksen (1979)). The results clearly show that the dispersion characteristics cannot be neglected.

The model spectra, when computed at latitudes outside the equatorial waveguide of the lowest meridional modes, take on the appearance of "blue-shifted inertial" peaks, as first pointed out by Eriksen (1979). We have observed these inertial peaks in several sea level spectra (Section 3.D.12). These spectra suggest that solutions to the equatorial β -plane equations do not accurately describe the structure of inertial oscillations poleward of 9° from the equator.

The possible existence of resonant, first-baroclinic mode inertia-gravity waves in the Indian Ocean (Sections 3.D.5 and 3.D.12) raises a perplexing question. What is the zonal structure of these inertia-gravity waves, which have wavelengths greater than the width of the ocean?

Pragmatically, many oceanographers will discover that the multi-day period equatorial waves, with their large thermocline fluctuations, are an important "noise" in synoptic studies of longer-period variability of the equatorial circulation.

With respect to the low-frequency dynamics of the equatorial oceans' response to changing winds, the most important discovery here is that fluctuations of sea level along the equator in the 35-80 day band have

Kelvin wave characteristics and, in particular, are found to propagate from the western Pacific to the coast of South America. The Kelvin waves are atmospherically-forced in the central-western Pacific and have a computed equivalent depth corresponding to the first-baroclinic mode. The degree to which energy is lost from the Kelvin waves as they propagate to the east, which might be expected from our previous observation of weak, low-mode, inertia-gravity waves in the eastern Pacific, is not known.

While searching for evidence of inertia-gravity waves near the meridional boundaries, we discovered signs of a 4-6 day oscillation which further investigation revealed to be basin-wide (Section 3.C). The oscillation is a non-static response to forcing by atmospheric pressure. Clear evidence of westward propagation and the lack of nodes led to the conclusion that the oscillation is dominated by the gravest, symmetric, planetary mode of the Pacific. Previously published computations of this mode, for idealized basins with the scale of the Pacific, are in good agreement with the wave characteristics observed here. The low Q of this mode reveals that the ocean is viscous with respect to large-scale barotropic oscillations.

The dynamical components of the sea level fluctuations due to the strongest long-period tides have been isolated for the first time using the "self-consistent" equilibrium tide of Agnew and Farrell (1978). The tides are slightly non-equilibrium with large horizontal scales. The gravest, circulating, Kelvin-like basin modes are definitely not observed, contrary to a postulation by Philander (1978). The relatively short-scale Rossby modes predicted by Wunsch (1967) are also not observed, although the dataset may not be adequate for observing these modes. Considering the low Q of the 4-6 day basin mode, we suggest that dissipation may be controlling the ocean's response to the long-period tidal forcing. The

long-period tides are strong enough so that prior to studying the propagation of equatorially-trapped waves in the 7-30 day band, using sea level observations, the tidal signals must be eliminated.

The oceanic waves, other than the tides, that yielded the strongest signals in the sea level auto- and/or cross-spectra (that is, the 4- and 5-day inertia-gravity waves, the 35-80 day Kelvin waves, and the 4-6 day basin mode), are all clearly atmospherically-forced. Moreover, the Kelvin waves and basin mode probably would not have been detectable if it were not for the fact that each is forced by an atmospheric wave that has structural similarities to the oceanic wave. Consequently, the surface expressions of these atmospheric waves that are strong in the tropics (i.e., 4-5 day Rossby-gravity waves, 40-50 day Kelvin waves and a 5-day global barotropic mode) were investigated with observations of the surface atmospheric fields (Chapter 2).

Much of what we have learned about the atmosphere awaits the construction of an accurate model of the oceanic boundary layer, that couples the surface wind stress to the internal waves. Until then, we cannot significantly improve upon the rough estimate of the transfer coefficients presented by Wunsch and Gill (1976) for inertia-gravity waves (or develop estimates for the other equatorial waves), or test ideas about the efficiency of the atmospheric waves in generating oceanic waves. We suspect that the ambiguous inertia-gravity sea level coherence phases (Section 3.D.7), for example, can be explained only in the context of a fully-forced model.

References

- Abramovitz, M. and I. Stegun, ed. (1972). Handbook of Mathematical Functions. Dover, New York, 1046 pp.
- Agnew, D.C. and W.E. Farrell (1978). Self-consistent equilibrium ocean tides. Geophys. J. Roy. Astr. Soc. 55, 171-181.
- Bell, T.H. Jr., A.B. Hayes and W.P. deWitt (1974). Upper Ocean Stability: a compilation of density and Brunt-Väisälä frequency distributions for the upper 500 m of the world ocean, Vol. I - Profiles; Vol. II - Tables. Naval Research Laboratory, Washington, D.C., NRL Report 7799, 7800.
- Bender, C.M. and S.A. Orszag (1978). Advanced Mathematical Methods for Scientists and Engineers. McGraw-Hill, New York, 593 pp.
- Bingham, C., M.D. Godfrey and J.W. Tukey (1967). Modern techniques of power spectrum estimation. IEEE Trans. on Audio and Electroacoustics AU-15, 56-66.
- Blandford, R. (1966). Mixed gravity-Rossby waves in the ocean. Deep-Sea Res. 13, 941-961.
- Boyd, J.P. (1978). The effects of latitudinal shear on equatorial waves. Part I: Theory and methods. J. Atm. Sc. 35, 2236-2258.
- Briscoe, M.G. (1975). Preliminary results from the trimoored Internal Wave Experiment (IWEX). J. Geophys. Res. 80, 3872-3884.
- Buchwald, V.T. (1973). Long-period divergent planetary waves. Geophys. Fl. Dyn. 5, 359-367.
- Burpee, R.W. (1974). Characteristics of North African Easterly waves during the summers of 1968 and 1969. J. Atm. Sc. 31, 1556-70.
- Burpee, R.W. (1976). Some features of global scale 4-5 day waves. J. Atm. Sc. 33, 2292-99.
- Burpee, R.W. (1977). Large-scale disturbances. In: Report to the U.S. GATE Central Program Workshop. NCAR, Boulder, Col., pp.38-56.
- Cairns, J.L. (1975). Internal wave measurements from a midwater float. J. Geophys. Res. 80, 299-306.
- Capon, J. (1969). High-resolution frequency-wavenumber spectrum analysis. Proc. IEEE 57, 1408-1418.
- Capon, J. and N.R. Goodman (1970). Probability distributions for estimators of the frequency-wavenumber spectrum. Proc. IEEE 58, 1785-1786.

- Cartwright, D.E. (1968). A unified analysis of tides and surges round north and east Britain. Phil. Trans. Roy. Soc. A 263, 1-55.
- Chang, C.-P. (1977). Viscous internal gravity waves and low-frequency oscillations in the tropics. J. Atm. Sc. 34, 901-910.
- Chapman, S. and R.S. Lindzen (1970). Atmospheric Tides. D. Reidel Publ., Dordrecht, Holland, 200 pp.
- Charney, J.G. (1955). The generation of oceanic currents by wind. J. Mar. Res. 14, 477-498.
- Christensen, N. Jr. (1973a). On free modes of oscillation of a hemispherical basin centered on the equator. J. Mar. Res. 31, 168-174.
- Christensen, N. Jr. (1973b). The effect of a coastal shelf on long waves in a rotating hemispherical basin. J. Mar. Res. 31, 175-187.
- Colborn, J.G. (1975). The Thermal Structure of the Indian Ocean. Univ. Press of Hawaii, Honolulu, 173 pp.
- Davis, R.E. and L.A. Regier (1977). Methods for estimating directional wave spectra from multi-element arrays. J. Mar. Res. 35, 453-477.
- Doodson, A.T. (1921). The harmonic development of the tide-generating potential. Proc. Roy. Soc. A 100, 305-329.
- Eckart, C. (1960). Hydrodynamics of oceans and atmospheres. Pergamon Press, Oxford, 290 pp.
- Eriksen, C.C. (1979). Evidence for a continuous spectrum of equatorial waves in the Indian Ocean. In review, J. Geophys. Res.
- Flierl, G.R. (1977). Simple applications of McWilliams' "A note on a consistent quasigeostrophic model in a multiply connected domain." Dyn. Atm. Oc. 1, 443-453.
- Garrett, C. and W. Munk (1972). Space-time scales of internal waves. Geophys. Fl. Dyn. 3, 225-264.
- Gill, A.E. (1974). Spectra of some time series from the equatorial Pacific. Unpublished manuscript.
- Gill, A.E. (1975). Models of equatorial currents, pp. 181-203 in: Numerical Models of Ocean Circulation. National Academy of Sciences, Washington, D.C., 364 pp.
- Godin, G. (1972). The Analysis of Tides. Univ. of Toronto Press, Toronto, 264 pp.
- Groves, G.W. (1956). Periodic variation of sea level induced by equatorial waves in the easterlies. Deep-Sea Res. 3, 248-252.

- Groves, G.W. and F. Griyel (1962). Some relationships between sea level and wind in the equatorial Pacific. Geofis. Int'l. 2, 1-14.
- Groves, G.W. and E.J. Hannan (1968). Time series regression of sea level on weather. Rev. Geophys. 6, 129-174.
- Groves, G.W. and M. Miyata (1967). On weather-induced long waves in the equatorial Pacific. J. Mar. Res. 25, 115-128.
- Groves, G. W. and B.D. Zetler (1964). The cross spectrum of sea level at San Francisco and Honolulu. J. Mar. Res. 22, 269-275.
- Harrison, D.E. (1979). On the equilibrium linear basin response to fluctuating winds and mesoscale motions in the ocean. J. Geophys. Res. 84, 1221-1224.
- Harvey, R.R. and W.C. Patzert (1976). Deep current measurements suggest long waves in the eastern equatorial Pacific. Science 193, 883-885.
- Holton, J.R. (1970). A note on forced equatorial waves, Mon. Wea. Rev. 98, 614-615.
- Holton, J.R. (1975). The Dynamic Meteorology of the Stratosphere and Mesosphere. Meteor. Monogr., No. 37, Amer. Meteor. Soc., 218 pp.
- Hwang, H.J. (1970). Power density spectrum of surface wind speed on Palmyra Island. Mon. Wea. Rev. 98, 70-74.
- Jenkins, G.M. and D.G. Watts (1968). Spectral Analysis and its Applications. Holden-Day, San Francisco, 525 pp.
- Julian, P.R. (1971). Some aspects of variance spectra of synoptic scale tropospheric wind components in mid-latitudes and in the tropics. Mon. Wea. Rev. 99, 954-965.
- Kagan, B.A., V.Y. Rivkind and P.K. Chernyayev (1976). The fortnightly lunar tides in the world ocean. Izv. Atm. Oc. Phys. 12, 274-276.
- Krishnamurti, T.N. and H.N. Bhalme (1976). Oscillations of a monsoon system. Part I: Observational aspects. J. Atm. Sc. 33, 1937-1954.
- Krishnamurti, T.N., C.E. Levy and H. Pan (1975). On simultaneous surges in the trades. J. Atm. Sc. 32, 2367-2370.
- Lamb, H. (1932). Hydrodynamics, 6th ed. Dover, New York, 738 pp.
- Larichev, V. (1974). Statement of an internal boundary problem for the Rossby wave equation. Izv. Atm. Oc. Phys. 10, 470-473.
- Larsen, J.C. (1977). Cotidal charts for the Pacific Ocean near Hawaii using f-plane solutions. J. Phys. Oc. 7, 100-109.

- LeBlond, P.H. and L.A. Mysak (1977). Waves in the Ocean. Elsevier, Amsterdam, 602 pp.
- Lindzen, R.S. (1967). Planetary waves on beta-planes. Mon. Wea. Rev. 95, 441-451.
- Lindzen, R.S. and J.M. Forbes (1978). Boundary layers associated with thermally forced planetary waves. J. Atm. Sc. 35, 1441-1449.
- Longuet-Higgins, M.S. (1964). Planetary waves on a rotating sphere. Proc. Roy. Soc. A 279, 446-473.
- Longuet-Higgins, M.S. (1965). Planetary waves on a rotating sphere, II. Proc. Roy. Soc. A 284, 40-54.
- Longuet-Higgins, M.S. (1966). Planetary waves on a sphere bounded by meridians of longitude. Phil. Trans. Roy. Soc. Lond. A 260, 317-350.
- Longuet-Higgins, M.S. (1968). The eigenfunctions of Laplace's Tidal Equations over a sphere. Phil. Trans. Roy. Soc. Lond. A 262, 511-607.
- Longuet-Higgins, M.S. (1971). On the spectrum of sea level at Oahu. J. Geophys. Res. 76, 3517-3522.
- Longuet-Higgins, M.S. and G.S. Pond (1970). The free oscillations of fluid on a hemisphere bounded by meridians of longitude. Phil. Trans. Roy. Soc. Lond. A 266, 193-223.
- Luther, D.S. and C. Wunsch (1975). Tidal charts of the central Pacific Ocean. J. Phys. Oc. 5, 222-230.
- Madden, R.A. and P.R. Julian (1971). Detection of a 40-50 day oscillation in the zonal wind in the tropical Pacific. J. Atm. Sc. 28, 702-708.
- Madden, R.A. and P.R. Julian (1972a). Description of global-scale circulation cells in the tropics with a 40-50 day period. J. Atm. Sc. 29, 1109-1123.
- Madden, R.A. and P.R. Julian (1972b). Further evidence of global-scale, 5-day pressure waves. J. Atm. Sc. 29, 1464-1469.
- Madden, R.A. and P.R. Julian (1973). Reply to "Comments on 'Further evidence of global-scale, 5-day pressure waves'" (by R.J. Deland). J. Atm. Sc. 30, 935-940.
- Madden, R.A. and J. Stokes (1975). Evidence of global-scale 5-day waves in a 73-year pressure record. J. Atm. Sc. 32, 831-836.
- Maksimov, I.V. (1966). Long-period lunisolar tides in the ocean. Oceanology 6, 20-30.

- Maksimov, I.V., V.N. Vorob'yev and N. P. Smirnov (1967). Study of the nine-day lunar tide in the seas at high latitudes. Oceanology 7, 307-314.
- McPhaden, M.J. and R.A. Knox (1979). Equatorial Kelvin and inertio-gravity waves in zonal shear flow. J. Phys. Oc. 9, 263-277.
- Miles, J.W. (1974). On Laplace's tidal equations. J. Fl. Mech. 66, 241-260.
- Miller, J.C.P. (1972). Parabolic cylinder functions. In: Handbook of Mathematical Functions, Dover, New York, pp. 685-720.
- Miller, S.P. and C. Wunsch (1973). The Pole tide. Nature 246, 98-102.
- Misra, B.M. (1975). Evidence of the 5-day period oscillations in the geopotential field. Tellus XXVII, 469-483.
- Miyata, M. (1970). Complex correlation applied to a sea level study. J. Mar. Res. 28, 202-214.
- Miyata, M. and G.W. Groves (1971). A study of the effects of local and distant weather on sea level in Hawaii. J. Phys. Oc. 1, 203-213.
- Mofjeld, H.O. and M. Rattray, Jr. (1971). Free oscillations in a beta-plane ocean. J. Mar. Res. 29, 281-305.
- Mofjeld, H.O. and M. Wimbush (1977). Bottom pressure observations in the Gulf of Mexico and Caribbean Sea. Deep-Sea Res. 24, 987-1004.
- Moore, D.W. (1968). Planetary-gravity waves in an equatorial ocean. Ph.D. dissertation, Harvard University, 207 pp.
- Moore, D.W. and S.G.H. Philander (1977). Modelling of the tropical oceanic circulation. In: The Sea, vol. VI, Wiley, New York, pp. 319-361.
- Munk, W.H. and D.E. Cartwright (1966). Tidal spectroscopy and prediction. Phil. Trans. Roy. Soc. A 259, 533-581.
- Munk, W.H. and N.A. Phillips (1968). Coherence and band structure of inertial motion in the sea. Rev. Geophys. 6, 447-472.
- Nitta, T. (1970). Statistical study of tropospheric wave disturbances in the tropical Pacific region. J. Met. Soc. Jap. 48, 47-60.
- Palmer, C.E. and W.D. Ohmstede (1956). The simultaneous oscillation of barometer along and near the equator. Tellus VIII, 495-507.
- Parker, D.E. (1973). On the variance spectra and spatial coherences of equatorial winds. Quart. J. Roy. Met. Soc. 99, 48-55.
- Philander, S.G.H. (1976). Variability of the general oceanic circulation in the tropical Atlantic (Preliminary results of the GATE ocean-

- graphic programme). Lecture given at the Joint Oceanographic Assembly, Edinburgh, Sept. 22, 1976.
- Philander, S.G.H. (1978). Forced oceanic waves. Rev. Geophys. Sp. Phys. 16, 15-46.
- Phillips, O.M. (1977). The Dynamics of the Upper Ocean, 2nd ed. Cambridge Univ. Press, Cambridge, 336 pp.
- Picaut, J. and J.-M. Verstraete (1976). Mise en évidence d'une onde de 40-50 jours de période sur les côtes du Golfe de Guinée. Cah. O.R.S.T.O.M., Ser. Oc. 14, 3-14.
- Picaut, J. and J.-M. Verstraete (1979). Propagation of a 14.7-day wave along the northern coast of the Guinea Gulf. J. Phys. Oc. 9, 136-149.
- Platzman, G.W. (1975). Normal modes of the Atlantic and Indian Oceans. J. Phys. Oc. 5, 201-221.
- Rattray, M. Jr. and R.L. Charnell (1966). Quasigeostrophic free oscillations in enclosed basins. J. Mar. Res. 24, 82-102.
- Rhines, P.B. (1969). Slow oscillations in an ocean of varying depth: Part 2. Islands and seamounts. J. Fl. Mech. 37, 191-205.
- Richman, J.G., C. Wunsch and N.G. Hogg (1977). Space and time scales of mesoscale motion in the western North Atlantic. Rev. Geophys. Sp. Phys. 15, 385-420.
- Ripa, P. (1978). Normal Rossby modes of a closed basin with topography. J. Geophys. Res. 83, 1947-1957.
- Shapiro, L.J. (1977). Tropical storm formation from Easterly waves: a criterion for development. J. Atm. Sc. 34, 1007-1021.
- Smart, W.M. (1971). Text-Book on Spherical Astronomy, 5th ed. Cambridge Univ. Press, Cambridge, 430 pp.
- Stevens, D.E. and G.H. White (1979). Comments on "Viscous internal gravity waves and low-frequency oscillations in the tropics" (by C.-P. Chang). J. Atm. Sc. 36, 545-546.
- Taft, B.A., B.M. Hickey, C. Wunsch and D.J. Baker, Jr. (1974). Equatorial Undercurrent and deeper flows in the central Pacific. Deep-Sea Res. 21, 403-430.
- Veronis, G. (1973). Large scale ocean circulation. Adv. in Appl. Mech. 13, 2-92.
- Wallace, J.M. (1971). Spectral studies of tropospheric wave disturbances in the tropical western Pacific. Rev. Geophys. Sp. Phys. 9, 557-612.

- Wallace, J.M. (1973). General circulation of the tropical lower stratosphere. Rev. Geophys. Sp. Phys. 11, 191-222.
- Wunsch, C. (1966). On the scale of the long period tides. Ph.D. dissertation, Massachusetts Institute of Technology, 147 pp.
- Wunsch, C. (1967). The long-period tides, Rev. Geophys. 5, 447-475.
- Wunsch, C. (1972). Bermuda sea level in relation to tides, weather and baroclinic fluctuations. Rev. Geophys. Sp. Phys. 10, 1-49.
- Wunsch, C. (1974). Dynamics of the Pole tide and the damping of the Chandler wobble. Geophys. J. Roy. Astr. Soc. 39, 539-550.
- Wunsch, C. (1976). Notes for equatorial array work. Unpublished manuscript.
- Wunsch, C. (1977). Response of an equatorial ocean to a periodic monsoon. J. Phys. Oc. 7, 497-511.
- Wunsch, C. (1978). Observations of equatorially trapped waves in the ocean: a review prepared for Equatorial Workshop, July 1977, 23 pp. In: FINE Workshop Proceedings, NOVA/N.Y.I.T. Press, Miami.
- Wunsch, C. and A.E. Gill (1976). Observations of equatorially trapped waves in Pacific sea level variations. Deep-Sea Res. 23, 371-390.
- Wunsch, C. and R. Hendry (1972). Array measurements of the bottom boundary layer and the internal wave field on the continental slope. Geophys. Fl. Dyn. 4, 101-145.
- Wyrтки, K. (1975). El Niño-dynamic response of equatorial Pacific Ocean to atmospheric forcing. J. Phys. Oc. 5, 572-582.
- Wyrтки, K. (1977). Sea level during the 1972 El Niño. J. Phys. Oc. 7, 779-787.
- Wyrтки, K. and G. Meyers (1975). The trade wind field over the Pacific Ocean, Part I. The mean field and the mean annual variation; Part II. Bimonthly fields of wind stress: 1950 to 1972. Hawaii Institute of Geophysics, Honolulu, HIG 75-1, HIG 75-2.
- Yanai, M. (1975). Tropical Meteorology. Rev. Geophys. Sp. Phys. 13, 685-710.
- Yanai, M. and M. Murakami (1970). Spectrum analysis of symmetric and antisymmetric equatorial waves. J. Met. Soc. Jap. 48, 331-347.

Biographical Note

Douglas S. Luther was born to Joanne T. and Joseph P. Luther on April 27, 1951, in the city of Lynwood, California. He lived in San Diego for eighteen years, graduating from Point Loma High School in June, 1969. Four years of undergraduate education at the Massachusetts Institute of Technology culminated in the reception of two Bachelor of Science degrees, in geophysics and electrical engineering, in June of 1973. Immediately following graduation, Luther enrolled in the Joint Program in Oceanography, Massachusetts Institute of Technology - Woods Hole Oceanographic Institution.

Publications:

- Luther, D. S. and C. Wunsch (1975). Tidal charts of the central Pacific Ocean. J. Phys. Oc. 5, 222-230.
- Whitehead, J. A. and D. S. Luther (1975). Dynamics of laboratory diapir and plume models. J. Geophys. Res. 80, 705-717.

OF FILM
SE REWIN